FACULTAD DE CIENCIAS

DEPARTAMENTO DE QUÍMICA INORGÁNICA

CARACTERIZACIÓN MECÁNICA DE MATERIALES CERÁMICOS MEDIANTE ENSAYOS DE FRACTURA ESTABLE

Memoria presentada por

Ana García Prieto

Para optar al grado de

DOCTORA EN CIENCIAS QUÍMICAS

Directora:

Dra. Carmen Baudín de la Lastra

Tutora:

Dra. Ana Mª González Vadillo

INSTITUTO DE CERÁMICA Y VIDRIO

CONSEJO SUPERIOR DE INVESTIGACIONES CIENTÍFICAS

MADRID 2015

Esta tesis ha sido realizada en el Departamento de Cerámica del Instituto de Cerámica y Vidrio (ICV) del Consejo Superior de Investigaciones Científicas (CSIC). Se enmarca dentro de los proyectos financiados por el Ministerio de Economía y Competitividad: MCI-MAT2006-13480-C02-01, MCI-MAT2009-14369-C02-01, MCI-MAT2009-14448-C02-01, CICYT-MAT2010-17753 y MAT2013-48426-C2-1-R, por la empresa Microtest S.A.: MCI-PET2008-0113 y por la red CYTED: HOREF312RT0453.

La autora agradece la financiación económica otorgada por el Consejo Superior de Investigaciones Científicas y el Fondo Social Europeo a través de la beca JAPre_2010_00274 para desarrollar esta tesis y para realizar una estancia de seis meses en Oxford University (Reino Unido). Además, agradece a la fundación JECS TRUST la financiación económica para realizar una estancia de tres meses en Montanuniversität Leoben (Austria).

RESUMEN

El objetivo principal de este trabajo ha sido el desarrollo de un nuevo dispositivo experimental y una metodología de ensayo y análisis de resultados para determinar la tenacidad de fractura de materiales cerámicos, que puedan ser utilizados como forma de caracterización de rutina en el laboratorio.

Se ha planteado como hipótesis básica la adecuación de los ensayos de fractura estable para la determinación de la tenacidad de fractura de los materiales.

Se ha propuesto la utilización de la apertura de los labios de la grieta como parámetro de control puesto que, junto con el tamaño de la grieta, crece de manera monótona durante todo el ensayo (carga y fractura).

Hasta la fecha de inicio de este trabajo sólo se habían reportado ensayos de fractura estable con control por apertura de los labios de la grieta en el caso de materiales no frágiles como ytria (Y-PSZ) y hormigones de alta resistencia.

El dispositivo experimental consta de un micrómetro óptico asociado a un dispositivo de flexión en tres puntos y se ensayan probetas prismáticas con entallas rectas en forma de V (SEVNB).

Con el fin de demostrar la validez del dispositivo experimental y la metodología de ensayo y análisis de resultados desarrollados, se ensayaron materiales cerámicos con comportamientos mecánicos muy diferentes:

Espinela de aluminio-magnesio ($MgAl_2O_4$), con comportamiento frágil.

Alúmina (Al_2O_3) de grano fino, con comportamiento frágil.

Mullita ($3Al_2O_3{\cdot}2SiO_2$), con comportamiento frágil y crecimiento subcrítico de grietas en aire significativo.

Refractarios comerciales, en los cuales ocurren mecanismos de refuerzo durante la fractura.

En todos los casos se alcanzaron ensayos de fractura estable demostrándose así la adecuación de la utilización de la apertura de los labios de la grieta como parámetro de control.

Se estudió la influencia de las condiciones experimentales en la tenacidad de fractura. La utilización de la apertura de los labios de la grieta como parámetro de control minimiza el efecto de factores como la inercia de la máquina y permite identificar el crecimiento subcrítico de grietas.

El valor del factor crítico de intensidad de tensiones en modo I, K_{IC}, obtenido a partir de ensayos estables es considerablemente inferior al obtenido a partir de ensayos inestables.

A partir de los ensayos de fractura estable fue posible obtener, además del K_{IC}, la energía de fractura, que caracteriza todo el proceso de fractura. No es posible obtener este parámetro a partir de ensayos inestables.

Una vez demostrada la validez del dispositivo experimental y de la metodología de ensayo y análisis de resultados desarrollados, se prepararon y caracterizaron materiales nanocompuestos de Al_2O_3/SiC y se ensayaron según la metodología propuesta, aportando valores de tenacidad de fractura desconocidos hasta la fecha. Estos resultados permitieron establecer las relaciones microestructura-comportamiento mecánico en los nanocompuestos de Al_2O_3/SiC.

Los resultados obtenidos para el sistema modelo Al_2O_3/SiC permiten inferir que la metodología de ensayo y análisis de resultados desarrollados son adecuados para la caracterización de otros nanocompuestos cerámicos.

NOTACIONES

a: Crack length / Longitud de la entalla (Figura 3.3)

B: Beam thickness / Espesor de la probeta (Figura 3.3)

CMCs: Ceramic Matrix Composites / Compuestos de matriz cerámica

CMOD: Crack Mouth Opening Displacement / Apertura de los labios de la grieta

CMOS: Complementary Metal Oxide Semiconductor / Semiconductor complementario de óxido metálico

CNB: Chevron Notched Beam / Probetas con entalla triangular "Chevron"

CT: Compact Tension / Tensión compacta

D: Displacement / Desplazamiento

d_{50}: Average grain size / Tamaño de grano medio

DCB: Double Cantilever Beam / Probetas de doble voladizo

DE: Digital Edge-detection / Procesador digital de borde

DT: Double Torsion / Doble torsión

E: Young's modulus / Módulo de Young

E': Generalized Young's modulus / Módulo de Young generalizado

E.d.: Experimental details / Detalles experimentales

ESIS: European Structural Integrity Society / Sociedad Europea de Integridad Estructural

G: Energy release rate / Tasa de liberación de energía

G_c: Critical energy release rate / Tasa crítica de liberación de energía

G_{Ic}: Critical energy release rate in mode I / Tasa crítica de liberación de energía en modo I

G_F: Specific fracture energy / Energía específica de fractura

G_F/G_{IC}: Toughness, flexibility or apparent ductility ratio

G_∞: Energy release rate in the stationary state of R-curve / Tasa de liberación de energía en el estado estacionario de la curva R.

GPSSN: Gas Pressure Sintered Silicon Nitride / Nitruro de silicio sinterizado en atmósfera gaseosa

HL-CCD: High speed Linear-Charge Coupled Device / Dispositivo de cargas eléctricas interconectadas de alta velocidad lineal.

HPSN: Hot Pressed Silicon Nitride / Nitruro de silicio prensado en caliente

IET: Impulse Excitation Technique / Técnica del impulso de excitación

IT: Indentation toughness / Tenacidad de fractura determinada por métodos de indentación

ISB: Indentation Strength in Bending

K: Stress intensity factor / Factor de intensidad de tensiones

K_I: Stress intensity factor in mode I / Factor de intensidad de tensiones en modo I

K_{Ic}: Critical stress intensity factor in mode I / Factor crítico de intensidad de tensiones en modo I

K_{I0}: Crack tip toughness

K_∞: Stress intensity factor in the stationary state of R-curve / Factor de intensidad de tensiones en el estado estacionario de la curva R

L: Span between loading supports / Distancia entre apoyos inferiores (Figura 3.3)

LED: Light-Emitting Diode / Diodo emisor de luz

LEFM: Linear Elastic Fracture Mechanics / Mecánica de la Fractura Elástica y Lineal

m: Weibull parameter / Parámetro de Weibull

MgO-PSZ: Mg-partially stabilized zirconium oxide / Circona parcialmente estabilizada con magnesia

P: Load / Carga aplicada

P_{max}: Maximum load point / Carga máxima

R curve: Resistance to crack growth / Resistencia al crecimiento de grieta

ROR: Ring-on-Ring method

s: Brittleness number / Número de fragilidad

SCG: Subcritical Crack Growth / Crecimiento Subcrítico de Grietas

SCF: Surface Crack in Flexure / Flexión con una grieta superficial

S.D.: Standard Deviation / Desviación estándar

SENB: Single Edge Notched Beam / Probetas con entalla recta

SEVNB: Single Edge Vee-Notched Beam/Probetas con entalla recta en forma de V

SEPB: Single Edge Pre-cracked Beam / Probetas con pre-entalla recta

SSiC: Sintered Silicon Carbide / Carburo de silicio sinterizado

t: Time / Tiempo

t_f: Fracture time / Tiempo de fractura

T.D.: Theoretical Density / Densidad teórica

TC6: Technical Committee "Ceramics" of the ESIS in Working Area 6

Y: Adimensional factor / Factor adimensional

YTZP: Yttria-stabilised tetragonal zirconia / Circona tetragonal policristalina estabilizada con itria.

W: Specimen width / Anchura de la probeta (Figura 3.3)

4-pb: Four-point bending / Flexión en cuatro puntos

3-pb: Three-point bending / Flexión en tres puntos

α: Relative notch depth / Longitud de entalla relativa

α_c: Critical relative notch depth / Tamaño de entalla crítico relativo

δ: Specimen's deflection / Deflexión de la probeta

δ_s: Specimen's deflection with crack/ Deflexión de la probeta con grieta

δ_m: Machine deflection / Deflexión del dispositivo experimental

ε_f: Unit deformation / Deformación unitaria

γ: Fracture energy / Energía de fractura

γ_0: Thermodynamic surface energy / Energía superficial termodinámica

γ_{eff}: Effective surface energy / Energía superficial efectiva

γ_{nbt}: Energy for crack initiation / Energía para la iniciación de la grieta

γ_p: Plastic deformation at the crack tip / Deformación plástica en el fondo de entalla

γ_{wof}: Work of fracture / Trabajo de fractura

λ: Adimensional compliance / Flexibilidad adimensional

λ_s: Adimensional compliance of the specimen / Flexibilidad adimensional de la probeta

λ_m: Adimensional compliance of the device / Flexibilidad adimensional del dispositivo

ν: Poisson's ratio / Coeficiente de Posisson

ρ: Notch tip radius / Radio de curvatura del fondo de entalla

σ: Stress or strength / Tensión

σ_f: Fracture strength / Tensión de fractura

σ_0: Weibull characteristic strength / Tensión característica de Weibull

En el capítulo 6 de materiales refractarios:

S: materiales refractarios de sílice

AS: materiales refractarios de alúmina-sílice

AZS: materiales refractarios de alúmina-zirconia-sílice

C: hormigones de alta alúmina

ÍNDICE DE CONTENIDOS

Capítulo 1
INTRODUCTION

1. INTRODUCTION

There are many different definitions for the term “ceramics” or “ceramic materials”. The traditional and most accepted one is that of ceramic materials being non-metallic inorganic solids obtained through thermal treatments[1]. This definition would have to be broadened to include the large series of ceramics that acquire their properties once installed, such as refractory concretes or magnesia-carbon refractories. Conventional solid-state reactions between oxides and/or carbonates at high temperatures produce relatively coarse, impure and agglomerated particles. However, the development of soft chemistry routes is a promising alternative for the synthesis of highly pure and homogeneous ceramic materials in controlled particle size and morphology at low reaction temperatures.

According to their applications ceramic materials may be classified in traditional and advanced ceramics. Traditional ceramics include porcelains (pottery, floor tiles, sanitaryware,…), refractories and building materials (bricks and roof tiles,...).

Advanced ceramics are materials obtained through substantial refining of the initial raw materials in order to achieve specific functions for each application[1]. Advanced ceramics are usually classified in structural and functional materials. The main aim of structural materials is to stand mechanical stresses at room or at high temperatures. Functional ceramics are materials with specific functions such as, biomedical, electric, electronic and magnetic applications amongst others.

In ASTM C1145:2013[2] advanced ceramic is defined as a highly engineered, high-performance, predominately non-metallic, inorganic, ceramic material having specific functional attributes.

According to ISO 20507:2014[3] and EN ISO 15732:2005[4] the use of terms as fine ceramic, advanced ceramic and advanced technical ceramic is interchangeably accepted

in business, trade, scientific literature and International Standards. In this work, the terms advanced ceramics and advanced technical ceramics will be used.

Ceramic materials have a series of advantages in comparison with metallic and plastic materials, such as chemical stability, resistance to corrosion and wear and the fact that they maintain high resistance to deformation at temperatures at which other materials develop generalized flow phenomena.

Main drawback is their brittleness and associated lack of reliability. Therefore, the definition and measurement of the mechanical properties of ceramic materials is a basic problem in experimental mechanics and in materials science. The data obtained can be used in specifying the suitability of structural and functional materials for many applications and for understanding their mechanical behaviour.

1.1. Basic fracture-mechanics parameters for brittle materials

The study of the mechanical behaviour of ceramic materials has attracted a notable part of the attention of the scientific community since the early ages of the existence of these materials as cutting tools or structural components in houses. The wide field of application of ceramic materials and their use in our routine lives as structural and functional components make necessary a detailed analysis of the causes that produce their failure.

Reviews about mechanical behaviour of structural ceramics can be found in references 5-7[5-7]. The type of fracture of a material subjected to stress is determined by its capacity to deform plastically. Due to the highly directional covalent-ionic bond in ceramic materials, they are characterized by the absence of significant plastic deformation up to relatively high temperatures. Thus, the form of fracture of ceramic materials is fundamentally brittle. There are three fracture modes: mode I or tensile opening (tension normal to the crack plane), mode II or in-plane shear (shear loading in

crack direction) and mode III or out-of-plane shear (loading). Ceramics usually fail in mode I (Figure 1.1).

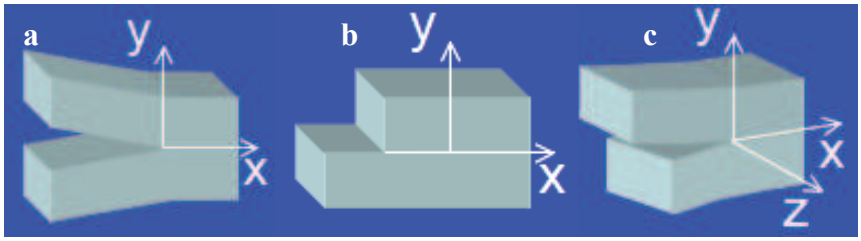

Figure 1.1: The three fracture modes[8]:
a) Mode I: Opening mode.
b) Mode II: In-plane shear mode.
c) Mode III: Out-of-plane shear mode.

Brittle behaviour is characterized because the stress level at which fracture starts is determined by the presence of defects which act as stress concentrators, producing the catastrophic failure in the material. Thus, the strength of ceramic materials is an extremely variable property, which depends on the shape and size of defects present in their interior and on their distribution and orientation relative to the applied load. Thus, the strength values are much lower than the theoretical fracture stress, or stress necessary to separate two atomic planes of the material.

The mechanical resistance of ceramics to catastrophic failure may be described by the fracture toughness which is defined as the material's resistance to the propagation of defects, determined by its microstructure and independent of the particular flaws present in it. Contrarily to the strength, the toughness of brittle materials is an intrinsic property.

There are two basic approaches to the concept of fracture toughness: the global approach based on an energy criterion and the local approach based on the evaluation of the distribution of stresses around a flaw, or criterion based on the stress intensity factor, K.

The energy criterion for fracture was formulated by Griffith who solved the problem of evaluating the fracture resistance of brittle materials by addressing the two-

dimensional situation of an infinite sheet with a crack, and considered the energy involved in the creation of new surfaces[9]. According to Griffith's energy criterion, the propagation of a crack is governed by the relationship between the elastic deformation energy stored in the system which contains the crack and the surface energy required to form new surfaces, G, which is denominated specific fracture energy or energy release rate. For mode I failure, when the elastic energy stored equals G_{IC}, the critical energy release rate in mode I, fracture starts. G_{IC} is the energy released by unit of extension of the crack front and by unit of body thickness, and is equal to twice the thermodynamic surface energy (γ_0) for brittle materials, ($G_{IC} = 2\gamma_0$). Thus G_{IC} is an intrinsic property which characterizes the material's fracture toughness deriving from the energy criterion.

Davidge[10] and Orowan[11] extended the Griffith's approach indicating that the surface energy of fracture in real materials is higher than the thermodynamic surface energy (γ_0), due to deviations from ideal perfectly brittle behaviour. Consequently, the fracture of the material is determined by a global energy term, γ, named effective surface energy (γ_{eff}) by these authors[10,11], which is defined as the energy necessary to initiate the crack propagation and is determined by the sum of the contribution of the thermodynamic surface energy (γ_0) and the plastic deformation at the crack tip (γ_p), ($\gamma = \gamma_0 + \gamma_p$).

Sakai and Bradt[12] proposed that, in addition to the thermodynamic surface energy (γ_0) and the energy associated to plastic yielding in frontal process zone, energy might be released by other processes such as crack deflection by interface debonding, microcracking in frontal process zone, dilatant phase transformation and/or microcracking in wake region, fibre bridging, grain bridging and interlocking, viscoelastic bridging and other phenomena, such as heat or sound, which are difficult to quantify.

The value of γ is conditioned by grain size and fracture mode, since the energy consumed during the transgranular fracture is different from the energy of fracture through the grain boundary[10,13] , and the length of the actual crack path would depend on fracture mode. Because of the diversity of contributions affecting γ, it is impossible to quantify theoretically its value in polycrystalline materials, consequently it has to be determined experimentally.

The approach based on the stress intensity factor was first developed by Irwin[14] in 1957, who used Westergard's previous research[15] as a basis of his work. According to this approach, in a piece of material subjected to a stress, σ, the stresses and deformations at the crack front are related by a universal proportionality factor called stress intensity factor. For ceramic materials which fail in mode I, the stress intensity factor is determined by equation 1.1:

$$K_I = Y\sigma\sqrt{a} \tag{1.1}$$

where, K_I, is the stress intensity factor in mode I, a, is the crack (or any pre-existing defect characteristic[16]) length and, Y, is an adimensional factor depending on the geometry of the loading system and the crack. The crack is propagated when the stress intensity factor reaches a critical value, K_{IC}, which depends exclusively on the material, thus, K_{IC}, is a measure of the material's fracture toughness.

A dimensional analysis, conducted by Irwin[17], considered that fracture starts when the stress, σ, and the stress intensity factor in mode I, K_I, reach their critical values, σ_f (fracture strength) and K_{IC} (critical stress intensity factor in mode I). Therefore, the fracture strength, σ_f, of a given ceramic specimen will be given by equation 1.2:

$$\sigma_f = \frac{K_{IC}}{Y\sqrt{a}} \tag{1.2}$$

The dependence described by equation 1.2 allows establishing a relationship of similarity between fracture toughness deriving from the energy criterion and that deriving from the criterion based on the stress intensity factor and, thus, the equivalence of the two criteria by equation 1.3:

$$G_{IC} = \frac{K_{IC}^{\ 2}}{E'} \tag{1.3}$$

where E' is the generalized Young's modulus, $E'=E/(1-\nu^2)$ for plane strain and $E'=E$ for plane stress (E is the Young's modulus and ν is the Poisson's ratio).

The fracture toughness of brittle materials would be characterized by any of these parameters K_{IC} or G_{IC} ($=2\gamma$). These two parameters are defined at the start of propagation of the crack and are intrinsic properties of the brittle materials, which do not depend on the load system or on the geometry of the cracks.

The critical parameters, σ_f, G_{IC} and K_{IC} provided the basis of the first theories of fracture. However, it is now well recognised that failure of ceramics can occur even for stresses well below the strength of the material. Indeed, K_{IC} (G_{IC}, σ_f) only represent a critical level for catastrophic crack growth. Ceramic materials are susceptible to slow crack propagation at K_I values under K_{IC}; this phenomenon is often referred as 'subcritical crack growth' (SCG). K_{I0} defines a K_I threshold below which no crack propagation occurs. SCG is notable for its extreme sensitivity to applied load and environment, temperature, and other extraneous variables. That means that under appropriate conditions, cracks keep on growing for some time until they cause fracture without warning. Since it is not possible to avoid completely imperfections and microcracks during the production of sintered ceramic materials, cracks might always grow in a slow manner before catastrophic failure[16,18].

1.2. Toughened ceramics

As discussed above, the relatively low and highly variable strengths of ceramics are the main drawback for their extensive use in engineering applications involving severe mechanical solicitations.

In the past, much of the effort to improve the mechanical behaviour of ceramics was placed in producing the highest degree of homogeneity in bulk monophase materials with very small flaws. However, in the last three decades new strategies directed towards the toughening of materials have been developed. Toughening is reached by the development of new microstructures and/or textures in single phase (i.e. silicon nitride and zirconia) or composite (monolithic or formed by a combination of layers of different microstructures) materials.

In particular, the toughening of silicon nitride is usually achieved by a highly anisotropic microstructure where elongated grains tend to be aligned[19]. Toughening of zirconia occurs when the particles are in the metastable tetragonal form[20]. Monolithic ceramic composites are being fabricated using hierarchical structures through artificial methods mimicking natural bio-structures, which significantly overcome the failure behaviour of the individual components. Besides, materials formed by a combination of layers of different microstructures and materials fabricated by directional solidification of compositions close to eutectic ones offer improved behaviour in comparison with the behaviour of monolithic materials. Another relatively new field of investigation, initially proposed by Niihara[21], is that of ceramic nanocomposites with a submicron and/or nanometric scale dispersed second phase which show an increase of the strength and wear performance as compared to that exhibited by the matrix materials[21,22]. The nanocomposite ceramics will be described further in section 7.

Toughening mechanisms reduce the characteristic brittle behaviour of ceramic materials by raising the inelastic deformation processes during the fracture. Main toughening mechanisms have been reviewed by different authors[7,23-25]. A most useful classification of the toughening mechanisms is the one done attending to their range of action (Figure 1.2).

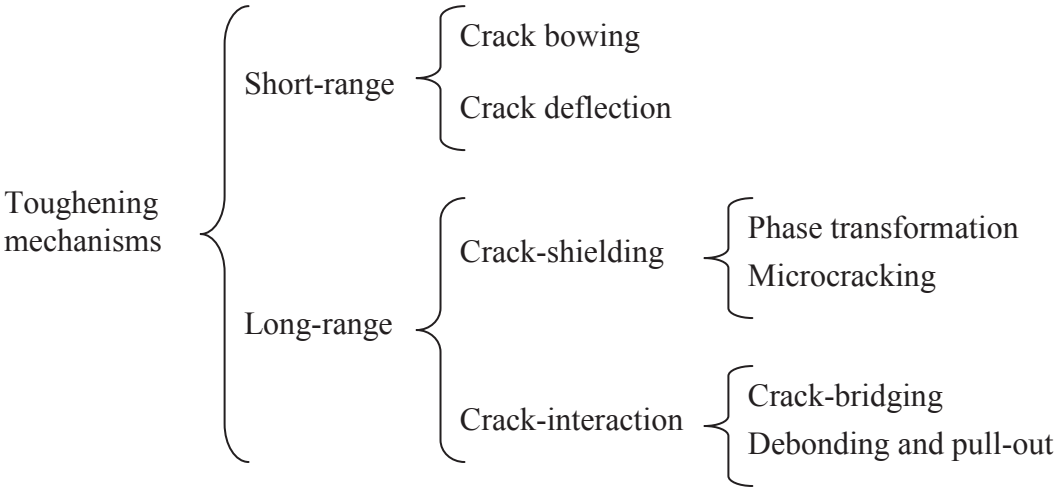

Figure 1.2. Scheme of the main toughening mechanisms attending to their range of action.

Short-range mechanisms are those which radii of action affect a zone of the microstructure of size smaller or of the same order as the material's microstructural characteristics. Thus, the interaction of the crack with the microstructure is practically limited to the crack tip. Such mechanisms cannot be identified if the crack lengths are longer than the size of the microstructural characteristics and can only produce limited flaw tolerance. Crack bowing and crack deflection are short-range toughening mechanisms.

Crack bowing appears when the front of the crack is stopped at several points due to the presence of inclusions of a second phase or heterogeneities of the matrix itself. The crack front curves because the part of the crack front which is not held back continues to advance and, it is necessary to impose higher stress to propagate it. The increase in

toughness produced while the crack is being bowed depends on the volumetric fraction of obstacles present, their shape and their toughness[24].

Crack deflection consists in changes in the direction of crack propagation. Such changes are determined by the presence of easy cleavage planes and/or residual thermal stresses in single phase ceramics and by the characteristics of the phases and the boundaries between different phases in ceramic composites. Crack deflection produces rough fracture surfaces. The effectiveness of crack deflection as a toughening mechanism depends on the shape, the density and the distribution of the deflecting objects but not on their size, and is a maximum for particles with a disk-like shape or elongated bars[24].

Long-range mechanisms are processes which occur around the crack tip and surrounding the crack wake and can produce extensive flaw tolerance. These mechanisms can be subdivided into crack-shielding and crack-interaction mechanisms. There are two kinds of processes that can be responsible for crack-shielding, they are phase transformation and microcracking[23,24]. Crack bridging and debonding and pull-out are mechanisms of crack-interaction.

In the crack-shielding mechanisms irreversible processes lead to microstructural changes that surround the crack wake as the crack propagates. These processes are activated in the process zone which is the area surrounding the crack tip. They give rise to dilatation which is transmitted in the form of compressive forces on the crack lips while the crack propagates[7].

In ceramics, the most representative example of phase transformation with large increases in toughness is the expansive transformation of zirconia from tetragonal to monoclinic phase induced by the stress field of a crack and accompanied by an increase in volume of 3-5%[23,24,26-28].

The opening of microcracks[7] under the action of the applied stress also leads to a volume increase around the crack. Moreover, when microcracking occurs the microcracked zone presents a lower elastic modulus than the rest of the material which contributes to the effect of shielding of the main crack because of the reduction of the elastic energy at the crack tip[23]. Anisotropy in thermal expansion in monophase materials, the presence of secondary phases with different coefficient of thermal expansion from that of the matrix and/or phase transformation may be the origin of the residual stresses that define the appearance of microcracks in the main crack's stress field. The increase in toughness produced by crack-shielding mechanisms depends on the density of elements which produce irreversible deformation, and the size and shape of the process zone[7].

In the other large group of long-range toughening mechanisms, crack interaction mechanisms, the increase in resistance to the propagation of cracks occurs as a result of the union of the fracture surfaces by means of microstructural objects, called ligaments[25,26]. Thus, additional energy is required to separate the fracture surfaces[26,29].

Crack bridging[7] occurs when the element acting as a ligament deforms elastically during the opening of the main crack until it breaks. The increase in toughness is determined by fracture stress, the elastic modulus and the size of the ligament. Toughening by crack-bridging is conditioned by the state of residual stresses of the particle and the matrix, since it determines whether the crack surrounds or draws nearer to the toughening ligament.

If, in addition to the effect of the union of the crack surfaces, the ligaments are debonded and pulled-out, the increase in toughness can be much greater. This contribution increases with the length of the ligaments and can occur at a relatively long distance from the main crack front[30].

In toughened ceramics whose behaviour cannot be regarded as complete brittle, the parameters deriving from linear elastic mechanics to characterize fracture toughness, K_{IC} or G_{IC} are not intrinsic properties. Thus, in this type of materials, specific treatment of fracture parameters is required[31-33]. One proposal is to extend the principles of linear elastic fracture to situations where the inelastic deformation occurs prior to fracture, so that fracture toughness can be determined. Parameters like resistance to crack growth, R-curve, and J integral arise from this approach.

The R-curve has been extensively used to characterize the fracture toughness of ceramic materials in which long-range toughening mechanisms are operative. To build the R-curve, the values of the parameters of linear elastic fracture mechanics, K_{IC} or G_{IC} are determined in standard tests conducted with long cracks and are represented as a function of crack size. The R-curve will show a rising part as long as the energy-consuming processes behind the crack tip (process wake zone) are taking place. Then, the R-curve will evidence a decline when the process zone ahead the crack tip arrives at the specimen edge.

Materials where long-range toughening mechanisms act show rising R-curves, as a result of the activation of the different mechanisms as the crack grows, until toughness reaches a stationary state (K_∞ or G_∞); from this point no new contributions are made to increase in toughness. The maximum value of toughness reached does not only depend on the materials, but also on the loading system, the size of the crack and its history prior to propagation.

When only short-range mechanisms act, toughness is determined by the details of the microstructure ahead the crack tip. As the crack grows, it intercepts different grains and grain boundaries, with different orientations from those on the original crack plane. Thus, toughness increases with the size of the crack until it reaches the value

corresponding to the polycrystalline material. From this moment, the crack can be treated macroscopically as if it were propagating in a homogeneous and isotropous body. Thus, the R-curve rise is extremely step because toughening occurs at the microstructural level, and it is not detected in standard tests for determining toughness using long cracks[23,26].

Unlike fracture toughness, the specific fracture energy, G_F, is defined as the average value of external work consumed to produce a crack unit during quasi-static fracture. Experimentally, it is determined on the basis of area under the load-displacement of the load point curve, obtained during stable tests, where all the work done produces new fracture surfaces. The work done is divided by the size of the fracture surface, which means that specific fracture energy is an average value for the entire fracture process. The advantage of this energy parameter is that it does not require any assumptions about the constitutive equation of the body with the crack to discuss its propagation[34]. Thus, it can be used to describe behaviours which separate from linearity and it is an additive parameter which makes it possible to quantify the different contributions to energy dissipation during fracture.

In refractory literature $G_F/2$ is usually called work of fracture, γ_{wof}. There has been a lot of research on the definition of γ_{wof} and the establishing of experimental methods for its determination, that will be discussed further in the corresponding section (section 6).

1.3. Determination of fracture toughness of ceramics

The high variability in flexural strength values for ceramic materials highlights the necessity to determine intrinsic fracture parameters, quantifying toughness; such as the critical stress intensity factor in mode I, K_{IC}, or the fracture energy, γ. The development of techniques to achieve accurate toughness values is critical to allow the use of ceramic materials in structural and functional applications.

1.3.1. Unstable fracture testing

Most toughness characterisation of ceramics is done in terms of the critical stress intensity factor in mode I, K_{IC}, using Linear Elastic Fracture Mechanics (LEFM) (Eq. 1.2). Basic assumptions for LEFM are that materials are homogeneous and isotropic with no discontinuities and analytic equations have been developed for cracks with zero tip radius.

In conventional K_{IC} testing a specimen with a notch of known geometry and size is subjected to increasing deformation until catastrophic failure occurs. Consequently K_{IC} can be measured if the load amplitude, the geometry factor and the length of the crack associated with the notch can all be determined at the moment of instability. Additionally, calculation of K_{IC} from the size of cracks emanating from indentations has extensively used to characterise ceramics (Indentation toughness, IT). This technique is attractive due to the small amount of volume of material needed; however, it presents increasing uncertainties as the microstructure of the materials separate from the continuous. A review on this technique raising the potential problems associated was published by Quinn and Bradt in 2007[35]. Indentation fracture (IF), is a technique in which the length of cracks emanating from the corners of a Vickers indentation is measured, according to EN 14425-1[36].

Fracture toughness tests of ceramics are usually performed in universal testing machines by subjecting the specimens located between the loading supports to increasing deformation by means of the displacement of the loading frame. This displacement can be controlled directly by imposing a constant rate to the movement of the frame and, thus, to the loading point (displacement control). Additionally, the movement of the frame can be indirectly controlled using increasing rates of different parameters such as the load (load control), the deflection of the specimen directly

measured at its central point in bending specimens (deflection control) and any parameter associated to the growth of the crack, such as the crack length or the Crack Mouth Opening Displacement (CMOD control). The simplest and therefore most widely used testing conditions involve the control by increasing rates of displacement or load.

There is not a unique method for K_{IC} determination and standardisation is relatively recent and practically limited to technical ceramics. All standards deal with beams tested in flexure. The series EN 14425 1-5:2004 'Advanced technical ceramics - Test methods for determination of fracture toughness of monolithic ceramics' contains five parts: Part 1[36]: Guide to test method selection. Part 2[37]: Single-edge pre-cracked beam (SEPB) method, equivalent to ISO 15732:2003[38]. Part 3[39]: Chevron notched beam (CNB) method, EN 14425-3:2010. Part 4[40]: Surface crack in flexure (SCF) method, equivalent to ISO 18756:2003[41]. Part 5[42]: Single-edge vee-notch beam (SEVNB) method, equivalent to ISO 23146:2012[43]). When reviewing papers on mechanical characterization of technical ceramics, it is observed that results for nominally the same material can differ up to 300% depending on the laboratory[44]. Such a large dispersion is partially due to the different microstructures that might present ceramic materials as a function of processing and to the different testing conditions. However, even specimens of the same material tested using the same geometry and strain rate, difficulties associated to specimen machining and crack introduction might lead to variability.

Due to the difficulties involved in machining ceramic parts with special shapes as well as to the tendency of brittle materials to fail under shear stresses originated by deficient clamping and/or alignment, the most widely geometry used for K_{IC} determination of advanced technical ceramics and refractories is that of parallelepiped bars subjected to bending in three or four points. In addition to the easiness of specimen

machining, bending of bars require simple testing setups[7]. Moreover, the analysis of such geometries is simple in comparison with other techniques as, e.g., the double torsion configuration[45].

The generation of suitable cracks is a fundamental requirement for the validity of the tests. In most cases, the cracks may be starting from indentations -Vickers or Knoop- or notches - straight or Chevron (triangular)-. The advantage of cracks introduced by indents is that they have small openings, in agreement with the requirements derived from LEFM. However, such small openings can be a disadvantage for the precise measurement of the crack size. An alternative way is to introduce a "pop-in" crack by controlled propagation of an existent notch or indentation crack (Single Edge Pre-cracked Beam, SEPB). This technique is adequate to introduce real cracks in the specimens; however, it presents experimental problems for brittle materials because of their proneness to uncontrolled crack growth[46]. Other technique is the Indentation Strength in Bending (ISB) which consists in precrack the tensile surface with a Vickers indenter and then test the beams in 3-point, 4-point or biaxial bending tests. The residual stress fields developed by indentation are not removed.

Even tough a round robin performed on technical ceramics[47] demonstrated the adequacy of indentation for crack initiation, which is nowadays standardised (SCF, EN 14425-4:2004)[40], the analysis of indentation cracks implies some uncertainties. The shape of cracks starting from indentations might not be well known, resulting in an uncertain geometry factor. Furthermore, as a consequence of the plastic deformation zone underneath the indent, undetermined internal stresses which would add to the applied ones might occur. Thus, σ_f, Y, and, a, in equation 1.2 cannot be exactly determined. Thermal treatments to eliminate the residual stresses and grinding the specimen surface to eliminate the plastically deformed zone are the two methods

proposed to partially overcome the problems associated with indentation induced cracking. Annealing or heat treating is not permitted by the standard EN 14425-4:2004[40] due to the risk of crack tip blunting or crack healing.

The use of beams with chevron notches has also been standardised for technical ceramics (CNB, EN 14425-3:2010)[39]. However, there are some practically unsolved problems regarding this technique. The geometry of cracks produced by loading a chevron notch is not exactly known and the crack length can not precisely be measured. Moreover, the introduction of chevron notches involves great difficulty in the control of the size of the crack generated and to ensure that the beams, made of brittle materials, do not break when the crack is being introduced[48-49].

Parallelepiped beams with straight through notches at their centre are usually called Single Edge Notched Beams (SENB). When the notch tip has been sharpened, specimens are called SEVNB, to account for the "V" shape of the notch. SENB and SEVNB are the specimen-crack geometries most commonly used to determine K_{IC} in flexure.

1.3.2. Flexure of Single Edge V Notched Beams

The straight through notches are the simplest to introduce and their geometry is well defined[45].

In general, they are produced by means of cutting tools such as thin grinding wheels or diamond discs, threads and cutters. The stress concentration at the notch tip might be weaker than that of a crack for finite notch radius, which might lead to a systematic overestimation of the fracture toughness, since additional energy is spent for the formation of a sharp crack from the blunt notch[50].

The Technical Committee "Ceramics" (TC 6) of the European Structural Integrity Society (ESIS) organized a round robin (1993-1994) on the determination of fracture

toughness of technical ceramic materials at room temperature, results which were summarized in Primas and Gstrein work[51]. Five technical ceramics -Al_2O_3, hot pressed Si_3N_4 (HPSN), sintered SiC (SSiC), Mg-partially stabilized ZrO_2 (MgO-PSZ) and Y_2O_3-tetragonal ZrO_2 polycrystal (YTZP)- were tested with five testing methods -chevron notched beam (CNB) in four point bending, direct measurement of the cracks emanating from a Vickers indentation (IF), indentation strength in four-point bending (ISB), single edge precracked beam (SEPB) in four-point bending, and single edge notched beam (SENB) in four-point bending- by eighteen laboratories. Main conclusion was that the measured fracture toughness value depends on the testing method and testing conditions. Regarding the testing methods, the SENB method produced the most reliable results for notch tip radius, ρ, below a critical one which depended on the tested material. Variability for SENB K_{IC} values ranged from 6% for Al_2O_3 (K_{IC} = 3.17 ± 0.19 MPa $m^{1/2}$) to 16% for HPSN (K_{IC} = 7.48 ± 1.22 MPa $m^{1/2}$). In the conclusions TC6 raised the problem associated to the experimental determination of the critical ρ for each material. At the time, notches were produced by sawing and their tips were relatively large. In this round robin, notches were introduced with diamond blades of width ≈ 100 μm with grains of 20-30 μm and the requirement to consider valid tests (notch width of 75 ± 25μm) could not be fulfilled by a number of participants. A critical ρ around 100 μm was found for the alumina material which had coarse microstructure (average grain size of 16 μm).

The dependence of K_{IC} on notch tip radius for notches introduced with diamond blades has been reported for different materials[50,52-55]. In particular, it is especially significant for phase transformation toughened ceramics[54] (section 1.2) that develop a crack shielding zone due to notch machining.

In order to overcome problems due to finite notch tip radii, Nishida et al.[55] introduced the technique of sharpen the notch tip by means of a razor blade sprinkled with diamond paste. A conventional notch is introduced with a blade in the first step and then, a sharp V-shaped notch is produced by using a razor blade and diamond paste. These authors claimed that notch tip radii as small as 2 μm over the entire width of the specimen could be produced applying this technique. Following the analysis by Fett[56] for "V" notches to be equivalent to real cracks, they should have tip radius smaller than 3 times the grain size or the largest microstructural characteristic of the material[52]. Ultra-short pulsed femtolaser ablation is being lately used also to obtain shallow sharp notches[57].

A round robin on the use of SEVNB in flexure (4pb) was done by the TC6 of ESIS[58]. Materials used were coarse ($d_{50} > 10$ μm, $d_{max} \approx 17$ μm) and fine ($d_{50} \approx 2$μm, $d_{max} \approx 5$μm) grained aluminas, gas pressure sintered silicon nitride (GPSSN), sintered silicon carbide (SSiC), and yttria-stabilised tetragonal zirconia (YTZP). Machining of notches with tip radius between 20 and 30 μm was found to be relatively easy and reproducible while thinner notches presented extremely different quality depending on the laboratory. No significant effect for tip notches less than 30 μm was found for any material when tests from all laboratories were considered. However, much lower critical tip radii were found when a single laboratory analysed the problem in a systematic way. The toughness determination by testing of SEVNB in flexure was proved to be adequate and robust for materials with grain size or major microstructural feature size over 1μm when using notch tip radius of 10 μm. On the basis of this work, the international standard for SEVNB tested in 4 point bending was established[43] (EN 14425-5:2004[42]). According to this standard, under well-controlled conditions, notch-tip radii in the range of 1 μm to 20 μm can be prepared depending on the grain size of the test material. For

many materials, this is a close approximation to a sharp crack, and the method has been found to give fracture toughness values very close to those of other methods such as the Single Edge Precracked Beam (SEPB) method[37] (EN 14425-2:2004) provided that a sharp crack forms at the root of the notch either during its preparation or during the subsequent fracture sequence.

1.3.3. Stable fracture testing

Most toughness testing of ceramics, particularly of advanced ceramics, is done under conditions of unstable fracture. However, when the fracture toughness values are determined from test configurations that do not allow stable crack growth the calculated toughness value might be over-evaluated (e.g. for a dense α-SiC, K_{IC} ~ 4 and 3 MPa $m^{1/2}$ for unstable and stable tests, respectively)[59]. Therefore, stable crack growth is necessary to get reliable and accurate fracture toughness data. Moreover, stable fracture tests supply much more information about the fracture process than the unstable fracture ones because, in addition to the conventional fracture toughness for crack initiation, stable fracture allows the determination of fracture energy.

Stable fracture tests for brittle materials, as most ceramics, are difficult to accomplish, therefore, they are not usually performed. Since the initial works of Nakayama et al.[60,61] and Tattersall and Tappin[62] different authors have developed innovative specimen designs and tests geometries[46,63-67] to attain stable fracture of materials using displacement controlled loading. Two main problems arise in this kind of tests. On the one hand, it is difficult to produce notches with well-defined special geometries in ceramic specimens. On the other hand, unstable crack growth can result as the amount of energy necessary to create the fracture surfaces is usually small compared to the elastic energy stored in the test rig unless extremely stiff machines are used. Unstable crack growth is avoided or limited by careful adaption of the testing

machine and the specimen geometry to the material to be tested. Such approach has made it possible to reach stable fracture for materials as brittle as glass[34,60] and fine grained MgO[62] using stiff machines.

From the broad spectrum of available fracture tests, bending of parallelepiped specimens with straight through notches (SENB) is a relatively simple way of testing and displacement or load controlled bending tests have been widely used for fracture toughness testing of ceramics. Therefore, different attempts to perform stable tests using loaded beams have been done.

In principle, four point bending would lead to more accurate toughness data because it is not necessary to align the crack tip with respect to the central loading roller, as occurs in three point bending[68]. However, Baratta and Dunlay[69] have shown that specimens loaded in three point bending are more likely to fracture in a stable manner than those loaded in four points. Therefore, different attempts to perform stable tests using three point bending loaded beams using displacement control have been done[34,70-72].

The origin of difficulties related to the attainment of stable fracture when using SENB specimens in three point bending and displacement as control variable is clear when the (simplified) graph Load versus Displacement of the loading point of Figure 1.3 is analysed, as done by Sigl[73]. In terms of stability, the use of the actual deflection of the specimen as control variable is equivalent to the use of displacement of the load frame. The curved line is the general stable fracture locus of SENB specimens of a brittle material tested in bending. This curve is called the Griffith locus and represents the fracture taking place with constant energy release rate, G, equalling G_c. As the straight line that represents the loading of the specimen hits the curve, the condition for crack growth ($G=G_c$) is satisfied. In order to get stable fracture, G has to be maintained

at its critical value and, thus, decreasing values of the load point displacement (regime I) followed by increasing values of this parameter (regime II) would be demanded. The load–displacement relationship of regime I is usually called snap back[74]. Therefore, it will not be possible to get stable fracture using constant displacement rates in regime I. The relative weight of the regions corresponding to regimes I and II depends on the material properties, the specimen and span sizes, the notch depth and the stiffness of the testing device. For the same material and testing geometry, stiff machines and deep notches increase the region of regime II. In this case, stable fracture can be reached controlling by constant displacement rate because increases in displacement after the maximum load still allow to follow the stable condition for crack growth $G=G_c$. From Figure 1.3 it is clear that the control by constant rates of increasing load can never lead to stable tests because load always decreases after cracking starts.

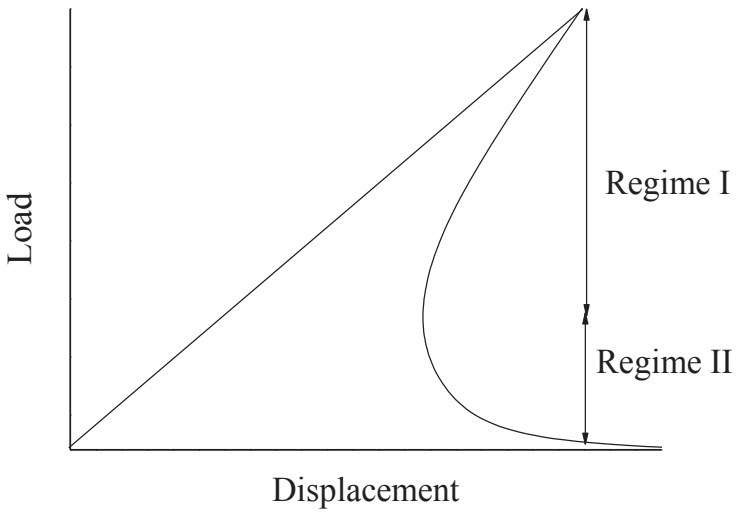

Figure 1.3. General plot Load – Displacement of the loading point for stable fracture of SENB specimens of brittle materials tested in three point bending. The straight line represents the loading of the specimen and the curved part corresponds to the Griffith locus.

Stable fracture for SENB specimens tested in three points bending using displacement control is relatively easy to attain for materials with R-curve fracture, for

which the crack resistance (i.e. G_c) increases as the crack propagates. For instance, stable fracture has been reported for materials with coarse microstructures such as silicoaluminate and high alumina refractories[61] and graphite[34,71], for dense alumina with relatively large grain size (d_{50} ~ 5.5 μm)[72] and for fine grained alumina–aluminium titanate composites (alumina: d_{50} ~ 3.2–3.9 μm, aluminium titanate: d_{50} ~ 2.2 μm)[72]. On the contrary, for brittle materials, very deep cracks and extremely stiff machines would be needed for stable fracture and thus, it is not possible in practice. In this sense, load–displacement curves showing unstable fracture or sudden load decreases ("pop-in") prior to further stable propagation (i.e. semi-stable fracture) have been reported for fine grained alumina (d_{50} ~ 3.5 μm)[72] and silicon nitride (d_{50} ~ 3 μm)[70].

Contrarily to the above-discussed parameters, parameters related to crack growth increase during the whole fracture test, thus, they are suitable to reach stable fracture. In particular, the Crack Mouth Opening Displacement (CMOD) increases through the whole fracture test, the loading of the specimen as well as during the crack growth. Thus, CMOD has been proposed and used as control parameter for stable fracture testing of high-strength concrete[74] and tetragonal zirconia stabilised with 3 mol% of Y_2O_3[75-77] specimens under conditions that would have led to unstable fracture for displacement controlled tests; both materials present R-curve behaviour. This parameter has never been used to test brittle specimens.

1.4. Magnesium-aluminate spinel materials

Magnesium-aluminate spinel ($MgAl_2O_4$) combines a set of attractive optical, thermal, electrical and mechanical properties such as transparency, moderate thermal conductivity (~16W/m·K at 298.15K)[78], moderate thermal expansion coefficient (~ 8 10^{-6} K^{-1})[78-81], high thermal stability[82,83], low electrical losses[75,76], high resistance to chemical attack[84,85], relatively high hardness (15-17 GPa)[78,86-89], moderate Young's

modulus (260-280; 295 GPa)[78,86-89] and good thermal shock resistance[90]. Spinel presents the characteristic low fracture toughness (1.2-3.0 MPa $m^{1/2}$)[78,82-84,86-102] and strength (185-300 MPa)[78,84-89,91,93] of brittle oxide materials.

The most common applications for spinel are high-refractory[84,85], electro-insulating[84,85,102], infrared windows/domes[78,82,93-95], transparent ceramic armour[82,95,98,103], laser hosts[104], lamp envelopes[105] and structural material with application in metallurgical, electrotechnical and radiotechnical industries[84,85]. Mechanical properties and transparency are known to depend on powder composition and subsequent sintering/hot isostatic pressing/spark plasma conditions.

Spinel is transparent in the wavelength range 0.2-6 μm and because of the cubic crystal structure it does not suffer from birefringent light scattering at grain boundaries[78,90,93-95,97,98,106]. To sinter highly transparent optical ceramics with high strength properties is necessary to provide the minimum (nanoscaled) size of the intergranular boundaries of the sintered ceramics with content of pores and impurities no more than 10^{-3} volume percent[82,96].

The mechanical behaviour of stoichiometric magnesium-aluminate spinels has been studied on single crystals[99-102,107,108] and polycrystalline samples[82-85,90,93-98,100,103].

The mechanical behaviour at room temperature of nano[82,95,96], fine[83,84,90,93-98,103] and coarse-grained[83,85,91,92,94,95] spinels has been reported. Materials have been prepared by different sintering routes: conventional sintering[84,85,90,95], hot isostatic pressing[83,91-96,98,100,103] and spark-plasma sintering[82,97]. Sintering additives such as LiF[90-92] (generally 1 wt.%) and Y_2O_3[90,95] have been used during the sintering processes. The main microstructural characteristics and the reported mechanical parameters at room temperature are summarised in table 1.1.

Table 1.1. Microstructural characteristics and mechanical parameters at room temperature for polycrystalline spinels.

Reference	T.D. %	d_{50} (S.D.) (μm)	K_{IC} (S.D.) ($MPa \cdot m^{1/2}$)		σ (S.D.) (MPa)			E (S.D.) (GPa)	
			E.d.	Values	E. d.	Values		E.d.	Values
Tokariev et al.[93,94], 2013,2012	99	5	IT^+	1.9 (0.1)	ROR	σ_0	169 (3)	ROR	260 (5)
			ITº	1.3 (0.05)		m	5 (2)	IT	210 (10)
			ISB	1.9 (0.2)				IET	270
			SENB 4-pb	1.8 (0.2)					
			Critical defect	1.6 (0.2)					
		60	IT^+	1.2 (0.05)	ROR	σ_0	77 (1)	ROR	242 (13)
			ITº	0.8 (0.05)		m	10 (2)	IT	225 (10)
			SENB	1.0 (0.4)				IET	270 (5)
Khasanov et al.[82], 2013	100		IT^+	2.4				IT	212
Borrero-López et al.[95], 2012 Mroz et al.[96], 2012	100	0.345	ITº	1.4	ROR	σ_0	470		
						m	6.2		
		2.1	ITº	1.4	ROR	σ_0	364		
						m	5.3		
		15	ITº	1.4	ROR	σ_0	160		
						m	9.6		
Boniecki et al.[90], 2012		2.1 (1.5)	SENB 3-pb	1.9 (0.1)	4-pb	σ_f	111(4)		
Morita et al.[97], 2009	>99.8	0.4	ITº	1.5 (0.1)	3-pb	σ_f	500 (60)		
					4-pb	σ_f	380 (107)		
Krell et al.[98], 2009	99	1.7	IT	2.0 (0.2)	4-pb	σ_f	225 (25)		275
Baudín et al.[84], 1995	98	1.5 (0.8)	SENB 4-pb	3.0 (0.1)	4-pb	σ_f	129 (20) 194 (20)	4-pb	206 (6)
								IET	258 (2)
White et al.[92], 1992	>99	75	CNB	2.2 (0.2)					
Ghosh et al.[91], 1991	99	35	SENB	1.46 (0.44)					
			CNB	1.79 (0.11)					
			SCF	1.81 (0.17)					
Stewart et al.[83], 1980	99	5	SCF	1.94 (0.10)				IET	258
		12		1.98 (0.14)					
		25		1.83 (0.14)					
		38		1.97 (0.14)					

T.D.: Theoretical density (%); d_{50}: Average grain size (μm); K_{IC}: Critical stress intensity factor in mode I ($MPa\ m^{1/2}$); σ: Strength (MPa); σ_f: Average strength (MPa); σ_0: Weibull characteristic strength (MPa); m: Weibull parameter; E: Young's modulus (GPa); IT: Indentation Toughness; ISB: Indentation Strength in Bending; SENB: Single Edge Notched Beam; CNB: Chevron Notched Beam; SCF: Surface Crack in Flexure; ROR: Ring on Ring; 3 or 4-pb: three or four point bending; IET: Impulse Excitation Technique; E.d.: Experimental details; (S.D.): Standard Deviation; $^+$: Niihara equation, º: Atkins equation).

Values for dynamic Young´s modulus are similar (≈260-270 GPa) for sintered[84] and hot pressed materials[83,93,94]. Static Young´s modulus values[84] (≈200 GPa) are lower than the dynamic ones and close to those obtained in indentation tests for hot pressed[93,94] and spark plasma sintered (SPS)[82] spinels. Ring-on-ring tests[93,94] led to much higher values of Young's modulus (≈240-260 GPa) than other static methods for fine (≈ 5μm) and coarse (≈ 60μm) grained materials[93,94].

All Young's modulus values obtained for polycrystalline spinels are lower than that one reported by Mitchell[108] (≈ 300 GPa) for $MgAl_2O_4$ single crystals using the Voigt average of the elastic constants. Different authors have demonstrated the anisotropy of Young´s modulus in spinel single crystals; Values for different cleavage planes are: 165, 198 GPa for <100>[109,110] and 282, 308 GPa for <110>[107,108].

Reported fracture strength values for spinels with micrometric grain sizes (≈ 1.7-60 μm) determined in 4 points bending[84,90,98] or using ring-on-ring bending tests[93,94,96,103] are in the range 100-360 MPa. Grain refinement to the nano-scale led to higher strengths (400-500 MPa) for SPS[97] and hot-isostatically pressed[95,96] materials. $MgAl_2O_4$ single crystals also present anisotropy in strength. Rice et al.[102,107] reported values of 269 ± 7 MPa and 200 ± 10 MPa parallel with and perpendicular to the tensile surface <100> and 210 ± 20 MPa and 165 ± 30 MPa parallel with and perpendicular to the tensile surface <110>.

Values of fracture toughness have been reported for polycrystalline[82-84,90-98] and for single crystals[99-102]. Different techniques have been used -SENB in flexure[84,90,91,94], biaxial tests[102], Chevron-notched beams in bending[91,92], Microcantilever[100], Double cantilever beam[101], being the most used the indentation test[82,83,93-99,102].

Vickers indentation toughness values in the range 1.8-2.2 MPa $m^{1/2}$ have been reported for hot-pressed and hot-isostatically pressed spinels with a wide range of grain

sizes[93,94,98] (≈ 2-60 μm). Spinels with finer microstructures (≈ 10^2 nm-1 μm) present slightly lower values (≈ 1.4-1.5 MPa $m^{1/2}$) of Vickers toughness[95-97]. Higher fracture toughness value, measured by Berkovich nanoindentation, is reported by Khasanov et al.[82] (2.4 MPa $m^{1/2}$) for a nanostructured spark-plasma sintered spinel.

Values obtained using beams with Knoop or Chevron flaws in bending[83,91,92] (≈ 1.8-2-2 MPa $m^{1/2}$) are also independent from grain size for hot pressed spinels with grain sizes ≈ 5-75 μm.

There are few papers reporting SENB toughness values for spinel materials[84,90,91,94]. Average values between 1.8 and 3 MPa $m^{1/2}$ have been reported for fine grained (≈ 1.5-5 μm) materials fabricated by conventional sintering[84,90] and hot-pressing[94]. Contrarily to Vickers values, a dependence on grain size has been reported, being lower (≈ 1-1.5 MPa $m^{1/2}$) the values for coarse grained spinels (≈ 35-60 μm)[91,94].

The large difference (≈ 50%) found for fine grained spinels between the initial work by Baudín et al.[84] and the more recent ones[90,94] could be partially attributed to the larger notch tip radius associated to the notching techniques available at the time.

As for the above described mechanical parameters, toughness of $MgAl_2O_4$ single crystals is anisotropic. Rice et al.[102] measured the fracture toughness using different techniques as double cantilever beams, biaxial bending tests, indentation tests, obtaining values of ~ 1.0 MPa $m^{1/2}$, for <100>. Wu et al.[101] reported fracture toughness values and fracture energies of 1.21 MPa $m^{1/2}$ and 4.4 J/m^2, and 1.28 MPa $m^{1/2}$ and 2.9 J/m^2 for <100> and <110> planes, respectively, using double cantilever beam tests.

Stewart et al.[99] reported fracture toughness values 1.18 ± 0.05, 1.54 ± 0.08, 1.90 ± 0.06 MPa $m^{1/2}$ and fracture energies 3.57, 4.07, 4.85 J/m^2 for the different cleavage planes of single crystals <100>, <110> and <111>, respectively. The lowest fracture

toughness corresponds to <100>, so it is the easier plane for fracture and lower energy is required to fracture.

1.5. Alumina materials

Alumina (Al_2O_3) is the ceramic material most extensively studied, both from theoretical and practical stand points. There exist several reviews about alumina materials -properties, production, and uses (Briggs, 2007; Doremus, 2008; Dörre & Hübner, 1984; Gitzen, 1970; Hart, 1990; Kingery, 1984; Mc Colm, 1990; Riley, 2009)[111-118]. An updated review (2014) can be found in chapter 2 of the encyclopaedia "Comprehensive Hard Materials"[119].

Alumina ceramics are widely applied because of the high hardness (for sapphire H = 9 in the Mohs scale and H_v is up to 30 GPa depending on the orientation), high melting point (2050ºC), good wear resistance, good corrosion resistance and outstanding mechanical properties at high-temperature. In fact, from all ceramics, alumina presents the highest thermal stability together with high hardness sustained up to temperatures over 1200ºC, therefore alumina is the natural ceramic for wear[119].

The excellent wear behaviour of alumina ceramics together with their biocompatibility and excellent corrosion resistance have carried out to widespread the use of the alumina to the field of biomaterials as femoral heads in total hip replacements as an alternative to acetabular cup of polyethylene or to metal-metal bearing devices[16].

Because of thermal expansion anisotropy ($\alpha_{25\text{-}1000ºC} \sim 9.2\ 10^{-6}\ K^{-1}$ and $8.4\ 10^{-6}\ K^{-1}$ parallel and perpendicular to c-axis, respectively[120]) stresses can appear when cooling alumina ceramics from the sintering temperature[121]. The stress level depends on the particular relative orientation of the grain boundaries. For grain sizes above a critical one, these stresses can lead to fracture. However, for the small grain sized (<30 μm) structural aluminas, the developed stresses remain as residual stresses in the sintered

materials and are partially responsible for the dependence of properties such as hardness, fracture toughness, and strength on grain size[13,72,122-126].

The mechanical behaviour of alumina materials has constantly improved since the years 1960's. Efforts have been directed towards the increase of the purity and the homogenisation and decrease of the grain size of the raw materials, the addition of dopants to control grain size as well as to the use of advanced sintering techniques. The development of alumina materials for metal machining and sealing as well as for prosthetic hip replacement has been the motor of such improvements.

Reported Young's modulus values for pure (>99%), fine grained (2-6 μm) and dense (≥98% of theoretical) alumina ceramics range form ~ 380-390 GPa for conventionally sintered materials[72] up to ~ 400-450 GPa for the optimised hot-pressed and hot-isostatically pressed aluminas[126,127].

Strength values determined in bending vary from 350-460 MPa for conventionally sintered materials with grain sizes ~ 3-6 μm to 500-600 MPa for hot-pressed and hot-isostatically pressed aluminas[72,127-129].

Since the initial systematic studies done by the group of Claussen[123,130] toughness values of alumina materials have been recognised as highly dependent on grain size and test technique. This fact is partially due to toughening mechanisms. Toughening mechanisms reported to alumina materials are mainly due to the effect of residual stresses and therefore, highly dependent on grain size. Crack deflection, microcracking, crack bridging and crack branching, for extremely large grain sizes have been observed in alumina materials. The action is revealed by the greater roughness of the fracture surfaces of the larger grain size aluminas, as it is shown in Freiman et al. work[131].

Table 1.2, summarises characteristic room temperature toughness values reported for alumina materials determined in flexure tests performed using the displacement of

the load frame as control parameter. When reported, values obtained using other techniques in the same study are also included for comparison.

For fine grained materials (d_{50}~2-8 μm) K_{IC} values from ~2 to ~6 MPa $m^{1/2}$ and specific fracture energy values from ~10 to ~20 J/m^2 are found. All K_{IC} values are higher than those reported for alumina monocrystals by Michalske et al.[132] (K_{IC} = 2.0 MPa $m^{1/2}$).

Bueno et al.[72] reported values recorded during semi-stable or stable fracture of SEVNB tested in flexure using the displacement of the frame load as control parameter, K_{IC} and γ values for the two aluminas studied by these authors are very similar to those determined by Sbaizero et al.[127] for aluminas with larger grain sizes using stable fracture tests.

However, K_{IC} values reported by Bueno et al.[72] and Sbaizero et al.[127] are lower (~35%) than those reported for aluminas with similar grain sizes determined from unstable fracture tests of SENB[13,52,123], in agreement to Bar-On et al.[70] who, as discussed in section 1.3.3, concluded that unstable crack extension would result in apparent increases of fracture toughness values compared to those determined during semi-stable or stable tests.

Additionally, the larger notch tip radius of SENB as compared to the SEVNB will also lead to higher results as discussed in previous section 1.3.2.

K_{IC} values reported by Bueno et al.[72] and Sbaizero et al.[127] are also lower than those obtained by double torsion (DT)[16,128,129,133]. It is well known that double torsion tests always give the highest values as compared to other methods. The specific geometry for the crack that has to be assumed for the calculations might not be accurate, leading to erroneous values.

Table 1.2. Characteristic room temperature toughness values reported for alumina materials.

Reference	T.D. (S.D) %	d_{50} (S.D.) (μm)	Method	K_{IC} (S.D.) ($MPa \cdot m^{1/2}$)	G_{IC} (S.D.) (J/m^2)	γ (S.D.) (J/m^2)
Palmero et al.[129], 2014	>98	<7	DT	5.5 (0.2)		
Bueno et al.[72], 2008	98.1 (0.3)	3.5 (0.3)	SEVNB ρ<20μm	2.9 ; 2.8	20.4 ; 19.6	10.5 ; 9.8
	98.1 (0.5)	5.5 (0.6)		3.2 (0.1)	26.2 (0.7)	20.1 (2.0)
Bueno et al.[136], 2007	98.1 (0.3)	3.5 (0.3)	SEVNB ρ<30μm	2.9 (0.2)		14.7 (1.9)
	98.1 (0.5)	5.5 (0.5)		3.0 (0.3)		20.4 (2.8)
De Aza et al.[16], 2002	~99	1.7	DT	4.2 (0.2)		
Sbaizero et al.[127], 1998	99	8	-	~3		20 (5)
Seidel et al.[135], 1997	>99	1.7	CT	3.16		
			ISB	3.6		
		10.5	CT	3.75		
			ISB	4.1		
Damani et al.[52], 1996	Low	10	SEVNB			
			ρ<9μm	2.8		
			ρ~25μm	3.0		
			ρ~67μm	3.5		
			ρ~92μm	3.9		
Mussler et al.[123], 1982	>95	<5	SENB ρ=40-70μm	4-6		
		6-30		4-4.5		
		2-50	DCB, ISB	3.8-5.8		
Claussen et al.[130],1982		1	SENB			50
		20				20
Rice et al.[13], 1981		3.5-20	SENB			27-36
			SEVNB			33-40
			DT			38-47
			DCB			38-48
			DCB*			35-70
Freiman et al.[131], 1973		4	DT, DCB, CNB, SENB	3.2 ;3.7		17 ; 19
		7		3.0		20
		8		3.7		18
		20		4.7 ;4.9		32 ; 35 ; 44
		35		4.1		22

T.D.: Theoretical density (%); d_{50}: Average grain size (μm); K_{IC}: Critical stress intensity factor in mode I ($MPa\ m^{1/2}$); G_{IC}: Critical energy release rate in mode I (J/m^2); γ: Fracture energy (J/m^2); ρ: notch tip radius (μm); DT: Double Torsion; SEVNB: Single Edge V Notched Beam; CT: Compact Tension; IT: Indentation Toughness; ISB: Indentation Strength in Bending; SENB: Single Edge Notched Beam; DCB: Double Cantilever Beam; (S.D.): Standard deviation.

The group of Chevalier[16,129] has tested by double torsion alumina materials used as prostheses in order to detect Subcritical Crack Growth (SCG) in different environments. The basic mechanism for this subcritical crack growth is the stress assisted corrosion by

environmental species (especially water) at the crack tip bonds, as it was first reported by Freiman et al.[131].

SCG in high purity alumina materials is an extremely slow process in air, as reported by Chevalier et al.[128]. These authors found crack growth velocities, $v \sim 10^{-10}$ m/s for K_{IC} values (~2.6 MPa $m^{1/2}$) slightly above than K_{I0} (~2.5 MPa $m^{1/2}$).

Values of specific fracture energy for fine grained[72] (~ 10 J/m^2) and coarse grained[72,127] (~ 20 J/m^2) materials are both higher than that reported by Wiederhorn et al.[134] (6 J/m^2) for the rombohedral plane which is the preferred cleavage plane in alumina monocrystals at room temperature. The fracture energies generally determined for polycrystals are higher than those for monocrystals due to the contribution of intergranular fracture, in the same way as crack tip toughness values in polycrystals are higher than those of the easy cleavage planes.

The similarity between the G_{IC} and 2γ for the fine grained alumina tested by Bueno et al.[72] revealed the absence of significant crack-size dependent toughening phenomena. On the contrary, for the coarse grain-sized alumina 2γ was much higher (~ 55 %) than G_{IC}, revealing toughening processes.

1.6. Mullite materials

Mullite (from $3Al_2O_3 \cdot 2SiO_2$ to $2Al_2O_3 \cdot SiO_2$) is the only stable compound in the system Al_2O_3-SiO_2 from medium up to high temperature at atmospheric pressure. Therefore, it is a main constituent of a number of oxide ceramics.

As Schneider et al.[137] have described in a review about 'Structure and properties of mullite', mullite and mullite ceramics display a large variety of appearances, from Czochralski-grown single crystals to polycrystalline and polyphase ceramics. Polycrystalline mullite ceramics may be classified in: monolithic mullite ceramics, mullite coatings and mullite matrix composites.

Mullite presents some attractive properties for high-temperature structural applications such as high melting point (1828 ± 10ºC)[138], low thermal conductivity (6 $kcal \cdot m^{-1} \cdot h^{-1} ºC^{-1}$, at 20ºC)[137], low thermal expansion coefficient ($\alpha_{25\text{-}800ºC} = (4.1 \pm 0.1) \cdot 10^{-6}\ ºC^{-1}$)[139], good chemical and thermal stability, low dielectric constant ($\varepsilon \sim 7$), high deformation resistance at high temperatures (or low creep rate). Most mullite materials present low characteristic fracture toughness (~ 2.5 MPa $m^{1/2}$) and moderate characteristic strength (~ 200 MPa)[137]. At room temperature, mullite ceramics present flat R-curve, -no toughening mechanisms have been reported for mullite ceramics-.

Initially used only for high temperature traditional applications (refractories and in pottery), mullite materials experienced a great development since the seminal work of Mazdiyasni[140] in 1972 where translucent polycrystalline bodies of stoichiometric mullite with relatively high strength and excellent thermal-shock resistance were described[138,140,141].

Schneider et al.[137] described some of the applications of monolithic mullite ceramics as refractory bricks in glass melting tanks and in furnaces for the temperature treatment of electronic packaging materials. Optical translucent mullite ceramics are used for high-temperature furnace windows. Due to the good chemical and thermal stability, mullite coatings are incorporated to panel for re-entry space vehicles. Also, components and structures made of mullite fiber-reinforced mullite matrix composites are employed in gas turbine engines, high duty kiln furnitures and burner tubes.

Reported values for the room temperature mechanical properties of mullite materials are summarised in table 1.3.

Table 1.3. Microstructural characteristics and room temperature mechanical properties of mullite materials.

Reference	T.D. (S.D) %	d_{50} (S.D.) (μm)	K_{IC} (S.D.) (MPa · $m^{1/2}$)		σ (S.D.) (MPa)		E (S.D.) (GPa)	
			E.d.	Values	E.d.	Values	E.d.	Values
Sivakumar et al.[149], 2001	98.3	2	IT	2.0 (0.75)	3-pb	441 (34)	IET	222
Casellas et al.[153], 1998		2	IT	2.5 (0.1)				
		4		2.5 (0.2)				
		1		2.4 (0.2)				
		1.5		2.2 (0.2)				
Baudín[145], 1997	95.2 (0.5)	0.7 (0.5)	SENB 4-pb ρ=200μm 0.05mm/min	2.30 (0.09)	4-pb	263	4-pb	175
							IET	195 (4)
Torrecillas et al.[142], 1997	High	2	SENB 4-pb ρ=300μm		4-pb	200-300	-	~200
			0.005mm/min	1.77				
			0.05mm/min	2.15;2.38				
			0.2mm/min	2.46;2.61				
			DT	1.9-2.05				
Osendi et al.[148], 1996	96.5 (0.5)	1.2 (0.9)	SENB 4-pb ρ=200μm		4-pb	168 (26)	4-pb	202 (2)
			0.005mm/min	2.00 (0.31)				
			0.05mm/min	2.52 (0.25)				
			5.0mm/min	3.50 (0.19)				
	95.2 (0.5)	0.7 (0.5)	SENB 4-pb ρ=200μm		4-pb	227 (35)	4-pb	195 (4)
			0.005mm/min	2.00 (0.32)				
			0.05mm/min	2.32 (0.08)				
			5.0mm/min	2.35 (0.10)				
Okamoto et al.[146], 1990	>98		IT	2.7 (0.1)	3-pb	300 (10)	IET	224
Ismail et al.[147], 1987	>98	1.04	IT	2.73	3-pb	400	IET	246
Mah et al.[138], 1983	99	6	SCF	~1.7	4-pb	128		
Mazdiyasni et al.[140], 1972	99.8 (0.2)	2.7			4-pb	269	IET	221

T.D.: Theoretical density (%); d_{50}: Average grain size (μm); K_{IC}: Critical stress intensity factor in mode I (MPa $m^{1/2}$); σ: Strength; E: Young's modulus; ρ: notch tip radius (μm); SCF: Surface Crack in Flexure; SENB: Single Edge Notched Beam; DT: Double Torsion; IT: Indentation Toughness; IET: Impulse Excitation Technique; 3-pb: Three-point bending; 4-pb: Four point bending; (S.D.): Standard deviation.

The availability of fine pure mullite powders and new processing routes has made it possible to obtain dense polycrystalline mullites with little or nearly no residual glassy

phase and with higher deformation resistance at higher temperatures than any ceramic oxide[137,141-144]. These materials present improved mechanical behaviour as compared to that of traditional mullite materials. For instance, Kanzaki et al.[144] measured bending strengths of mullite ceramics as high as 360 MPa and fracture toughness of 2.8 MPa $m^{1/2}$ at room temperature. The bending strength of these mullite ceramics decreased only slightly up to 1400ºC, while other advanced ceramics such as silicon carbide, silicon nitride, alumina and zirconia display a rather strong reduction of mechanical properties at elevated temperature, especially in air.

The different processing methods used to obtain the mullite ceramics strongly influence their mechanical behaviour through the particle size and the homogeneity of the precursors, the porosity, the existence of impurities and their nature and distribution.

Young's modulus values between 180 and 250 GPa[140,145-148] have been reported for different mullites. Differences can be explained by different amounts of alumina and test techniques (static versus dynamic). Contrarily, no dependence on nature and distribution of impurities on this property has been found on Young's modulus.

A wide range, 128-440 MPa of strength values has been reported by several researchers[138,140,142,146-151] for mullites with different microstructures. The lowest value (128 MPa) corresponds to a hot-pressed mullite with average grain size of 6 μm determined by Mah and Mazdiyasni[138] by four-point bending. The authors explained this low strength as a consequence of large porosity nests which acted as strength-controlling flaws.

The high mechanical strength (360 MPa) of mullite ceramics published by Kanzaki et al.[144] can be explained by the high purity powders synthesized by spray pyrolysis of alkoxides used for the processing. Ismail et al.[147], Sivakumar et al.[149] and Ohira et al.[150] reported even higher bending strengths (400 to 440 MPa) starting from commercial high

purity sol-gel mullite powders. The same is true for Itoh et al.[151] who published bending strengths of 415 MPa for mullite prepared from a mixture of kaolinite and aluminium hydroxide.

The influence of the Al_2O_3 content of mullite ceramics on the mechanical properties has systematically been examined by Kumazawa et al.[152], who found a significant increase (~50%) of bend strength with Al_2O_3 content between 46 to 61 mol.% followed by slightly decrease for 67 mol.% Al_2O_3. Multiple factors such as porosity, mullite, α-Al_2O_3 and specially glass phase contents may be responsible from this development. Compared with the changes in bending strength versus Al_2O_3 content of mullite ceramics only little variation was observed in the fracture toughness by these authors.

Different researchers have provided fracture toughness values obtained using different unstable fracture test configurations for mullites with various microstructures[137,138,142,143,145,146,148,153]. The range of reported values of the critical stress intensity factor in mode I, K_{IC}, are around 1.7-3.5 MPa $m^{1/2}$. In particular, for fracture testing of SENB in three point bending, 2.0-3.5 MPa $m^{1/2}$ for load displacement rates between 0.005 and 5 mm/min have been reported[148].

Main differences in SENB toughness values have been attributed to differences in the rate of displacement of the load frame during the tests[142,148]. This fact is due to the proneness of mullite to subcritical crack growth at room temperature[141,148,153]. For the same mullite materials, SENB toughness values[148] are similar to those obtained by using the indentation strength four point bending method at equivalent deformation rates[153].

Subcritical crack growth (SCG) has been shown to occur in fine grained 3:2 mullites at room temperature[142,148,153]. Even though SCG occurs in materials presenting intergranular[148] as well as transgranular[142,153] fracture mode, it is enhanced by the presence of a silica glass film at the grain boundaries. This fact was evidenced by results

obtained for two materials fabricated using the same mullite powder and sintered at 1630ºC[148] and 1700ºC[142]. Both materials presented SCG under static loading and double torsion[142] tests. However, in SENB toughness tests, performed at different displacement rates (0.005-5 mm/min), SCG was only evidenced in the material sintered at the highest temperature, in which a silica glass film was formed at grain boundaries during sintering[142]. Toughness values determined using the slowest (0.005 mm/min) rate presented relatively high variability (~10 %) for both materials. Slow crack growth in air is a relatively rapid process in these high purity mullites. Torrecillas et al.[142] reported a crack velocity, $v \sim 10^{-4}$ m/s, for $K_{IC} \sim 1.9\text{-}2.05$ MPa $m^{1/2}$.

Up to know no accurate and reliable fracture toughness data have been provided from stable fracture tests in mullite ceramics. The subcritical crack growth is an important factor to take in account in this material.

1.7. Refractory materials

1.7.1. General properties

Refractories are essential for all high-temperature industrial processes. They play the triple role of providing mechanical strength, protection against corrosion and thermal insulation. Refractory materials, by definition, are supposed to be resistant to high temperature while exposed to corrosion from solids, liquids and gases, gas diffusion, different degrees of mechanical stress and strain and mechanical abrasion. Refractories are mostly used (70%) in metal industry. In petrochemical refining, although the temperature is much lower than in metal industries the refractories suffer a high rate of abrasion due to the flow of high-velocity particles at a continuous rate[154].

Refractories are broadly divided into two categories: shaped (bricks and cast shapes) and unshaped (monolithic) refractories[154]. For shaped refractories the main requirements are their density and porosity and dimensional tolerance. In recent years, the use of

unshaped refractories has significantly increased reaching ~60-65% of all refractory use.

Ceramic properties of a refractory material are defined by its nature or reaction when exposed to high temperature[154]. For fired bricks like fireclay, high-alumina, magnesia-chrome-type bricks, the ceramic reactions and bonds have already been instituted by high-temperature firing, hence, when they are exposed to high temperature, they do not exhibit any further change. But for unfired refractories, like magnesia or alumina-carbon bricks and unshaped refractories, the formulations are designed so that the ceramic properties will be developed at use temperatures. Thus, it is necessary to understand and predict the ceramic reactions that take place at or before service temperatures.

Due to the extreme service conditions, the main selection criterion for the application of refractories is their behaviour at high temperature under specific corrosive environment, which is mostly done on the basis of their chemistry. However, microstructure and texture have to be carefully monitored because of the extreme mechanical solicitations involved in the uses of refractories.

The thermal stress fracture of refractory components, due to temperature cycling and/or temperature differences through the material, is a widespread problem of industrial importance. In the same way, mechanical overload as may be originated by impact during the loading of the process vessel, as occurs in electrical arc furnaces, or by deformations of the kiln shell, as observed in the cement industry, can lead to fracture. Fracture as a result of thermal or mechanical shocks could lead to catastrophic failure of the refractories with strong consequences for the process in which they are used. However, fracture can also result just in the development of a crack pattern[155]. The extension of fracture due to thermal or mechanical strains, i.e: the damage would be

determined by the ratio between the amount of energy available and the energy needed to create new crack surfaces or specific fracture energy. Therefore, this ratio will characterise the resistance of materials to subcritical crack growth and the proneness to catastrophic failure.

The behaviour of refractories under mechanical loadings is directly related to their microstructure and texture which, in turn, is determined by the characteristics of the raw materials (chemical and mineralogical composition and size and shape distribution) and by the processing or installation procedure. In this regard, it should be pointed out that the conventional characterisation of the mechanical properties of refractory products is done in terms of the flexural strength or modulus of rupture, as it is called in the refractories field. Even though the modulus of rupture is successfully used in industry for quality control purposes, this parameter does not allow the analysis of the fracture processes that occur in the material. Therefore, it cannot be used for design and development purposes.

Refractory products are heterogeneous ceramic materials which fracture exhibits notable deviations from pure linear elastic and this behaviour has been well documented[155-161]. Several of the previously discussed (section 1.2) toughening mechanisms ahead and behind the crack tip are considered to contribute to this behaviour. However, these mechanisms present particularities in refractories. Microcracking is usually accompanied by multiple cracks branching in the frontal process zone, while the aggregates might act as elastic bridges in the crack wake and/or debond and be pulled-out. The presence of aggregates in the wake leads to friction of crack faces when submitted to cycling. As a result, refractories usually present rising R-curve behaviour, as it was mentioned in section 1.2, in contrast with the flat R-curve

observed for the fine grain size ceramics magnesium-aluminate spinel, alumina and mullite materials described before in sections 1.4, 1.5 and 1.6, respectively.

The fracture toughness of refractories is usually in the range of about 0.2 to 1.5 MPa $m^{1/2}$. Refractory castables are at the lower portion of this range and fired bricks at the higher end[155]. Young's modulus of refractories range from about 30 to 70 GPa and the work of fracture is in the range of about 70-300 J/m^2. Therefore, G_{IC} (1-31 J/m^2) of refractories with well designed microstructures is always significantly lower than the specific fracture energy, G_F ($2\gamma_{wof}$). The ratio between the specific fracture energy and the critical energy release rate in mode I, G_F/G_{IC}, has been defined as a toughness, flexibility or apparent ductility ratio. It will have a large value, higher than 10, for refractories with high energy consumption for crack propagation relative to crack initiation. The higher this relation, the higher is the resistance of the material to damage by thermal or mechanical strains[155]. An important point to consider when determining the specific fracture energy (or the work of fracture) of refractories is the potential influence of the specimen size ("size effect") in the obtained values because G_F will increase with increasing fracture surface until the specimen geometry allows the development of a well developed wake zone.

1.7.2. Toughness testing of refractories

Nakayama, in the 1960s[60], was the first researcher that applied the concepts related to the extension of a single crack to analyse refractory fracture and developed the work-of-fracture test to characterise toughness of refractories.

Nakayama, Tattersall and Tappin, and Davidge and Tappin accomplished a wide series of studios on the measurement of work of fracture in the 60´s[60,62,71]. Since then, many laboratories have conducted work of fracture analysis but a standard test has not yet been established.

As discussed before in sections 1.2 and 1.3.3, the concept of work of fracture, introduced by Nakayama as the mean work per unit of projected fracture area required to propagate a crack in a stable way, is equivalent to that of specific fracture energy. In Nakayama´s work of fracture test a parallelepiped bar with a triangular (chevron) notch at its centre is loaded in three point bending. Using this geometry, refractory specimens fracture in a stable way when a sufficient stiff machine is used. The value of work of fracture is determined from the total area under the Load–Displacement curve recorded during the experimental and the size of the projected fracture surface. Chevron notch experiments often imply high variability[157,158,162-164] (>10%) because coarse aggregates cause very high work of fracture values as compared to the average for the material when located close to the apex of the chevron notch. For example, 10-23% variability in γ_{wof} has been reported for alumina-spinel castables[164]. For alumina matrix refractory compositions (60-100 Al_2O_3 wt.%[158]) with fused mullite-zirconia aggregates, and for high-alumina refractories with 45-99 Al_2O_3 wt.%[162], variability of 3-38% up to 1-26%, respectively, have been found.

In the 1980´s the wedge-splitting fracture test was developed to perform stable fracture tests and patented by Tschegg[165]. This test is a special form of the so-called compact tension test, the specimen with a groove and notch is split in two halves while monitoring the load and crack mouth opening displacement (CMOD). In this experimental setup, large specimens of the size of bricks can be tested[156,159,166-168]. Several researchers have provided data for high alumina castables and alumina-based shaped materials[166,169-173] using the wedge-splitting test. Recently, a new methodology was presented using the wedge-splitting test complemented with images obtained during mechanical loading to determine the crack propagation for a pure alumina and alumina with titania and zirconia additives refractory compositions[171,173]. Jin et al.[174]

have proposed a methodology to estimate the tensile strength, and Young´s modulus of refractories in addition to the specific fracture energy from wedge splitting test results.

It should be pointed out that variability of data of mechanical properties in the refractory literature is most of the time not reported. Moreover, in many cases only one data for each material experimental condition is provided. This is often the case of work of fracture values determined by the splitting test so, it is not possible to discuss in a general way the repeatability associated with this technique. Nevertheless, the scarce data available reveal rather high variability of results. For two commercial alumina based low cement (2wt.%) castables heat-treated at 1100ºC, 12 and 18% variability have been reported in the γ_{wof} values[169] and variability between 5-22% in γ_{wof} has been reported for basic refractories by Harmuth et al.[168].

Despite the fact that there is an evident interest in the wedge splitting test for work of fracture determination of refractories due to its capability for testing relatively large specimens in order to average the whole fracture process, it is complicate to establish this method as a laboratory routine one. Moreover, as mentioned before, variations in reported ranges of result would mask the effect of microstructural differences on toughness.

From the extensive spectrum of available fracture toughness tests, bending of parallelepiped specimens with straight through notches (SENB, Single Edge Notched Beam) using as control variable the displacement of the load frame (displacement control) is also a relatively simple way of testing heterogeneous materials, as refractories. In general, in the refractory field this method is used to determine toughness parameters describing the initiation of fracture, critical stress intensity factor in mode I, K_{IC}, and the energy for crack initiation, γ_{nbt} which is a measure of the critical energy release rate G_c, $G_c = 2\gamma_{nbt}$. The advantage of using stable fracture tests of SENB

in three point bending is that both parameters for initiation, γ_{nbt}, and propagation, γ_{wof}, of fracture can be extracted from a single test.

1.8. Nanocomposite ceramic materials

1.8.1. General properties

As described in section 1.1 ceramics are brittle and show catastrophic failure limiting their applications as structural engineering materials. Therefore, during the last two decades much effort has been made to develop a new design concept of structural ceramics throughout the processing improvement and incorporating second phases in order to overcome the inherent brittleness and the associated low strength and lack of reliability.

In particular a wide range of monolithic ceramic composites have been developed, i.e. ceramic matrix composites (CMC), with metallic or ceramic second phases. CMCs are considered as enabling technology for advanced aeropropulsion, space propulsion, space power, aerospace vehicles, space structures, ground transportation, as well as nuclear and chemical industries. They would find applications in advanced aerojet engines, stationary gas turbines for electrical power generation, heat exchangers, hot gas filters, radiant burners, heat treatment and materials growth furnaces, nuclear fusion reactors, automobiles, biological implants, etc. Other applications of CMCs are as machinery wear parts, cutting and forming tools, valve seals, high precision ball bearing for corrosive environments, and plungers from chemical pumps[175].

According to Niihara[21], ceramic matrix composites can be divided into two types: microcomposites and nanocomposites. In the microcomposites, micro-size second phases such as particulate, platelet, whisker and fibre are dispersed at the grain boundaries of the matrix. The main purpose of these composites is to improve the fracture toughness.

There are three types of nanocomposites: intragranular and intergranular micro-nanocomposites and nano/nano composites. In the intragranular nanocomposite, submicrometer and/or nano-size particles of second phase are dispersed mainly within the matrix grains of micrometer size, whereas in the intergranular nanocomposite, the second phase particles are dispersed at the grain boundaries of the matrix. Niihara proposed that the aim of the micro-nano composites was to improve not only the mechanical properties such as hardness, fracture strength and toughness and reliability at room temperature but also high-temperature mechanical properties such as hardness, strength, and creep and fatigue fracture resistances. The nano/nano composites are composed of the dispersoids and matrix grains with the nanometre-size. The primary purpose of the nano-nanocomposites, according to Niihara, is to add the new functions such as machinability and superplasticity like metals to ceramics[21].

Originally a number of combinations of ceramic nanocomposites, such as Si_3N_4/TiN prepared by chemical vapour deposition and Al_2O_3/SiC, Al_2O_3/Si_3N_4, Al_2O_3/TiC, mullite/SiC, B_4C/SiC, B_4C/TiB_2, SiC/amorphous SiC, Si_3N_4/SiC prepared by pressureless sintering, hot pressing and hot isostatic pressing, were reported by Niihara's group[21]. Strength values at room temperature two to five times higher than those of monolithic materials were claimed. Moreover, superior high temperature hardness and creep behaviour as well as resistance to thermal shock fracture were also reported.

Since the seminal work by Niihara[21], the development of ceramic nanocomposites has generated considerable research activity due to the potential appealing mechanical, physical and tribological properties. A major challenge in this research field is the understanding of the basic properties of the materials focusing new developments. In this sense, several studies investigating the relationships between microstructure and

strength at room and elevated temperatures, hardness, wear resistance, creep resistance and toughness have been conducted by various authors in composites ceramic matrix-ceramic nanoparticles[22,72,139,176-254], ceramic matrix-metal nanoparticles[127,246,255-260], and ceramic matrix nanotubes[261-264].

Alumina-based nanocomposites have been extensively studied because alumina exhibits some excellent properties, such as high hardness, low electrical conductivity, oxidation resistance, good chemical stability and high wear resistance, as it was mentioned before in section 1.5.

Most researches focus on particle-dispersed alumina composites in order to improve their mechanical properties. The second phase particles may be SiC[176,178,181,184,188-202,205,206,211,212,214,215,218,220,221,223,226,228,229,231,233,235-241,249-254,265], ZrO_2[242,243], TiN/TiC/TiO_2/TiCN[244,245,248,267], BN[268], and metal particle such as Cr[255], W[257], Mo[258], Ni[259], Cu[260].

Al_2O_3/SiC nanocomposites have been the most studied. They are produced by the incorporation of small (50-200 nm) SiC particles in alumina matrices with typical grain sizes ~1–5 μm. Several reviews describing processing, microstructure and mechanical behaviour of this family of nanocomposites are available[22,176,191]. To highlight the work done by the group of the Institute of Scientific and Industrial Research (Osaka, Japan)[175,238,223,205], Leigh University (Pennsylvania, USA)[190,195,209,218,219,227,234,269-271], Leeds University and Oxford University (Great Britain)[176,178,179,181,182-184,188,192,193,196-208,200-202,208,210,211,216,217,222,224,225,230,232,241,247], Kyoto Institute of Technology[209,212,213,272], Nagoya Institute of technology[22,203,214,266]. Other groups[177, 178,189,190, 199,206,207,215, 220,221,226,229,233,235-237,239,240,246,248,251,254,265,273].

A dispersion of SiC submicron-sized particles has been proved as beneficial for some behavioural properties such as creep[189,195,214,218,227] and thermal shock[182,183]. The

most remarkable and reproducible benefits offered by the Al_2O_3/SiC nanocomposites are in their tribological properties where great improvements compared with pure alumina occur in the resistance to severe wear and surface finish following grinding and polishing as have been reported by different researchers[193,176,178,200,180,196,224,225,190,193,207,218,248,274].

One of the most studied properties of Al_2O_3/SiC nanocomposites has been the flexural strength[188,175,209,272,177,181,22,238,182,184,190,192,194,196,198,202,205,207,226,235,236,240]. It has not been possible to reproduce the high values of strength reported by the seminal work by Niihara[21] (from 350 MPa to 1520 MPa for Al_2O_3/5vol.% SiC composite). Most authors report moderately higher strength values for the nanocomposites than for single phase alumina[188,175,209,181,192,22,26,196,202,226,235,236,237,240,254].

The addition of one or more components into the base material to form ceramic matrix nanocomposites has been found to be effective to enhance the fracture toughness and to improve strength[175,240,247,22,248,266,26,275,276]. In the nanocomposites the mechanical properties are determined by many critical factors, such as Al_2O_3 and SiC particle size (micrometer or nanosized), composition of powder mixtures (volume fraction of SiC, content of silica as the product of oxidation of SiC particles), and distribution of SiC inclusions (intergranular, intragranular or both)[226].

1.8.2. Toughness testing of Al_2O_3/SiC nanocomposites

Main drawback in understanding the mechanical behaviour of nanocomposites is the lack of accurate and reliable toughness values. Most reported values have been determined by indentation[188-190,192,194,198,199,202,226,235,236,239,251,254,183].

Table 1.4 summarises indentation toughness values reported for Al_2O_3/SiC nanocomposites together with their main microstructural characteristics and strength values.

Table 1.4. Microstructural characteristics, strength and indentation toughness for Al_2O_3/SiC nanocomposites.

Reference	vol.% SiC	T.D. (S.D.) %	d_{50}(S.D.) (μm)	K_{IC} (S.D.) ($MPa \cdot m^{1/2}$)	σ (S.D.) (MPa)	
					E.d	Values
Parchovianski et al.[226], 2013	0	98.4	1.6 (0.1)	5.0 (0.3)	4-pb	300 (125)
	5	99.5	11.0 (0.1)	5.6 (0.4)		300 (50)
	10	99.5	2.0 (0.1)	5.6 (0.4)		420 (40)
	15	99.5	1.4 (0.1)	5.2 (0.6)		420 (40)
	20	99.4	0.8 (0.05)	5.1(0.5)		670 (110)
Shi et al.[235], 2010	0	99.2	11	3.2 (0.4)	3-pb	280 (33)
	1.6	98.2	4.8	7.6 (0.2)		364 (68)
	3.1	97.9	3.4	6.0 (0.4)		268 (29)
	4.7	96.4	2.3	5.0 (0.4)		-
	6.2	95.8	1.9	4.1 (0.1)		460 (12)
Shi et al.[254], 2010	0	99.2	10	3.2 (0.4)	3-pb	280 (33.0)
	0.3	99.5		4.9 (0.3)		516 (20.8)
	0.6	99.3		5.1 (0.1)		484 (17.3)
Reveron et al.[189], 2010	0	99.3	28.2 (12.8)	$2.7(0.4)^{++}$		
				$3.6\ (0.4)^{+++}$		
	1	99.2	12.7 (7.9)	$3.4\ (0.6)^{++}$		
				$4.3\ (0.6)^{+++}$		
	5	97.1	1.4 (0.4)	$4.0\ (0.7)^{++}$		
				$5.2\ (0.7)^{+++}$		
Dong et al.[236], 2009	0	99.2	-	3.7 (0.4)	3-pb	280.0 (33.0)
	0.3	99.8	6.85	4.8 (0.6)		282.2 (50.2)
	0.6	99.5	3.41	4.4 (0.3)		-
	1.6	98.2	1.21	7.4 (0.2)		363.8 (67.8)
	3.1	97.9	-	5.9 (0.4)		-
	4.7	96.5	-	5.0 (0.3)		-
	6.2	95.8	-	-		459.7 (11.2)
Galusek et al.[251], 2007	5	98	1.5	4.5 (02)		
	8	98	1.2	4.8 (0.1)		
Maensiri et al.[183], 2002	0	99.6 (0.06)	4.10 (0.94)	2.6 (0.2)	4-pb	371 (10)
	1	100 (0.9)	6.85 (2.47)	2.3 (0.2)		369 (66)
	2.5	98.1 (1.4)	6.66 (2.48)	2.2 (0.1)		409 (67)
	5	99.9 (0.6)	2.82 (0.51)	2.6 (0.1)		417 (56)
Anya[198], 1999	0	99.9	3.5 (1.3)	3.2 (0.2)	4-pb	431 (53)
	5	99.8	4.0 (1.1)	4.6 (0.1)		646 (41)
	10	99.7	2.9 (0.5)	5.2 (0.2)		560 (8)
	15	99.6	2.6 (0.3)	5.5 (0.4)		549 (30)
Zhang et al.[194], 1997	0	99.8	-	3.25 (0.12)	3-pb	560 (40)
	3	99.3		2.99 (0.15)		887 (67)
	6	99.5		3.42 (0.15)		853 (53)
	12	99.4		4.08 (0.13)		867 (33)
	24	99.4		4.63 (0.19)		747 (27)
Xu et al.,[239] 1997	0	-		4.20 (0.10)		
	6		1.7 (0.9)	4.70 (0.11)		
	12		1.3 (0.7)	4.85 (0.03)		
Hoffman et al.[277], 1997	0		0.9	2.1	4-pb	
	5	98.8	2.5	1.9		595 (82)

Reference	vol.% SiC	T.D. (S.D.) %	d_{50}(S.D.) (μm)	K_{IC} (S.D.) ($MPa \cdot m^{1/2}$)	σ (S.D.) (MPa)	
					E.d	Values
Sternitzke et al.[188], 1998	0	99.6 (0.4)	5.0	3.25 (0.27)	4-pb	491 (63)
	2.5	99.6 (0.4)	3-5	2.89 (0.34)		475 (35)
	5	99.3 (0.4)	2.1	3.47 (0.61)		689 (85)
	10	100	3.5	3.52 (0.41)		539 (56)
Carroll et al.[192], 1996	0	99.6 (0.4)	5.0	3.53 (0.02)^{H}	4-pb	491 (63)
				3.25 (0.27)		
	1.6	97.8 (0.4)	3.5	4.23 (0.15)^{H}		738 (115)
				3.02 (0.21)		
		98.8 (0.4)	4.0	4.00 (0.08)^{H}		549 (125)
				2.76 (0.31)		
		98.5 (0.4)	2.1	3.71 (0.05)^{H}		593 (95)
				3.04 (0.39)		
		99.3 (0.4)	3.5	3.63 (0.05)^{H}		689 (80)
				3.47 (0.61)		
Zhao et al.[190], 1993	0	99.5	4.8	2.9 (0.1)	4-pb	559 (51)
		99.3	3.2	2.9 (0.1)	3-pb	569 (72)
	5	99.9	4.2	3.3 (0.1)	4-pb	1001 (102)
		99.9	4.2	3.6 (0.1)	4-pb	760 (28)
		98.3	5.4	2.7 (0.1)	3-pb	586 (72)
Niihara[21], 1991	0	~100	23	3.5	-	350 (42)
	5	~100	3	4.8		1520 (125)

T.D.: Theoretical density (%); d_{50}: Average grain size (μm); K_{IC}: Critical stress intensity factor in mode I (MPa $m^{1/2}$); σ: Strength (MPa); 3 or 4-pb: Three or Four point bending; E.d: Experimental details; (S.D.): Standard deviation; $^{++}$: Anstis equation; $^{+++}$: Liang equation; ^{H}: Hertzian indentation.

In fact, no conclusive reported data are found for Vickers toughness of Al_2O_3/SiC nanocomposites. Considering those studies where limited variability of data is reported, in general, toughness of the composites are comparable to those of monolithic alumina[183,187,197,247] or relatively low increases in average values are associated with the presence of SiC nanoparticles (e.g.: ≈12 vol.%)[239].

Table 1.5 summarises the main microstructural characteristics, strength and fracture toughness for Al_2O_3/SiC nanocomposites tested by techniques different from IT, such as CT, SENB/SEVNB, ISB and calculated from the critical defect size and the strength.

Much less toughness testing of nanocomposites has been done with notched beams in flexure[181,22,249,277,278] Davidge et al.[181] tested single edge notched beams (SENB) in flexure and found no statistically significant difference between K_{IC} values for nanocomposites containing 5, 10 and 15 vol.% SiC. The variability of values reported

by these authors increased with SiC content. Hoffman and Rödel[277] performed Compact Tension tests to determine crack tip toughness of nanocomposites and found that it was similar to that of fine grained alumina and equivalent to the fatigue limit of the nanocomposite. The R-curve determined for the nanocomposite was extremely weak. As signalled by the authors, main problem of the results was the high variability found due to the heterogeneous microstructure of the nanocomposite. Choi and Awaji[22] used Single Edge V Notched Beams with notch radius tips lower than 20 μm tested in three point bending, and found a significant increase in toughness from 3.72 MPa $m^{1/2}$ for single phase alumina to 5.06 MPa $m^{1/2}$ for Al_2O_3/3vol.% SiC. Pérez-Rigueiro et al.[278] did not find any difference between values obtained for reference aluminas with slightly higher densities (≈99% of theoretical) and average grain sizes (2.3-4.6 μm) than those of composites with 5 and 20 vol.% (≈98% of theoretical and 0.6-1.8 μm). Belmonte et al.[249] reported 3 point bending SEVNB toughness results for Al_2O_3/20vol.% SiC; four SiC powders were considered. They found an increase (14-37%) in toughness as compared to those for a reference alumina with slightly higher density (≈99% of theoretical) and similar average grain size (0.83 ± 0.52 μm) than those of the composites (≈98% of theoretical and 0.4-0.8 μm). In these works, unstable tests were used and the reported values might be over-estimated.

Summarising, there is not a well established method for toughness testing of Al_2O_3/ /SiC nanocomposites and most available data lead to inconsistent conclusions about the nanocomposite effect. Potential reasons for this fact are that materials with different degrees of homogeneity have been tested and results have been compared to those corresponding to single-phase alumina materials with large microstructural differences. However, the main reason for such a lack of conclusive results is that most data have been obtained using indentation toughness. This situation for the Al_2O_3/SiC

nanocomposites, which are the most well known, is still worse for other systems that have been less studied.

Table 1.5. Microstructural characteristics, strength and fracture toughness for Al_2O_3/SiC nanocomposites tested by techniques different from indentation toughness (IT).

Reference	vol.% SiC	T.D. (S.D) %	d_{50} (S.D.) (μm)	K_{IC} (S.D.) ($MPa \cdot m^{1/2}$)		σ (S.D.) (MPa)	
				E.d.	Values	E.d	Values
Belmonte et al.[249], 2006	0	99.9	0.83 (0.52)	SEVNB	4.3 (0.1)		
	20	99.2	0.86 (0.53)		5.9 (0.3)		
		99.5	0.80 (0.51)		5.2 (0.4)		
		98.7	0.44 (0.42)		4.9 (0.2)		
		92.4	0.24 (0.16)		3.0 (0.4)		
Sun et al.[199], 2005	0	99.85		ISB + 3-pb	3.1	3-pb	345 (55)
	2	99.24	15		3.75		380 (55)
	3	99.37	11		4.1		405 (55)
	4	99.56	4		4.25		500 (65)
	5	99.67	2.2		4.75		610 (65)
	6	99.79	2		4.5		530 (55)
	7	99.21	1		4.15		495 (55)
Choi et al.[22], 2005	0		2	SEVNB 3-pb	3.72	3-pb	462
	3				5.06		760
Davidge et al.[181], 1997	0	>99.5	2-5	SENB	3.1 (0.1)	4-pb	462 (90)
	5	>99.5	2-5		3.3 (0.3)		760 (60)
	10	>99.5	2-5		3.5 (0.2)		806 (33)
	20	>99.5	2-5		3.6 (0.4)		793 (55)
Hoffman et al.[277], 1997	0	>99.5	0.8	CT	2.3	4-pb	630 (40)
	5	98.8	2.5		2.07		595 (82)
Perez-Rigueiro et al.[278], 1997	0	100	4.6	SEVNB 3-pb	4.0 (0.3)	3-pb	409 (21)
				Critical defect 3-pb	4.4		
		99.8	2.3	SEVNB 3-pb	3.8		390 (20)
	5	99.0	2.6	SEVNB 3-pb	3.6 (0.2)		492 (60)
				Critical defect 3-pb	3.1		
		99.0	3.5	SEVNB 3-pb	2.5 (0.2)		396 (19)
	20	97.6	1.8	SEVNB 3-pb	3.1 (0.1)		473 (22)
		96.5	0.6	SEVNB 3-pb	3.36 (0.04)		436 (29)
				Critical defect 3-pb	2.7		

T.D.: Theoretical density (%); d_{50}: Average grain size (μm); K_{IC}: Critical stress intensity factor in mode I (MPa $m^{1/2}$); σ: Strength (MPa); SEVNB: Single Edge V Notched Beam; CT: Compact Tension; SENB: Single Edge Notched Beam; 3 or 4-pb: Three or Four point bending; E.d: Experimental details; (S.D.): Standard deviation.

Capítulo 2

OBJETIVOS E HIPÓTESIS

2. OBJETIVOS E HIPÓTESIS

A partir de todo lo expuesto anteriormente:

Se evidencia la necesidad de contar con un ensayo para la determinación precisa de la tenacidad de materiales cerámicos, que pueda ser utilizado de manera rutinaria en el laboratorio.

Por lo tanto, el objetivo principal de este trabajo ha sido el desarrollo de un dispositivo experimental y una metodología de ensayo y análisis de resultados para la determinación de la tenacidad de fractura de materiales cerámicos.

La hipótesis básica de este trabajo es la adecuación de los ensayos de fractura estable para la determinación de la tenacidad de fractura de los materiales.

Con objeto de alcanzar fractura estable se propone:

i) La idoneidad de la apertura de los labios de la grieta como parámetro de control para alcanzar ensayos de fractura estable. Se ha elegido este parámetro indirecto como variable de control puesto que crece de manera continua y su detección por medios ópticos es más simple que la detección directa de la grieta.

ii) Las altas prestaciones de los equipos electromecánicos modernos van a permitir el uso de la apertura de los labios de la grieta.

Se han seleccionado ensayos de flexión en tres puntos de probetas SEVNB porque los medios actuales de introducción de entallas en forma de V conducen a resultados reproducibles. El uso de este ensayo está ampliamente extendido.

Con el fin de demostrar la validez del dispositivo experimental y la metodología de ensayo y análisis de resultados desarrollados, se ensayaron materiales cerámicos con comportamientos mecánicos muy diferentes:

Espinela de aluminio-magnesio ($MgAl_2O_4$), con comportamiento frágil.

Alúmina (Al_2O_3) de grano fino, con comportamiento frágil.

Mullita ($3Al_2O_3 \cdot 2SiO_2$), con comportamiento frágil y crecimiento subcrítico de grietas en aire significativo.

Refractarios comerciales, en los cuales ocurren mecanismos de refuerzo durante la fractura.

Se han propuesto los materiales nanocompuestos de Al_2O_3/SiC como sistema modelo para evaluar la validez del dispositivo experimental y de la metodología de ensayo y análisis de resultados desarrollados para la caracterización de otros materiales cerámicos avanzados.

Capítulo 3

DESARROLLO DEL DISPOSITIVO EXPERIMENTAL

3. DESARROLLO DEL DISPOSITIVO EXPERIMENTAL

El diseño, desarrollo y puesta en servicio del dispositivo experimental y de los procedimientos de ensayo para la realización de ensayos de fractura estable de materiales cerámicos utilizando como variable de control la apertura de los labios de la grieta, se ha llevado a cabo en el marco de un Proyecto de Investigación Fundamental Orientada a la Transmisión de Conocimiento a la Empresa (TRACE), MCI-Microtest SA:"Desarrollo de un equipo para ensayos de fractura estable de materiales", contrato Microtest-Instituto de Cerámica y Vidrio (MCI-PET 2008-0113, 11/2009-12/2011).

Parte de los resultados derivados de esta investigación dieron lugar a una publicación en la revista Journal of Strain Analysis for Engineering Design (Anexo I).

Se ha seleccionado la flexión en tres puntos de probetas en forma de "V" por su simplicidad y la repetibilidad de sus resultados (apartado 1.3.2).

Hasta la fecha los parámetros de control de la deformación de las probetas más utilizados han sido carga y desplazamiento del marco de carga, como se explicó en el apartado 1.3.3. En este trabajo se propuso la utilización de la apertura de los labios de la grieta (CMOD) como parámetro de control puesto que aumenta de manera continua durante la fractura y de esta manera, al menos a nivel teórico, sería posible alcanzar ensayos de fractura estable. El CMOD se plantea además como parámetro de medida indirecta como respuesta a la difícil detección de grietas por medidas ópticas debido a su pequeña apertura.

Teniendo en cuenta la pequeña apertura de los labios de la grieta en los materiales cerámicos, se adhirieron unas espigas de 1.5 mm de diámetro y 12 mm de longitud a ambos lados de la entalla, para poder detectar y medir la apertura de los labios de la grieta durante el ensayo.

El dispositivo experimental utilizado se muestra en la figura 3.1. Los elementos necesarios son un emisor que permite la iluminación de la probeta a ensayar, delimitando la zona de medida a la distancia existente entre dos espigas adheridas a ambos lados de la grieta, un receptor, un convertidor y un procesador que permitan monitorizar y registrar la medida.

Figura 3.1. Equipo para la realización de ensayos de fractura estable que consta de una máquina electromecánica con un dispositivo de flexión en tres puntos, un micrómetro óptico conectado a un controlador que permite monitorizar y registrar el CMOD, y el soporte informático que integra el sistema SCM3000.

3.1. Unidad de medida de apertura de los labios de la grieta

Existen dos grandes grupos de sistemas de medida sin contacto que podrían ser utilizados para medir la apertura de los labios de la grieta: los denominados "micrómetros ópticos", basados en la detección y análisis de señales láser (reflexión láser, interferometría Doppler, difracción láser, barrido láser, interferometría láser, etc.) y los basados en visión artificial, mediante cámaras digitales[44].

Se plantearon, en concreto, dos opciones para la instrumentación de medida:

- Micrómetro óptico serie LS-7600
- Visión artificial de 2 megapixeles CV-2600P

Se eligió el micrómetro óptico en función del rango de medida y la precisión necesarios y el tipo de señal proporcionada. Si bien el intervalo exacto de valores de apertura de los labios de la grieta dependerá del material ensayado, la geometría específica del ensayo- tamaño de probeta y distancia interapoyos- y el tamaño de la grieta, una evaluación preliminar del rango necesario se ha realizado a partir de resultados previos. Se han considerado ensayos de flexión en tres puntos de probetas prismáticas con entallas en forma de V (SEVNB) de circona tetragonal policristalina estabilizada con ytria (Y-TZP)[76], uno de los materiales cerámicos de mayor tenacidad (K_{IC}~8 MPa $m^{1/2}$). Asimismo, se han considerado los resultados obtenidos en un material de alúmina-mullita[279] de muy baja tenacidad (K_{IC}~2-3 MPa $m^{1/2}$). Para este material solo se consiguieron ensayos estables o semiestables para tamaños de entalla relativamente grandes (α>0.7), por lo que la mayor parte de las probetas fallaban durante el mecanizado. Para las geometrías utilizadas, Y-TZP[76]: probetas 50x10x5 mm^3, distancia interaopoyos 40 mm; alúmina-mullita[279]: probetas 50x6x4 mm^3, distancia interapoyos 40 mm, la mayor parte de la fractura ocurría en intervalos de CMOD menores a 25 y 15 μm para Y-TZP y el material compuesto, respectivamente[76,279]. Los resultados obtenidos han permitido inferir que la precisión requerida estaba por debajo de 1 μm.

El micrómetro óptico seleccionado es de alta precisión del tipo LS7010M (Keyence, Japón). El principio de medida del sistema es el siguiente (figura 3.2): un LED (Light-Emitting Diode) verde de alta intensidad GaN irradia luz, que es transformada en un haz paralelo uniforme a través de la unidad de difusión especial y de lentes colimadoras, en el intervalo de medida que va desde 0.04 mm hasta 6 mm. Este haz paralelo "ilumina" el área de medida. La imagen de la sombra de la probeta aparece en el HL-CCD (High-speed Linear Charge Coupled Device) a través del sistema óptico telecéntrico. Con el

sistema telecéntrico de lentes el tamaño de la imagen en el CCD se mantiene, incluso si se mueve, por lo tanto, se obtiene la misma precisión todo el tiempo. La señal incidente de salida del HL-CCD es procesada por el procesador DE (Digital Edge-detection) en el controlador y la CPU. El equipo incorpora una cámara CMOS (Complementary Metal Oxide Semiconductor) para capturar la imagen en tiempo real.

A continuación se exponen las características más significativas del micrómetro óptico de alta precisión seleccionado:

El micrómetro óptico seleccionado dispone de un sistema de detección basado en un dispositivo de carga aplicada (HL-CCD) que ofrece una repetibilidad de ±0.06 μm.

El sistema óptico telecéntrico permite la medición con alta precisión, ± 0.5 μm, muy superior a la precisión alcanzada mediante el uso de micrómetros de barrido láser (± 2 μm) que no sería adecuada a los requerimientos descritos (< 1 μm). Para mejorar la precisión de la medida pueden eliminarse valores anormales que superan un valor prefijado, por lo que puede evitarse una detección incorrecta debida, p.ej., a polvo en el aire o gotas de agua.

El sensor HL-CCD permite una alta velocidad de muestreo, 2400 datos/segundo, dos veces más rápido que los sensores convencionales utilizados en los métodos de barrido. Esta alta velocidad es necesaria para permitir la respuesta ágil del equipo a desviaciones de la rampa de incremento de CMOD programada.

El micrómetro óptico convierte las distancias detectadas en señales analógicas que son procesadas en la unidad de control de la máquina de ensayos donde el software SCM3000 (Microtest, España) convierte estas señales analógicas en digitales.

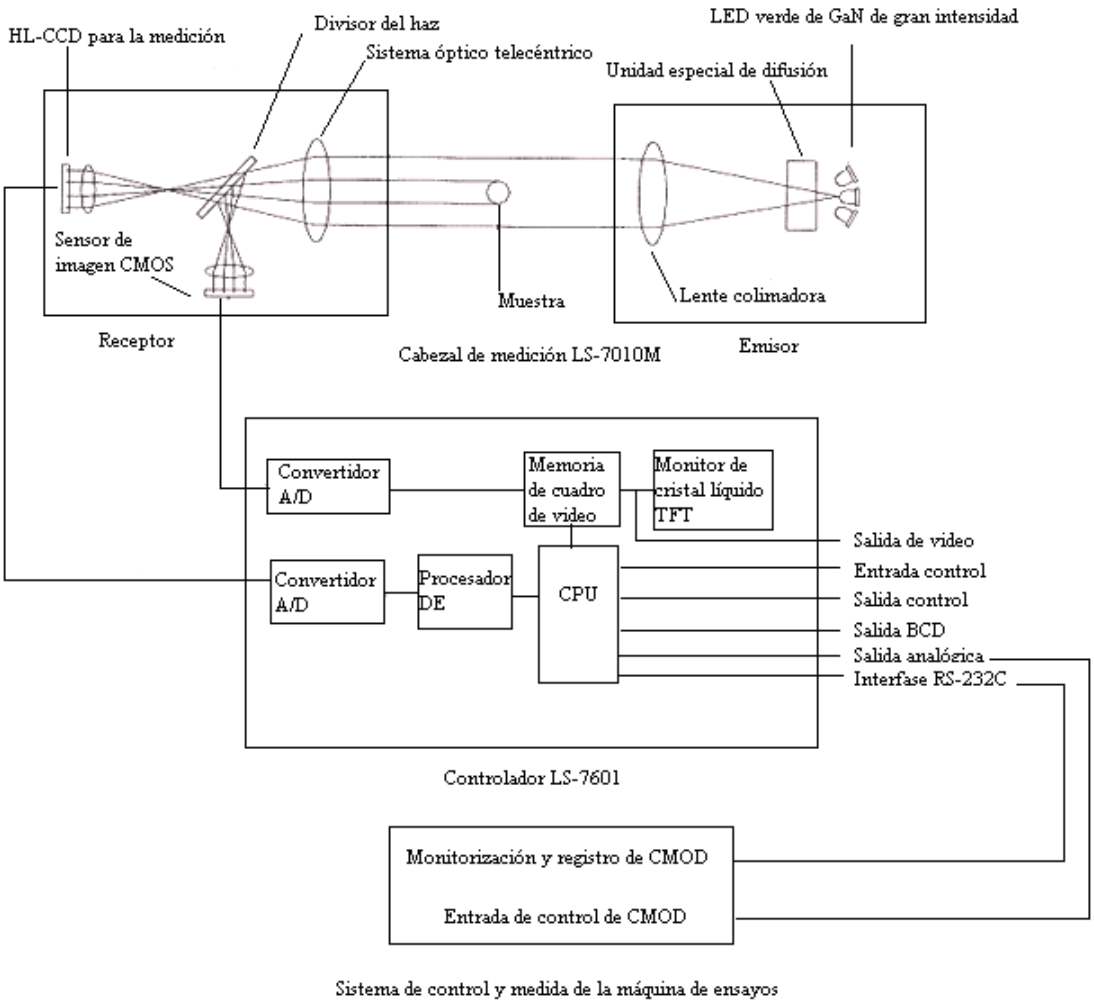

Figura 3.2. Principio de medida del micrómetro óptico y sistema SCM3000.

3.2. Sistema y geometría de carga

La máquina de ensayos es electromecánica del tipo EM1/50 (Microtest, España) de un husillo y doble columna. Las máquinas de ensayo universales electromecánicas se utilizan sobre todo para ensayos con variaciones monótonas de la carga en modo de tracción o de compresión. Mediante un sistema electrónico se genera la señal de control que hace que el actuador mueva el puente inferior en dirección ascendente o descendente. El desplazamiento del puente inferior está controlado y es medido por medio de un codificador óptico colocado en el eje motor.

El controlador electrónico SCM3000 (Microtest, España) incluye canales de carga y posición, así como otros canales de posición auxiliares que permiten la adición de canales de deformación para extensómetros que posibilitan el uso de variables de control externas a la máquina, no sólo carga y posición, como es el caso de la apertura de los labios de la grieta (CMOD).

Se ha elegido una máquina de ensayos universal electromecánica porque con ella se pueden alcanzar variaciones de posición extremadamente pequeñas, como son las requeridas para ensayos de fractura de materiales frágiles. Si bien tradicionalmente han sido necesarias las máquinas hidráulicas para asegurar respuestas rápidas del marco de carga; p.ej., en los ensayos de fatiga, ha sido posible el uso de una máquina electromecánica debido al gran desarrollo que se ha producido últimamente en los sistemas de control y en la mecánica de este tipo de máquinas.

El intervalo de carga máxima para la máquina de ensayos seleccionada es de 50 kN, tanto a tracción como a compresión. El rango de desplazamiento es de 0-100 mm y la velocidad máxima es de 100 mm/min. Las cargas reales aplicadas se miden mediante las células de carga extensométricas montadas en la línea de aplicación de la fuerza. Se ha seleccionado una célula de carga de 5kN para asegurar la alta rigidez del dispositivo experimental que es ~ $2\ 10^8$ N/m.

Las probetas a ensayar se colocan en un dispositivo de flexión en tres puntos entre el marco de carga y el puente inferior móvil.

En la figura 3.3 se muestra un esquema general del dispositivo de flexión en tres puntos, donde, P, es la carga aplicada, L, es la distancia entre los apoyos inferiores del marco de carga, B, es el espesor de la probeta, W, es la anchura de la probeta y, a, es la longitud de la grieta.

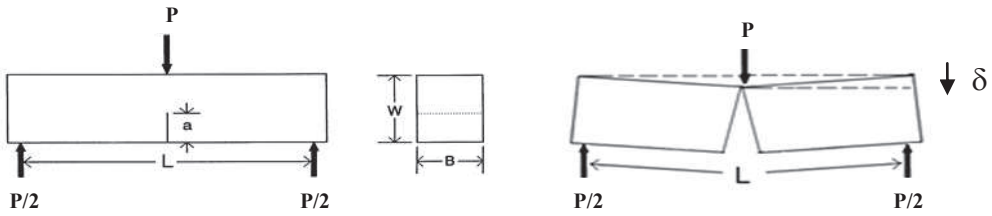

Figura 3.3. Representación esquemática de la geometría de carga para ensayos de flexión en tres puntos, donde P es la carga aplicada, L es la distancia entre apoyos inferiores, B es el espesor de la probeta, W es la anchura de la probeta y a es la longitud de la grieta. Para materiales elástico-lineales, la deflexión de la probeta (δ) puede igualarse al desplazamiento del marco de carga.

3.2.1. Cerámicas técnicas avanzadas

Para las cerámicas técnicas avanzadas se ha elegido la geometría de la norma clásica ASTM STP601 puesto que es la que más se ha utilizado y se dispone de un mayor número de datos sobre materiales cerámicos. Esta geometría consiste en probetas de 50x6x4 mm^3 y una distancia interapoyos de 40 mm. Los soportes de flexión son rígidos de acero inoxidable (Figuras 3.4 y 3.5).

La flexibilidad de la máquina, célula de carga y sistema de apoyos se determinó experimentalmente ensayando una barra de alúmina sin agrietar de 4 mm de espesor (B), 6 mm de anchura (W) y 50 mm de longitud; el valor obtenido fue 1.5 10^{-7} m/N hasta 150 N.

Para la determinación de la tenacidad de fractura, como se ha mencionado anteriormente (apartado 1.3.2), se seleccionaron probetas prismáticas con entalla en forma de V (SEVNB). La entalla inicialmente se hizo con un disco diamantado de 300 μm de espesor. Usando esta pre-entalla como guía, la parte restante de la entalla se corrigió con una cuchilla de 150 μm de espesor, impregnada con pasta de diamante de 15, 6 y 1 μm, de tal manera que se consiguió un radio de curvatura de fondo de entalla por debajo de 10 μm, de acuerdo con las recomendaciones derivadas de las conclusiones del round robin descrito en el apartado 1.3.2 (Figura 3.6).

Figura 3.4. Máquina de ensayos Microtest EM1/50 con el dispositivo experimental para cerámicas técnicas avanzadas.

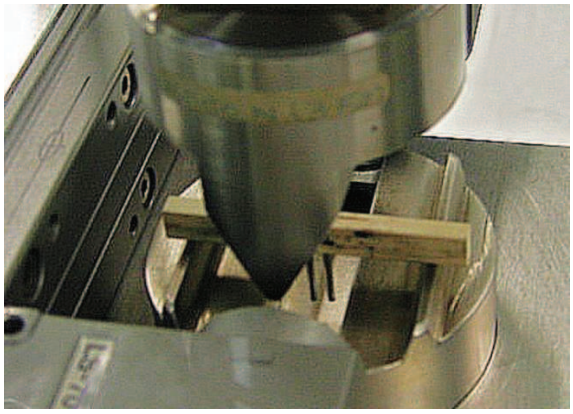

Figura 3.5. Detalle del dispositivo de flexión en tres puntos con el micrómetro óptico para cerámicas técnicas avanzadas.

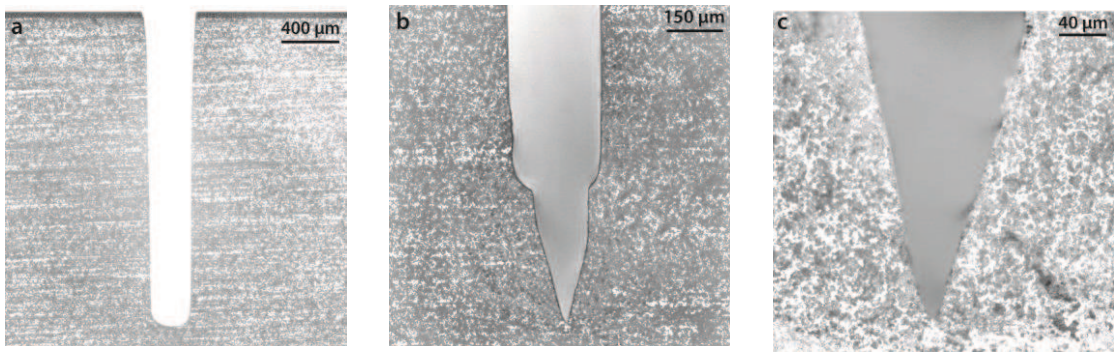

Figura 3.6. Superficie lateral de una probeta del material de alúmina ensayado. Microscopia óptica de luz reflejada.
(a) Corte con disco diamantado, pre-entalla.
(b) y (c) Se muestra el fondo de entalla en forma de "V" corregido con una cuchilla impregnada en pasta de diamante.

3.2.2. Materiales refractarios

Para los materiales refractarios se han seleccionado dos tamaños de probetas 150x25x25 y 200x40x40 mm^3, siendo la distancia interapoyos 125 y 180 mm, respectivamente. Estas dimensiones son las recomendadas para la determinación del módulo de rotura de materiales refractarios conformados densos según norma UNE-EN 993-6:1995[280]. El rodillo de carga es articulado mientras que los rodillos de soporte tienen posibilidad de giro sin articulación. (Figuras 3.7 y 3.8).

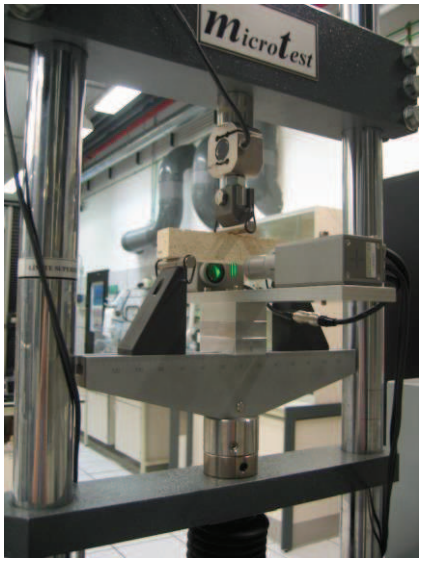

Figura 3.7. Máquina de ensayos Microtest EM1/50 con el dispositivo experimental para materiales cerámicos refractarios conformados densos.

Figura 3.8. Detalle del dispositivo de flexión en tres puntos con el micrómetro óptico para materiales cerámicos refractarios conformados densos.

La flexibilidad de la máquina, célula de carga y sistema de apoyos se determinó experimentalmente ensayando una barra de alúmina densa sin agrietar de 25 mm de espesor (B), 25 mm de anchura (W) y 150 mm de longitud. El valor obtenido fue 1.5 10^{-7} m/N hasta 150 N, el mismo valor que el obtenido con el dispositivo de flexión para la configuración de cerámicas avanzadas.

Para la determinación de la tenacidad de fractura de los materiales refractarios se utilizaron probetas de flexión en tres puntos con entallas rectas, SENB. Como el tamaño de agregados en estos materiales heterogéneos es ~ 3-5 mm, no es necesario utilizar entallas con forma en "V", y la entalla se realizó con un disco diamantado de 300 μm obteniéndose radios de fondo de entalla alrededor de 100-150 μm (Figura 3.9).

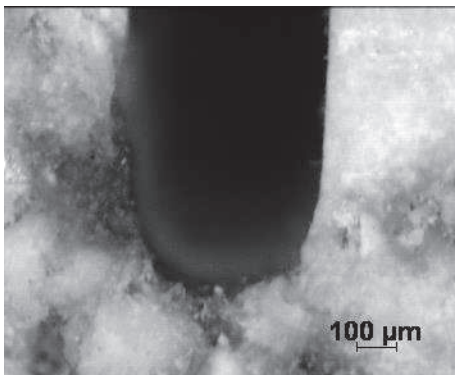

Figura 3.9. Superficie lateral de una probeta del material refractario silico-aluminoso ensayado. Microscopia óptica de luz reflejada.

3.3. Dispositivo experimental

Una vez definido el sistema de carga y el micrómetro óptico como unidad de medida sin contacto de la apertura de los labios de la grieta, ha sido necesario asegurar el acoplamiento global. Por una parte fue preciso asegurar el ajuste mecánico entre la máquina de ensayos y el micrómetro óptico. Para evitar interferencias mecánicas y asegurar una correcta orientación del haz luminoso con respecto al eje de carga y el montaje de flexión, el micrómetro óptico se unió al apoyo de carga inferior.

Por otra parte, ha sido preciso desarrollar una interfaz entre la máquina de ensayos y el micrómetro óptico que permita tanto registrar el CMOD como la realización de ensayos en control de este parámetro.

Para el tamaño de probeta de 50x6x4 mm^3 se seleccionó un rango de medida de ± 50 μm, según las variaciones de CMOD detectadas en ensayos previos, este rango en términos de señal analógica se corresponde con un voltaje de escala de 5 μm/V, lo que se traduce en una resolución teórica de 0.02 μm.

Para los tamaños de probetas de 150x25x25 y 200x40x40 mm^3 fue necesario aumentar el rango de escala hasta ± 5 mm obteniéndose entonces una resolución teórica de ± 2 μm.

Durante la realización de los ensayos se registraron los valores de carga (P), posición (d), apertura de los labios de la grieta (CMOD) y tiempo (t), de forma continua.

3.4. Análisis de estabilidad de ensayos de probetas SENB en control por posición

Como se describió en el apartado 1.3.3, es difícil conseguir fractura estable de materiales frágiles en ensayos de flexión en tres puntos de probetas SENB utilizando el desplazamiento del marco de carga como parámetro de control. Es posible justificar esta

dificultad a partir del análisis del locus de Griffith que describe las relaciones carga-deflexión de la probeta durante el proceso de fractura estable.

De acuerdo a los análisis realizados por Sigl[73], se produce crecimiento inestable de grieta cuando $(\partial G/\partial \alpha) \geq (\partial G_c/\partial \alpha_c)$ y crecimiento estable de grieta cuando $(\partial G/\partial \alpha) < (\partial G_c/\partial \alpha_c)$, donde G_c es la tasa crítica de liberación de energía (energy release rate, apartado 1.1) y α la longitud de entalla relativa (α=a/W). Por lo tanto la condición de equilibrio que define el locus de Grifftith es $G=G_c$.

Para representar los locus de Griffith correspondientes a ensayos de fractura estable de materiales bajo condiciones experimentales dadas, Biolzi y col.[74] definieron los parámetros carga y deflexión de la probeta (equivalente al desplazamiento, figura 3.3) adimensionales.

Teniendo en cuenta que la relación entre la carga aplicada (P) y el factor de intensidad de tensiones en modo I (K_I) para ensayos de flexión en tres puntos, viene dada por la ecuación 3.1[281]:

$$K_I = \frac{3PL}{2BW^{3/2}} K_\beta(\alpha) \tag{3.1}$$

donde P, L, B y W tienen el mismo significado que anteriormente (figura 3.3) y $K_\beta(\alpha)$ es una función geométrica válida para cualquier valor de longitud de grieta relativa ($0 \leq \alpha \leq 1$) y relaciones de distancia entre los apoyos-anchura de la probeta (β = L/W) mayores que 2.5 ($2.5 \leq \beta \leq 16$) (ecuación 3.2)[281]:

$$K_\beta(\alpha) = \frac{\sqrt{\alpha}\{p_\infty(\alpha) + 4/\beta[p_4(\alpha) - p_\infty(\alpha)]\}}{(1-\alpha)^{3/2}(1+3\alpha)} \tag{3.2}$$

Las funciones $p_4(\alpha)$ y $p_\infty(\alpha)$ definidas en las ecuaciones (3.3) y (3.4) son polinomios cúbicos para $\beta = 4$ (equivalente a una probeta de referencia con L/W = 4) y $\beta = \infty$ (formalmente equivalente a flexión pura)[281].

$$p_4(\alpha) = 1.9 + 0.41\alpha + 0.51\alpha^2 - 0.17\alpha^3 \tag{3.3}$$

$$p_\infty(\alpha) = 1.99 + 0.83\alpha - 0.31\alpha^2 + 0.14\alpha^3 \tag{3.4}$$

La fractura tendrá lugar para una carga máxima aplicada (P_{max}) tal que el factor de intensidad de tensiones en modo I (K_I) en la punta de la grieta alcance el factor crítico de intensidad de tensiones en modo I (K_{IC}) del material, ecuación 3.5.

$$K_{IC} = \frac{3P_{\max} L}{2BW^{3/2}} K_\beta(\alpha) \tag{3.5}$$

Al dividir ambos términos de la ecuación 3.5 entre $\sigma_f/W^{1/2}$, se obtiene la ecuación 3.6[74]:

$$\frac{K_I}{\sigma_f W^{1/2}} = \frac{3P\,L}{2\sigma_f BW^2} K_\beta(\alpha) = s \tag{3.6}$$

siendo σ_f la tensión de fractura determinada en flexión y s un número adimensional que describe la fragilidad de la muestra.

De esta manera queda descrita la carga adimensional según la ecuación (3.7)[74]:

$$\frac{P\,L}{\sigma_f BW^2} = \frac{2s}{3K_\beta(\alpha)} \tag{3.7}$$

La deflexión de la probeta, δ_s, viene determinada por la deflexión de la probeta sin grieta (δ) y la deflexión debida a la grieta ($\Delta\delta$),$\delta_s = \delta+\Delta\delta$, ecuaciones 3.8-3.11.

$$\delta = \frac{2P}{EB}(L/2W)^2 \left\{ L/2W + \left[2.85/(L/2W) - 0.42/(L/2W)^2 \right] / 4 \right\} \tag{3.8}$$

$$\Delta\delta = \frac{18(L/2W)^2}{EB} P \int_0^\alpha \left[K_\beta(\alpha)\right]^2 \partial\alpha \tag{3.9}$$

$$\delta_s = \frac{2P}{EB}(L/2W)^2 \left\{ L/2W + \left[2.85/(L/2W) - 0.42/(L/2W)^2 \right] \Big/ 4 + 9\int_0^{\alpha} \alpha \left[f(\alpha)^2 \right] \right\} \tag{3.10}$$

$$\delta_s = \frac{P}{EB}\lambda_s \tag{3.11}$$

donde, E, es el módulo de Young, λ_s, es la flexibilidad adimensional de la probeta y $f(\alpha)$ es igual a $K_\beta(\alpha)/\alpha^{1/2}$.

En una primera aproximación, el análisis teórico de estabilidad se hace suponiendo máquinas de ensayo totalmente rígidas, de tal manera que la flexibilidad de la máquina y dispositivos de ensayo, δ_m, sea igual a cero y la flexibilidad total, $\delta_t=\delta_s+\delta_m$, sea equivalente a la de la probeta.

Al dividir ambos términos de la ecuación 3.11 entre $\sigma_f/W^{1/2}$, se obtiene la ecuación 3.12:

$$\frac{\delta_s}{\sigma_f W^{1/2}} = \frac{P}{\sigma_f EBW^{1/2}}\lambda_s \tag{3.12}$$

Aplicando la ley de Hooke ($\sigma_f = E\cdot\varepsilon_f$, donde ε_f es la deformación unitaria) y relacionando la ecuación 3.12 con la ecuación 3.7 queda descrita la deflexión adimensional de la probeta según la ecuación 3.13:

$$\frac{\delta_s L}{\varepsilon_f W^2} = \frac{PL}{\sigma_f BW^2}\lambda_s = \frac{2s}{3K_\beta(\alpha)}\lambda_s \tag{3.13}$$

De esta manera, se puede representar, para una geometría de carga determinada (siendo L y W conocidos) la carga adimensional frente a la deflexión adimensional, para distintos valores de la fragilidad de la muestra (s). De acuerdo con esta aproximación, la grieta crecerá de manera estable cuando se cumpla que ($\partial P/\partial\delta$) es menor o igual a cero.

En la figura 3.10 se representan las curvas características carga-deflexión adimensional para la geometría de ensayo utilizada en este trabajo para caracterizar los

materiales avanzados. Se representa el locus de Griffith para distintos números de fragilidad de la probeta (s). Se observa como primero la deflexión de la probeta disminuye con la carga (régimen I) y después la deflexión aumenta mientras la carga sigue disminuyendo (régimen II), para distintos valores de fragilidad de la probeta (s)[74]. Conforme aumenta el número de fragilidad de la probeta (s) el locus de Griffith se desplaza hacia la derecha aumentando la región correspondiente al régimen II. La curva P-δ de la figura 3.10 presenta una derivada positiva para $a/W < 0.4$ y una derivada negativa para $a/W \geq 0.4$. Por lo tanto, para la geometría de ensayo utilizada en este trabajo para cerámicas técnicas avanzadas, si se utilizara una máquina con rigidez infinita, se alcanzaría crecimiento estable de grieta (régimen II) a velocidades crecientes del desplazamiento del marco de carga (control por desplazamiento), a partir de longitudes de entalla relativas (a/W) superiores a 0.4.

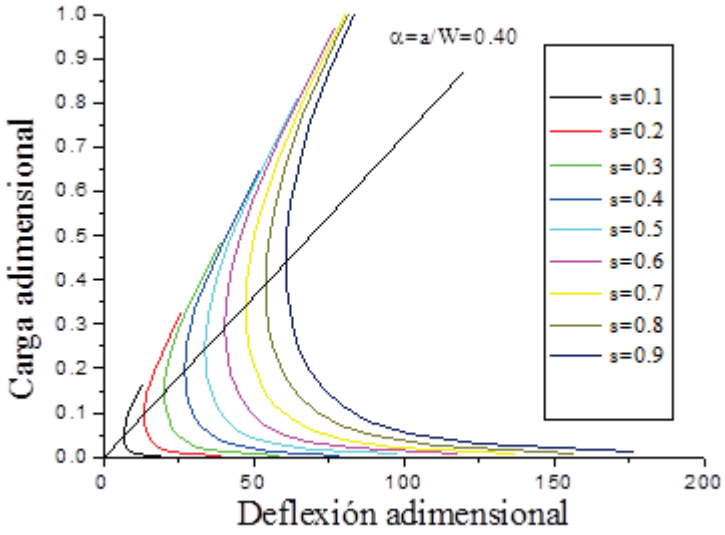

Figura 3.10. Locus de Griffith correspondiente a los valores numéricos carga-deflexión adimensionales para la geometría de ensayo de cerámicas técnicas avanzadas (apartado 3.2.1). Cálculos realizados para flexibilidad de la máquina igual a cero y probetas con diferentes números de fragilidad, s. La línea recta corresponde al tamaño relativo de entalla crítico, (α_c=0.40).

En la figura 3.11 se representan las curvas características carga-deflexión adimensionales para la geometría de ensayo utilizada para caracterizar los materiales refractarios, (probetas pequeñas 150x25x25 mm^3). La curva P-δ presenta una derivada positiva para $a/W < 0.6$ y una derivada negativa para $a/W \geq 0.6$. Se alcanzaría pues crecimiento estable de grieta (régimen II) a velocidades crecientes del desplazamiento del marco de carga (control por desplazamiento), a partir de longitudes de entalla relativas (a/W) superiores a 0.6. El mismo resultado se obtiene para la geometría seleccionada para el ensayo de probetas mayores 200x40x40 mm^3, figura 3.12.

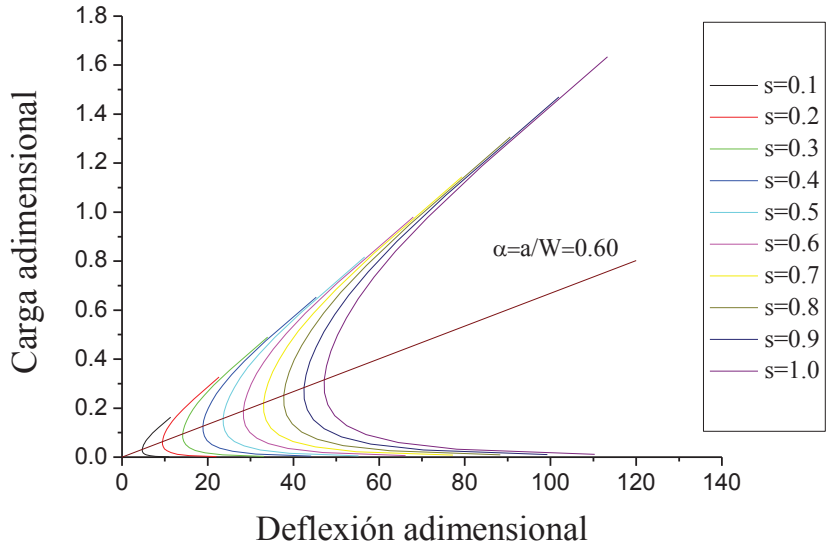

Figura 3.11. Locus de Griffith correspondiente a los valores numéricos carga-deflexión adimensionales para la geometría de ensayo de refractarios (probetas pequeñas 150x25x25 mm^3, apartado 3.2.2). Cálculos realizados para flexibilidad de la máquina igual a cero y probetas con diferentes números de fragilidad, s. La línea recta corresponde al tamaño relativo de entalla crítico, (α_c=0.60).

Los valores de α obtenidos por Biozi y col.[74] a partir de los cuales se alcanzan ensayos de fractura estable, son coincidentes con aquellos obtenidos por Bar-On y col[70].

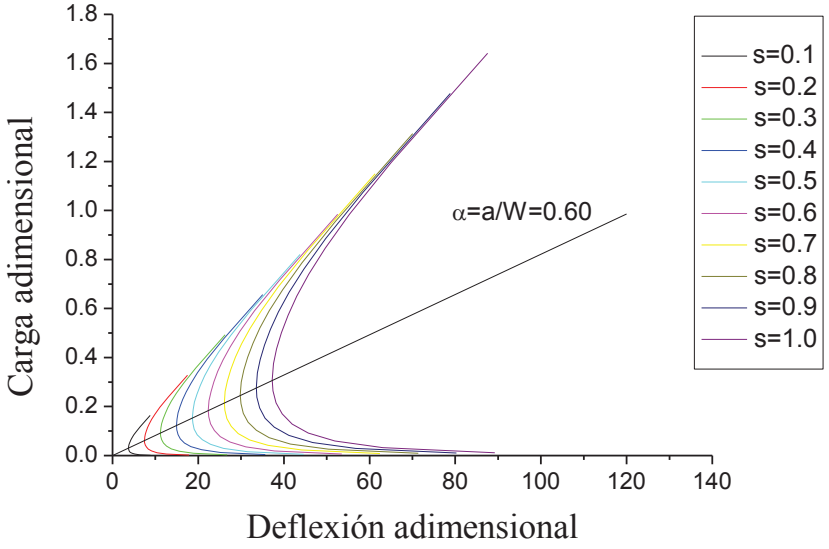

Figura 3.12. Locus de Griffith correspondiente a los valores numéricos carga-deflexión adimensionales para la geometría de ensayo de refractarios (200x40x40 mm^3, apartado 3.2.2). Cálculos realizados para flexibilidad de la máquina igual a cero y probetas con diferentes números de fragilidad, s. La línea recta corresponde al tamaño relativo de entalla crítico, (α_c=0.60).

3.5. Verificación del dispositivo experimental y procedimiento de ensayo

Para verificar la adecuación del sistema desarrollado y del CMOD como parámetro de control del movimiento del marco de carga durante el ensayo, se seleccionó una espinela de magnesio-aluminio que se caracteriza por ser un material cerámico frágil (sección 1.4).

Las propiedades del material ensayado[84] se describieron en el capítulo 1, tabla 1.1. Se trata de una espinela de grano fino (1.5 μm) y alta densidad (98% teórica) obtenida a partir de un polvo comercial prensado isostáticamente en frío y sinterizado en aire con

una velocidad de calentamiento y enfriamiento de 2ºC/min hasta 1630 ºC y un tiempo de permanencia de 2 h.

La geometría de ensayo fue la correspondiente a cerámicas técnicas avanzadas descrita anteriormente en el apartado 3.2.1. Las características de las entallas fueron: α=0.64 y radio de curvatura del fondo de entalla alrededor de 25 μm.

En la figura 3.13 se representa el locus de Griffith determinado teniendo en cuenta la flexibilidad del equipo (ecuación 3.11) y las propiedades del material de espinela (s=0.22). Para alcanzar ensayos estables en control por desplazamiento del marco de carga serían necesarios $\alpha \geq 0.70$, superior al valor obtenido considerando la flexibilidad de la máquina nula (figura 3.10).

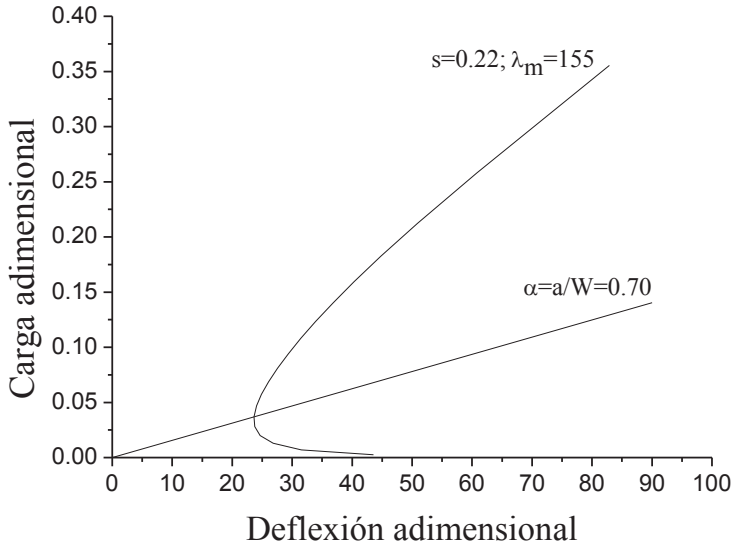

Figura 3.13. Locus de Griffith correspondiente a los valores numéricos carga-deflexión adimensionales para la geometría de ensayo de cerámicas técnicas avanzadas (apartado 3.2.1). Cálculos realizados para la flexibilidad adimensional, λ_m, correspondiente a la flexibilidad del dispositivo utilizado, $(\delta_m/P)=1.5\ 10^{-7}$ m/N. La línea recta corresponde al tamaño relativo de entalla crítico, (α_c=0.70).

Con el fin de constatar la posibilidad del CMOD como parámetro de control, se realizaron ensayos a velocidades constantes de CMOD desde 0.05 hasta 1 μm/min,

como se observa en la figura 3.14, las velocidades programadas se alcanzaron en todos los casos con variaciones inferiores a 0.02 μm/min.

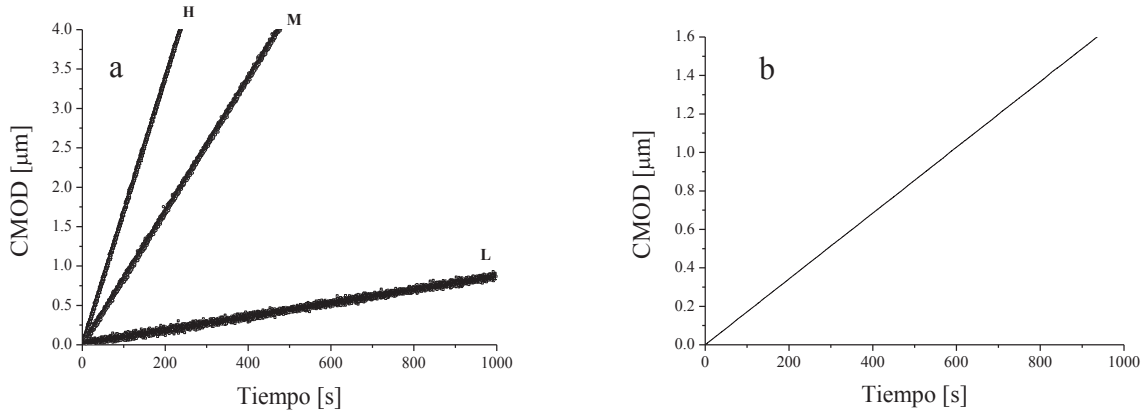

Figura 3.14. Valores experimentales CMOD-tiempo para distintas velocidades de ensayo programadas:
(a) L = 0.05 μm/min, M = 0.5 μm/min, H = 1 μm/min.
(b) 0.1 μm/min

En la figura 3.15 se muestra una curva experimental característica carga-tiempo correspondiente a la espinela ensayada en este trabajo a 0.1 μm/min, se observa una disminución monótona de la carga con el aumento de tiempo después de alcanzar la carga máxima, como corresponde a los ensayos de fractura estable.

En la figura 3.16 se muestra la curva experimental característica carga-desplazamiento correspondiente al ensayo de la figura 3.15, se observa cómo, a partir del valor de carga máxima, es necesaria una disminución del desplazamiento para alcanzar ensayos estables.

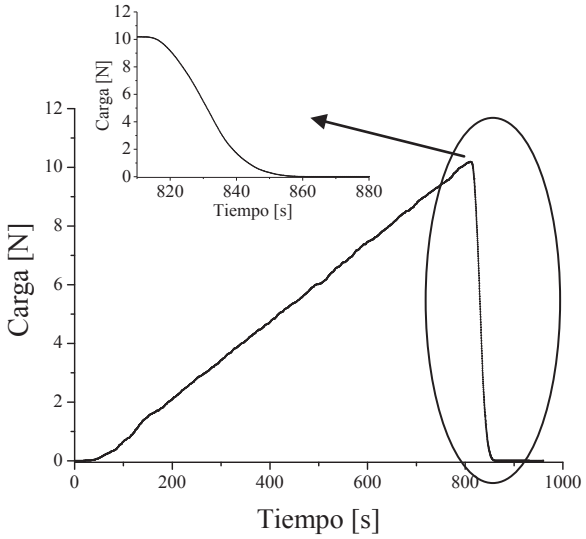

Figura 3.15. Curva experimental característica carga-tiempo correspondiente a la espinela caracterizada en este trabajo. Se muestra en detalle la zona de fractura donde se aprecia una disminución monótona de la carga con el tiempo después de alcanzar la carga máxima, correspondiente a la fractura estable.

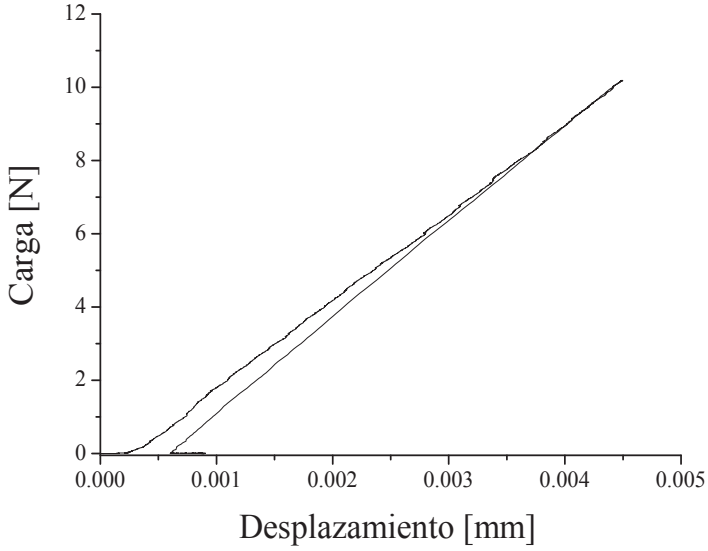

Figura 3.16. Curva experimental característica carga-desplazamiento. Se observa una disminución de la posición tras alcanzar el punto de carga máximo característica de los ensayos de fractura estable en control por CMOD.

En la tabla 3.1 se muestran los valores de tenacidad de fractura obtenidos en este trabajo a partir de ensayos estables y los valores obtenidos en ensayos inestables de probetas con igual geometría y mayor radio de curvatura (apartado 1.4) por Baudín y

col[84]. Los valores de K_{IC} y G_{IC} son la media de los obtenidos a partir de tres ensayos y S.D. es la desviación estándar.

Para calcular K_{IC} se utilizó la ecuación 3.1. A partir del valor de K_{IC}, el módulo de Young y el coeficiente de Poisson (0.294 para espinela de aluminio-magnesio)[282] se calculó la tasa crítica de liberación de energía en modo I, G_{IC}, de acuerdo con el análisis de Irwin para condiciones de deformación plana, según la ecuación 1.3.

El valor de K_{IC} es un 65% inferior al valor reportado previamente para este mismo material[84]. Esta diferencia se hace más patente cuando se considera G_{IC}, que es un orden de magnitud inferior. El efecto combinado del mayor radio de curvatura del fondo de entalla (apartado 1.4) y la energía adicional involucrada en la fractura inestable, es responsable de esta disparidad en los valores.

Tabla 3.1. Parámetros de tenacidad de fractura para el material de espinela.

Baudín y col.[84]		Este trabajo	
K_{IC} (S.D.) (MPa $m^{1/2}$)	G_{IC} (S.D.) (J/m^2)	K_{IC} (S.D.) (MPa $m^{1/2}$)	G_{IC} (S.D.) (J/m^2)
3.0 (0.1)	32 (2)	1.04 (0.06)	3.94 (0.01)

K_{IC}: Factor crítico de intensidad de tensiones en modo I (MPa $m^{1/2)}$; G_{IC}: Tasa crítica de liberación de energía en modo I (J/m^2); S.D.: Desviación estándar.

3.6. Conclusiones

- Se ha desarrollado un dispositivo experimental que utiliza la señal analógica correspondiente a la apertura de los labios de la grieta (CMOD), medida por un micrómetro óptico de alta precisión, para controlar el movimiento del marco de carga de las máquinas de ensayos electromecánicas comercializadas por Microtest (España).

- La apertura de los labios de la grieta (CMOD) es un parámetro de control válido para alcanzar ensayos de fractura estable de manera rutinaria en laboratorio de probetas estándar SEVNB en flexión en tres puntos.

- Para un material de espinela de grano fino, modelo de material con fractura frágil, el valor de K_{IC}, obtenido a partir de ensayos estables es sensiblemente inferior (65%) al obtenido a partir de ensayos inestables utilizando el desplazamiento del marco de carga como parámetro de control y radios de fondo de entalla superiores a los empleados en este trabajo.

ANEXO I

Este trabajo se presentó como póster en la Conferencia Ibérica de Fractura e Integridad Estructural celebrada en Oporto en 2010.

- C. Baudín, A. García, J. Hernández, M. López. "Controlled fracture tests of brittle ceramics". Conferencia Ibérica de Fractura e Integridad Estructural 2010. Oporto, Portugal. 17-19 de Marzo de 2010.

Los trabajos presentados en esta conferencia aparecen publicados en los libros colectivos Anales de Mecánica de la Fractura:

- C. Baudín, A. García, J. Hernández, M. López. "Controlled fracture tests of brittle ceramics". Proceedings XXVII Encuentro del Grupo Español de Fractura. Volumen I. p: 291-295. Ed. Secretaría del Grupo Español de Fractura, Madrid (2010).

A raíz de la presentación de este trabajo se recibió una invitación para su publicación en la revista Journal of Strain Analysis for Engineering Design:

- A. García-Prieto, J. Hernández, M. López and C. Baudín., "Controlled fracture test for brittle ceramics", J. Strain Anal. Eng. Des., 46 (1) 27-32 (2011). (DOI: 10.1243/03093247JSA685).

Journal Citation reports 2011 (JCR): IF=1.085, posición 10 de 32 en la categoría "Materials Science, Characterisation and Testing".

Mensaje recibido para la invitación de la publicación de este trabajo en la revista JSA:

-----Mensaje original-----
De: gustavovictor.guinea@upm.es [mailto:gustavovictor.guinea@upm.es]
Enviado el: miércoles, 21 de abril de 2010 12:43
Para: Baudín de la Lastra Carmen
CC: Paulo de Castro T
Asunto: Invitation to submit your paper to JSA

Dear Mrs. Baudín,

On behalf of the Selection Committee, it is our pleasure to inform you that your work entitled "CONTROLLED FRACTURE TESTS OF BRITTLE CERAMICS" and co authored by "C. Baudín, A. García, J. Hernández, M. López" presented at the past CIFIE 2010 conference held at Porto on March 16-19, 2010, has been pre-selected for recommended publication in the Journal of Strain Analysis for Engineering Design (JSA) (http://journals.pepublishing.com/content/119785) following the agreement between the Spanish Group of Fracture and this journal.

Please let us know at your earliest convenience, and in any case before April 30, 2010, if you –on behalf of the other authors– agree to submit your work to this journal, under the understanding that all the pre-selected works will be peer-reviewed before publishing.

If your answer is positive, we will contact you again to send detailed instructions on how to proceed.

Looking forward to hearing from you.

With best regards.

Gustavo Guinea
Paulo de Castro

Controlled fracture test for brittle ceramics

A García-Prieto[1], **J Hernández**[2], **M López**[2], and **C Baudín**[1*]
[1]Instituto de Cerámica y Vidrio, CSIC-Campus de Cantoblanco, Madrid, Spain
[2]Microtest S.A., Madrid, Spain

The manuscript was received on 15 June 2010 and was accepted after revision for publication on 29 July 2010.

DOI: 10.1243/03093247JSA685

Abstract: Controlled fracture tests that ensure the full conversion of supplied energy into crack surface energy are required for the accurate determination of the toughness parameters of materials. In this work, a new experimental configuration to perform three-point-bending single-edge V-notch beam stable fracture tests controlled by the crack mouth opening displacement (CMOD) is presented. The CMOD is chosen as the control variable because it is the only parameter that increases throughout the whole fracture process. Results obtained by applying the proposed approach to a fine-grained test sample of the spinel-structured phase of magnesium aluminium oxide are presented. The results obtained demonstrate that the proposed configuration allows stable fracture tests to be performed on extremely brittle ceramics.

Keywords: ceramics, spinel, stable fracture, toughness, work of fracture

1 INTRODUCTION

Stable crack growth conditions are required for reliable and accurate fracture toughness data to be obtained. If the fracture toughness values are determined using test configurations that do not allow stable crack growth, then the measurements are only valid for the crack initiation process [**1**]. In such cases, the calculated value of the fracture toughness will be over-evaluated unless the kinetic energy term in the growth process is ignored [**2**]. In addition to the fracture toughness, stable fracture tests allow the determination of fracture energy and crack-growth resistance curves.

Controlled fracture tests for brittle materials, such as the majority of ceramics, are difficult to accomplish and therefore they are not usually performed. A chevron notched geometry allows stable fractures to be created in brittle specimens using the displacement of the loading frame as a control parameter; however, test specimens are difficult to fabricate especially for fine-grained materials. For other geometries, such as straight notch beams in flexure and load-frame-displacement tests, stable fracture is only reached for materials that display some level of R-curve behaviour [**3**, **4**] since there has to be a mechanism to allow the load frame displacement to decrease after the peak load for stable testing of brittle materials.

The crack mouth opening displacement (CMOD) is the only parameter that increases throughout the whole fracture process, thus, it has been proposed as a control variable for stable fracture testing of ceramics. CMOD-controlled stable fracture tests have been reported for advanced ceramics that display R-curve behaviour such as yttria-partially-stabilized zirconia [**5**] but not for extremely brittle ceramics such as the spinel-structured phase of magnesium aluminium oxide ($MgAl_2O_4$). Such tests are performed using specific experimental laboratory setups.

In this work, a new experimental configuration to perform stable fracture tests on ceramics controlled by the CMOD parameter is presented together with results obtained using different experimental conditions for a fine-grained test sample of the spinel-structured phase of magnesium aluminium oxide.

2 EQUIPMENT

2.1 Loading device

The Microtest EM1/50 (Microtest, Madrid, Spain) is a single-screw dual-column servo-controlled elec-

*Corresponding author: Department of Ceramics, Instituto de Ceramica y Vidrio, CSIC, Kelsen 5, Madrid, 28049, Spain.
email: cbaudin@icv.csic.es

tromechanical test machine (Fig. 1). Electromechanical or universal testing machines are most commonly used for static testing in either tensile or compression modes within a single frame. The control is performed by an electronic system that generates the control signal to make the actuator move the crosshead in an upward or downward direction via a drive system. The test samples are placed between the rigid frame (stiffness $\sim 2\times10^8$ N/m) and the moving crosshead.

The maximum load range of the machine is 50 kN, both in tension and compression. The displacement range is 0–100 mm and the maximum velocity is 100 mm/min. The actual applied loads are measured by extensometer load cells mounted along the line of force application. The displacement of the moving crosshead is controlled and measured by means of an optical encoder placed in the motor axis.

The SCM3000 electronic controller (Microtest, Madrid, Spain) includes load and position channels as well as position auxiliary channels with the option to add additional strain channels for extensometers. In this case, the signal from the contact-free optical measurement system for CMOD determination is directed to one of these auxiliary channels. Therefore, the control parameters can be not only force and displacement but also CMOD.

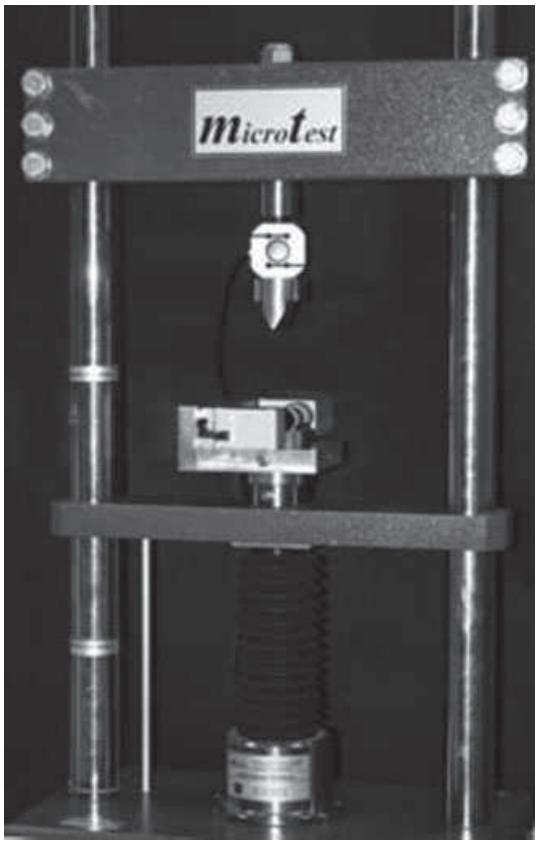

Fig. 1 A Microtest EM1/50 test machine and the experimental set-up

The test specimen was placed between the rigid frame and the moving crosshead in a stainless steel three-point bending test fixture with a span (S) of 40 mm (Figs 1 and 2). A load cell of 5 kN was selected to ensure a high stiffness of the loading set-up. The compliance of the machine, load cell, and support arrangement, in the load range used for testing (up to 150 N) was determined experimentally using an uncracked alumina bar of 4 mm thickness (B), 6 mm width (W), and 50 mm length; the obtained value was 1.5×10^{-7} m/N.

2.2 CMOD measurement unit

For the CMOD measurement and control, a high-precision optical micrometer a Keyence LS7010 (Keyence, Osaka, Japan) that incorporates a complementary metal oxide semiconductor (CMOS) camera was used to capture real-time images of the target (Figs 1 and 2). This optical system provided a measuring accuracy of $\pm0.5\,\mu$m.

The principle of measurement of the optical system is as follows (Fig. 3). A high-intensity GaN light-emitting diode (LED) radiates light which is converted into a uniform parallel beam by the special diffusion unit and collimator lens and this beam is used to illuminate the measurement area. The shadow image of the target is projected on to the high-speed linear charge coupled device (HL-CCD) by the telecentric optical system. The system of lenses ensures that the size of the image on the CCD does not change even if it moves, thus, the same precision is maintained. The output incident signal of the HL-CCD is processed by the digital edge-detection (DE) processor in the controller and central processing unit (CPU). The controller of the optical system incorporates a function that eliminates abnormal values in order to

Fig. 2 The three-point bending device with the optical micrometer

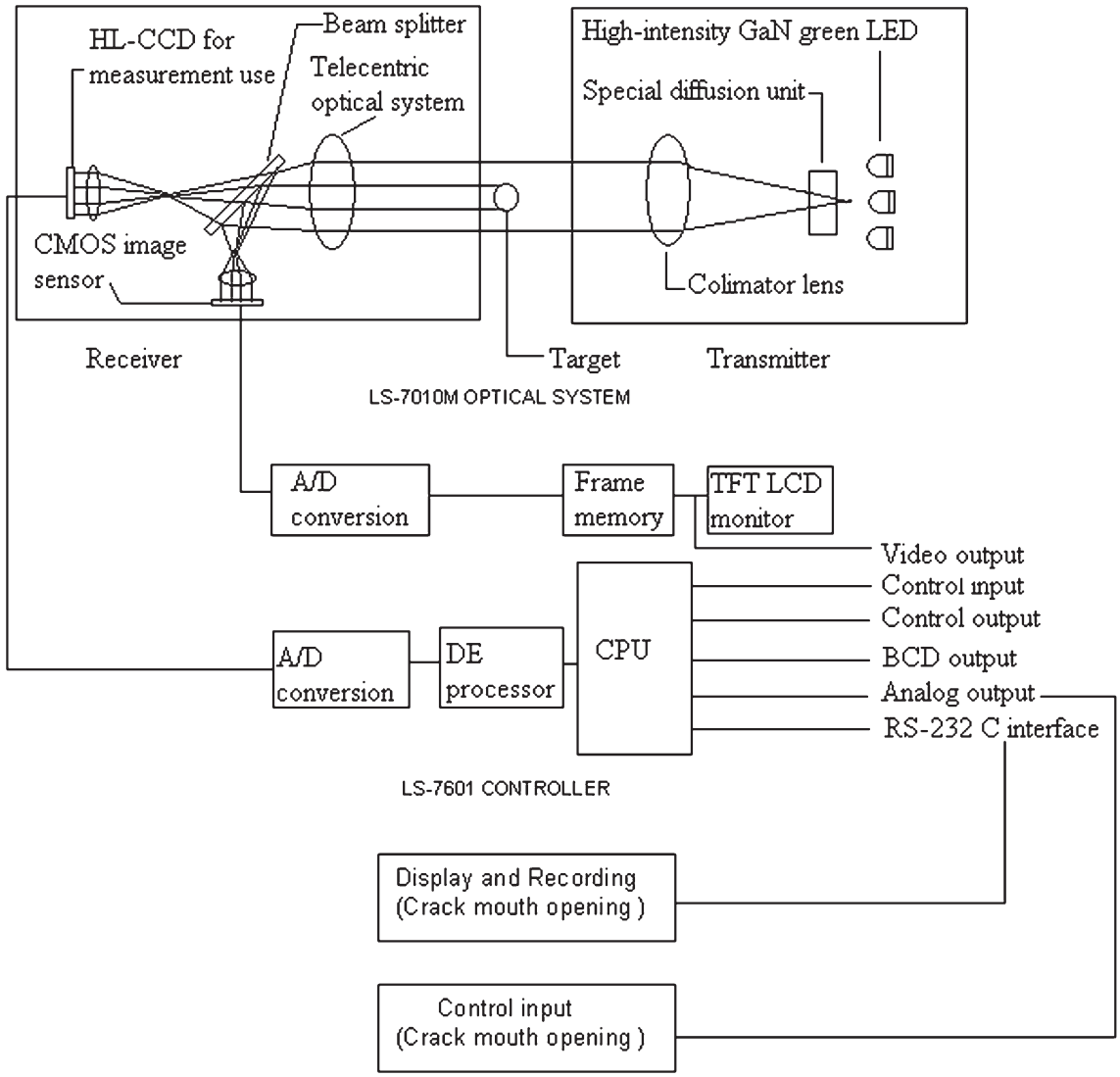

Fig. 3 Schematic diagram of the SCM 3000 control system

improve the precision of the measurement, with the detection threshold being the adjustable parameter.

2.3 Set-up

The optical micrometer was attached to the lower loading support; in this way mechanical obstructions are avoided and a correct orientation of the light beam with respect to the axis of load and the bending fixture is ensured. Given the small opening displacement of the notch, in order to be able to detect and measure its width during the test, pins of 1.5 mm diameter and 12 mm length were adhered to both sides of the notch ensuring that they were perpendicular to the light beam. To reach the highest accuracy the tests were performed at 20 °C, with a separation between the pins of 1 mm. The repeat accuracy of the optical micrometer for this separation was checked to be $\pm 0.06\,\mu$m using a 1.0 mm diameter round bar located in the centre of the measuring area. The equipment performed continuous measurements at a rate of 512 samples per second.

The optical micrometer converts the detected distances into analogue signals that are used as input to the control unit of the mechanical testing machine where the software in the SCM3000 converts them to discrete digital numbers. The whole range of the optical micrometer (6 mm) that corresponds to ± 10 V of analogue signal is converted into 2^{16} levels (65 536 values), thus, a theoretical resolution of 0.1 μm is obtained for the extreme point of the range. For the tests, a smaller range of measurement of the micrometer, $\pm 50\,\mu$m, was selected to detect the CMOD variations. In terms of analogue signal, this range corresponds to a scaling value of

5 μm/V and, therefore, with a theoretical resolution of about 0.02 μm.

3 SPECIMEN PREPARATION

Fine-grained test samples of the spinel-structured phase of magnesium aluminium oxide, labelled SP, with a density of $3.491 \pm 0.002\,g/cm^3$ and dynamic Young's modulus of 258 ± 2 GPa, were prepared from a commercial $MgO{\cdot}Al_2O_3$ powder and were sintered in air with a heating rate of 2 °C/min up to 1630 °C, a cooling rate of 2 °C/min and a dwell time of 2 h [**6**].

Single-edge V-notch beams of 4 mm thickness (B), 6 mm width (W), and 50 mm length were diamond machined. The notch was initially cut with a 300 μm wide diamond wheel. Using this pre-notch as a guide, the remaining part of the notch was created with a 150 μm wide razor blade sprinkled with diamond pastes of successively 15, 6, and 1 μm grain size. Tip radii of about 25 μm were obtained (Fig. 4). The relative notch depth, $\alpha = a/W$ (a = notch length), was 0.64.

4 TESTS AND DATA ANALYSIS

Figure 5 shows the CMOD–time plots corresponding to tests performed at different constant CMOD rates. The programmed CMOD rates with variations lower than 0.02 μm/min were reached in all cases. The SP specimens were tested at 0.1 μm/min (Fig. 6).

Using the compliance value (1.5×10^{-7} m/N) determined for maximum loads up to 150 N, the Young's modulus of the material ($E = 258 \pm 2$ GPa),

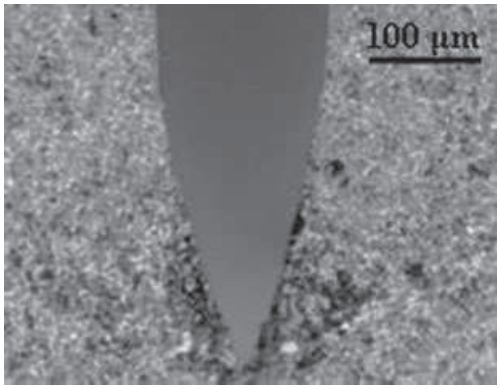

Fig. 4 Final notch in a tested specimen. The black colouration of the tip is a result of using diamond paste. Tip radii of about 25 μm are obtained

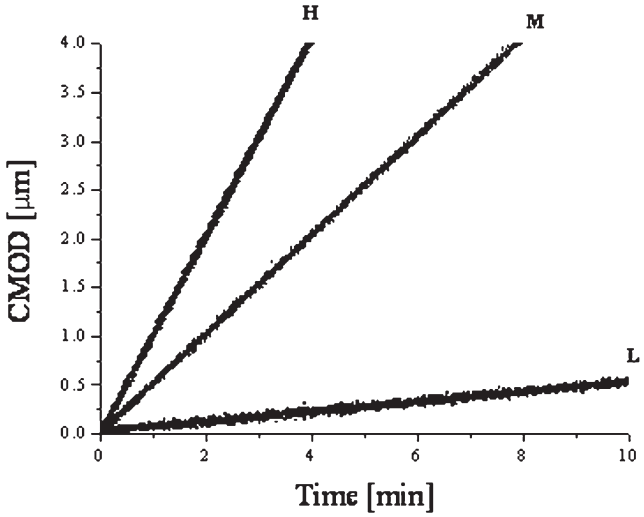

Fig. 5 CMOD–time plots for bending tests performed at different CMOD rates: $L = 0.05$ μm/min, $M = 0.5$ μm/min, and $H = 1$ μm/min

the geometry of the specimens, and bending device parameters ($B = 4$ mm, $W = 6$ mm, and $S = 40$ mm), and the analysis according to Bar-On *et al.* [**7**], stable fracture tests could not be obtained under displacement control for this material. However, stable fracture tests have been performed for specimens with a relative depth of about 0.64 using CMOD control, as shown in Fig. 7. In the CMOD-controlled tests performed in this work, continuously decreasing loads after the maximum load were observed with increasing time, as shown in Fig. 7, which correspond to controlled fracture.

Figure 8 shows the load–displacement plot corresponding to the tests of Figs 6 and 7. From the

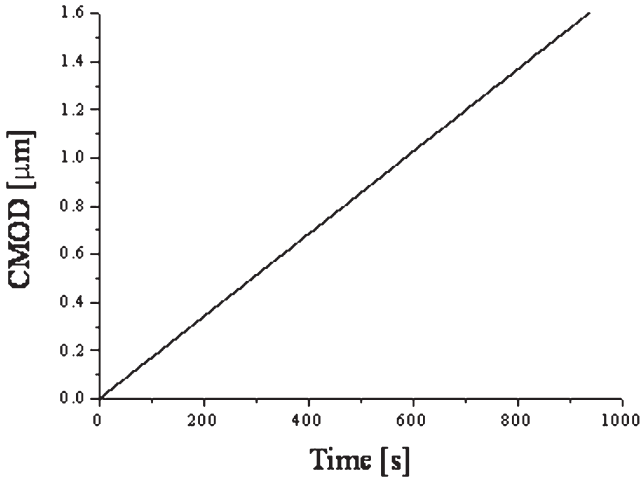

Fig. 6 CMOD–time plot for the selected testing conditions used to characterize the magnesium aluminium oxide test material

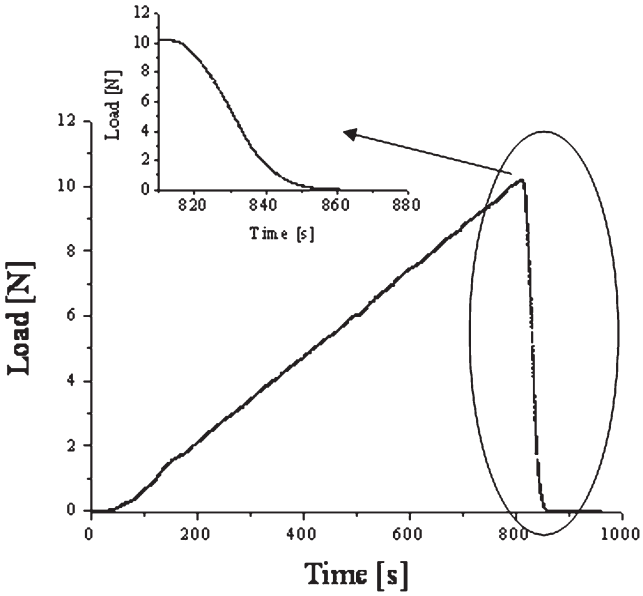

Fig. 7 Stable fracture test for a SP test specimen. The insert shows the continuous decrease in load with increasing time which corresponds to controlled fracture

maximum load, decreases in the displacement were needed to reach stable tests.

The critical stress intensity factor in mode I, K_{IC}, was calculated using the general expression of the stress intensity factor for three-point bend specimens (equation (1)) [**8**]

$$K_{IC} = \frac{3SP}{2BW^{3/2}} K_\beta(\alpha) \tag{1}$$

The S, P, B, and W parameters were defined in previous sections and K_β (α) is a general shape function (equation (2)), which is valid for any value of the relative notch depth ($0 \leqslant \alpha \leqslant 1$) and span-to-depth ratios ($\beta = S/W$) larger than 2.5 ($2.5 \leqslant \beta \leqslant 16$)

$$K_\beta(\alpha) = \frac{\sqrt{\alpha}\{p_\infty(\alpha) + 4/\beta[p_4(\alpha) - p_\infty(\alpha)]\}}{(1-\alpha)^{3/2}(1+3\alpha)} \tag{2}$$

The $p_4(\alpha)$ and $p_\infty(\alpha)$ given by equations (3) and (4) are cubic polynomials for $\beta = 4$ (equivalent to a reference beam with fixed $S/W = 4$) and $\beta = \infty$ (formally equivalent to pure bending), respectively.

$$p_4(\alpha) = 1.9 + 0.41\alpha + 0.51\alpha^2 - 0.17\alpha^3 \tag{3}$$

$$p_\infty(\alpha) = 1.99 + 0.83\alpha - 0.31\alpha^2 + 0.14\alpha^3 \tag{4}$$

The onset of crack propagation was considered at the peak load. The obtained value of K_{IC} for this test sample was $1.04 \pm 0.06\,\mathrm{MPa}\sqrt{\mathrm{m}}$, about one-third of the value determined in unstable tests ($\sim 3.0\,\mathrm{MPa}\sqrt{\mathrm{m}}$) [**6**].

The critical energy release rate, G_{IC}, was calculated from the K_{IC} and Young's modulus values using the result of Irwin for plane strain conditions

$$G_{IC} = \frac{{K_{IC}}^2}{E'} \tag{5}$$

where $E' = E/(1-\nu^2)$ is the generalized Young's modulus for plane strain (E is Young's modulus and ν is Poisson's ratio). The obtained value of G_{IC} is $3.83 \pm 0.004\,\mathrm{J/m^2}$ using 0.294 as Poisson's ratio for SP [**10**].

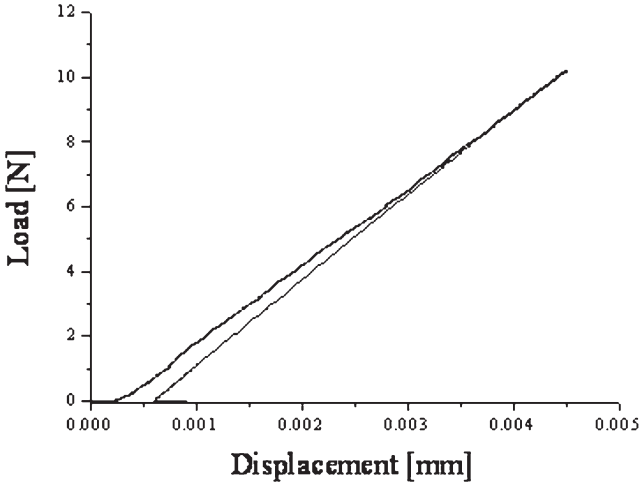

Fig. 8 Load–displacement plot for a SP test specimen

5 CONCLUSIONS

The following conclusions can be drawn from the presented work.

1. It is possible to control an electromechanical testing machine using an analogue output from an optical micrometer.
2. Using the CMOD as a control parameter, stable fracture tests can be performed for extremely brittle ceramics such as fine-grained samples of the spinel-structured phase of magnesium aluminium oxide.
3. The critical stress intensity factor in mode I determined for stable fracture is lower than the value measured for unstable tests. For the fine-grained test sample measured in this work this parameter is about one-third of that obtained using unstable testing conditions.

ACKNOWLEDGEMENTS

The authors gratefully acknowledge Professor Dr J. Y. Pastor for helpful discussions and MICINN (Spain) for their financial support under grants MAT2006-13480 C02 and MICINN and Microtest S.A MCI-PET 2008-0113.

REFERENCES

1 **Sørensen, B. F., Horsewell, A., Jørgensen, O., Kumar, A. N.,** and **Engbæk, P.** Fracture resistance measurement method for in situ observation of crack mechanisms. *J. Am. Ceram. Soc.*, 1998, **81**(3), 661–669.

2 **Blackman, B. R. K., Kinloch, A. J., Rodriguez Sanchez, F. S., Teo, W. S.,** and **Williams, J. G.** The fracture behaviour of structural adhesives under high rates of testing. *Eng. Fracture Mech.*, 2009, **76**, 2868–2889.

3 **Wieninger, H., Kromp, K.,** and **Pabst, R. F.** Crack resistance curves of alumina and zirconia at room temperature. *J. Mater. Sci.*, 1986, **21**, 411–418.

4 **Bueno, S., Berger, M. H., Moreno, R.,** and **Baudín, C.** Fracture behaviour of microcrack-free alumina-aluminium titanate ceramics with second phase nanoparticles at alumina grain boundaries. *J. Eur. Ceram. Soc.*, 2008, **28**, 1961–1971.

5 **Pastor, J. Y., Planas, J.,** and **Elices, M.** Ambient and high-temperature stable fracture tests in ceramics: applications to yttria-partially-stabilized zirconia. *J. Am. Ceram. Soc.*, 1993, **76**(11), 2927–2929.

6 **Baudín, C., Martinez, R.,** and **Pena, P.** High-temperature mechanical behavior of stoichiometric magnesium spinel. *J. Am. Ceram. Soc.*, 1995, **78**(7), 1857–1862.

7 **Bar-On, I., Baratta, F. I.,** and **Cho, K.** Crack stability and its effect on fracture toughness of hot-pressed silicon nitride beam specimens. *J. Am. Ceram. Soc.*, 1996, **79**(9), 2300–2308.

8 **Guinea, G. V., Pastor, J. Y., Planas, J.,** and **Elices, M.** Stress intensity factor, compliance and CMOD for a general three-point-bend beam. *Int. J. Fracture*, 1998, **89**, 103–116.

9 **Irwin, G. R.**, ''Fracture'', pp. 551–589 in Encyclopaedia of Physics, 1958, Ed. S. Flüge, (Springer Verlag, Berlin, Germany).

10 **Shackelford, J. F., Alexander, W.,** and **Park, J. S.** (Eds) *CRC materials science and engineering handbook*, 1994, pp. 537–539 (CRC Press, Boca Raton, Florida).

Capítulo 4

TENACIDAD DE FRACTURA DE CERÁMICAS FRÁGILES: ALÚMINA

4. TENACIDAD DE FRACTURA DE CERÁMICAS FRÁGILES: ALÚMINA

Una vez verificados el dispositivo experimental y el procedimiento de ensayo desarrollados, se procedió a establecer una metodología de ensayo y análisis de resultados para materiales frágiles. Para ello se seleccionó como material modelo una alúmina de grano fino que, como se ha descrito en el apartado 1.5, presenta fractura frágil.

Los resultados derivados de esta investigación dieron lugar a una publicación en la revista Journal of the European Ceramic Society (Anexo II).

Para el análisis de los resultados experimentales se han propuesto los siguientes parámetros:

- K_{IC}: factor crítico de intensidad de tensiones en modo I (apartado 1.1), calculado a partir de la carga máxima registrada en el ensayo (ecuación 3.1).
- G_{IC}: tasa crítica de liberación de energía en modo I (apartado 1.1), calculada a partir de K_{IC}, el módulo de Young (E) y el coeficiente de Poisson (ν), (ecuación 1.3).
- γ: energía de fractura (apartado 1.1), calculada a partir del área encerrada bajo la curva carga-desplazamiento (A) y el área de las nuevas superficies creadas, ecuación 4.1:

$$\gamma = \frac{A}{2B(W-a)} \tag{4.1}$$

donde B y W son el espesor y la anchura de la probeta, respectivamente, y a es la longitud de la entalla (Figura 3.3).

Se han comparado tanto las curvas experimentales como los valores de los parámetros de tenacidad calculados a partir de las curvas carga-desplazamiento

obtenidas para el mismo material, con igual geometría de ensayo y características de la entalla, en ensayos realizados en control de desplazamiento[72].

4.1. Condiciones experimentales

Las propiedades del material ensayado[72] se describieron en el capítulo 1, tabla 1.2. Se trata de una alúmina de grano fino (3.5 μm) y alta densidad (98% teórica). El material en verde fue obtenido por colaje de una suspensión estable de alúmina en moldes de escayola y sinterizado en aire con una velocidad de calentamiento y enfriamiento de 2 ºC/min hasta 1450 ºC y un tiempo de permanencia a la máxima temperatura de 2 h. En la rampa de calentamiento se incluyó un tratamiento isotermo a 1200ºC durante 4 h.

Para la determinación de la tenacidad de fractura se utilizó la geometría de ensayo de cerámicas técnicas avanzadas (apartado 3.2.1). Las características de la entalla fueron: α=0.5 y ρ~15 μm (figura 3.6).

Se realizaron ensayos a velocidad constante de apertura de los labios de la grieta (CMOD) de 1.8 μm/min.

4.2. Resultados y discusión

Según el análisis de estabilidad expuesto en el capítulo 3, apartado 3.1.2, para este material y dispositivo experimental (s=0.08; E~379 GPa; λ_m=232; C=1.5 10^{-7} m/N) no se conseguirían ensayos estables en control por desplazamiento a menos que las grietas fueran muy profundas, con un $\alpha \geq 0.75$, superior al valor obtenido considerando la flexibilidad de la máquina nula (Figura 4.1).

Se compararon los resultados obtenidos en este trabajo con aquellos reportados en ensayos previos[72], utilizando el mismo radio de curvatura del fondo de entalla y la misma longitud de entalla relativa.

En la figura 4.2 se muestran curvas experimentales características carga-desplazamiento correspondientes a ensayos realizados en control por CMOD y por desplazamiento[72]. Una vez alcanzada la carga máxima, la variación de la carga con el desplazamiento depende del tipo de control utilizado.

En la curva correspondiente al control por desplazamiento se observa una caída brusca de la carga para el desplazamiento fijo, seguida de una disminución monótona para desplazamientos crecientes. Este tipo de comportamiento es característico de fractura semiestable[72].

En la curva correspondiente al control por CMOD se observa cómo la posición del marco de carga disminuye desde el valor de carga máxima hasta un desplazamiento del marco de carga ~ 0.009 mm (régimen I, apartado 1.3.3), a partir de dicho valor la posición del marco de carga vuelve a alcanzar valores crecientes de desplazamiento (régimen II, apartado 1.3.3.). Este tipo de comportamiento es característico de fractura estable.

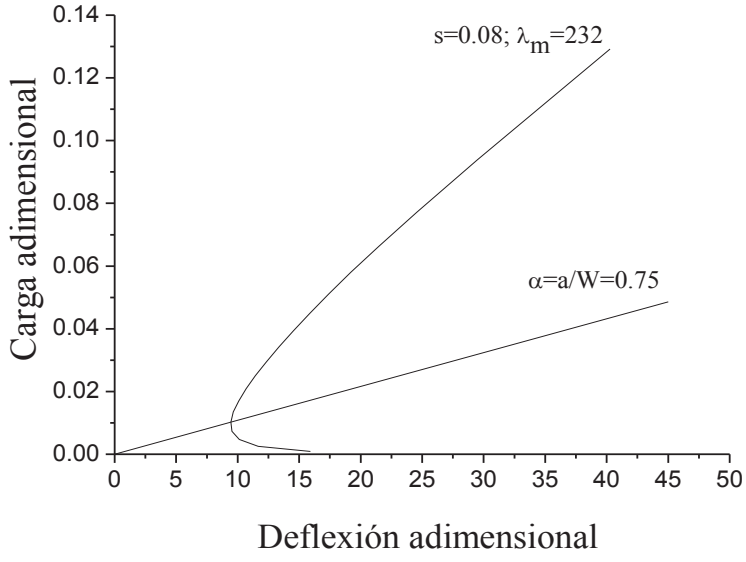

Figura 4.1. Locus de Griffith correspondiente a los valores numéricos carga-deflexión adimensionales para la alúmina (apartado 3.2.1). Cálculos realizados para la flexibilidad adimensional, λ_m, correspondiente a la flexibilidad del dispositivo utilizado, $(\delta_m/P)=1.5\ 10^{-7}$ m/N. La línea recta corresponde al tamaño relativo de entalla crítico, $(\alpha_c=0.75)$.

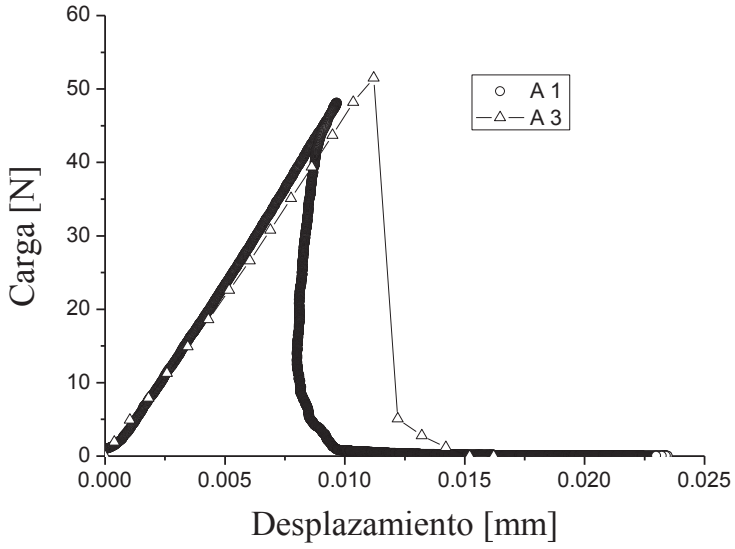

Figura 4.2. Curvas carga-desplazamiento para las probetas ensayadas usando diferentes parámetros de control.
(A1): control por apertura de los labios de la grieta, CMOD.
(A3): control por desplazamiento.

Los parámetros de tenacidad calculados a partir de las curvas carga-desplazamiento se recogen en la tabla 4.1. Todos los parámetros determinados en ensayos estables (CMOD) son inferiores a los determinados en ensayos semiestables (desplazamiento)[72]:

- K_{IC} es un 10% inferior.
- G_{IC} es un 18-22% inferior.
- γ es un 29-33% inferior.

Estos resultados se deben a que, como se discutió en el apartado 1.3.3, la energía suministrada durante los ensayos estables se emplea exclusivamente en la formación de nuevas superficies.

Tabla 4.1. Parámetros de tenacidad de fractura para el material de alúmina.

Bueno y col.[72]			Este trabajo		
K_{IC} (S.D.) (MPa $m^{1/2}$)	G_{IC} (J/m^2)	γ (J/m^2)	K_{IC} (S.D.) (MPa $m^{1/2}$)	G_{IC} (S.D.) (J/m^2)	γ (S.D.) (J/m^2)
2.9;2.8	20.4;19.6	10.5;9.8	2.5 (0.2)	16.4 (2.3)	7.0 (0.3)

K_{IC}: Factor crítico de intensidad de tensiones en modo I (MPa $m^{1/2)}$; G_{IC}: Tasa crítica de liberación de energía en modo I (J/m^2); γ: Energía de fractura (J/m^2). S.D.: Desviación estándar.

4.3. Conclusiones

- Utilizando control por CMOD, se han obtenido ensayos de fractura estable para un material de alúmina, en condiciones experimentales en las que los ensayos en control de desplazamiento son semiestables.

- De acuerdo con la hipótesis básica de este trabajo, los ensayos de fractura estable son adecuados para la determinación precisa de los parámetros de la tenacidad de este material de alúmina.

- El valor de G_{IC} obtenido a partir de la carga máxima es coincidente con el valor correspondiente a dos veces la energía de fractura, como corresponde a un material frágil.

ANEXO II

Este trabajo ha dado lugar a las siguientes publicaciones:

- A. Garcia-Prieto y C. Baudín, "Crack mouth opening displacement controlled fracture tests of brittle ceramics", J. Eur. Ceram. Soc., 30 (16) 3297-3302 (2010). (*DOI:* 10.1016/j.jeurceramsoc.2010.08.007).

Journal Citation reports 2010 (JCR): IF=2.575, posición 1 de 25 en la categoría "Materials Science, Ceramics".

- A. García-Prieto, C. Baudín. "Tenacidad y trabajo de fractura de un material frágil de alúmina". XXVIII Encuentro del Grupo Español de Fractura. Anales de Mecánica de la Fractura, 28, Vol.1, pp. 125-130. Ed. Secretaría del Grupo Español de Fractura, Madrid, España, 2011.

Available online at www.sciencedirect.com
ScienceDirect
Journal of the European Ceramic Society 30 (2010) 3297–3302
www.elsevier.com/locate/jeurceramsoc

Crack mouth opening displacement controlled fracture tests of brittle ceramics

A. García-Prieto, C. Baudín *

Instituto de Cerámica y Vidrio, CSIC, CSIC-Campus de Cantoblanco, Kelsen 5, 28049 Madrid, Spain

Received 23 June 2010; received in revised form 27 July 2010; accepted 2 August 2010

Abstract

Controlled fracture tests are required for the accurate determination of the toughness parameters of materials in order to assure the full conversion of the supplied energy into crack surface energy. From the three parameters involved in the test, load, displacement of the load point and crack mouth opening displacement (CMOD), this latter is the only one that continuously increases as fracture proceeds. Therefore, the CMOD has been proposed as control variable for the stable fracture tests. In this work, a new equipment to perform stable fracture tests of single edge V-notch beams (SEVNB) of ceramics in three points bending controlled by the CMOD is presented. The developed equipment allows performing stable fracture tests of extremely brittle materials. The equipment is presented together with results obtained for fine grained aluminium–magnesium aluminate and alumina ceramics.

Keywords: Al_2O_3; Spinel; Toughness; Stable fracture; Work of fracture

1. Introduction

It is well known that stable crack growth is necessary to get reliable and accurate fracture toughness data. When the fracture toughness values are determined from test configurations that do not allow stable crack growth the calculated toughness value might be over-evaluated (e.g. for a dense α-SiC, $K_{IC} \sim 4$ and 3 MPa $m^{1/2}$ for unstable and stable tests, respectively).[1] Moreover, controlled fracture tests supply much more information about the fracture process than the fast fracture ones because, in addition to the conventional fracture toughness for crack initiation, controlled fracture allows the determination of fracture energy and crack-growth resistance curves.

Fracture toughness tests of ceramics are usually performed in universal testing machines by subjecting the specimens located between the loading supports to increasing deformation by means of the displacement of the loading frame. The deformation of the specimen can be controlled by imposing a constant rate to the increase of the displacement of the frame and, thus, to the loading point (displacement control), the load (load control), the deflection of the specimen directly measured at the central point, in bending specimens, (deflection control) or the crack mouth opening displacement (CMOD control). The simplest and therefore most widely used testing conditions are the control of the specimen deformation by constant rates of increasing displacement or load.

Controlled fracture tests for brittle materials, as most ceramics, are difficult to accomplish, therefore, they are not usually performed. Since the initial works of Nakayama et al.[2,3] and Tattersall and Tappin[4] different authors have developed innovative specimen designs and tests geometries (e.g. 5–10) to attain stable fracture of materials using displacement controlled loading. Such approach has made it possible to reach stable fracture for materials as brittle as glass[2,11] and fine grained MgO[4] using hard machines. In general, the specimens required for these tests are difficult to fabricate especially for brittle ceramics.

From the broad spectrum of available fracture tests, bending of parallelepiped specimens with straight trough notches (SENB) is a relatively simple way of testing and displacement or load controlled bending tests have been widely used for fracture toughness testing of ceramics. Therefore, different attempts to perform stable tests using three point bending loaded beams, which are generally more stable than the four point bending ones,[12] have been done.

* Corresponding author.
E-mail address: cbaudin@icv.csic.es (C. Baudín).

0955-2219/$ – see front matter © 2010 Elsevier Ltd. All rights reserved.
doi:10.1016/j.jeurceramsoc.2010.08.007

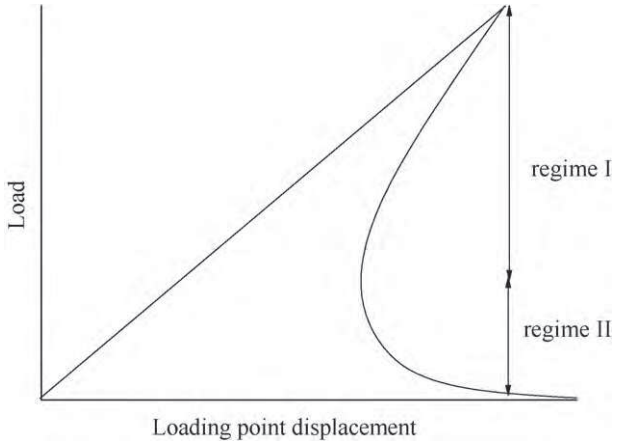

Fig. 1. General load–loading point displacement plot for beams of brittle materials with straight through notches (SENB). The curved part corresponds to the fracture taking place with constant energy release rate, G, equalling G_c. As the straight line that represents the loading of the specimen hits the curve, the condition for crack growth ($G = G_c$) is satisfied. To keep $G = G_c$ the load point displacement has to decrease initially (regime I) and then increase (regime II).

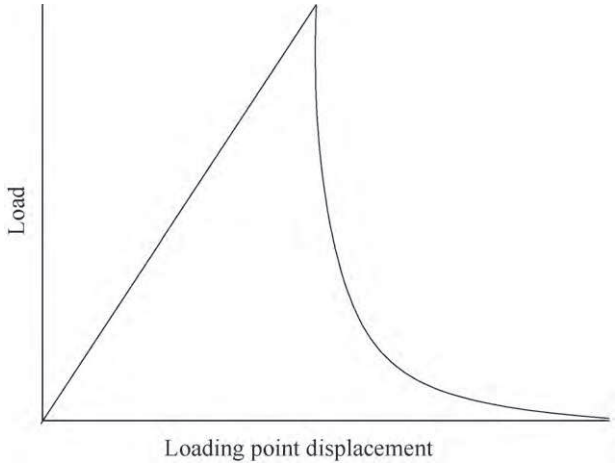

Fig. 2. Load–loading point displacement plot for stable fracture reached using constant displacement rate.

The schematic representation of Fig. 1 allows discussing some aspects about the stable crack growth in SENB specimens of brittle materials, as done by Sigl.[13] The curved line is the general stable fracture locus of a material with flat R curve (Griffith locus, critical energy release rate, G_c = constant). This curve represents the fracture taking place with constant energy release rate, G, equalling G_c. As the straight line that represents the loading of the specimen hits the curve, the condition for crack growth ($G = G_c$) is satisfied. In order to get stable fracture, G has to be maintained at its critical value and, thus, decreasing values of the load point displacement (regime I) followed by increasing values of this parameter (regime II) would be demanded. The load–displacement relationship of regime I is usually called snap back.[14] Therefore, it will not be possible to get stable fracture using constant displacement rates. The relative weight of the regions corresponding to regimes I and II depend on the material properties, the specimen and span sizes, the notch depth and the stiffness of the testing device. For the same material and testing geometry, stiff machines and deep notches increase the region of regime II and situations such as that plotted in Fig. 2 can occur. In this case, stable fracture can be reached controlling by constant displacement rate because increases in displacement after the maximum load still allow to follow the stable condition for crack growth $G = G_c$. In terms of stability, the use of the actual deflection of the specimen as control variable is qualitatively the same as the use of displacement. From Figs. 1 and 2 it is clear that the control by constant rates of increasing load can never lead to stable tests because load always decreases after cracking starts.

Stable fracture for SENB specimens tested in three point bending using displacement control is relatively easy to attain for materials with R-curve fracture, for which the crack resistance (i.e. G_c) increases as the crack propagates. For instance, stable fracture has been reported for materials with coarse microstructures such as silicoaluminate and high alumina refractories[3] and graphite,[11,15] for dense alumina with relatively large grain size ($d_{50} \sim 5.5\ \mu m$)[16] and for fine grained alumina–aluminium titanate composites (alumina: $d_{50} \sim 3.2$–$3.9\ \mu m$, aluminium titanate: $d_{50} \sim 2.2\ \mu m$).[16] On the contrary, for extremely brittle materials, very deep cracks and extremely stiff machines would be needed for stable fracture and thus, it is not possible in practice. In this sense, load–displacement curves showing unstable fracture or sudden load decreases ("pop-in") prior to further stable propagation (i.e. semi-stable fracture) have been reported for fine grained alumina ($d_{50} \sim 3.5\ \mu m$)[16] and silicon nitride ($d_{50} \sim 3\ \mu m$)[17].

Contrary to the above-discussed parameters, the CMOD increases through the whole fracture test, the loading of the specimen as well as during the crack growth. Thus, CMOD has been proposed and used as control parameter for stable fracture testing of high-strength concrete[14] and tetragonal zirconia stabilised with 3 mol% of Y_2O_3[18–20] specimens under conditions that would have led to unstable fracture for displacement controlled tests.

In order to perform in a routine way stable fracture tests of ceramics, a new experimental setup to perform three point bending stable fracture tests of ceramics controlled by the crack mouth opening displacement (CMOD) was developed.[21] The set up combined an electromechanical universal testing machine with a high precision optical micrometer. An electromechanical machine was chosen because the extremely small displacement variations required for the testing of brittle materials can be reached by small turns of the motor in standard electromechanical machines whereas they would require special hydraulic machines with highly precise servo valves. The use of an optical micrometer permits the measurement of the CMOD without contact with the specimen. Nowadays, the high performance of the control systems avoids the necessity of using hydraulic machines to assure rapid responses of the load frame and allows the use of control variables external to the machines such as the CMOD. Using this equipment it has been possible to test an extremely brittle ceramic such as fine grained magnesium–aluminium spinel for which a toughness value ($\sim 1\ MPa\ m^{1/2}$) about 66% lower than the previously

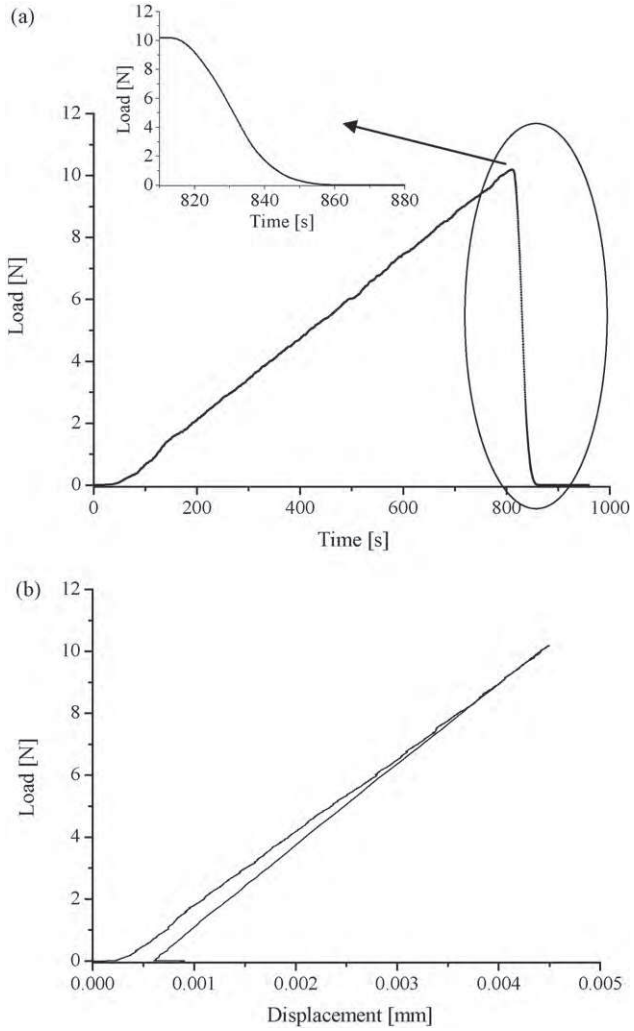

Fig. 3. Plots corresponding to a stable fracture test for a fine grained magnesium–aluminium spinel.[21] (a) Load–time plot. Monotonous load decrease with increasing times during fracture corresponding to controlled fracture is highlighted in the detail of the fracture part of the plot. (b) Load–displacement plot. During fracture the displacement has to decrease to reach stable fracture.

obtained in unstable tests ($\sim$3 MPa m$^{1/2}$)[22] was obtained. In Fig. 3 characteristic plots recorded during CMOD controlled tests for this material are shown. The shape of the load–time curve with monotonous load decreases with increasing time during fracture is characteristic of stable fracture (Fig. 3a). This behaviour is attained using a constant rate of increasing CMOD. The displacement has to decrease thorough the whole fracture process in order to maintain such rate (Fig. 3b).

In this work, after a brief description of the experimental setup, the fracture behaviour of a fine grained alumina using CMOD controlled tests is described and compared to that previously reported for displacement controlled tests for which only semi-stable fracture could be reached.[16]

2. Experimental

2.1. Material and specimen preparation

The fabrication and properties of the alumina material tested are described elsewhere.[16] Monophase alumina blocks were obtained by colloidal filtration in plaster moulds of aqueous alumina (Al_2O_3) stable suspensions. Sintering of the green blocks was performed in air in an electrical box furnace (Termiber, Spain) at heating and cooling rates of 2 °C min^{-1}, with 4 h, dwell at 1200 °C during heating and 2 h, dwell at the maximum temperature 1450 °C. The microstructural and mechanical properties for this material are summarised in Table 1.

Single Edge V-Notch Beams (SEVNB) of 4 mm thickness (B), 6 mm width (W) and 50 mm length were diamond machined from the sintered blocks. The notch was initially cut with a 300 μm wide diamond wheel (Fig. 4a). Using this pre-notch as a guide, the remaining part of the notch was done with a 150 μm wide razor blade sprinkled with 1 μm diamond paste (Fig. 4b and c). Tip radii of about 15 μm were obtained (Fig. 4c). The relative notch depth, a/W (a = notch depth, W = specimen width), was 0.5.

2.2. Mechanical testing set up

The mechanical tests were performed in a single screw, dual column and servo-controlled electromechanical universal testing machine with 50 kN load capacity and rigid frame (stiffness $\sim 2 \times 10^8$ N/m, Microtest EM1/50, Spain). The displacement of the moving crosshead is measured and controlled by means of an optical encoder placed in the motor axis. The electronic controller (Microtest SCM3000, Spain) includes load and position channels as well as position auxiliary ones with the option to add additional strain channels for extensometers. The signal from the system for CMOD determination is directed to one of these auxiliary channels so CMOD can also be a control variable. The test specimen is placed between the rigid frame and the moving crosshead in a stainless steel three point bending test fixture with a span of 40 mm. A load cell of 5 kN was selected to assure high stiffness of the loading setup. The compliance of the machine, load cell, and supports arrangement was determined experimentally using an uncracked alumina bar (4 mm × 6 mm × 50 mm); the obtained value was 1.5×10^{-7} m/N up to 150 N.

For the CMOD measurement and control, a high precision optical micrometer Keyence LS7010 (Keyence, Japan) that

Table 1
Microstructural and mechanical parameters for the alumina material tested in this work, A-1450.[16] G_A = average grain size, ρ = relative density, E = static Young's modulus, σ_f = three point bending strength, K_{IC} = critical stress intensity factor in mode I. S.D. = standard deviation.

Material	G_A (S.D.) (μm)	ρ (S.D.) (%theoretical)	E (S.D.) (GPa)	σ_f (S.D.) (MPa)	K_{IC} (MPa m$^{1/2}$)
A-1450	3.5 (0.3)	98.1 (0.3)	379 (8)	456 (29)	2.9 2.8

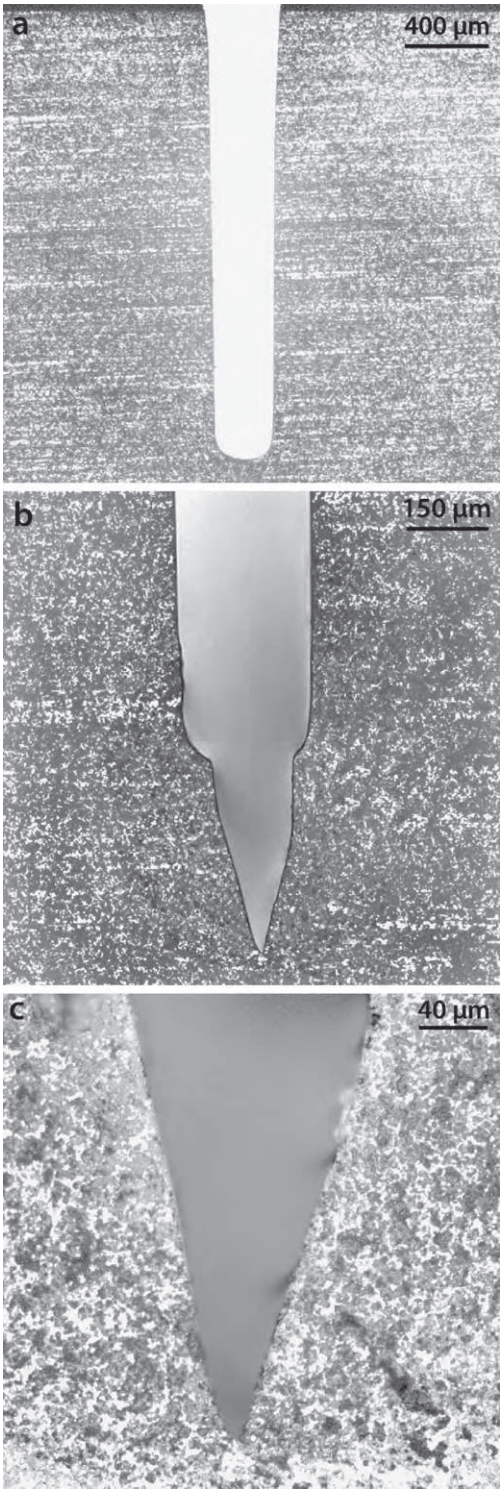

Fig. 4. Optical micrographs of a lateral surface of an alumina specimen showing the procedure to introduce the "V" notches. (a) A pre-notch is introduced with a thin (300 μm) diamond disc. (b and c) The notch tip is corrected with a razor blade with diamond past (1 μm) to reduce the tip radius below 15 μm.

incorporates a CMOS (Complementary Metal Oxide Semiconductor) camera to capture real-time image of the target was used. This optical system provides a measurement accuracy of ±0.5 μm. The equipment carries out a continuous measurement averaging up to 2400 samples/s. For the tests performed in this work, the sampling frequency of 512 s^{-1} used gave very stable readings.

The principle of measurement of the optical system is as follows. A high-intensity GaN green LED (Light-Emitting Diode) radiates light, which is changed into uniform parallel light through the special diffusion unit and collimator lens and emitted to the target in the measuring range. This parallel beam "illuminates" measurement area. Then the shadow image of the target appears on the HL-CCD (High-Speed Linear Charge Coupled Device) through the telecentric optical system. With the telecentric system of lenses the size of the image on the CCD does not change even if it moves, thus, the same accuracy all along is maintained. The output incident signal of the HL-CCD is processed by the DE (Digital Edge-detection) processor in the controller and CPU. The controller of the optical system incorporates a function of elimination of abnormal values, to improve the precision of the measurement, which detection threshold is an adjustable parameter.

The optical micrometer is attached to the lower loading support; in this way the mechanical interferences are avoided and a correct orientation of the light beam with respect to the axis of load and the bending fixture is assured. Given the small opening displacement of the notch, in order to be able to detect and measure its width during the test (the size of detectable minimum object by the system is of 0.04 mm), pins of 1.5 mm in diameter and 12 mm length are adhered to both sides of the notch assuring that they are perpendicular to the light beam. To reach the highest accuracy the tests were performed at 20 °C, with a separation between the pins of 1 mm. The repeating accuracy of the optical micrometer for this separation was checked to be ±0.06 μm using a 1.0 mm diameter round bar located in the centre of the measuring area.

The optical micrometer converts the distances detected to analog signals that are input in the controlling unit of the mechanical testing machine where the software SCM3000 (Microtest, Spain) converts them to discrete digital numbers. The whole range of the optical micrometer (6 mm) that corresponds to ±10 V of analog signal is converted in 2^{16} levels (65,536 values), thus, a theoretical resolution of 0.1 μm is obtained for the maximum range. For the tests, a smaller range of measurement of the micrometer, ±50 μm, was selected to detect the CMOD variations. In terms of analog signal, this range corresponds with a scaling value of 5 μm/V and, therefore, with a theoretical resolution of about 0.02 μm.

2.3. Testing conditions

The alumina specimens were tested in the above described experimental setup using CMOD control at rate of 1.8 μm min^{-1}. This velocity was chosen in order to use a rate of the deformation of the specimen similar to that previously used to test this material (0.005 mm min^{-1}). To determine this velocity, several specimens were tested using different CMOD rates to establish the correspondence between the displacement and CMOD rates from the time and displacement values needed to reach the maximum loads. The programmed CMOD rate was attained in all tests with variations of less than 0.02 μm min^{-1}.

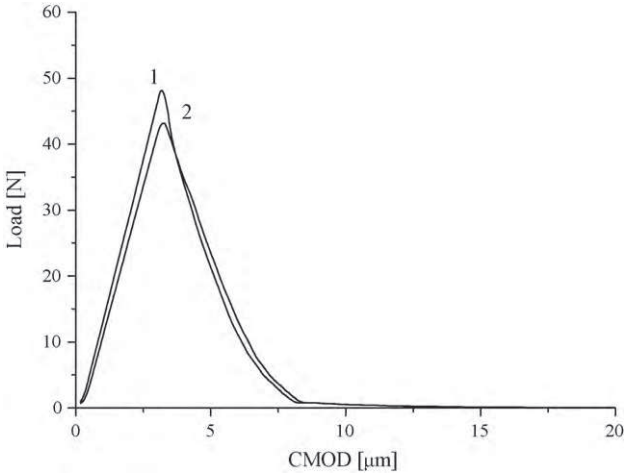

Fig. 5. Load–crack mouth opening displacement (CMOD) plots recorded during the CMOD controlled tests for two different alumina specimens showing the repeatability of the tests.

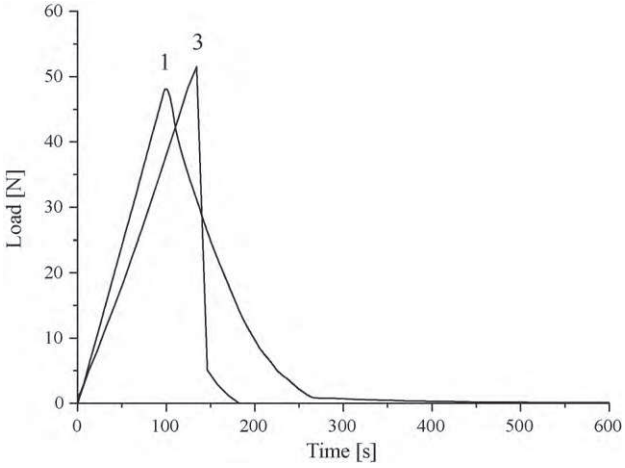

Fig. 6. Characteristic load–time plots for alumina specimens tested using different control parameters for the deformation of the specimen. (1): Crack mouth opening displacement control; stable fracture is shown. (3) Displacement control; semi-stable fracture is shown.[16]

3. Results and discussion

In which follows, the results obtained previously using the same testing and specimen geometries and displacement controlled tests[16] are compared to those obtained in this work using CMOD control. From calculations[17] using the compliance value of the whole testing system (1.5×10^{-7} m/N) and the properties of the material (Table 1), stable fracture tests could not be obtained under displacement control for any relative notch depth value for this alumina material. In fact, only semi-stable fracture was obtained for a limited number of tests of specimens with relative notch depths of 0.5 in the previously reported study. The introduction of larger notches led to the failure of the specimens during machining.

As it is shown in the load–CMOD curves of Fig. 5, similar results were obtained in this work for different specimens tested using the same CMOD rate and similar values of a/W the conditions which gave relatively low standard deviations for the fracture toughness parameters.

Fig. 6 shows characteristic load–time plots recorded using the two different control parameters. The sudden load decrease for constant time prior to further monotonous load decrease observed under displacement control is characteristic of semi-stable fracture.[16] On the contrary, in the CMOD controlled tests monotonous load decreases with increasing times as correspond to controlled fracture were always obtained. The load–displacement curves corresponding to the tests of Fig. 6 are plotted in Fig. 7. As discussed in the introduction, a decrease of displacement was needed to reach stable fracture after the maximum load which could only be attained by using CMOD control.

The critical stress intensity factor in mode I, K_{IC}, was calculated using the general expression of the stress intensity[23] and the value of the maximum load attained during the test (Eq. (1)). The onset of crack propagation was considered in the peak load.

$$K_{IC} = \frac{3SP}{2BW^{3/2}} K_\beta(\alpha) \tag{1}$$

where S is the span, P is the maximum load, B and W are the geometrical parameters defined in Section 2 and $K_\beta(\alpha)$ is a general shape function which is valid for any value of the relative notch depth ($0 \le \alpha \le 1$) and span-to-depth ratios ($\beta = S/W$) larger than 2.5 ($2.5 \le \beta \le 16$) (Eq. (2)):

$$K_\beta(\alpha) = \frac{\sqrt{\alpha}\,\{p_\infty(\alpha) + 4/\beta[p_4(\alpha) - p_\infty(\alpha)]\}}{(1-\alpha)^{3/2}(1+3\alpha)} \tag{2}$$

The $p_\infty(\alpha)$ and $p_4(\alpha)$ given by Eqs. (3) and (4) are cubic polynomial for $\beta = 4$ (equivalent to a reference beam with fixed $S/W = 4$) and $\beta = \infty$ (formally equivalent to pure bending).

$$p_\infty(\alpha) = 1.99 + 0.83\alpha - 0.31\alpha^2 + 0.14\alpha^3 \tag{3}$$

$$p_4(\alpha) = 1.9 + 0.41\alpha + 0.51\alpha^2 - 0.17\alpha^3 \tag{4}$$

The value of K_{IC} obtained for CMOD controlled tests was 2.5 ± 0.2 MPa m$^{1/2}$, about 10% lower than the value determined in semi-stable tests.[16]

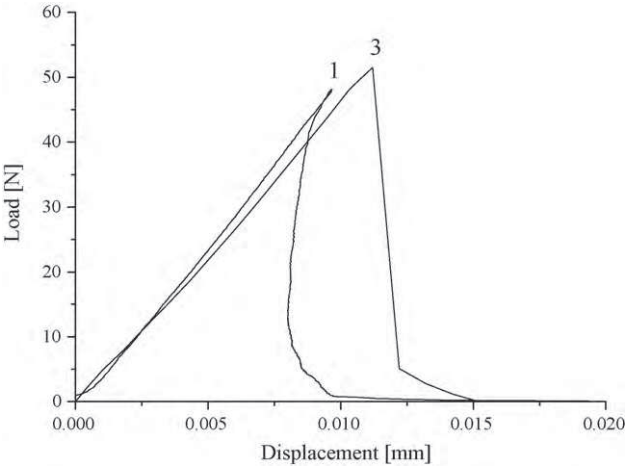

Fig. 7. Load–displacement plots corresponding to the test of Fig. 6. (1) Crack mouth opening displacement control; a decrease of displacement after the maximum load is needed to reach stable fracture tests. (3) Displacement control.[16]

From K_{IC} and Young's modulus (Table 1), the critical energy release rate, G_{IC}, was calculated according to the analysis of Irwin for plane strain conditions (Eq. (5)):

$$G_{IC} = \frac{K_{IC}^2}{E'} \quad (5)$$

where $E' = E/(1-\nu^2)$ is the generalized Young's modulus for plane strain (E is the Young's modulus and ν is the Poisson's ratio). The Poisson's ratio for dense and fine grained alumina is 0.223 ± 0.004.[24] The value of G_{IC} obtained was $16.4 \pm 2.3\,J\,m^{-2}$ that is about 20% lower than the value previously obtained in semi-stable tests.[16]

The work of fracture, γ_{WOF}, was calculated by dividing the work done on the specimen to propagate the crack, calculated as the integral of the load–displacement plot, by the area of the newly created surfaces (Eq. (6)). For parallelepiped bars with straight trough notches tested in flexure, this area is twice the area of the unnotched part of the cross-section of the specimens.

$$\gamma_{WOF} = \frac{A}{2B(W-a)} \quad (6)$$

where A is the area under the load–displacement curves and B, W and a were defined in Section 2.

The value of γ_{WOF} obtained was $7.0 \pm 0.3\,J\,m^{-2}$ that is about 30% lower than the value obtained in semi-stable tests.[16]

4. Conclusions

An experimental setup to perform stable fracture tests in an electromechanical machine using the analog output from an optical micrometer was developed. This set up allows using the crack mouth opening displacement (CMOD) as a control parameter for fracture toughness testing.

Stable fracture tests can be performed for brittle ceramics by using the CMOD as control parameter and three points bending of Single Edge V-Notch Beams as testing geometry.

Stable fracture tests for fine grained alumina performed using this device have given fracture toughness parameters ($K_{IC} = 2.5 \pm 0.2\,MPa\,m^{1/2}$, $G_{IC} = 16.4 \pm 2.3\,J\,m^{-2}$, $\gamma_{WOF} = 7.0 \pm 0.3\,J\,m^{-2}$) lower than those determined in semi-stable tests: about 10%, 20% and 30% for critical stress intensity factor in mode I, critical energy release rate and work of fracture, respectively.

Acknowledgements

This work has been supported by MCI-MAT2009-14448-C02 and PET2008-0113 and Microtest S.A. (Spain). Discussions with Prof. J.Y. Pastor from ETSI Caminos, Canales y Puertos (Madrid) are gratefully acknowledged.

References

1. Ghosh A, Jenkins MG, White KW, Kobayashi AS, Bradt RC. Elevated-temperature fracture resistance of a sintered α-silicon carbide. *J Am Ceram Soc* 1989;**72**(2):242–7.
2. Nakayama J. Direct measurement of fracture energies of brittle heterogeneous materials. *J Am Ceram Soc* 1965;**48**(11):583–7.
3. Nakayama J, Abe H, Bradt RC. Crack stability in the work-of-fracture test: refractory applications. *J Am Ceram Soc* 1981;**64**(11):671–5.
4. Tattersall HG, Tappin G. The work of fracture and its measurement in metals, ceramics and other materials. *J Mater Sci* 1966;**1**:296–301.
5. Calomino AM, Brewer DN. Controlled crack growth specimen for brittle systems. *J Am Ceram Soc* 1992;**75**(1):206–8.
6. Sørensen BF, Horsewell A, Jørgensen O, Kumar AN, Engbæk P. Fracture resistance measurement method for in situ observation of crack mechanisms. *J Am Ceram Soc* 1998;**81**(3):661–9.
7. Wan D, Bao Y, Peng J, Zhou Y. Fracture toughness determination of $Ti_3Si(Al)C_2$ and Al_2O_3 using a single gradient notched beam (SGNB) method. *J Eur Ceram Soc* 2009;**29**:763–71.
8. Kuszyk JA, Bradt RC. Influence of grain size on effects of thermal expansion anisotropy in $MgTi_2O_5$. *J Am Ceram Soc* 1973;**56**(8):420–3.
9. Sørensen BF, Brethe P, Skov-Hansen P. Controlled crack growth in ceramics: the DCB specimen loaded with pure moments. *J Eur Ceram Soc* 1996;**16**(9):1021–5.
10. Ebrahimi ME, Chevalier J, Fantozzi G. *R*-curve evaluation and bridging stress determination in alumina by compliance analysis. *J Eur Ceram Soc* 2003;**23**(6):943–9.
11. Sakai M, Urashima K, Inagaki M. Energy principle of elastic–plastic fracture and its application to the fracture mechanics of a polycrystalline graphite. *J Am Ceram Soc* 1983;**66**(12):868–74.
12. Baratta FI, William AD. Crack stability in simply supported four-point and three-point loaded beams of brittle materials. *Mech Mater* 1990;**10**:149–59.
13. Sigl LS. On the stability of cracks in flexure specimens. *Int J Fract* 1991;**51**:241–54.
14. Biolzi L, Cangiano S, Tognon G, Carpinteri A. Snap-back softening instability in high-strength concrete beams. *Mater Struct* 1989;**22**:429–36.
15. Davidge RW, Tappin G. The effective surface energy of brittle materials. *J Mater Sci* 1968;**3**:165–73.
16. Bueno S, Berger MH, Moreno R, Baudín C. Fracture behaviour of microcrack free alumina–aluminium titanate ceramics with second phase nanoparticles at alumina grain boundaries. *J Eur Ceram Soc* 2008;**28**:1961–71.
17. Bar-On I, Baratta FI, Cho K. Crack stability and its effect on fracture toughness of hot-pressed silicon nitride beam specimens. *J Am Ceram Soc* 1996;**79**(9):2300–8.
18. Pastor JY, Planas J, Elices M. Ambient and high-temperature stable fracture tests in ceramics: applications to yttria-partially-stabilized zirconia. *J Am Ceram Soc* 1993;**76**(11):2927–9.
19. Pastor JY, Planas J, Elices M. A new technique for fracture characterization of ceramics at room and at high temperature. *J Test Eval* 1995;**23**(3):209–16.
20. Pastor JY, Planas J, Elices M. Ensayos de fractura estables en materiales cerámicos. *Bol Soc Esp Ceram V* 1992;**31**(4):322–5.
21. Baudín C, García A, Hernández J, López M. Anales de Mecánica de la Fractura. In: Proceedings of the Conferencia Ibérica de Fractura e Integridad Estructural 2010, vol. 1. Controlled fracture tests of brittle ceramics, Secretaría del Grupo Español de Fractura, Madrid, Spain; 2010. p. 291–5.
22. Baudín C, Martínez R, Pena P. High-temperature mechanical behavior of stoichiometric magnesium spinel. *J Am Ceram Soc* 1995;**78**(7):1857–62.
23. Guinea GV, Pastor JY, Planas J, Elices M. Stress intensity factor, compliance and CMOD for a general three-point-bend beam. *Int J Fract* 1998;**89**:103–16.
24. Burgos-Montes O, Moreno R, Baudín C. Effect of mullite additions on the fracture mode of alumina. *J Eur Ceram Soc* 2010;**30**:857–63.

Capítulo 5

EFECTO DE LAS CONDICIONES EXPERIMENTALES EN LA TENACIDAD DE FRACTURA DE UN MATERIAL DE MULLITA

5. EFECTO DE LAS CONDICIONES EXPERIMENTALES EN LA TENACIDAD DE FRACTURA DE UN MATERIAL DE MULLITA

Una vez demostrada la validez del dispositivo experimental y del procedimiento de ensayo (capítulo 3) y de la metodología de ensayo y análisis de resultados (capítulo 4) se ha estudiado la influencia de las variables experimentales, velocidad de desplazamiento y radio de curvatura del fondo de entalla, en los parámetros de tenacidad. Para ello se seleccionó un material de mullita (Al_2O_3:SiO_2, 3:2) como caso de estudio porque presenta comportamiento frágil y crecimiento subcrítico de grietas (SCG) significativo en aire, (apartado 1.6).

Los resultados derivados de esta investigación dieron lugar a una publicación en la revista Journal of the European Ceramic Society (Anexo III).

5.1. Condiciones experimentales

Las propiedades del material ensayado[148] (MB0) se recogen en la tabla 1.3. Se trata de una mullita de grano fino (0.7μm) y alta densidad (95% teórica) obtenida a partir de una mullita comercial Baikowski en polvo y sinterizada en aire a 1630 ºC durante 4 h[148].

Para la determinación de la tenacidad de fractura se utilizó la geometría de ensayo de cerámicas técnicas avanzadas (apartado 3.2.1). Las características de la entalla fueron α=0.64 y $\rho\sim$ 60 y 6 μm.

Se realizaron ensayos a velocidades constantes de apertura de los labios de la grieta (CMOD) de 1 y 18 μm/min y a una velocidad constante de desplazamiento del marco de carga de 0.05 mm/min. Se eligieron estas velocidades porque dan lugar a velocidades de deformación de la probeta similares a las utilizadas en ensayos previos para estudiar el

efecto del crecimiento subcrítico de grietas para este mismo material en control por desplazamiento, 0.005 y 0.05 mm/min[148].

5.2. Resultados y discusión

Según el análisis de estabilidad expuesto en el capítulo 3, apartado 3.1.2, para este material y dispositivo experimental (s=0.11; E=195 GPa; λ_m=117; C=1.5 10^{-7} m/N) no se conseguirían ensayos estables en control por desplazamiento a menos que las grietas fueran muy profundas con un $\alpha \geq 0.7$ (Figura 5.1), superior al valor obtenido considerando la flexibilidad de la máquina nula (figura 3.10). Hasta la fecha de realización de este trabajo no habían sido reportados parámetros de tenacidad determinados en ensayos de fractura estable para materiales avanzados de mullita.

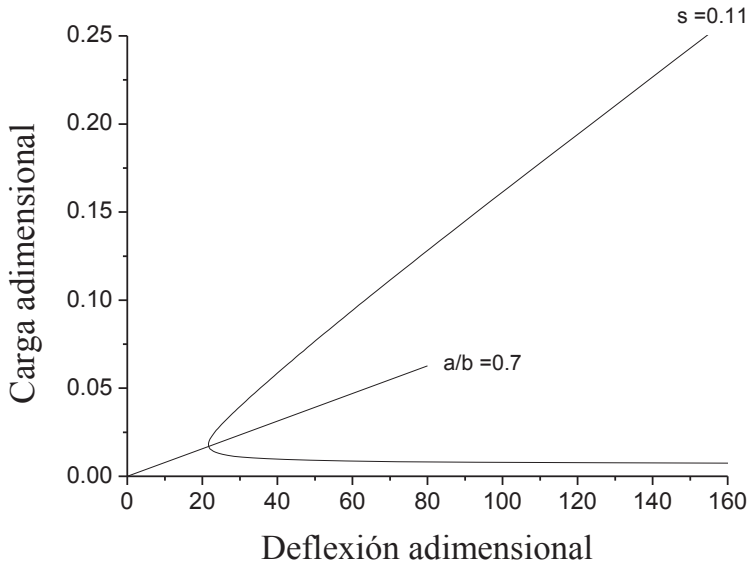

Figura 5.1. Locus de Griffith correspondiente a los valores numéricos carga-deflexión adimensionales para la mullita (apartado 3.2.1). Cálculos realizados para la flexibilidad adimensional, λ_m, correspondiente a la flexibilidad del dispositivo utilizado, (δ_m/P)=1.5 10^{-7} m/N. La línea recta corresponde al tamaño relativo de entalla crítico, $(\alpha_c$=0.70).

Todos los ensayos realizados en control por CMOD dieron lugar a fractura estable. En la figura 5.2 se muestran las curvas experimentales características carga-tiempo para

ensayos realizados a alta velocidad del desplazamiento del marco de carga en control por CMOD y desplazamiento. Al igual que ocurría en el caso de la alúmina (figura 4.2) no se obtienen ensayos estables en control por desplazamiento, en cambio en control por CMOD sí se alcanzan ensayos estables a pesar de la alta velocidad empleada.

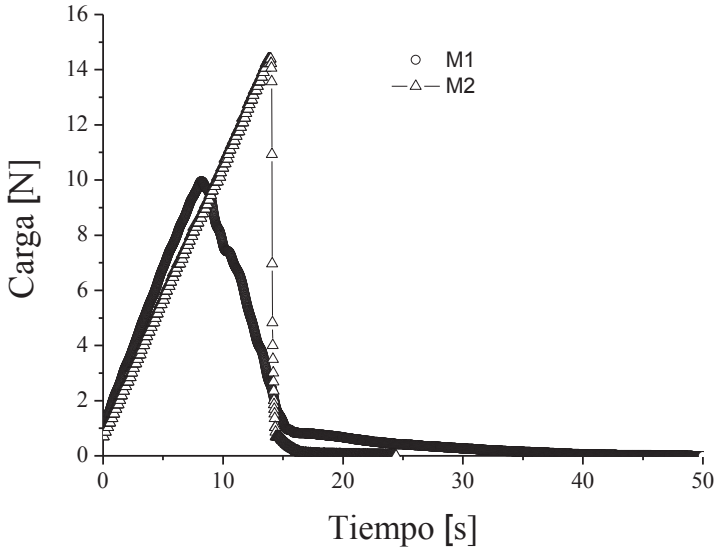

Figura 5.2. Curvas experimentales características carga-tiempo para el material de mullita.
(M1): control por apertura de los labios de la grieta, CMOD.
(M2): control por desplazamiento.

En la figura 5.3 se muestra una curva experimental característica carga-desplazamiento en control por CMOD del material ensayado de mullita donde se aprecia, a partir del valor de carga máxima, una disminución del desplazamiento (régimen I) seguida de un aumento del desplazamiento (régimen II). Este tipo de comportamiento es característico de fractura estable de materiales frágiles.

Las propiedades mecánicas de este material se recogen en la tabla 5.1. Los valores de K_{IC}, G_{IC} y γ fueron calculados a partir de tres medidas y los errores corresponden a las desviaciones estándar. El coeficiente de Poisson empleado para esta mullita fue 0.274[139].

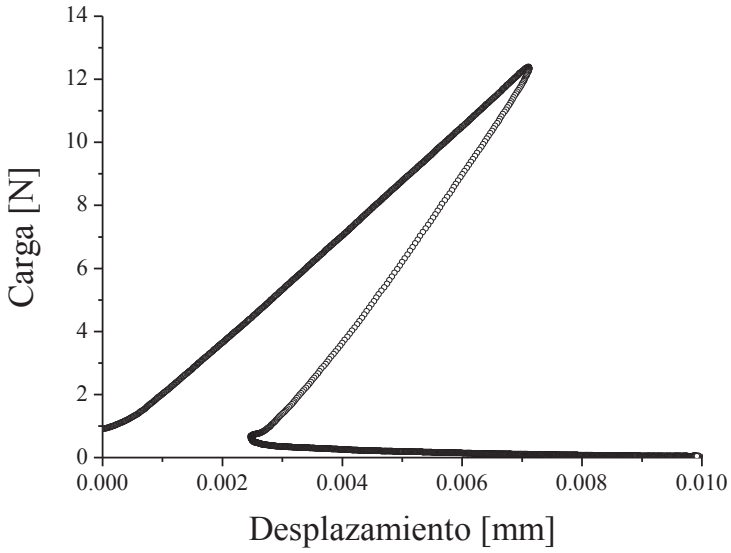

Figura 5.3. Curva experimental característica carga-desplazamiento para el material de mullita ensayado a una velocidad constante de CMOD de 1 μm/min y un radio de curvatura de fondo de entalla igual a 60μm.

Tabla 5.1. Parámetros de tenacidad de fractura para el material de mullita.

Osendi y Baudín.[148]		Este trabajo				
Condiciones de ensayo	K_{IC} (S.D.) (MPa $\cdot m^{1/2}$)	Condiciones de ensayo	t_f (S.D.) (s)	K_{IC} (S.D.) (MPa $\cdot m^{1/2}$)	G_{IC} (S.D.) (J / m^2)	γ (S.D.) (J / m^2)
v=0.05mm/min ρ=200μm	2.32 (0.08)	v=0.018mm/min ρ=6μm	30	0.86 (0.06)	3.5 (0.5)	1.9 (0.1)
		v=0.001mm/min ρ=60μm	500	1.11 (0.06)	5.9 (0.7)	0.9 (0.2)
v=0.005mm/min ρ=200μm	2.0 (0.3)	v=0.001mm/min ρ=6μm	500	0.72 (0.07)	2.5 (0.5)	0.65 (0.05)
		v=0.05mm/min ρ=6μm	-	1.17 (0.09)	-	-

K_{IC}: Factor crítico de intensidad de tensiones en modo I (MPa $m^{1/2}$); G_{IC}: Tasa crítica de liberación de energía en modo I (J/m^2); γ: Energía de fractura (J/m^2); v: velocidad (mm/min); ρ: radio de curvatura del fondo de entalla (μm); t_f: tiempo de fractura (s); S.D.: Desviación estándar.

El valor de la tenacidad correspondiente al inicio de fractura (K_{IC}) es muy dependiente de las características de la entalla. Se han obtenido valores significativamente diferentes de K_{IC} calculados a partir de la carga máxima, siendo este valor un 60% superior para $\rho = 60$ μm con respecto a los obtenidos para $\rho = 6$ μm. Esta diferencia no se observa en la energía de fractura (γ), parámetro referente a todo el proceso de fractura.

A la máxima velocidad de ensayo (v= 18 μm/min) los valores de G_{IC} y 2γ son coincidentes. En cambio, para la velocidad lenta (v = 1 μm/min) G_{IC} es muy superior a 2γ. Este hecho puede explicarse por el fenómeno de crecimiento subcrítico de grieta (SCG), que para este material es un proceso relativamente rápido, produciéndose a una velocidad de $6 \cdot 10^{-3}$ m/s. Esta velocidad es superior a la reportada por Torrecillas y col.[142] para un material de mullita sinterizado a 1700ºC, con velocidades de crecimiento de $\sim 10^{-4}$ m/s para K_{IC} ~1.9-2.05 MPa $m^{1/2}$ (apartado 1.6). Este fenómeno no es detectable para tiempos cortos de ensayo, como corresponde a los tiempos involucrados en los ensayos realizados a alta velocidad (18 μm/min, 30s, figura 5.4 1) o los necesarios para alcanzar la carga máxima en ensayos lentos (1 μm/min, 100s, figura 5.4 2). El fenómeno de SCG tampoco había podido ser identificado en este material a partir de los valores de K_{IC} obtenidos en ensayos inestables. Sin embrago, este fenómeno es observable para los tiempos correspondientes al crecimiento estable de la grieta (1 μm/min, 400s, figura 5.4 2).

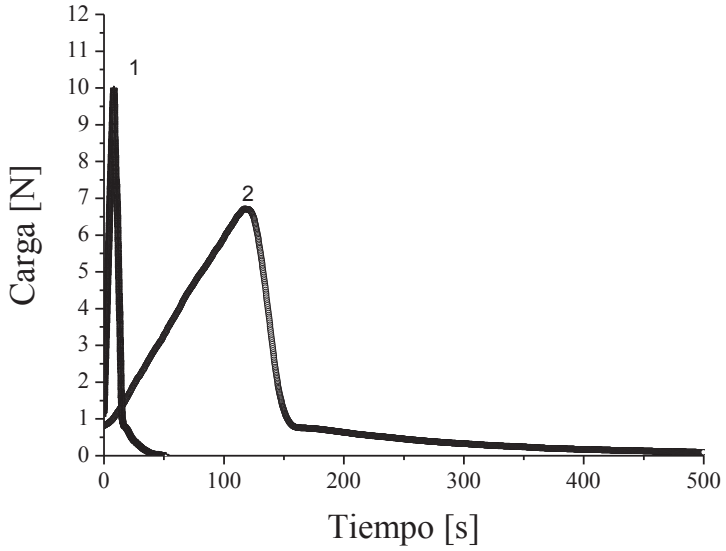

Figura 5.4. Curvas experimentales características carga-tiempo correspondientes a ensayos de fractura en control por CMOD para el material de mullita.
1: velocidad constante de CMOD=18 μm/min.
2: velocidad constante de CMOD=1 μm/min.

5.3. Conclusiones

- Se han alcanzado ensayos de fractura estable para un material de mullita de grano fino con comportamiento frágil y crecimiento subcrítico de grieta.

- Para este material frágil y que presenta crecimiento subcrítico de grieta significativo en aire, sólo es posible obtener valores reales de los parámetros de tenacidad en ensayos estables realizados utilizando velocidades altas de apertura de los labios de la grieta (CMOD, v= 18 μm/min).

ANEXO III

Este trabajo ha dado lugar a las siguientes publicaciones:

- A. García-Prieto, C. Baudín. "Influence of experimental variables on fracture toughness determined on SEVNB in three points bending. Mullite a case study", J. Eur. Ceram. Soc. 32 (16) 4241-4248 (2012).
  (DOI : 10.1016/j.jeurceramsoc.2012.06.018).

Journal Citation reports 2012 (JCR): IF=2.360, posición 1 de 27 en la categoría "Materials Science, Ceramics".

- A. García-Prieto, C. Baudín. "Efecto de las condiciones experimentales en la tenacidad de fractura de un material de mullita". XXIX Encuentro del Grupo Español de Fractura. Anales de Mecánica de la Fractura, 29, Vol.2, pp. 617-622. Ed. Secretaría del Grupo Español de Fractura, Madrid, España, 2012.

Available online at www.sciencedirect.com

SciVerse ScienceDirect

Journal of the European Ceramic Society 32 (2012) 4241–4248

www.elsevier.com/locate/jeurceramsoc

Influence of experimental variables on fracture toughness determined on SEVNB in three points bending. Mullite a case study

A. García-Prieto, C. Baudín *

Instituto de Cerámica y Vidrio, CSIC, CSIC-Campus de Cantoblanco, Kelsen 5, 28049 Madrid, Spain

Received 24 April 2012; received in revised form 15 June 2012; accepted 24 June 2012
Available online 20 July 2012

Abstract

The effect of testing variables on toughness of single edge "V" notched beams (4 mm × 6 mm × 50 mm, $\alpha = 0.6$) of a fine grained mullite ($d_{50} = 0.7 \pm 0.5$ μm) in three points bending (span = 40 mm) is analysed. Mullite was selected as case material because it presents flat *R*-curve and subcritical crack propagation. Stable fracture was reached by using the CMOD as control variable (0.001 and 0.018 mm/min). Results for stable test and unstable displacement (0.05 mm/min) controlled tests are analysed. K_{IC} has been calculated from maximum loads, K_{ICp}, and from the total fracture energy determined in stable tests, $K_{IC\gamma}$. The fact that for materials with flat *R*-curve both K_{IC} values are coincident has been used as criterion for adequacy of the test. Stable fracture at high deformation rates is required to fulfil $K_{ICp} = K_{IC\gamma}$. Under such conditions, an intrinsic $K_{IC} = 0.86 \pm 0.06$ MPa m$^{1/2}$, less than one half of those previously reported has been obtained.

Keywords: Toughness; Mechanical testing; Crack propagation; Mullite

1. Introduction

Stable crack growth is necessary to determine reliable and accurate fracture toughness data. When the fracture toughness values are determined from mechanical testing configurations that lead to unstable fracture the calculated values might be over-estimated. For instance, for a dense α-SiC, $K_{IC} \sim 4$ and 3 MPa m$^{1/2}$ have been reported for unstable and stable tests, respectively.[1] Moreover, stable fracture supplies much more information about the fracture process than fast fracture because, in addition to the conventional fracture toughness for notch initiation, calculated from the maximum attained load, stable fracture allows the determination of fracture energy and crack-growth resistance curves.

In fracture toughness testing a specimen with a notch with known geometry is subjected to deformation until failure occurs. Controlled increasing deformation is imposed by the displacement of the loading frame. The simplest and therefore most widely used means for controlling the test is imposing a constant rate to the displacement of the frame and, thus, to the loading point (displacement control). Alternatively, other parameters can be used to indirectly govern the rate of displacement of the frame. These parameters can be load (load control) or any parameter related to crack growth such as the distance between both sides of the notch, usually known as crack mouth opening displacement (CMOD).

Up to now, stable fracture tests for ceramics have been considered as extremely difficult to realise, thus, they are not usually performed. Since the initial works of Nakayama et al.[2] and Tattersall and Tappin,[3] different authors have developed innovative specimen designs and test geometries (e.g. 4–9) to attain stable fracture using displacement controlled deformation. The unstable crack growth is avoided or limited by careful adaptation of the testing machine and the specimen geometry to the material to be tested. Such approach has made it possible to reach stable fracture for materials as brittle as glass[10] and fine grained MgO.[3] Two main problems arise in this kind of tests. On the one hand, it is difficult to produce notches with well-defined special geometries in ceramic specimens. On the other, unstable crack growth can result as the amount of energy necessary to create the fracture surfaces is usually small compared to the elastic energy stored in the test rig unless extremely stiff machines are used.

In our laboratory a special set up for the routine stable fracture testing of single edge notched beams (SENB) of brittle

* Corresponding author.
E-mail address: cbaudin@icv.csic.es (C. Baudín).

0955-2219/$ – see front matter © 2012 Elsevier Ltd. All rights reserved.
http://dx.doi.org/10.1016/j.jeurceramsoc.2012.06.018

ceramics in three points bending using the CMOD as control parameter has been developed.[11,12] The objective of this work is to determine the effect of testing variables on the K_{IC} values calculated from the maximum loads, K_{ICp}, determined in stable and unstable tests, and from the total fracture energy determined in stable tests, $K_{IC\gamma}$. Traditionally, the total fracture energy in ceramics has been named work of fracture, however, the more standard term fracture energy will be used in this paper. Mullite has been selected as case material because it is a well known brittle ceramic used in structural applications which presents subcritical crack propagation at room temperature. As criterion for adequacy of the testing conditions the fact that for materials with flat *R*-curve both K_{IC} values, K_{ICp} and $K_{IC\gamma}$, have to be coincident has been used. Additionally, this coincidence will demonstrate that the time-dependent effects have been avoided.

1.1. Stability analysis for fracture of SENB in three points bending

From the broad spectrum of available fracture toughness tests, bending of parallelepiped specimens with straight trough notches (SENB) is a relatively simple way of testing and displacement or load controlled tests have been widely used for ceramics. Different attempts to reach stable fracture under such configuration have been done.[13–16]

The well known criteria for assessing the stability of cracks are based on an energy balance (Griffith criterion)[17]: the external work performed during crack growth dW must be greater than (or at least equal to) the associated change in the elastic energy dU_e stored in the entire testing device (test rig + specimen) and the energy RdA necessary to create the new fracture surface dA: $dW \geq dU_e + RdA$ (*R:* crack resistance). The work performed and the changes in the elastic energy are usually combined in one new variable, the energy release rate G: $G = (dW - dU_e)/dA$. Crack growth occurs when $G \geq R$ and does not occur when $G < R$. Stable crack growth is then possible when, on the one hand, the Griffith criterion is met ($G \geq R$) and, on the other hand, the increase in the energy released during crack growth is lower than the increase in the energy necessary for the creation of new fracture surfaces ($dG/dA < dR/dA$).

The schematic representation of Fig. 1 allows discussing some aspects about the stable crack growth in SENB brittle specimens in three points bending, as done by Sigl.[18] The curved line is the general stable fracture locus of a material with flat *R*-curve (critical energy release rate, G_c = constant), called Griffith locus. This curve represents the fracture taking place with constant energy release rate, G, equalling G_c. Initially the load increases linearly with specimen deflection (in three points bending the deflection of the specimen at the central point is associated to the displacement of the load point), the proportionally constant depending on the relative notch depth ($\alpha = a/W$, a = notch depth, W = specimen width) and material properties. In Fig. 1, the linear relationships that represent the loading of identical specimens with different α are also plotted. As the straight lines hint the Griffith locus the condition for crack growth ($G = G_c$) is satisfied. In order to get stable fracture, G has to be maintained at its critical value thus, decreasing loads are always needed.

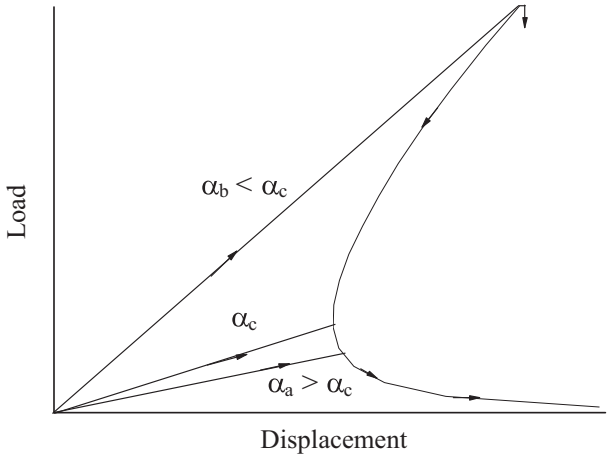

Fig. 1. General plot load (P)–displacement (d) of the loading point for fracture of SENB brittle specimens in three points bending. The straight lines correspond to the loading of specimens with different relative notch depths $\alpha = a/W$ (a = notch depth, W = specimen width). The curved part corresponds to the Griffith locus, i.e.: fracture taking place with constant energy release rate, G, equalling G_c. For a critical relative notch depth, α_c, the derivative, $\delta P/\delta d$, changes from positive to negative. For $\alpha_a > \alpha_c$ loading intersects the lower branch of the stability curve, thus, the Griffith locus can be followed using constant displacement rates. For $\alpha_b < \alpha_c$ loading intersects the upper branch of the stability curve and any further increase in displacement would result in unstable fracture; to keep $G = G_c$ the displacement has to decrease initially and then increase.

Therefore, it is not possible to reach stable fracture by using constant load rates to control the movement of the frame.

For a critical relative notch depth, α_c, the slope of the Griffith locus ($\delta P/\delta d$) changes from positive to negative; α_c is calculated using the condition $\delta P/\delta d = 0$. For specimens containing relative notch depths (α_a) larger than the critical one (α_c) the straight line intersects the lower branch of the stability curve, regime II, thus, the Griffith locus can be followed using constant rates of displacement of the loading point. For specimens containing relative notch depths (α_b) smaller than α_c the load/displacement straight line intersects the upper branch of the stability curve (regime I) and any further increase in displacement would result in unstable fracture. In regime I, decreasing values of the load point displacement for decreasing loads (snap-back) are needed for stable fracture, therefore, it is not possible to get stable fracture using constant displacement rates. In terms of stability, the use of the actual deflection of the specimen (associated to the load point displacement) as control parameter is qualitatively the same as the use of displacement of the load frame.

The relative weight of the regions corresponding to regimes I and II depend on the material properties, the specimen and span sizes, the notch depth and the stiffness of the testing device. For the same material and testing geometry, stiff machines and deep notches increase the region of regime II.

Stable fracture using displacement control is relatively easy to attain for materials presenting *R*-curve, for which the crack resistance (R) increases as the crack propagates. For instance, stable fracture has been reported for materials with coarse microstructures such as silicoaluminate and high alumina refractories[10] and graphite,[13,15] for dense alumina with relatively large grain size ($d_{50} \sim 5.5\ \mu m$[16]) and for fine grained alumina–aluminium

Table 1
Microstructural and mechanical properties for the mullite material tested in this work.[25,30,32] G_A: average grain size; ρ: relative density; E: Young's modulus; ν: Poisson's ratio; σ_f: 3-points bending strength; K_{IC}: critical stress intensity factor in mode I. (S.D.): standard deviation.

G_A (S.D.) μm	ρ (S.D.) % theoretical	E (S.D.) GPa	ν (S.D.)	σ_f (S.D.) MPa	K_{IC} (S.D.) MPa m$^{1/2}$
0.7 (0.5)	95.0 (0.3)	195 (4)	0.274 (0.006)	227 (24)	2.0 (0.6)

titanate composites (alumina: $d_{50} \sim 3.2$–3.9 μm, aluminium titanate: $d_{50} \sim 2.2$ μm[16]). On the contrary, for extremely brittle materials stable fracture is not possible in practice because very deep notches and stiff machines would be needed, as it was discussed before. In this sense, load–displacement curves showing unstable fracture or sudden load decreases ("pop-in") prior to further stable propagation (i.e.: semi-stable fracture) have been reported for fine grained alumina ($d_{50} \sim 3.5$ μm[16]) and silicon nitride ($d_{50} \sim 3$ μm[14]).

Contrary to displacement and load, parameters related to crack growth increase during the whole fracture test, thus, they are suitable to reach stable fracture. In particular, the crack mouth opening displacement (CMOD) has been proposed and used as control parameter for stable fracture testing of high-strength concrete[19] and tetragonal zirconia stabilised with 3 mol% of Y_2O_3[20–22] specimens under conditions that would have led to unstable fracture for displacement controlled tests; both materials present *R*-curve behaviour. In our laboratory a special set up for the routine stable fracture testing of brittle ceramics using CMOD as control parameter has been developed; stable fracture of materials such as fine grained magnesium–aluminium spinel and alumina has been attained.[11,12] The fracture toughness values obtained are lower than those previously obtained from the maximum load values in unstable tests using displacement control.

1.2. Mullite

Mullite presents some attractive properties for structural applications such as high melting point (1828 ± 10 °C),[23] low thermal conductivity (6 kcal m^{-1} h^{-1} °C^{-1})[24] and low thermal expansion coefficient ($\alpha_{25-800\,°C} = (4.1 \pm 0.1) \times 10^{-6}$ °C^{-1}).[25]

Initially used only for high temperature traditional applications, mullite materials experienced a great development since the seminal work of Mazdiyasni[26] where translucent polycrystalline bodies of stoichiometric mullite with relatively high strength and excellent thermal-shock resistance were described.[23,26,27] The availability of fine pure mullite powders and new processing routes has made it possible to obtain dense polycrystalline mullites with little or nearly no residual glassy phase and with higher deformation resistance at higher temperatures than any ceramic oxide.[24,27–29]

Mullite ceramics present flat *R*-curve and can experience subcritical crack propagation during fracture at room temperature.[30–32] Different researchers have provided fracture toughness values obtained using different unstable fracture test configurations and relatively large notch tip radii (~200–300 μm) for mullites with various microstructures.[24,28,29,32] Reported values of the critical stress intensity factor in mode I, K_{IC}, are around 2.0–2.8 MPa m$^{1/2}$. In particular, for fracture testing of SENB in three points bending (beams: 4 mm × 6 mm × 50 mm, span: 40 mm, width notches ~200 μm, relative notch depth: 0.5), 2.0–2.4 MPa m$^{1/2}$ for load displacement rates between 0.005 and 5 mm/min have been obtained.[24,28,29,32] Up to now no definitive value for intrinsic K_{IC} of fine grained mullite has been provided.

In this work, the stable fracture behaviour of a fine grained mullite tested using CMOD as control variable at rates 0.001 and 0.018 mm/min and notch tip radii of ~6 μm and ~60 μm is presented and compared to that corresponding to displacement controlled tests performed at a rate (0.05 mm/min) equivalent to the largest CMOD one.

2. Experimental procedures

2.1. Material and specimen preparation

Mullite specimens have been fabricated from high purity (99.99%) powders (193CR, Baikowski Chimie, France) following the procedure described elsewhere.[30] Starting powders (1.8 μm) were attrition milled with mullite balls down to 0.8 μm, isostatically pressed (200 MPa) and sintered at 1630 °C for 4 h. The microstructural and mechanical properties for this mullite are summarised in Table 1.

Single edge "V" notched beams (SEVNB) of 4 mm thickness (B), 6 mm width (W) and 50 mm length (S) were diamond machined from the sintered blocks (10 mm × 40 mm × 65 mm). Notches were initially machined using a 300 μm wide diamond wheel. Using the pre-notch as a guide, the remaining part of the notch was done with a 150 μm wide razor blade sprinkled with 15, 6 and 1 μm diamond paste. Tip radii of about 60 and 6 μm respectively, and relative notch depths, $\alpha \sim 0.6$, were obtained (Fig. 2a and b). Fig. 2c shows a characteristic fracture surface; straight pre-notch and final notch ($\alpha \sim 0.6$) tips are observed.

2.2. Testing conditions

The development and complete description of the experimental setup used is described elsewhere.[11,12] It combines an electromechanical machine with a high-precision optical micrometre. The compliance of the test rig, C (machine, load cell and support arrangement), is 1.5×10^{-7} m/N up to 150 N and the resolution for the whole system for CMOD recording and control (micrometre + testing device) is 0.02 μm.

The CMOD was used as control parameter (rates = 0.001 and 0.018 mm/min) for mullite beams with tip notch radii of ~60 μm (range from 63 to 56 μm) and ~6 μm (range from 10 to 3 μm). Additional displacement controlled tests were performed using a rate of 0.05 mm/min. This rate was determined from the

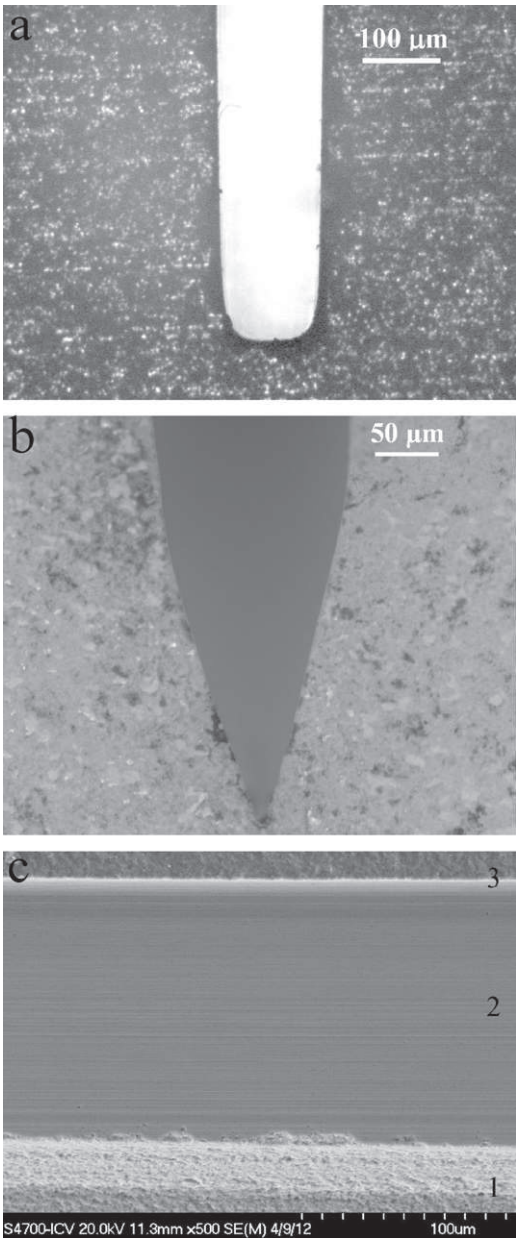

Fig. 2. Characteristic notch tips used for testing. (a, b) Optical microscopy micrographs of "as machined" lateral surfaces. (c) Scanning electron micrograph of fracture surface. (a) Tip radius ~60 μm machined with a diamond disc. (b) Tip radius ~6 μm machined from notches such as (a) and finished with a razor blade wrinkled with diamond paste. (c) Low magnification micrograph showing the process of machining of V notch and initiation of fracture. (1) Pre-notch done with the diamond disc. (2) Zone machined with the razor blade. The end of the notch is straight. (3) Initiation of fracture.

displacement and times needed to attain the maximum loads in the CMOD controlled tests to get equivalent deformation rates.

3. Results

3.1. Stability analysis

In Fig. 3 the Griffith locus corresponding to the numerical values of dimensionless load ($PL/\sigma_f BW^2$) and dimensionless displacement ($dL/\varepsilon_f W^2$) calculated using the test geometry of this work (span, $L = 40$ mm; width, $W = 6$ mm and thickness, $B = 4$ mm) is plotted for specimens with different brittleness numbers ($s = K_I/\sigma_f W^{1/2}$). Calculations have been done for a totally stiff machine (compliance, $C = 0$). The critical relative notch depth that satisfies $\delta P/\delta d = 0$ and, thus, limits the regimes I and II of crack growth is $\alpha_c = 0.4$ for all values of the brittleness number.

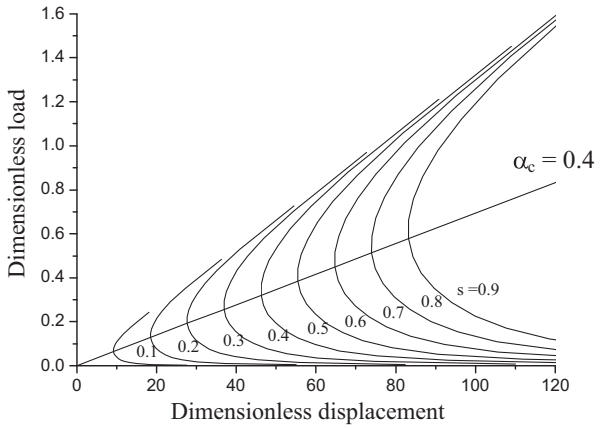

Fig. 3. Griffith locus corresponding to the numerical values of dimensionless load ($PL/\sigma_f BW^2$) and dimensionless displacement ($dL/\varepsilon_f W^2$) for the test geometry of this work (span, $L = 40$ mm; width, $W = 6$ mm and thickness, $B = 4$ mm). Calculations have been done for a test rig compliance, $C = 0$, and for specimens with different brittleness numbers, $s = K_I/\sigma_f W^{1/2}$. The critical relative notch depth, α_c, is the same for all s.

As described in the introduction, for real test rigs with compliance different from zero, the relative weights of regimes I and II changes. In these cases, calculations have to take into account the compliance of the test rig and the characteristics of the material being tested, through the brittleness number. For the compliance of the experimental set up and the testing geometry used in this work and the properties of the material summarised in Table 1, $s = 0.05$. The corresponding Griffith

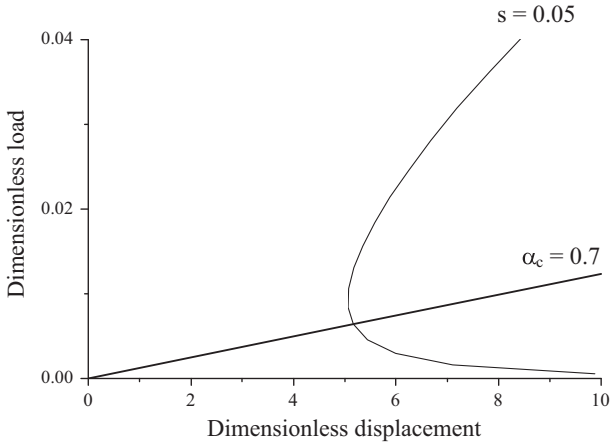

Fig. 4. Griffith locus corresponding to the numerical values of dimensionless load ($PL/\sigma_f BW^2$) and dimensionless displacement ($dL/\varepsilon_f W^2$) for the geometry (span, $L = 40$ mm; width, $W = 6$ mm; thickness, $B = 4$ mm) and test rig compliance ($C = 1.5 \times 10^{-7}$ m/N) used in this work. The critical relative notch depth, α_c, is larger than for $C = 0$ (Fig. 3).

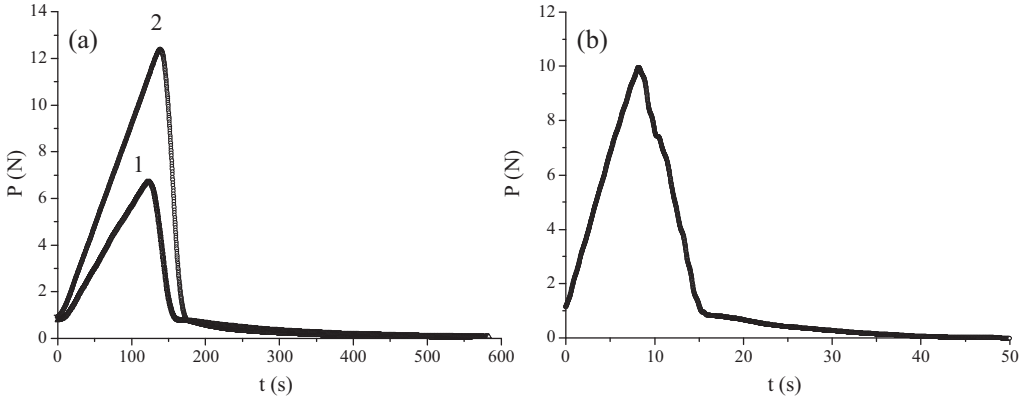

Fig. 5. Characteristic load (P)–time (s) experimental curves corresponding to CMOD controlled fracture tests. (a) CMOD rate of 0.001 mm/min for tip radius ~ 6 μm (1) and ~60 μm (2). The maximum load is higher for larger radius. Stable fracture tests were attained. (b)CMOD rate of 0.018 mm/min for tip radius ~ 6 μm.

locus is plotted in Fig. 4; very deep notches ($\alpha_c \geq 0.7$) are needed to achieve stable fracture using the displacement as control parameter.

3.2. Fracture tests

The experimental set up permitted to follow the CMOD rate requirements for the range used (0.001 and 0.018 mm/min). Characteristic plots recorded for CMOD and displacement controlled tests are shown in Figs. 5 and 6. Stable fracture, characterised by a continuous decrease of the load for increasing time, was always attained when CMOD was used as control parameter (Fig. 5). A decrease of displacement after the maximum load was needed to keep stable fracture (Fig. 6a).

As expected for the notch sizes used ($\alpha \sim 0.6 < \alpha_c = 0.7$), stability was never achieved in displacement control as a sudden load drop occurred once fracture initiated (Fig. 6b).

In Table 2 the quantitative parameters of the fracture tests are summarised. Two test time values were considered as characteristic, the time to reach maximum loads (t_p) and the time required to complete fracture once the maximum load was attained (t_γ).

The critical stress intensity factor in mode I, K_{ICp}, for the maximum load attained during the test (P_{max}), was calculated as[33]:

$$K_{ICp} = \frac{3P_{max}L}{2BW^{3/2}} K_\beta(\alpha) \quad (1)$$

where L is the span (40 mm), B and W are the geometrical parameters defined before and K_β (α) is a general shape function which is valid for any value of the relative notch depth ($0 \leq \alpha \leq 1$) and span-to-depth ratios ($\beta = L/W$) larger than 2.5 ($2.5 \leq \beta \leq 16$).[33] As described in the introduction, this parameter characterises the initiation of fracture. To evaluate the fracture process, $K_{IC\gamma}$, was calculated according to:

$$K_{IC\gamma} = \left[\frac{2E\gamma}{1-\nu^2}\right]^{1/2} \quad (2)$$

where E and ν are the Young's modulus and the Poisson ratio of the material (Table 1) and γ is the fracture energy. γ was calculated as the integral of the load–displacement plot divided by twice the area of the unnotched cross-section of the specimens, which evaluates the newly formed fracture surfaces.

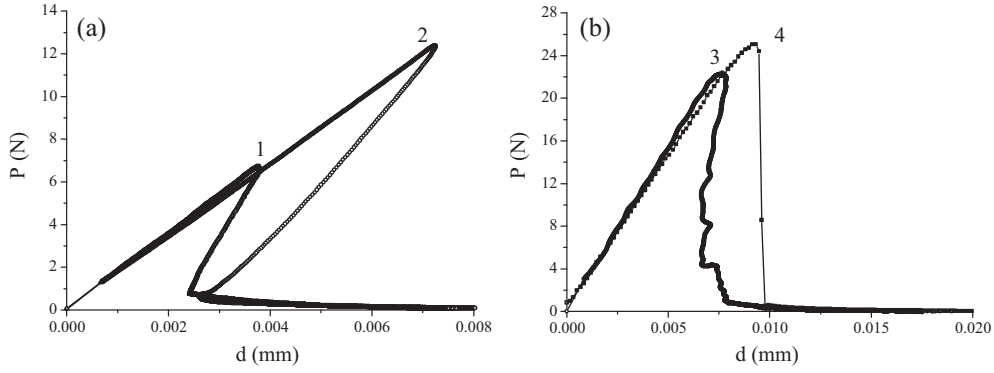

Fig. 6. Characteristic load (P)–displacement (d) experimental curves. (a) CMOD controlled fracture tests using a rate of 0.001 mm/min for tip radius ~ 6 μm (1) and ~60 μm (2). Decreasing of the displacement (snap-back) was needed to reach stability. (b) (3) CMOD controlled fracture test using a rate of 0.018 mm/min for tip radius ~ 6 μm. Decreasing of the displacement (snap-back) was needed to reach stability. Stable fracture was attained. (4) Displacement controlled fracture test using a rate of 0.05 mm/min for tip radius ~ 6 μm. Unstable fracture occurred. The actual maximum load is higher than for test (3).

Table 2
Fracture toughness values determined in this work. v: deformation rate; ρ: notch tip radius; t_p: time required to reach maximum load; t_γ: time required to complete fracture once the maximum load was attained; K_{ICp}: fracture toughness calculated from the maximum load. $K_{IC\gamma}$: fracture toughness calculated from the fracture energy. (S.D.): standard deviation.

	CMOD control			Displacement control
v, mm/min	0.001		0.018	0.05
ρ, μm	60	6	6	6
t_p, s	100	100	10	10
t_γ, s	500	500	30	0
K_{ICp} (S.D.), MPa m$^{1/2}$	1.11 (0.06)	0.72 (0.07)	0.86 (0.06)	1.17 (0.09)
$K_{IC\gamma}$ (S.D.), MPa m$^{1/2}$	0.66 (0.15)	0.53 (0.02)	0.88 (0.02)	–

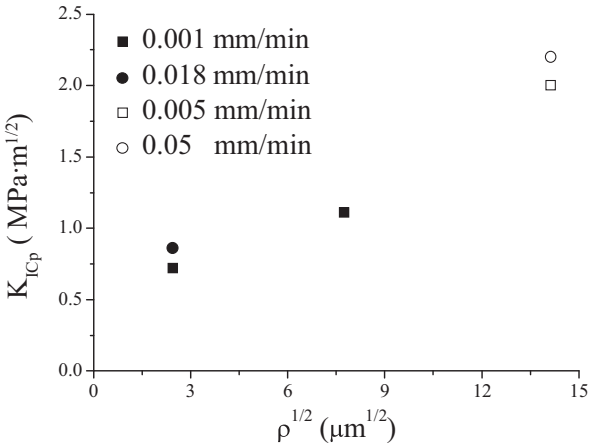

Fig. 7. Dependence of the K_{IC} values, calculated from the maximum load point (K_{ICp}), on notch tip radius (ρ). Legends stand for the used rate of the control variable. Solid symbols correspond to this work (Table 2) and open symbols correspond to.[30] A decrease of fracture toughness with notch tip radius is shown.

For the slow CMOD rate, the times to reach the maximum load (∼100 s) as well as the times required to complete fracture (∼500 s) are similar for both notch tip radii. In both cases, toughness values calculated for the initiation of fracture, K_{ICp}, are larger (∼36%) than those which average the whole fracture process, revealing a time effect due to subcritical crack propagation in this material that will be discussed latter.

For the same CMOD rate (0.001 mm/min, characteristic plots in Figs. 5a and 6a), there are significant differences between K_{ICp} for different notch tip radius, as highlighted in Fig. 7. Values for the largest radius (∼60 μm) are about 54% higher than for the smallest one (∼6 μm). On the contrary, $K_{IC\gamma}$ values are coincident for the range of notch tip radius used, revealing that the characteristics of the notch are not so critical when calculations are done by averaging the whole fracture process.

In Fig. 7, values previously reported for notch tip radius ∼ 200 μm are also plotted for comparison. A decrease of K_{IC} values with notch tip radius down to a plateau value, which should be considered as the intrinsic value for the material, has been observed in a number of ceramics[34–36] and theoretically predicted by Fett and Munz.[37,38] Essentially, this fact is due to the non-adequacy of the equations used for calculations of K_{IC} from the maximum load values for notches which geometry separates from real cracks. When such equations are to be used, different specimens with different radius should be tested until the plateau value is reached. However, it is not possible to introduce notches with radius smaller than a few microns by standard techniques in fine grained material such as the one studied here, for which a radius ∼ 6 μm has been obtained. This tip notch radius, 6 μm, is lower than the critical radius predicted by Damani et al.,[34] 15 μm, so we can consider that the value measured for the 6 μm is independent of the tip notch radius and corresponds with the intrinsic fracture toughness value.

For fast CMOD controlled tests (rate = 0.018 mm/min), which imply fracture times about one order of magnitude shorter than the above discussed (10–30 s, Table 2), and small notch tip radius (∼6 μm) there are no differences between K_{ICp} and $K_{IC\gamma}$, which fulfils the criteria of validity of the determined values. Moreover, these values are higher than those obtained in slow tests (Table 2).

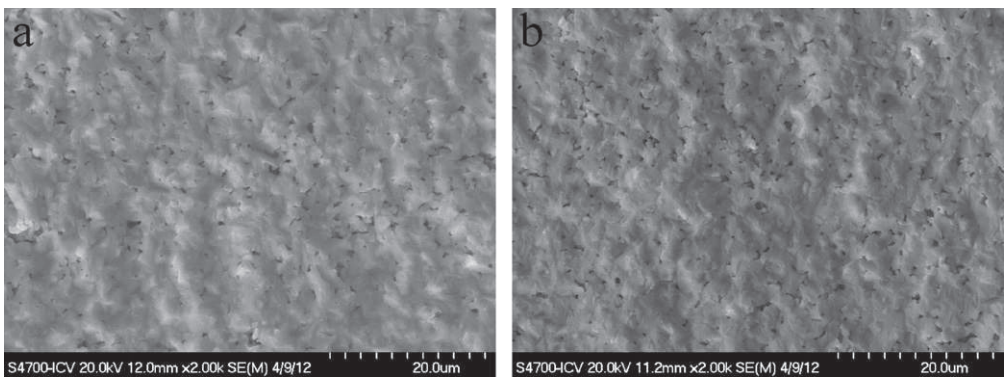

Fig. 8. Characteristic fracture surfaces of CMOD controlled tests. Scanning electron micrographs. (a)CMOD rate of 0.018 mm/min for tip radius ∼ 6 μm. Mainly transgranular fracture. (b)CMOD rate of 0.001 mm/min for tip radius ∼ 6 μm. Mixed trans/intergranular fracture.

As described in the introduction, subcritical crack propagation has been reported for this material.[30,31] In Fig. 8, characteristic fracture surfaces for fast and slow CMOD controlled tested specimens are shown. For each testing condition, the same fracture mode was observed through the whole fracture surface. When 0.018 mm/min was used as CMOD rate, fracture was mainly transgranular (Fig. 8a) while the slowly tested specimens presented a major proportion of intergranular fracture (Fig. 8b). This features would indicate that subcritical crack propagation is due to the characteristics of the grain boundary, probably to the presence of a residual silica glassy phase, as proposed in other works.[39,40]

The above discussion demonstrates that relatively fast tests are required to avoid subcritical crack propagation. When this process is avoided, K_{ICp} calculated from the maximum load for specimens with a notch tip radius of ~6 μm will be the intrinsic value. However, when tests are performed in displacement control using a rate of (0.05 mm/min) equivalent to the fast CMOD rate (0.018 mm/min), the value of K_{ICp} obtained in the unstable tests is ~36% higher than that obtained for stable fracture (Fig. 6b, Table 2). This fact can be attributed to the actual load required to initiate fracture being masked by the effect of the inertia of the loading frame.

4. Conclusions

The effect of experimental variables on the K_{IC} values determined in SEVNB in three points bending has been analysed. The analysis has been possible due to the possibility of comparison of results obtained in stable and unstable fracture tests.

Stable facture tests have been reached for a fine grained mullite by using the CMOD as control variable. Using the same geometrical setup, tests performed using the displacement of the frame as control variable led to unstable fracture.

In order to determine accurate fracture toughness of materials with flat *R*-curve and that experience subcritical crack propagation stable fracture tests at high deformation rates are required. Under such conditions, an intrinsic $K_{IC} = 0.86 \pm 0.06\ \text{MPa m}^{1/2}$, less than one half of those previously reported has been obtained for the studied mullite with average grain size 0.7 ± 0.5 μm.

Acknowledgements

The authors acknowledge the financial support by projects: MAT2009-14448-C02 and MCI-PET2008-0113 and Microtest S. A. (Spain). García-Prieto acknowledges the financial support of the JAE-CSIC fellowship program (Spain).

References

1. Ghosh A, Jenkins MG, White KW, Kobayashi AS, Bradt RC. Elevated-temperature fracture resistance of a sintered α-silicon carbide. *J Am Ceram Soc* 1989;**72**(2):242–7.
2. Nakayama J, Abe H, Bradt RC. Crack stability in the work-of-fracture test: refractory applications. *J Am Ceram Soc* 1981;**64**(11):671–5.
3. Tattersall HG, Tappin G. The work of fracture and its measurement in metals, ceramics and other materials. *J Mater Sci* 1966;**1**:296–301.
4. Calomino AM, Brewer DN. Controlled crack growth specimen for brittle systems. *J Am Ceram Soc* 1992;**75**(1):206–8.
5. Sørensen BF, Horsewell A, Jørgensen O, Kumar AN, Engbæk P. Fracture resistance measurement method for in situ observation of crack mechanisms. *J Am Ceram Soc* 1998;**81**(3):661–9.
6. Wan D, Bao Y, Peng J, Zhou Y. Fracture toughness determination of $Ti_3Si(Al)C_2$ and Al_2O_3 using a single gradient notched beam (SGNB) method. *J Eur Ceram Soc* 2009;**29**:763–71.
7. Kuszyk JA, Bradt RC. Influence of grain size on effects of thermal expansion anisotropy in $MgTi_2O_5$. *J Am Ceram Soc* 1973;**56**(8):420–3.
8. Sørensen BF, Brethe P, Skov-Hansen P. Controlled crack growth in ceramics: the DCB specimen loaded with pure moments. *J Eur Ceram Soc* 1996;**16**(9):1021–5.
9. Ebrahimi ME, Chevalier J, Fantozzi G. *R*-curve evaluation and bridging stress determination in alumina by compliance analysis. *J Eur Ceram Soc* 2003;**23**(6):943–9.
10. Nakayama J. Direct measurement of fracture energies of brittle heterogeneous materials. *J Am Ceram Soc* 1965;**48**(11):583–7.
11. García-Prieto A, Baudín C. Crack mouth opening displacement controlled fracture tests of brittle ceramics. *J Eur Ceram Soc* 2010;**30**:3297–3302.
12. García-Prieto A, Hernández J, López M, Baudín C. Controlled fracture test for brittle ceramics. *J Strain Anal* 2011;**46**:27–42.
13. Sakai M, Urashima K, Inagaki M. Energy principle of elastic–plastic fracture and its application to the fracture mechanics of a polycrystalline graphite. *J Am Ceram Soc* 1983;**66**(12):868–74.
14. Bar-On I, Baratta FI, Cho K. Crack stability and its effect on fracture toughness of hot pressed silicon nitride beam specimens. *J Am Ceram Soc* 1996;**79**(9):2300–8.
15. Davidge RW, Tappin G. The effective surface energy of brittle materials. *J Mater Sci* 1968;**3**:165–73.
16. Bueno S, Berger MH, Moreno R, Baudín C. Fracture behaviour of microcrack free alumina–aluminium titanate ceramics with second phase nanoparticles at alumina grain boundaries. *J Eur Ceram Soc* 2008;**28**:1961–71.
17. Irwin GR. *Fracture in encyclopedia of physics*. Berlin: Springer Verlag; 1958. p. 551–89.
18. Sigl LS. On the stability of cracks in flexure specimens. *Int J Fract* 1991;**51**:241–54.
19. Biolzi L, Cangiano S, Tognon G, Carpinteri A. Snap-back softening instability in high-strength concrete beams. *Mater Struct* 1989;**22**:429–36.
20. Pastor JY, Planas J, Elices M. Ambient and high-temperature stable fracture tests in ceramics: applications to yttria–partially-stabilized zirconia. *J Am Ceram Soc* 1993;**76**(11):2927–9.
21. Pastor JY, Planas J, Elices M. A new technique for fracture characterization of ceramics at room and at high temperature. *J Test Eval* 1995;**23**(3):209–16.
22. Pastor JY, Planas J, Elices M. Ensayos de fractura estables en materiales cerámicos. *Bol Soc Esp Ceram V* 1992;**31**(4):322–5.
23. Mah T-I, Mazdiyasni KS. Mechanical Properties of Mullite. *J Am Ceram Soc* 1983;**66**:699–703.
24. Schneider H, Schreuer J, Hildmann B. Structure and properties of mullite: a review. *J Eur Ceram Soc* 2008;**28**:329–44.
25. Burgos-Montes O, Moreno R, Baudín C. Effect of mullite additions on the fracture mode of alumina. *J Eur Ceram Soc* 2010;**30**:857–63.
26. Mazdiyasni KS, Synthesis Brown LM. Mechanical properties of stoichiometric aluminum silicate (Mullite). *J Am Ceram Soc* 1972;**55**:548–52.
27. Dokko PC, Pask JA, Mazdiyasni KS. High-temperature mechanical properties of mullite under compression. *J Am Ceram Soc* 1977;**60**:150–5.
28. Torrecillas R, Fantozzi G, de Aza S, Moya JS. Thermomechanical behaviour of mullite. *Acta Mater* 1997;**45**:897–906.
29. Fernandez E, Baudín C. Creep damage in different $3Al_2O_3{\cdot}2SiO_2$ mullites tested in 4-point bending. *J Eur Ceram Soc* 2001;**21**: 2243–51.
30. Osendi MI, Baudín C. Mechanical properties of mullite materials. *J Eur Ceram Soc* 1996;**16**:217–24.
31. Casellas D, Baudín C, Osendi MI, Llanes L, Anglada M. Fracture resistance of mullite under static and cyclic loads. *Scripta Mater* 1998;**38**:39–44.
32. Baudín C. Fracture mechanisms in a stoichiometric $3Al_2O_3{\cdot}2SiO_2$ mullite. *J Mater Sci* 1997;**32**:2077–86.

33. Guinea GV, Pastor JY, Planas J, Elices M. Stress intensity factor, compliance and CMOD for a general three-point-bend beam. *Int J Fract* 1998;**89**:103–16.
34. Damani R, Gstrein R, Danzer R. Critical notch-root radius effect in SENB-S fracture toughness testing. *J Eur Ceram Soc* 1996;**16**:695–702.
35. Nishida T, Hanaki Y, Pezzoti G. Effect of notch-root radius on the fracture toughness of a fine-grained alumina. *J Am Ceram Soc* 1994;**77**: 606–8.
36. Kübler J. Fracture Toughness of ceramics using the SEVNB method: preliminary results. In: *Proceedings of the 21st annual conference on composites, advanced ceramics, materials and structures-B: ceramic engineering and science proceedings, vol. 18*. 1997. p. 155–62.
37. Fett T. Influence of a finite notch root radius on fracture toughness. *J Eur Ceram Soc* 2005;**25**:543–7.
38. Fett T, Munz D. Influence of narrow starter notches on the initial crack growth resistance curve of ceramics. *Arch Ap Mech* 2006;**76**:667–79.
39. Michalske TA, Freiman SW. A molecular mechanism for stress–corrosion in vitreous silica. *J Am Ceram Soc* 1983;**66**:284–8.
40. Thomson R. The molecular wedge in a brittle crack: a simulation of mica water. *J Mater Res* 1990;**5**:524–34.

Capítulo 6

INFLUENCIA DE LAS CARACTERÍSTICAS MICROESTRUCTURALES EN LA TENACIDAD DE FRACTURA DE MATERIALES REFRACTARIOS

6. INFLUENCIA DE LAS CARACTERÍSTICAS MICROESTRUCTURALES EN LA TENACIDAD DE FRACTURA DE MATERIALES REFRACTARIOS.

Una vez determinada la validez del dispositivo experimental, el procedimiento de ensayo y la metodología de ensayo y análisis de resultados para materiales frágiles (capítulos 3-5), se ha estudiado la adecuación y potencial necesidad de los ensayos controlados por CMOD para la caracterización de materiales en los que actúan mecanismos de refuerzo durante la fractura. Para ello se seleccionaron materiales refractarios comerciales que, a pesar de su importancia tecnológica, no suelen ser objeto de estudios sistemáticos debido a la dificultad para controlar su composición química y/o su microestructura a escala industrial (apartado 1.7).

Se caracterizaron un amplio rango de materiales refractarios comerciales, tales como materiales refractarios de sílice (S), alúmina-sílice (AS), alúmina-zirconia-sílice (AZS) y hormigones de alta alúmina (C). Se estudiaron las relaciones entre las características químicas, estructurales y microestructurales de estos materiales con su comportamiento mecánico usando los parámetros de tenacidad descritos en los apartados 1.2 y 1.7. Como se indicó en el capítulo 1 estos materiales son heterogéneos y poseen porosidades del orden del 20-60% frente a un 2% para las cerámicas técnicas avanzadas analizadas en los capítulos anteriores.

Parte de este trabajo se englobó en el marco de un proyecto final de Carrera titulado "Puesta a punto de un método de ensayo de fractura estable para la determinación de la tenacidad de fractura y el trabajo de fractura de materiales refractarios utilizando la apertura de la grieta como variable de control", realizado por Manuel Dos Ramos Lotito, estudiante del Departamento de Ciencia de Materiales de la Universidad Simón Bolívar, Caracas, Venezuela, durante su estancia en el Instituto de Cerámica y Vidrio.

Las investigaciones derivadas de este trabajo han dado lugar a una estrecha colaboración entre el Instituto de Cerámica y Vidrio y la Universidad Simón Bolívar, quedando reflejados dichos resultados en la publicación de un artículo en la revista Journal of the European Ceramic Society (Anexo IV).

6.1. Condiciones experimentales

Se emplearon técnicas de análisis químico por fluorescencia de rayos-X, difracción de rayos-X, microscopía óptica de luz reflejada y microscopía electrónica de barrido con el fin de realizar una completa caracterización microestructural de los materiales.

Para la determinación de la tenacidad de fractura se utilizaron las geometrías de ensayo para materiales refractarios descritas en el apartado 3.2.2. Se alcanzaron fondos de entalla con un radio de curvatura de aproximadamente 130 μm.

Se realizaron ensayos en control por CMOD a 70 μm/min y en control por desplazamiento a 0.2 mm/min, se seleccionaron estas velocidades porque son equivalentes a la velocidad de incremento de la tensión, 0.15 MPa/s, según norma UNE-EN 993-6: Métodos de ensayo para productos refractarios conformados densos[286].

6.2. Resultados y discusión

Los análisis realizados permitieron caracterizar completamente la microestructura y la textura de los materiales seleccionados.

Se alcanzaron ensayos de fractura estable tanto en control por desplazamiento como en control por CMOD para todos los materiales caracterizados en este trabajo para las dos geometrías y longitudes de entalla relativas (α) utilizadas. Este hecho demuestra que para materiales cerámicos en los que tienen lugar mecanismos de refuerzo durante la fractura, si se emplean máquinas suficientemente rígidas, no es necesario el uso del CMOD como parámetro de control.

No se encontraron diferencias significativas entre los parámetros de tenacidad de fractura determinados para un mismo material utilizando distintos parámetros de control y diferentes geometrías de probetas y longitudes de entalla.

En la figura 6.1 se muestran los parámetros de tenacidad de fractura definidos en el capítulo 1, K_{IC}, γ_{wof}, $\gamma_{nbt.}$ Se observa como estos valores varían en función de las diferentes características microestructurales de estos materiales. Se encontraron diferencias significativas entre los tres parámetros de tenacidad correspondientes tanto al inicio como a la propagación de la fractura para materiales diferentes.

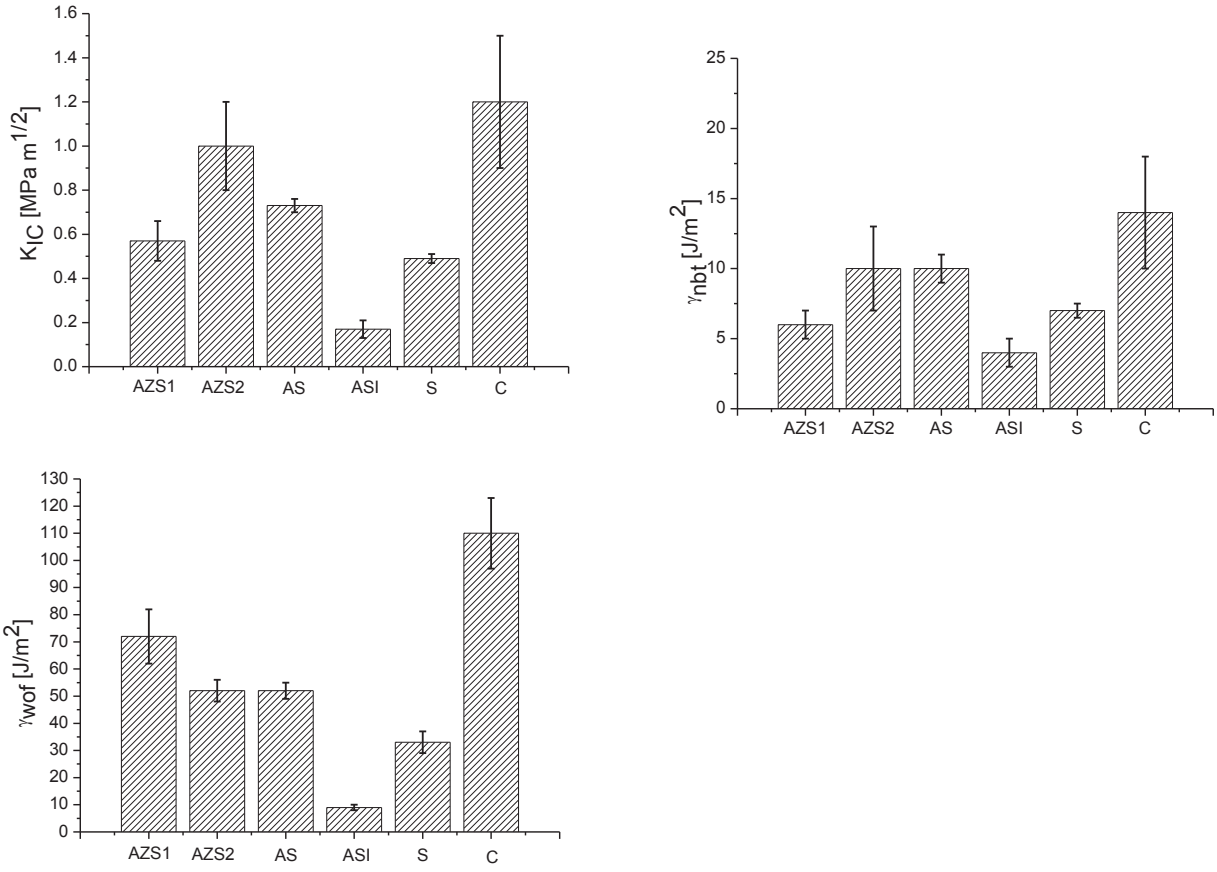

Figura 6.1. Parámetros de tenacidad de fractura para los materiales refractarios.
(a) Factor crítico de intensidad de tensiones en modo I, K_{IC}.
(b) Energía para el inicio de la grieta, γ_{nbt}.
(c) Trabajo de fractura, γ_{wof}.

6.3. Conclusiones

- Es posible alcanzar de manera rutinaria a nivel de laboratorio ensayos de fractura estable utilizando el desplazamiento del marco de carga como parámetro de control, si se utiliza un dispositivo de alta rigidez.

- Se ha demostrado la adecuación de los ensayos de fractura estable de probetas SENB en flexión en tres puntos para la caracterización de la tenaciad de materiales refractarios.

- Incluso utilizando el menor de los tamaños estandarizados para la caracterización de estos materiales (150x25x25 mm^3) y con una longitud de entalla relativa, α=0.5, se han encontrado diferencias significativas entre los parámetros de tenacidad en función de la microestructura de los diferentes materiales refractarios caracterizados.

- Las características microestructurales que determinan la resistencia al inicio de la fractura son diferentes a las que regulan el proceso de propagación de la grieta. Las características de los agregados determinan la tenacidad en el inicio de la fractura, mientras que, para alcanzar altos valores del trabajo de fractura, es preciso la presencia de elementos microestructurales que originen los mecanismos de refuerzo.

ANEXO IV

Este trabajo ha dado lugar a la siguiente publicación:

- Ana García-Prieto, Manuel Dos Ramos-Lotito, Delia Gutiérrez- Campos, Pilar Pena, Carmen Baudín. "Influence of microstructural characteristics on fracture toughness of refractory materials". J. Eur. Ceram. Soc. 35 (6) 1955-1970 (2015). (DOI:10.1016/j.jeurceramsoc.2014.12.020).

Available online at www.sciencedirect.com

ScienceDirect

Journal of the European Ceramic Society 35 (2015) 1955–1970

www.elsevier.com/locate/jeurceramsoc

Influence of microstructural characteristics on fracture toughness of refractory materials

Ana García-Prieto [a], Manuel Dos Ramos-Lotito [a,b], Delia Gutiérrez-Campos [b], Pilar Pena [a], Carmen Baudín [a,*]

[a] *Instituto de Cerámica y Vidrio, CSIC, Kelsen 5, Madrid 28049, Spain*

[b] *Universidad Simón Bolívar, Dept. Ciencia de los Materiales, Valle de Sartenejas, Caracas 1080, Venezuela*

Received 28 July 2014; received in revised form 15 December 2014; accepted 16 December 2014

Available online 13 January 2015

Abstract

Basic relationships between the microstructure and the texture of refractories and their toughness have been established. A series of commercial materials has been chosen in order to highlight the influence of microstructural characteristics on fracture behaviour and associated toughness. Silica, silica–alumina and silica–alumina–zirconia based shaped refractories and a calcium aluminate cement bonded concrete have been analysed. Extensive microstructural characterisation has been performed using a combination of techniques, including chemical analysis by X-ray fluorescence, X-ray diffraction, reflected light optical microscopy and scanning electron microscopy with analysis by dispersive energies. Fracture has been characterised using stable fracture tests of SENB tested in 3 point bending. Stability was reached in displacement and crack mouth opening displacement controlled tests. Size effect has been analysed by using two different specimen sizes and relative notch lengths. For the range of microstructures studied, the obtained results have allowed to characterise toughness and establish the relationships toughness-microstructure and texture.

Keywords: Alumina; Castables; Microstructure; Refractories; Toughness

1. Introduction

The study of commercial refractories is quite uncommon due to the challenges generated by the impossibility of controlling the chemical composition and/or the microstructure of the material. Nevertheless, tackling this task has the advantage of avoiding problems linked to reproducing the manufacturing process at a laboratory scale, which is not a trivial issue due to inherent differences between laboratory and refractory plants processes.

The performance of refractories in use is directly related to their microstructure and texture which, in turn, is determined by the characteristics of the raw materials (chemical and mineralogical composition and size and shape distribution) and by the processing or installation procedure. Thus, the study of commercial products imposes the necessity of characterising them in a comprehensive manner. It is particularly important for the understanding of their behaviour in terms of the basic material science relationships between their composition, microstructure and properties. By using several complementary techniques like chemical analysis, mineralogical studies, and microstructural and textural analysis, it is possible to obtain useful data for generating a detailed description of the material.

Refractories are applied in processes involving mechanical strains, variable high temperatures and aggressive environments including corrosion and erosion from solids, liquids and gases in movement. In particular, the thermal stress fracture of refractory components, due to temperature cycling and/or temperature differences through the material, is a widespread problem of industrial importance. In the same way, mechanical overload as may be originated by impact during the loading of the process vessel, as occurs in electrical arc furnaces, or by deformations

* Corresponding author. Tel.: +34 917355840.
E-mail address: cbaudin@icv.csic.es (C. Baudín).

http://dx.doi.org/10.1016/j.jeurceramsoc.2014.12.020
0955-2219/

of the kiln shell, as observed in the cement industry, can lead to fracture. Fracture as a result of thermal or mechanical shocks could lead to a catastrophic failure of the refractories with strong consequences for the process in which they are used. However, fracture can also result just in the development of a crack pattern.[1] In this regard, it should be pointed out that the conventional characterisation of the mechanical properties of refractory products is done in terms of two properties: crushing strength and modulus of rupture. Even though such properties might be adequate for quality control purposes, the results achieved do not allow the evaluation or study of the fracture processes, and more basic mechanical properties are needed for characterisation.

The extension of fracture due to thermal or mechanical strains, i.e.: the damage would be determined by the ratio between the amount of energy available and the energy needed to create new crack surfaces or specific fracture energy. Therefore, this ratio will characterise the resistance of materials to subcritical crack growth and the proneness to catastrophic failure.[2,3]

Refractory products are heterogeneous ceramic materials which fracture exhibits notable deviations from pure linear elastic.[1,4–10] Several energy-consuming processes ahead (process zone) and behind (process wake) the crack tip are considered to contribute to this behaviour. Microcracking and multiple crack branching are usually observed in the frontal process zone, while grain bridging and friction of the crack faces are able to consume energy in the process wake zone. As a result, the parameters that evaluate toughness of refractories are no longer material constants but they increase for increasing crack extension. In the field of advanced ceramics, this fracture pattern is called rising *R*-curve behaviour, with *R* representing toughness; in contrast with the brittle flat *R*-curve observed for glass or for fine grain size ceramic specimens.

The *R*-curve concept is not used for the characterisation of refractories because of the experimental difficulties associated to follow a single crack in such heterogeneous microstructures. Unlike the *R*-curve, the work of fracture, γ_{wof}, has been successfully used to describe the fracture of refractories.[6] The advantage of this energy parameter is that it does not require any assumptions about the constitutive equation of the body with the crack to discuss its propagation.[11,12] In terms of energy, the critical energy release rate, G_c, of refractories with well designed microstructures is always significantly lower than the specific fracture energy, G_F ($2\gamma_{wof}$). The ratio between the specific fracture energy and the energy release rate, G_F/G_c, has been defined as a toughness, flexibility or apparent ductility ratio.[1] The higher this relation, the higher is the resistance of the material to damage by thermal or mechanical strains.

An important point to consider when determining the specific fracture energy (or the work of fracture) of refractories is the potential influence of the specimen size ("size effect") in the obtained values because G_F increases with increasing fracture surface until the specimen geometry allows the development of a well developed wake zone.

Nakayama, Tattersall and Tappin, and Davidge and Tappin accomplished the first studios on the determination of work of fracture in the 60s,[13–15] and since then, many laboratories have conducted such analyses but a standard test has not yet been established. The concept of work of fracture introduced by Nakayama[4,13] is defined as the mean work per unit of projected fracture area required to propagate a crack in a stable way. In Nakayama's test a parallelepiped bar with a triangular (chevron) notch at its centre is loaded in three point bending (3-pb). Using this geometry, refractory specimens fracture in a stable way when a sufficient stiff machine is used. The value of work of fracture is determined from the total area under the Load–Displacement curve recorded during the experiment and the size of the projected fracture surface. Chevron notch experiments often imply high variability (>10%)[6,7,16–18] because coarse aggregates at the apex of the chevron notch give very high values as compared to the average for the material. For example, 10–23% variability in γ_{wof} has been reported for alumina-spinel castables,[18] and for high alumina refractories (45–100 wt.% alumina) variability up to 38%[7,16] has been found.

In the 1980s the wedge-splitting fracture test was developed to perform stable fracture tests and patented by Tschegg.[19] This test is a special form of the so-called compact tension test, the specimen with a groove and notch is split in two halves while monitoring the load and crack mouth opening displacement (CMOD). In this experimental setup, large specimens of the size of bricks can be tested.[5,8,20–30] Most data produced using the wedge-splitting test are reported for pure magnesia, magnesia spinel and magnesia carbon refractories,[5,8,9,24–27] which are out of the scope of this paper. A relatively low number of studies provide data for high alumina castables and alumina-based shaped materials.[20,22,23,28–30]

Ribeiro and Rodrigues[22] applied the wedge splitting method to characterise fracture energy of two high-alumina refractory castables. Miyaji et al.[29] analysed five different castable formulations and introduced a figure of merit derived from the Load–Displacement curve to evaluate the thermal shock damage resistance. More recently, a methodology was presented using the wedge-splitting test complemented with images obtained during mechanical loading to determine the crack propagation for a pure alumina and alumina with titania and zirconia additives refractory compositions.[28,30] Jin et al.[27] have proposed a methodology to estimate the tensile strength, and Young's modulus of refractories in addition to the specific fracture energy from wedge splitting test results.

It should be pointed out that variability of data of mechanical properties in the refractory literature is most of the time not reported, and, in many cases, only one data for each material experimental condition is provided. This is often the case of work of fracture values determined by the splitting test so, it is not possible to discuss in a general way the repeatability associated with this technique. Nevertheless, the scarce data available reveal rather high dispersion of γ_{wof} results; for two commercial alumina based low cement (2 wt.% alumina) castables heat-treated at 1100 °C, 12 and 18% variability have been reported[22] and variability between 5 and 22% has been reported for basic refractories.[24]

Despite the fact that there is an evident interest in the wedge splitting test for work of fracture determination of refractories due to its capability for testing relatively large specimens in order to average the whole fracture process, it is complicate to establish this method as a laboratory routine one. Moreover, as mentioned before, variations in reported ranges of result would mask the effect of microstructural differences on toughness.

From the extensive spectrum of available fracture toughness tests, bending of parallelepiped specimens with straight through notches (SENB, Single Edge Notch Beam) using as control variable the displacement of the load frame (displacement control) is a relatively simple way of testing materials with *R*-curve fracture, like refractory products. In general, in the refractory field this method is used to determine toughness parameters describing the initiation of fracture, critical stress intensity factor in mode *I*, K_{IC}, and the energy for crack initiation, γ_{nbt} which is a measure of the critical energy release rate G_c, $G_c = 2\gamma_{nbt}$.[4,15,31–33]

The advantage of using stable fracture tests of SENB in 3-pb is that both parameters for initiation, γ_{nbt}, and propagation, γ_{wof}, of fracture can be extracted from a single test. The size of the specimen can be readily adjusted to ensure that the ligament is large enough to encompass the fracture process zone; in this way, the results will be statistically valid. As a term of comparison, a representative volume 3–4 times the largest aggregate size was determined by Romero and Masad[34] and Wagoner et al.[35] for SENB testing of asphalt concrete. However, there are two main experimental problems to solve with regard to this test.[1] On the one hand, the attainment of stability for this geometry is more difficult than for the chevron specimens and, on the other hand, straight through notches are more prone to lead to the wandering of the propagating crack from the initial plane.

When displacement of the load frame is used as control variable for SENB in 3-pb, a general requirement to reach stability is to use a high stiffness machine.[36–39] The crack mouth opening displacement (CMOD) has been proposed and used as control parameter for stable fracture testing under conditions that would have led to unstable fracture for displacement controlled tests. In this regard, detailed procedure and theoretical considerations for performing CMOD controlled fracture tests of brittle materials have been previously reported by the authors.[37–39]

In this work six different types of commercial refractory materials with distinctive specifications in chemical composition and microstructural characteristics were tested. The products were evaluated using CMOD and displacement of the load frame as control parameters using equivalent rates and two relative notch lengths (0.25 and 0.50). Once assured the significance of the obtained data, the important challenge in the study has been to correlate the microstructural features of the refractory materials with the fracture behaviour.

From the stable fracture tests different toughness parameters have been evaluated; the usual terminology used in refractory practice has been assumed for reporting. The critical stress intensity factor in mode *I*, K_{IC}, has been calculated from the maximum load according to Guinea et al.[40]:

$$K_{IC} = \frac{3PL}{2BW^{3/2}} K_\beta(\alpha) \quad (1)$$

where P is the applied load, L is the span, B and W are the geometrical parameters of thickness and width of the specimen, respectively. K_β (α) is a general shape function which is valid for any value of the relative notch length ($0 \le \alpha \le 1$) and span-to-depth ratios ($\beta = L/W$) larger than 2.5 ($2.5 \le \beta \le 16$).[40] From K_{IC} and Young's modulus, the energy for crack initiation, γ_{nbt} ($= G_c/2$) was calculated according to the analysis of Irwin for plane strain conditions[41]:

$$G_C = \frac{K_{IC}^2(1-\nu^2)}{E} \quad (2)$$

where K_{IC} is the critical stress intensity factor in mode *I*, ν is the Poisson's ratio and E is the Young's modulus.

To evaluate the fracture process, γ_{wof} has been calculated from the area under the Load–Displacement curve and the projection of the fracture surface following the procedure of Nakayama.[4,13]

In order to estimate the inelastic energy contribution to fracture, the ratio between the specific fracture energy and the energy release rate, G_F/G_c, has been calculated using the experimental γ_{wof} and γ_{nbt} values.

The chemical, structural and microstructural characteristics of the six studied refractory materials were correlated with their fracture behaviour using the different toughness parameters above described.

2. Experimental

Six different types of commercial refractory materials were studied: two alumina–silica–zirconia (AZS), a superduty fireclay, one group 28 insulating firebrick, one standard silica brick and a high-alumina regular castable heat treated at the use temperature (1100 °C). They were labelled as follows: AZS1, AZS2, AS, ASI, S and C, respectively. Fig. 1 shows the macroscopic aspect of these six refractories.

Chemical analysis was carried out with a Philips (Holland) X-ray fluorescence equipment, model MagiX PW 2424. Samples were prepared with the standard procedure of forming a fused pellet. $Li_2B_4O_7$ was added to the ground powder and prepared capsules were heat treated at 1000 °C.

Bulk and true densities and apparent and true porosity were determined following the procedures described in two standards: EN 993-1[42] and EN 993-2.[43] He picnometry was done using a Quantachrome (USA) apparatus.

Determination of crystalline phases was performed on ground samples in a Bruker (Germany) X-ray diffractometer, model D8 Advance, with copper anode ($CuK\alpha_1$ $\lambda = 0.15418$ nm) working at 40 kV and 40 mA. Scans were performed in continous mode with steps of 0.05° at a rate of 153 s per step. The analysis of the XRD patterns was accomplished using the EVA 6.0 Diffrac plus software (Bruker, Germany). The experimental diffraction

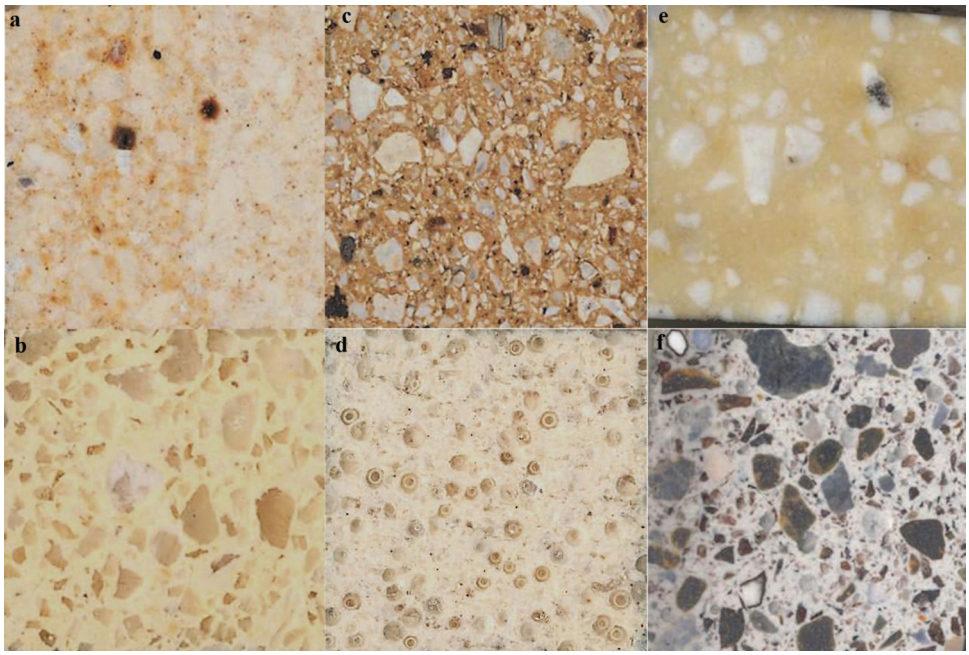

Fig. 1. Macroscopic aspect of the six commercial refractory materials studied. Scanned images of polished cross sections of tested specimens (25 mm × 25 mm). (a) Alumina–silica–zirconia brick, AZS1. (b) Alumina–silica–zirconia brick, AZS2. (c) Superduty fireclay brick, AS. (d) Group 28 insulating brick, ASI. (e) Standard silica brick, S. (f) High-alumina regular castable, C.

patterns were compared to the files of the International Centre for Diffraction Data (ICDD).[44]

Standard specimens (EN 993-6)[45] for mechanical characterisation (150 mm × 25 mm × 25 mm and 200 mm × 40 mm × 40 mm) were diamond machined from the received bricks and concrete pieces.

The size distributions of the aggregates were evaluated from scanned (HP Scanjet 5370 C, USA) images of the lateral surfaces (150 mm × 25 mm × 25 mm) of the specimens used for mechanical testing with the Leica Qwin software (UK). The equivalent diameter was calculated from the surface of the particles assuming spherical shape. A minimum of 560 particles was analysed for each material. This study was not performed for the insulating brick because its largest microstructural features were the pores which all had similar size (≈1200 μm).

Specimens for microstructural evaluation were embedded in resin in vacuum environment to assure the penetration of the resin in the pores. Then, microstructural characterisation of the materials was carried out using a reflected-light optical microscopy, RLOM, with a Zeiss (Axiophot, Germany) microscope and field emission scanning electron FE-SEM with analysis by energy dispersive X-ray spectroscopy (EDS) microscope (Hytachi S-4700 type I, Japan).

Young's modulus of the refractory materials was determined from the resonance of the parallelepiped bars (150 mm × 25 mm × 25 mm) tested in flexure by impact (Grindosonic, Belgium). Calculations were performed using the common value of Poisson's ratio for refractory materials (0.17). Given values are the average of 6 determinations and errors are the standard deviations.

Room temperature modulus of rupture (MOR) was determined by three point bending, 3-pb, (span 125 mm; 0.5 mm/min) following the procedure of EN 993-6 standard,[45] using a universal testing machine (Instron 1114, USA). Reported values are the average of 3 determinations and errors are the standard deviations.

Notches for toughness testing were done using a Buehler (USA) sawing machine model IsoMet 4000 with diamond disc of 300 μm width to reach notches with tip radius around 100 μm. Specimens with relative notch lengths $\alpha = a/W = 0.25$ and 0.50 (a = notch length, W = specimen width) were prepared and tested in three point bending using spans of 125 mm and 180 mm for the small and large specimens, respectively. All tests were conducted in universal testing machine (model EM1/50/FR, Microtest, Spain) with capability of crack mouth opening displacement (CMOD) recording and controlling. This equipment has been described elsewhere.[37,38] Tests were performed using the CMOD and the displacement of the frame load as control parameters. Rates of 70 μm/min and 0.02 mm/min for CMOD and displacement, respectively, were applied. Three tests were performed for each testing condition; reported values of the toughness parameters are the average of the three determinations and errors are the standard deviations.

3. Results

3.1. Physico-chemical characterisation

Table 1 shows the complete chemical analyses for the studied refractories. As expected, major constituents of both AZS materials (AZS1 and AZS2) are Al_2O_3, SiO_2 and ZrO_2. SiO_2 content is more than double in AZS2 than in AZS1 while Al_2O_3 and ZrO_2 contents are close for both products. Main differences

Table 1
Chemical analysis of the studied materials (wt.%).

wt%	AZS 1	AZS 2	AS	ASI	S	C
Al_2O_3	68.8 ± 0.4	57.7 ± 0.4	44.6 ± 0.3	48.9 ± 0.3	0.71 ± 0.5	74.2 ± 0.4
SiO_2	10.8 ± 0.3	22.8 ± 0.2	48.9 ± 0.4	45.7 ± 0.3	95.2 ± 0.3	13.2 ± 0.2
Fe_2O_3	0.20 ± 0.04	0.16 ± 0.04	3.08 ± 0.03	1.09 ± 0.03	0.22 ± 0.04	0.82 ± 0.03
K_2O	0.038 ± 0.005	–	0.61 ± 0.05	1.32 ± 0.05	0.16 ± 0.06	0.11 ± 0.05
MgO	<0.001	–	0.31 ± 0.05	0.39 ± 0.05	0.17 ± 0.04	0.10 ± 0.04
CaO	0.096 ± 0.006	0.093 ± 0.006	0.48 ± 0.08	0.69 ± 0.08	3.3 ± 0.07	9.36 ± 0.04
TiO_2	0.48 ± 0.01	0.20 ± 0.01	1.67 ± 0.01	1.41 ± 0.01	0.16 ± 0.01	1.89 ± 0.01
P_2O_5	0.050 ± 0.002	–	0.13 ± 0.002	0.19 ± 0.002	0.02 ± 0.004	0.058 ± 0.002
Na_2O	0.19 ± 0.05	0.091 ± 0.02	0.096 ± 0.04	0.20 ± 0.05	<0.08	–
ZrO_2	15.9 ± 0.1	18.0 ± 0.1	0.084 ± 0.04	0.071 ± 0.04	0.036 ± 0.04	0.094 ± 0.04
Y_2O_3	0.25 ± 0.02	0.25 ± 0.02	–	–	–	–
HfO_2	0.36 ± 0.02	0.39 ± 0.02	–	–	–	–
WO_3	–	0.05	–	–	–	–
Loss of ignition	–	0.28 ± 0.03	–	–	–	–

Table 2
Density and porosity values of the studied materials. ρ_b: bulk density; ρ_t: true density; π_t: true porosity; π_a: apparent porosity.

Material	ρ_b (g/cm^3)	ρ_t (g/cm^3)	π_t (vol.%)	π_a (vol.%)
AZS 1	3.11 ± 0.03	3.944 ± 0.002	21.0 ± 0.8	13.8 ± 0.2
AZS 2	2.65 ± 0.03	3.74 ± 0.01	29.1 ± 0.8	19.9 ± 0.4
AS	2.12 ± 0.06	2.85 ± 0.01	26 ± 2	17.7 ± 0.5
ASI	0.9 ± 0.1	2.84 ± 0.01	68 ± 3	66 ± 9
S	1.84 ± 0.01	2.34 ± 0.02	21.3 ± 0.5	15.8 ± 0.1
C	2.67 ± 0.02	2.93 ± 0.01	19.6 ± 0.7	17.3 ± 0.7

in the compositions of the dense fireclay (AS) and the insulating firebrick (ASI) are the higher Al_2O_3 and lower impurity (TiO_2, Fe_2O_3) contents in the latter. The analysis of the silica brick (S) corresponds to a standard one with around 1 wt.% total amount of characteristic impurities (Al_2O_3, TiO_2 and alkalis). The composition of the castable (C) is that of a regular high-alumina one with high cement content (>8 wt.% CaO).

Table 2 summarises porosity and density values. For four of the shaped materials (AZS 1 and 2, AS and S) and the castable (C), porosity values range between 15 and 30% whereas material ASI presents the high porosity characteristic of insulating bricks. Apparent porosity constitutes about 66–74% and 88% of the total porosity for the four conventional bricks and the unshaped material high-alumina castable (C), respectively.

The crystalline phases identified in the materials are summarised in Table 3 along with the ICDD (International Centre for Diffraction Data) files used for identification.[44] The minor phases correspond to impurities that are usually present in the raw materials of these products.

Zircon ($ZrSiO_4$) is one of the major phases in both AZS materials being corundum (α-Al_2O_3) and mullite ($Al_6Si_2O_{13}$) the second phases in AZS1 and AZS2, respectively. A significant amount of baddeleyite (monoclinic zirconia; m-ZrO_2) was also detected in AZS2. The presence of $AlPO_4$ in AZS1 was identified taking into account the chemical analysis (Table 1).

The dense fireclay and the insulating bricks (AS and ASI) are constituted mainly by mullite ($Al_6Si_2O_{13}$) and minor amounts of quartz, corundum and cristobalite. This last silica phase was more abundant in the dense fireclay than in the insulating brick. The diffractogram of $AlPO_4$ overlaps with those of the silica polymorphs so its presence could not be conclusively established only by this technique. But, from the XRF analysis (Table 1), both materials probably had phosphoric additives in their composition.

Table 3
Crystalline phases detected by X-ray diffraction in the studied materials.

	Zircon ($ZrSiO_4$)	Baddeleyite (m-ZrO_2)	Mullite ($Al_6Si_2O_{13}$)	Corundum (α-Al_2O_3)	Quartz (SiO_2)	Tridymite (SiO_2)	Cristobalite (SiO_2)	Fluorite (CaF_2)	$CaAl_2O_4$	Other minors
ICDD file[44]	81-0589	37-1484	15-0776	46-1212	46-1045	71-00261	82-0512	35-0816	70-134	
AZS 1	Major			Major						($AlPO_4$) 11-500
AZS 2	Major	Abundant	Major	Minor						
AS			Major	Minor	Abundant		Major			
ASI			Major	Minor	Abundant		Minor			
S					Minor	Abundant	Major			($pWCaSiO_3$) 74-0874
C			Abundant	Major				Abundant	Abundant	($CaAl_4O_7$) 23-1037

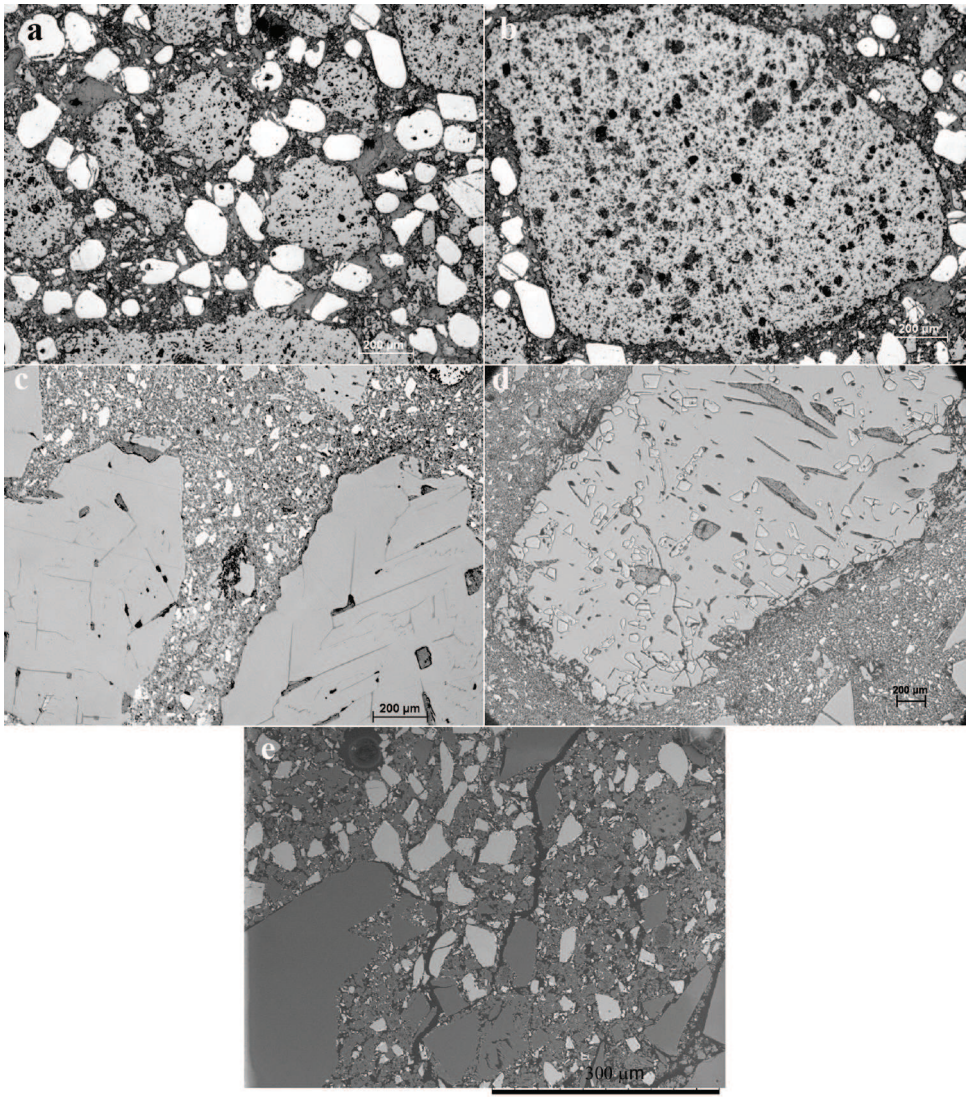

Fig. 2. Characteristic microstructural features of the alumina–silica–zirconia materials. Polished surfaces. (a) AZS1. Porous alumina aggregates (grey), zircon sand (white) and fine alumina (grey) are observed. Reflected light optical microscopy micrograph. (b) AZS1. Detail of a porous aggregate. Reflected light optical microscopy micrograph. (c) AZS2. Electrofused mullite aggregates surrounded by a mullite matrix (grey) with dispersed zircon flour (white). Reflected light optical microscopy micrograph. (d) AZS2. Detail of an electrofused mullite aggregate with alumina particles embedded. Reflected light optical microscopy micrograph. (e) AZS2. Detail of the matrix showing partially decomposed zircon flour (grey particles surrounded by nanometric white zirconia particles). Scanning electron microscopy micrograph.

The silica brick (S) is composed of the silica polymorphs cristobalite and tridymite with minor amount remnant quartz; traces of wollastonite ($CaSiO_3$) are also present in this brick.

The major phase in the conventional high-alumina castable (C) is corundum, followed by mullite. The hydraulic phases of these types of refractories ($CaAl_2O_4$ and $CaAl_4O_7$) were also clearly identified in the XRD pattern. Fluorite (CaF_2) was also detected in this material.

3.2. Microstructure

Condensed information of quantitative data for aggregate size distributions of the five dense materials is presented in Table 4. Maximum aggregate sizes for S, C and AZS2 compositions are similar and the largest (≈5000 μm). Minimum value of this parameter corresponds to the dense fireclay material (AS, ≈4000 μm) while for AZS1 it is intermediate (≈4400 μm). The silica refractory, S, has the widest distribution from 5400 μm down to about 100 μm. Aggregates for the AS material are

Table 4
Parameters of the distributions of aggregate size in the studied materials.

Grain size (μm)	AZS 1	AZS 2	AS	S	C
Average	1709	1591	1227	1736	1393
Standard deviation	597	694	539	923	732
Maximum	4396	5178	3901	5370	5212
Minimum	634	623	457	91	315
No. of particles analysed	643	729	567	563	943

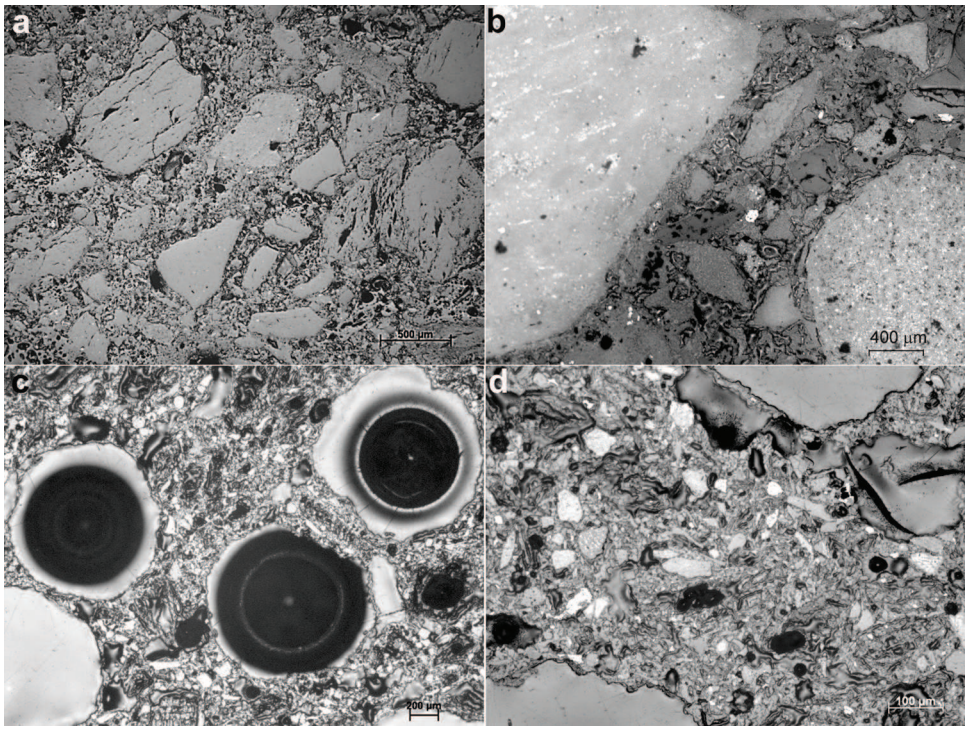

Fig. 3. Characteristic microstructural features of the fireclay-based bricks. Reflected light optical micrographs of polished surfaces. (a) Superduty fireclay brick, AS. Mullite chamote aggregates in a mullite matrix. (b) Detail of the aggregate- matrix interface showing bonding. (c) Group 28 insulating brick, ASI. Spherical pores are observed. (d) Detail of the mullite matrix in figure (c).

smaller than those of the AZS being the distribution centred around 1200 μm.

Micrographs summarising the characteristic microstructural features of the studied refractory materials are shown in Figs. 2–5.

Microstructure of AZS1 is constituted by grey rounded porous aggregates (4400–600 μm, Table 4, Fig. 2a) in a matrix of fine and medium porous grey particles and dense rounded white particles (≈180 μm) (Fig. 2b). Significant porosity is also observed in the matrix. According to the crystalline phases detected by XRD (Table 3) and the morphology and colour of the particles in RLOM, the grey particles were identified as alumina and the dense white particles as zircon sand.

The microstructure of AZS2 (Fig. 2c–e) is dominated by dense grey aggregates (5000–600 μm, Table 4) constituted by columnar grains and significant amounts of glassy phase at the boundaries. Clearer particles are observed in the interior of some of the aggregates. Such features, together with the XRD (Table 3) and chemical analyses (Table 1), allowed identifying these aggregates as electrofused mullite, with corundum and glass as secondary phases. Fine (<50 μm) white angular particles and medium and small grey particles are present in the matrix (Fig. 2d). Taking into account the XRD (Table 3) and the chemical analyses (Table 1) the grey ones could be identified as mullite and the white ones as flour zircon particles. These latter were partially decomposed at the grain boundaries (Fig. 2e) in agreement with m-ZrO_2 being detected by XRD (Table 3).

The dense fireclay material (AS) was formed by coarse and medium dense (down to 200 μm) aggregates bonded by a matrix of similar colour and pores (Fig. 3a and b). According to the XRD (Table 3) and the chemical analyses (Table 1), the aggregates (4000–500 μm, Table 4) present in this material are a mullite chamote with low alumina content (typically wt.% ≈65% mullite, 15% cristobalite, 20% glassy phase). The matrix would have similar composition as that of the aggregates. In this material, a good bonding between the aggregates and the matrix is observed.

No aggregates are present in the insulating brick (ASI) (Fig. 3c and d) and its microstructure is formed by relatively small particles and round pores (diameter ≈ 1200 μm), which, as described before, are the largest microstructural features. Considering the XRD (Table 3) and the chemical analysis (Table 1), the composition of this material is similar to that of the matrix of AS.

Brick S presents the standard microstructure of a silica brick (Fig. 4a and b), made of relatively large (100–5400 μm, Table 4) aggregates with well-defined grain boundaries in RLOM (Fig. 4a). These aggregates with the typical fish-scale substructure are constituted by the smaller cristobalite particles formed during the transformation of quartzite, in agreement with the XRD (Table 3). Two different phases are observed in the porous matrix (Fig. 4b). The clearest one- in which additives, CaO and main impurities were detected by EDS- is a Ca-rich silicate glass in which the conversion of cristobalite into tridymite is favoured.[46] The darker phase in contact with the glass should be the tridymite detected by XRD (Table 3).

Material C (Fig. 5a and b) was constituted by rounded aggregates (5200–300 μm, Table 4) embedded in a matrix with medium sized angular particles. The aggregates presented a

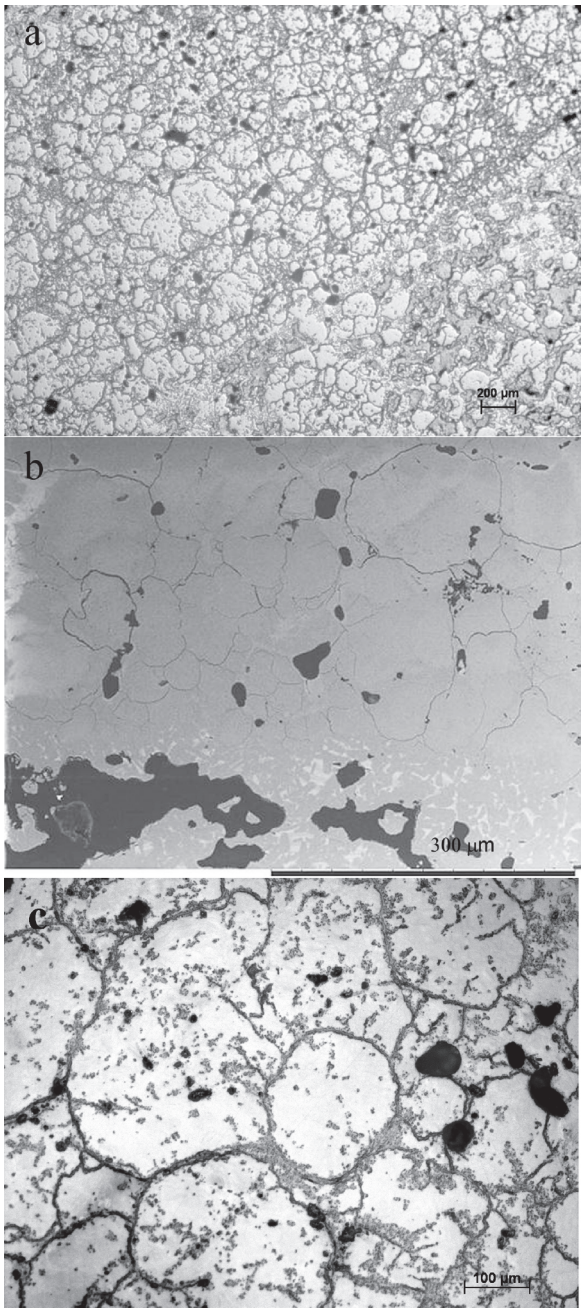

Fig. 4. Characteristic microstructural features of the standard silica brick, S. Polished surfaces. (a) General aspect of the microstructure. Reflected light optical microscopy micrograph. (b) Detail showing the highly transformed silica grains (cristobalite) and the tridymite grains embedded in the CaO-rich glassy phase formed in the matrix of the refractory. Scanning electron microscopy micrograph. (c) Reflected light optical micrograph showing the grain boundary cracking.

substructure formed by two main phases (Fig. 5b) typical of bauxite aggregates, in agreement with the crystalline phases observed by XRD (Table 3). They were formed by corundum, mullite and secondary Fe and Ti containing phases. Medium fraction was constituted of brown corundum. According to the XRD (Table 3), the matrix was constituted by calcium aluminates.

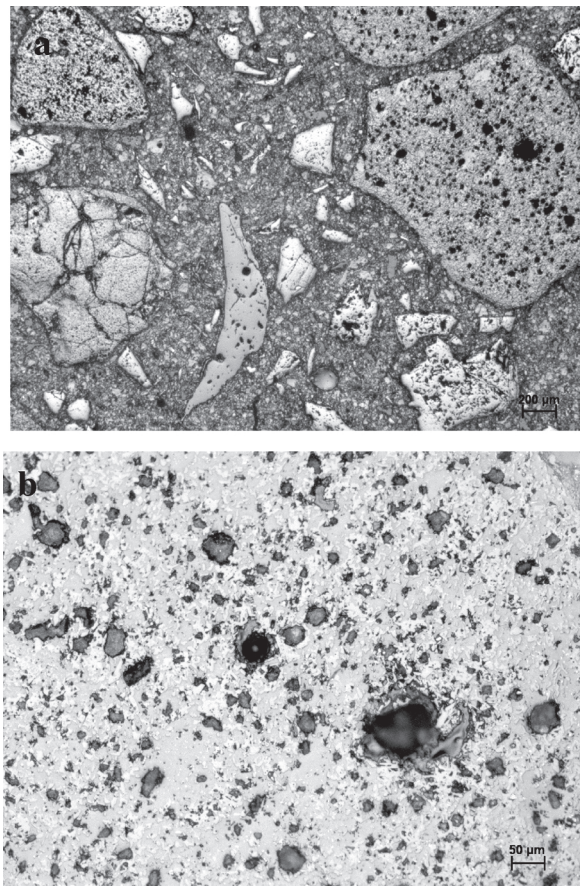

Fig. 5. Characteristic microstructural features of the high-alumina regular castable, C. Polished surfaces. Reflected light optical microscopy micrographs. (a) General aspect of the microstructure. Coarse bauxite aggregates and medium brown corundum particles (angular) are observed. (b) Detail showing the substructure of the bauxite aggregates constituted by mullite (grey) and corundum (white).

3.3. Mechanical characterisation

Young's modulus (E) and modulus of rupture (MOR) values are summarised in Table 5. Both parameters follow the same trend, being the largest for the AZS2 material and the high-alumina castable, C, and the lowest for the insulating material, ASI. Intermediate range of values was obtained for AZS1, AS and S.

Table 5
Young's modulus (E and E_0) and modulus of rupture (MOR) of the studied materials. E tested in flexure by impact. E_0 calculated from the MSA model.[51] MOR determined from 3-pb tests. Main crystalline phases detected by X-ray diffraction are also shown: ZS = zircon, A = corundum, M = mullite, m-Z = baddeleyite, Q = quartz, C = cristobalite, CAC = calcium aluminates.

Material	E (GPa)	E_0 (GPa)	MOR (MPa)	Crystalline phases
AZS 1	29 ± 3	54	9.2 ± 0.6	ZS + A
AZS 2	46 ± 2	110	14 ± 2	M + ZS + m-Z
AS	26 ± 1	57	8.0 ± 0.9	M
ASI	4 ± 1	30	1.0 ± 0.2	M
S	17 ± 1	33	8.2 ± 0.5	Q + C + A
C	50 ± 4	91	13 ± 2	A + CAC + others

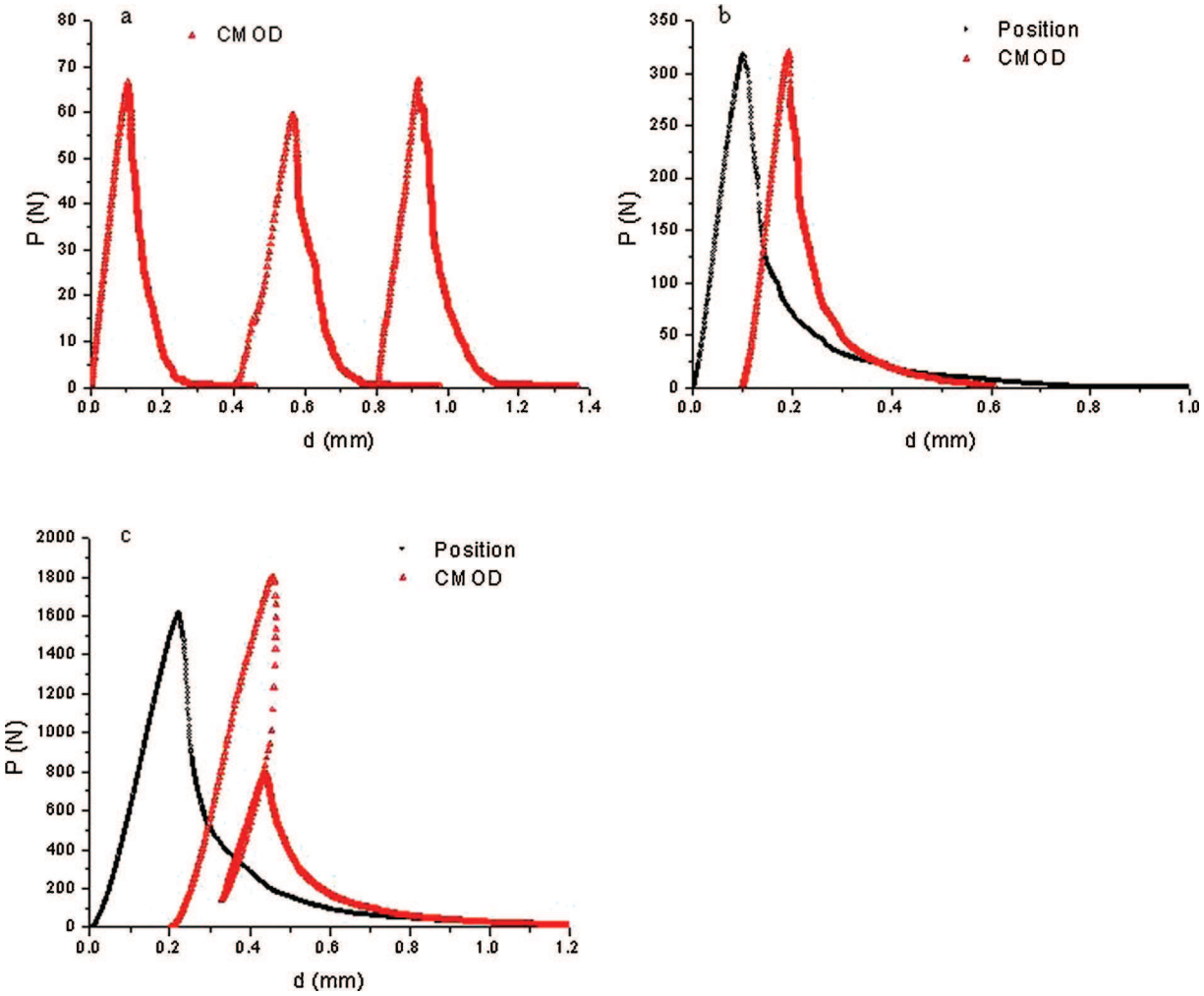

Fig. 6. Characteristic Load (P)–Displacement (d) curves. The dimensions of the beams tested were 150 mm × 25mm × 25 mm for (a) and (b) and 200mm × 40mm × 40 mm for (c). The relative notch lengths were 0.25 for (a) and (c) and 0.50 for (b). (a) Group 28 insulating brick, ASI. For the same material, similar curves were obtained for different tests performed under the same conditions. (b) Alumina–silica–zirconia brick, AZS2. Similar results were obtained for both control parameters. (c) High-alumina regular castable, C. Notice the apparent snap-back for specimens tested using the crack mouth opening displacement as control parameter.

Characteristic Load–Displacement curves recorded during the fracture tests are plotted in Fig. 6 and values for the toughness parameters are summarised in Tables 6 and 7.

A monotonous decrease of load with time was found in all tests indicating that stable fracture was reached both in displacement and in CMOD controlled tests. All Load–Displacement curves showed a linear elastic region followed by a long tail of monotonous decreasing load for increasing displacement from the maximum load. Just before reaching the maximum load, some of the curves showed a moderate non-linear region.

The only case in which it was not possible to reach stability using CMOD control at the experimental rate used in this work was the combination of the largest specimen size and the smallest notch ($\alpha = 0.25$) (Fig. 6c). In this case, an apparent snap-back was observed in the Load–Displacement curves, which would indicate that the material presented brittle fracture. However, fracture in displacement control was stable and, in fact, the obtained curves were coincident with those obtained in CMOD control when the Load–Displacement loop associated with the apparent snap-back present in the latter was relieved.

Load–Displacement curves obtained for the same material and experimental conditions were similar (Fig. 6a) and, consequently, variability of the calculated toughness parameters was relatively low (≈10% in most cases, Tables 6 and 7). For the same material, specimen and span dimensions and relative notch lengths, curves obtained using both control parameters were similar (Fig. 6b).

As shown in Tables 6 and 7, for each material there are no significant differences between the toughness parameters determined using different specimen and span dimensions, relative notch lengths and control parameters. Therefore, the average values obtained for relative notch lengths, $\alpha = 0.5$, in CMOD controlled tests (Table 6) are plotted in Fig. 7 to facilitate comparison. For all materials, values of the energy for crack initiation, γ_{nbt}, are lower than those of the work of fracture, γ_{wof}. The largest value of the toughness ratio corresponds to material AZS1, followed by C.

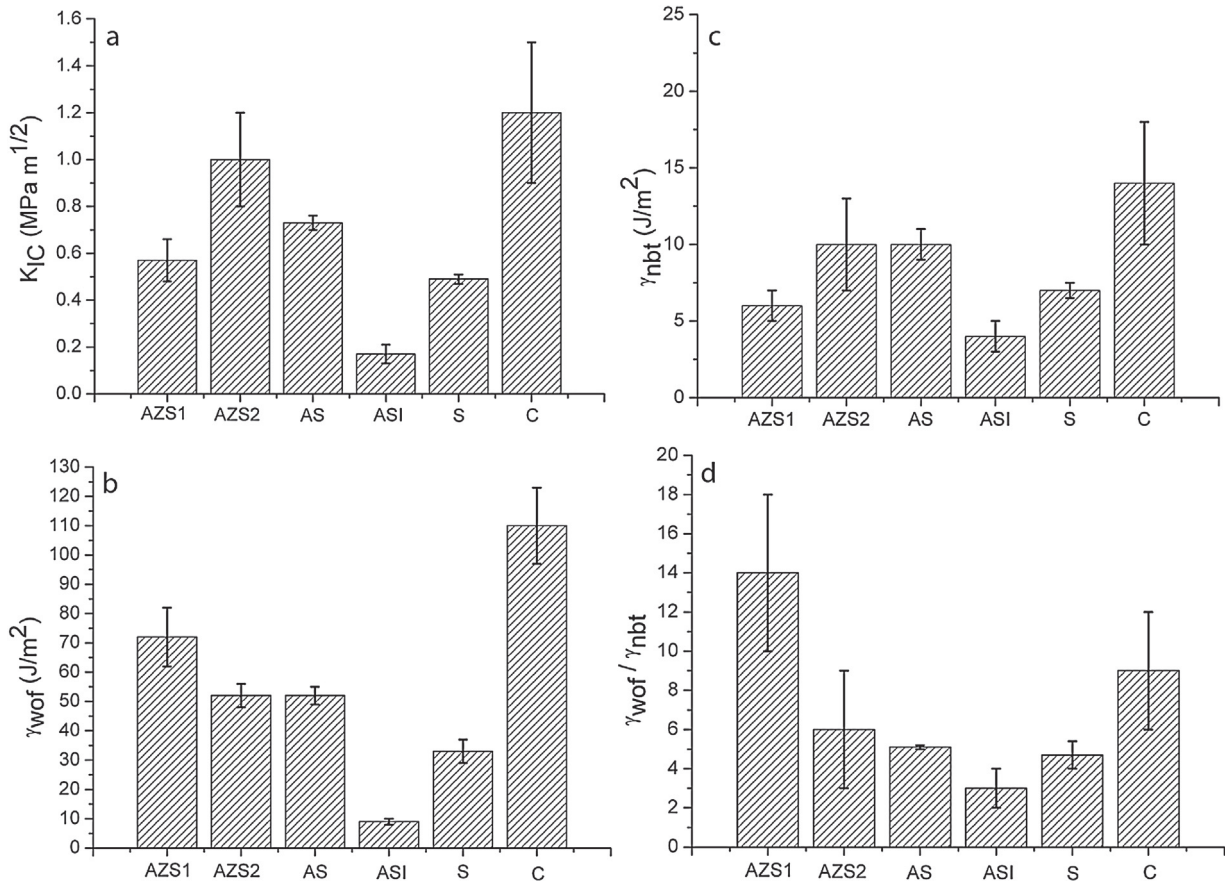

Fig. 7. Average toughness parameters for the studied materials calculated from the values recorded during stable tests ($\alpha = 0.50$, crack mouth opening displacement controlled tests, Table 6). (a) Critical stress intensity factor in mode I, K_{IC}. (b) Work of fracture, γ_{wof}. (c) Energy for crack initiation, γ_{nbt}. (d) Toughness ratio, $\gamma_{wof}/\gamma_{nbt}$.

Materials AZS2 and C present the maximum K_{IC} values (≈1 MPa m$^{1/2}$), followed by AS, AZS1 and S (≈0.5–0.7 MPa m$^{1/2}$); the lowest value corresponds to the insulating firebrick (ASI) (Fig. 7a). The work of fracture does not follow the same trend. The high-alumina castable (C), presents the highest value, followed by AZS1. AZS2 and AS present similar values, which are higher (≈40%) than those of the silica material, S. The lowest value is again found for the insulating brick, ASI (Fig. 7b).

Characteristic fracture surfaces are shown in Fig. 8. Both AZS materials presented tortuous fracture even though the aggregates behaved differently. Most aggregates in AZS1 were traversed by the crack (Fig. 8a) whereas most aggregates of AZS2 were surrounded by the main crack (Fig. 8b). Fracture in the matrix of the dense fireclay and insulating materials (AS and ASI) was rather flat and the main crack traversed the aggregates in the former (Fig. 8c and d). The fracture surface of the silica material (S, Fig. 8e) was the flattest with the main crack traversing all particles. The fracture surface of the high-alumina castable (C, Fig. 8f), presented opposite features, as it was tortuous and most aggregates were surrounded by the main crack.

4. Discussion

4.1. Microstructure

The nature and estimated relative amounts of phases identified by XRD (Table 3) were consistent with the main constituents of the refractories according to their chemical and microstructural analysis (Table 1, Figs. 2–5).

In the AZS refractories appeared the typical zircon impurities, Fe_2O_3 and TiO_2 in the form of ilmenite and rutile, and Y_2O_3 and HfO_2 in solid solution. The presence of significant impurities of $Na_2O + K_2O$ in AZS1 material is attributed to the porous alumina aggregates obtained by Bayer process. Very little alkali content was detected in AZS2 which had electrofused mullite aggregates (Tables 1 and 3, Fig. 2).

Both dense fireclay and insulating materials, AS and ASI, contained significant amounts of the typical impurities for aluminosilicate natural raw materials: iron oxides (assumed as Fe_2O_3 for the chemical analyses), TiO_2, CaO and MgO. The presence of relatively large amounts of K_2O compared to other alkalis suggests that these materials were manufactured with raw materials

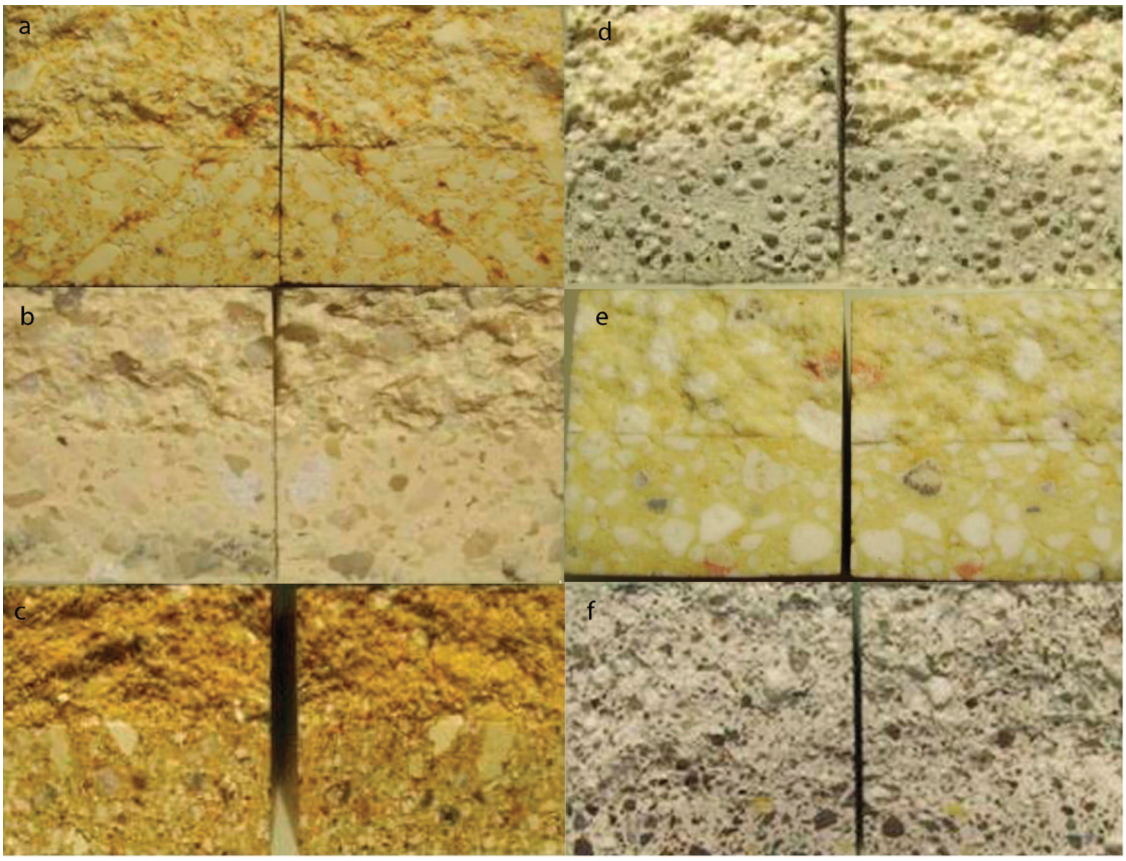

Fig. 8. Characteristic fracture surfaces. Optical images for tested specimens (150mm × 25 mm × 25 mm). (a) Alumina–silica–zirconia brick, AZS1. (b) Alumina–silica–zirconia brick, AZS2. (c) Superduty fireclay brick, AS. (d) Group 28 insulating brick, ASI. (e) Standard silica brick, S. (f) High-alumina regular castable, C.

containing K-feldspar (K,Na,Ca,Ba)(Si,Al)$_4$O$_8$ (Tables 1 and 3, Fig. 3).

Material S was a conventional silica brick (95–97 wt.% SiO_2, 2.5–3.5 wt.% CaO), well converted into cristobalite and tridymite. Wollastonite ($CaSiO_3$) probably comes from the reaction of lime with silica.[46] It should be pointed out that a low content of CaO (typically 2–4 wt.%) may be used as binder in silica bricks without loss of refractoriness (Tables 1 and 3, Fig. 4).

The common impurities of bauxites and brown corundum, iron oxides (Fe_2O_3 in the chemical analyses) and TiO_2, were present in the high-alumina castable, C, due to the nature of the aggregates (Tables 1 and 3, Fig. 5).

The phosphorous (assumed as P_2O_5 for calculations in the chemical analyses) present in most materials is attributed to the use of H_3PO_4 (phosphoric acid), $Al(H_2PO_4)_3$ (aluminium dihydrogen phosphate) or sodium polyphosphate as additives. In fact $AlPO_4$ was identified in AZS1, AS and ASI.

As a first approach for analysing the expected phases in complex materials as a function of temperature, simplified average compositions considering only the three major components can be plotted in ternary phase equilibrium diagrams. Fig. 9 shows simplified average compositions of both AZS materials (AZS1 and AZS2) inside the ternary phase diagram Al_2O_3–ZrO_2–SiO_2.[47] AZS1 lies in the Al_2O_3 primary field of the ternary system while AZS2 is located in the primary mullite field of the ternary system and in the binary system $Al_6Si_2O_{13}$–ZrO_2. Taking into account the average composition of these refractories both should form stable liquid phases at temperatures higher than 1750 °C (close to the temperatures of the ZrO_2–Al_2O_3–$Al_6Si_2O_{13}$ and ZrO_2–$Al_6Si_2O_{13}$ eutectics of the ternary and binary systems). However, temperature for first liquid formation in the matrix would be lower (≈1555 °C) due to the formation of transient liquid phases at the zircon-mullite interfaces (temperature of the $ZrSiO_4$–$Al_6Si_2O_{13}$–SiO_2 eutectic

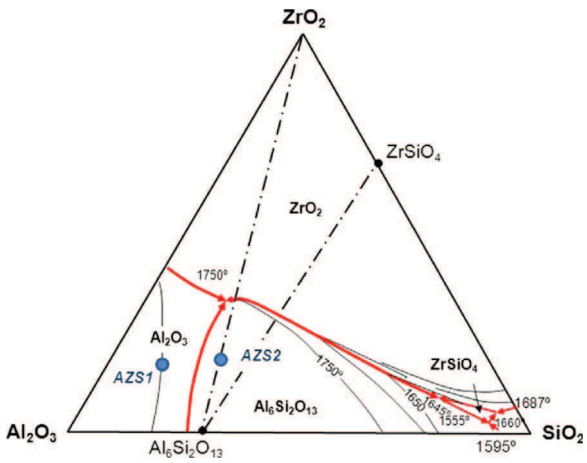

Fig. 9. Phase equilibrium diagram of the system Al_2O_3–ZrO_2–SiO_2.[47]

Table 6
Toughness parameters determined using CMOD controlled tests. K_{IC} is the stress intensity factor in mode I calculated from the maximum load point, in MPa $m^{1/2}$; γ_{nbt} is the energy for crack initiation in J/m^2; γ_{wof} is the work of fracture in J/m^2 and $\gamma_{wof}/\gamma_{nbt}$ is the toughness ratio.

	150 mm × 25 mm × 25 mm								200 mm × 40 mm × 40 mm			
	α = 0.25				α = 0.50				α = 0.25			
	K_{IC}	γ_{nbt}	γ_{wof}	$\gamma_{wof}/\gamma_{nbt}$	K_{IC}	γ_{nbt}	γ_{wof}	$\gamma_{wof}/\gamma_{nbt}$	K_{IC}	γ_{nbt}	γ_{wof}	$\gamma_{wof}/\gamma_{nbt}$
AZS1	0.69 ± 0.05	8 ± 3	76 ± 7	9 ± 2	0.57 ± 0.09	6 ± 1	72 ± 10	14 ± 4				
AZS2	1.0 ± 0.1	10 ± 5	60 ± 7	6.0 ± 0.5	1.0 ± 0.2	10 ± 3	52 ± 4	6 ± 3				
AS	0.74 ± 0.05	10 ± 1	64 ± 8	6.3 ± 0.2	0.73 ± 0.03	10 ± 1	52 ± 3	5.1 ± 0.1	0.80 ± 0.07	12 ± 2	72 ± 7	6.1 ± 0.5
ASI	0.11 ± 0.01	1.4 ± 0.2	8 ± 1	5.7 ± 0.8	0.17 ± 0.04	4 ± 1	9 ± 1	3 ± 1	0.081 ± 0.007	0.8 ± 0.1	50.0 ± 0.6	6.3 ± 0.4
S					0.49 ± 0.02	7 ± 0.5	33 ± 4	4.7 ± 0.7				
C	1.1 ± 0.2	12 ± 4	112 ± 17	9 ± 2	1.2 ± 0.3	14 ± 4	110 ± 13	9 ± 3	1.3 ± 0.14	18 ± 3	130 ± 13	7.3 ± 0.9

Table 7
Toughness parameters determined in displacement controlled tests. K_{IC} is the stress intensity factor in mode I calculated from the maximum load point, in MPa $m^{1/2}$; γ_{nbt} is the energy for crack initiation in J/m^2; γ_{wof} is the work of fracture in J/m^2 and $\gamma_{wof}/\gamma_{nbt}$ is the toughness ratio.

	150 mm × 25 mm × 25 mm								200 mm × 40 mm × 40 mm			
	α = 0.25				α = 0.50				α = 0.25			
	K_{IC}	γ_{nbt}	γ_{wof}	$\gamma_{wof}/\gamma_{nbt}$	K_{IC}	γ_{nbt}	γ_{wof}	$\gamma_{wof}/\gamma_{nbt}$	K_{IC}	γ_{nbt}	γ_{wof}	$\gamma_{wof}/\gamma_{nbt}$
AZS1	0.61 ± 0.03	6 ± 1	75 ± 12	11 ± 1	0.62 ± 0.03	6.5 ± 0.5	75 ± 14	11 ± 1				
AZS2	1.1	12	66	5.24	1.05 ± 0.08	11 ± 2	62 ± 4	5.44 ± 0.87				
AS	0.68 ± 0.05	8 ± 1	65 ± 8	7.52 ± 0.65					0.69 ± 0.04	9 ± 1	69 ± 7	7.7 ± 0.1
ASI												
S	0.72	15	42	2.8	0.53 ± 0.05	7 ± 1	35 ± 2	4.37 ± 0.85				
C	1.3 ± 0.2	16 ± 4	126 ± 18	7.9 ± 0.5					1.2 ± 0.1	13.5 ± 2.5	136 ± 15	10 ± 0.6

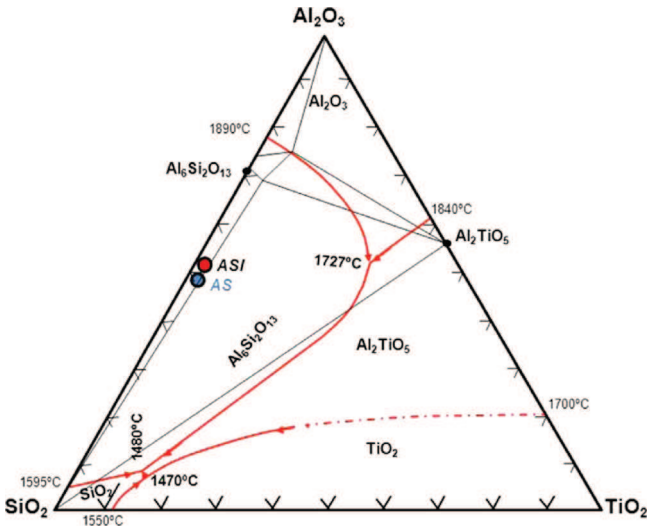

Fig. 10. Phase equilibrium diagram of the system Al_2O_3–SiO_2–TiO_2.[49]

point of the ternary system). The presence of impurities as TiO_2 or iron could lower this temperature (1450 °C for iron,[48] 1450 or 1500 °C for TiO_2).[47]

Considering the chemical (Table 1), the mineralogical analysis (Table 3) and the microstructure (Fig. 2a and b) of AZS1, this material was formulated with aggregates of porous calcined alumina (≈73 wt.%) and the source of ZrO_2 was a pure $ZrSiO_4$ sand (≈27 wt.%). No evidence of reaction between corundum and zircon was observed. The porosity of the brick and the little or no reaction of $ZrSiO_4$ with the finest particles of Al_2O_3 present in the matrix, suggest a temperature of sintering lower than 1450 °C (the lowest invariant point of the Al_2O_3–ZrO_2–SiO_2–TiO_2 system).[47]

AZS2 (Tables 1 and 3, Fig. 2c–e) was fabricated with ≈70 wt.% of electrofused mullite. Electrofusion originates mullite of composition 2:1, in agreement with the presence of some remnant corundum inside the aggregates (Fig. 2d). From the average composition and the microstructure of this material and the composition of the aggregates (mullite + alumina), it can be concluded that the source of ZrO_2 was ≈30 wt.% of angular particles of zircon flour of sizes smaller than 50 μm. The presence of glass at the zircon/alumina interfaces (Fig. 2e) would indicate a sintering temperature higher than 1450 °C[47] (Fig. 9).

The simplified average compositions of the fireclay and the insulating materials (AS and ASI, Table 1) are displayed inside the ternary phase diagram Al_2O_3–SiO_2–TiO_2 in Fig. 10.[49] The compositions of both materials lie in the primary field of mullite in the binary system $Al_6Si_2O_{13}$–SiO_2 (eutectic at 1595 °C) and in the ternary system $Al_6Si_2O_{13}$–SiO_2–Al_2TiO_5 (eutectic at 1480 °C). Therefore, both materials would form liquid phases at temperatures higher than 1480 °C. Taking into account the microstructures and compositions of these materials, both were formulated by mixing a kaolinitic chamote (aggregates) with plastic refractory clay. As the matrix of the fireclay brick had similar composition as that of the chamote aggregates, a good bonding between the aggregates and the matrix was observed.

The porosity of the insulating firebrick (ASI) was due to the addition of pore generators to the fireclay formulation; several processes for pore generation are well reported in the literature.[50] As described above, the average aggregate size in the dense fireclay material (≈1200 μm, Table 4) was comparable to the diameters of the main macrostructural characteristics of the insulating firebrick which are the pores (Fig. 3c).

4.2. Mechanical behaviour

In order to correlate the microstructural characteristics of the refractory materials with the Young's modulus, E, obtained in the present study, values for the fully dense materials, E_0, have been calculated using the exponential equation derived from the minimum solid area models (MSA)[51] using the experimental E values (Table 5) and the true porosities (Table 2).

Calculated E_0 values for all materials (Table 5) are lower than those expected for crystalline bonded zero porosity materials constituted by the major crystalline phases detected ($E_0 \approx 220$, 400, 280, 70–90 GPa for mullite,[52] corundum,[53] zircon[53] and silica polymorphs,[54] respectively). This is a typical characteristic of refractories due to the weak bonding between the large and inert aggregates and the fine matrix, as discussed below.

E_0 for the silica brick is about one half of what could be expected for a mixture of silica polymorphs (≈70–90 GPa).[54] This fact can be explained considering the microstructure of this material, formed by large cristobalite particles surrounded by a transformation zone of tridymite + glass (Fig. 4). The large thermal expansion mismatch between the two crystalline phases ($\alpha \approx 10$ and $21 \times 10^{-6}\,°C^{-1}$ for cristobalite and tridymite, respectively)[54] would lead to grain boundary cracking during cooling from the fabrication temperature. In fact, in the RLOM, the boundaries present the typical dark colour of cracks (Fig. 4c).

No cracks were observed in the AZS2 brick constituted by phases with similar thermal expansion coefficients ($\alpha \approx 4.1$ and $4.5 \times 10^{-6}\,°C^{-1}$, for mullite[52] and zircon,[55] respectively). Even though there is a significant thermal expansion mismatch between the major phases present in AZS1 (zircon and corundum-alumina, $\alpha \approx 4.5$ [55] and $8.4 \times 10^{-6}\,°C^{-1}$ [52]) no cracks were observed in AZS1 specimens (Fig. 2a and b), which can be explained by the low stiffness of the porous aggregates and weakly bonded to the matrix. These two latter characteristics will be responsible for the extremely low E_0 of AZS1 as compared to AZS2, contrary to what could be expected from the major crystalline phases present in the materials (AZS1: corundum + zircon, AZS2: mullite + zircon + baddeleyite).

There are also differences between E_0 for the dense fireclay and the insulating materials, which presented similar chemical composition and crystalline phases, which can be attributed to the presence of stiff aggregates in the dense material. The stiffest constituents have a determining influence on the Young's modulus values obtained from the response of specimens to the small and instantaneous deformations associated with the impact test.[56]

The relative performances of the materials in terms of modulus of rupture (MOR) and Young's modulus (E) were similar (Table 5). This behaviour is characteristic of refractories with aggregate sizes within the typical ranges (3000–6000 μm). Differences in the MOR of such materials are determined by E

because they present only slightly differences in K_{IC}, and the effect of the critical defect size is masked by the dispersion of results associated with the statistical character of strength.

The characteristics of the load–displacement curves with monotonous decrease of the load for increasing displacement during fracture are those corresponding to materials with rising *R*-curve during fracture. This material characteristic allows obtaining stable fracture in displacement control for sufficiently stiff and performing machines, as observed (Fig. 6b and c). Such fracture behaviour is reflected in the fact that values of the energy for crack initiation, γ_{nbt}, are lower than those averaging the whole fracture process, γ_{wof}, as occurs for all the studied materials (Fig. 7b and c), and is highlighted by the toughness ratio values higher than 1 (Fig. 7d).

The creation or not of the fully developed process zone during testing depends on the scale of the microstructural features of the material tested and the experimental set up. The fact that there are no significant differences between the values of the work of fracture obtained using different notch sizes for any material, indicates that, even for the smallest specimens with the largest notches used in this work (specimens of 25 mm × 25 mm section and $\alpha = 0.50$), the fracture area is sufficiently large to generate the steady state of fracture. As discussed in the introduction, rather small specimen sizes relative to the microstructural features have been found adequate for SENB in 3-pb testing heterogeneous materials as asphalt concrete.[34,35]

In order to highlight the influence of the microstructural characteristics on the mechanical parameters summarised in Fig. 7, the six materials have been compared in terms of their mechanical behaviour and their microstructural features, according to the following considerations:

(1) AZS1 and AZS2 were two AZS materials with aggregates with similar size distributions (Table 4) and extremely different physicochemical and microstructural characteristics of the constituents. Aggregates were porous alumina for AZS1 and dense mullite for AZS2. The matrix in AZS1 was formed by fine alumina particles and represented a small part of the total volume of the material in which a significant amount of medium size zircon particles was present (Fig. 2a-b). In AZS2 there was a high amount of matrix composed by mullite, zircon and zirconia particles (Fig. 2c-e). Aggregates were weakly linked to the matrix in AZS1 and strongly bonded to the matrix in AZS2. AZS1 presented K_{IC} and γ_{wof} values similar to those reported for alumina-zircon refractories with similar phase composition[32] ($K_{IC} = 0.62$ MPa m$^{1/2}$ and $\gamma_{wof} = 66$ J/m^2).The fracture path in the materials is determined by the characteristics of the aggregates, the matrix and the matrix-aggregate bonds. In this way, the weak porous aggregates present in AZS1 were easily traversed by the crack whereas the dense ones in AZS2 were surrounded. The dense aggregates with higher strength present in AZS2 impeded the initiation of fracture leading to K_{IC} and γ_{nbt} values for this material higher than those for AZS1. The medium size zircon particles in AZS1 were responsible for crack arrest and deflection during propagation leading to higher values of work of fracture than that of AZS2. As a consequence, the toughness ratio was much higher for AZS1.

(2) AS and ASI had matrices of similar fireclay composition but very different microstructural features of similar sizes. The major microstructural characteristics of these two materials were chamote aggregates firmly bonded to the matrix in AS and pores in ASI (Figs. 3a–d and 7a–d).

AS presented γ_{nbt} and γ_{wof} values similar to the classical ones reported by Nakayama for fireclay refractories[4] ($\gamma_{nbt} = 10.6$ J/m^2, $\gamma_{wof} = 60$ J/m^2), however the γ_{nbt} values for AS were lower than those for mullite-rich laboratory mixes[31] ($\gamma_{nbt} = 18$–25 J/m^2) and lower than those reported for similar compositions with improved matrix due to the addition of medium particles[33] ($\gamma_{nbt} = 44$ J/m^2).

All toughness parameters, K_{IC}, γ_{nbt} and γ_{wof}, of the porous material (ASI) were much lower (15–20%) than those of the dense one (AS), as expected. The pores in ASI act as stress intensity sinks during fracture which leads to an increased fracture energy as compared to that for crack initiation. Therefore, the toughness ratio for this material was about 60% of that of AS.

(3) Composition and microstructure of S and C materials were totally different. S was formed by particles of equal composition whereas C presented a well differentiated cementitious matrix and sintered alumina aggregates. The large differences in the toughness ratios of these materials suggest that the inelastic crack propagation processes of these two refractory types are markedly different,[6] as corresponds to the large differences in the microstructural features. The crack path was straight, traversing all grains, in the single-composition material S and highly tortuous in the high-alumina castable C. In this latter, the aggregates were surrounded by the cracks because they were tougher than the matrix.

In general, work of fracture values for oxide refractories run from about 30 J/m^2 for the most brittle ones to 100–120 J/m^2 for those with well-designed microstructures, as the castable studied here.[1] This material (C) presented γ_{wof} values similar to those reported for a series of high alumina castables (70–90 alumina wt.%, 110–120 J/m^2, [7] 115 J/m^2)[22] with designed microstructures for thermal shock. Those materials included high strength zirconia mullite aggregates which conferred the castables extremely high values and, consequently, lower toughness ratios ($\gamma_{wof}/\gamma_{nbt} \approx 2$–$4$)[7] than the value obtained here for material C.

From the above discussion, it is clear that the characteristics of the aggregates determine the toughness values for fracture initiation, K_{IC} and γ_{nbt} (Fig. 7a and c). For similar crystalline phase composition (Table 3), alumina, the two extreme cases would be that of the castable, with well sintered alumina aggregates (Fig. 5a and b) and material AZS1 (Fig. 2a and b), in which the aggregates presented high levels of porosity. The insulating material, in which the aggregates were substituted by pores, would be the lowest limit for this trend.

Differently than in the case of fracture initiation, the presence of microstructural features capable for crack arrest

and deflection is needed for high resistance to crack propagation, γ_{wof} (Fig. 7b). The microstructure that most clearly demonstrates this fact is that of material AZS1 (Fig. 2a and b), with medium-sized dense particles dispersed in the matrix and the highest toughness ratio (Fig. 7d). Materials AS and S are examples of the opposite trend. These materials, with homogeneous composition through the microstructure and well bonded microstructural constituents presented the lowest toughness ratios of the dense materials.

The effectiveness of the microstructural elements for toughening is determined, not only by their nature, but also by the characteristics of their bonding to the matrix. Material C is the typical case of strong aggregates weakly bonded to the matrix and presents the highest γ_{wof} of all studied materials (Fig. 7b).

5. Conclusions

The capability of stable fracture tests of SENB tested in 3 point bending to characterise toughness of refractories has been demonstrated. When carefully performed using the high stiffness and performing machines nowadays available it is possible to establish displacement controlled tests as routine laboratory tests for stable fracture. For the typical microstructural characteristics of commercial refractories studied here, standard size specimens (150 mm × 25 mm × 25 mm) tested with span 125 mm and relative notch length ($\alpha = 0.5$) give differentiated toughness values for different microstructures.

The main microstructural features that influence the resistance of materials to initiation of fracture are different from those that regulate crack propagation. The characteristics of the aggregates determine toughness for crack initiation while, for high values of work of fracture the presence of microstructural features capable for crack arresting and deflection are needed.

Acknowledgements

The authors acknowledge the financial support of CYTED through the network ref. 312RT0453 and project MAT2013-48426-C2-1R; and the supplying of materials by INSERTEC S.A. (Spain). Ana García-Prieto acknowledges the financial support of the JAE-CSIC fellowship program JAEPre_2010_00274.

References

1. Bradt RC. Fracture of refractories. In: Schacht CA, editor. *Refractories handbook*. New York: Marcel Dekker Inc; 2004. p. 11–38.
2. Hasselman DPH. Figures-of-merit for the thermal stress resistance of high-temperature brittle materials: a review. *Ceram Int* 1978;**4**(4):147–50.
3. Hasselman DPH. Thermal stress resistance of engineering ceramics. *Mater Sci Eng* 1985;**71**:251–64.
4. Nakayama J, Abe H, Bradt RC. Crack stability in the work-of-fracture test: refractory applications. *J Am Ceram Soc* 1981;**64**(11):671–5.
5. Harmuth H, Rieder K, Krobath M, Tschegg E. Investigation of the nonlinear fracture behaviour of ordinary ceramic refractory materials. *Mater Sci Eng A* 1996;**214**:53–61.
6. Homeny J, Darroudi T, Bradt RC. J-Integral measurements of the fracture of 50% alumina refractories. *J Am Ceram Soc* 1980;**63**(5–6):326–31.
7. Salvini VR, Pandolfelli VC, Bradt RC. Extension of Hasselman's thermal shock theory for crack/microstructure interactions in refractories. *Ceram Int* 2012;**38**(7):5369–75.
8. Harmuth H, Tscheg EK. A fracture mechanics approach for the development of refractory materials with reduced brittleness. *Fatig Fract Eng Mater Struct* 1997;**20**(11):1585–603.
9. Harmuth H, Bradt RC. Investigation of refractory brittleness by fracture mechanical and fractographic methods. *Refract Man* 2010:6–10.
10. Palmer GB, Baker G. A load-cycling technique for *R*-curve behaviour: application to a low cement refractory. *Int J Fract* 1993;**62**(3):233–44.
11. Bueno S, Baudín C. Mechanical behaviour of structural ceramics. *Bol Soc Esp Ceram V* 2007;**46**(3):103–18.
12. Sakai M, Urashima K, Inagaki M. Energy principle of elastic-plastic fracture and its application to the fracture mechanics of a polycrystalline graphite. *J Am Ceram Soc* 1983;**66**(12):868–74.
13. Nakayama J. Direct measurement of fracture energies of brittle heterogeneous materials. *J Am Ceram Soc* 1965;**48**(11):583–7.
14. Tattersall HG, Tappin G. The work of fracture and its measurement in metals, ceramics and other materials. *J Mater Sci* 1966;**1**(3):296–301.
15. Davidge RW, Tappin G. The effective surface energy of brittle materials. *J Mater Sci* 1968;**3**(2):165–73.
16. Larson DR, Coppola JA, Hasselman DPH, Bradt RC. Fracture toughness and spalling behavior of high-Al_2O_3 refractories. *J Am Ceram Soc* 1974;**57**(10):417–21.
17. Chlup Z, Boccaccini DN, Leonelli C, Romagnoli M, Boccaccini AR. Fracture behaviour of refractory ceramics after cyclic thermal shock. *Ceram-Silikaty* 2006;**50**(4):245–50.
18. Ko YC. Influence of the total fines content on the thermal shock damage resistance of Al_2O_3-spinel castables. *Ceram Int* 2001;**27**(5):501–7.
19. Tschegg EK, Austria Patent Specification AT 390,328 (1986).
20. Brühwiler E, Wittmann FH. The wedge splitting test, a new method of performing stable fracture mechanics tests. *Eng Fract Mec* 1990;**35**(1/2/3):117–25.
21. Harmuth H. Stability of crack propagation associated with fracture energy determined by wedge splitting specimen. *Theor Appl Fract Mec* 1995;**23**(1):103–8.
22. Ribeiro S, Rodrigues JA. The influence of microstructure on the maximum load and fracture energy of refractory castables. *Ceram Int* 2010;**36**:263–74.
23. Ribeiro S, Ribeiro DC, Souza Dias MB, Ribeiro Garcia GC, Bento dos Santos EM. Study of the fracture behavior of mortar and concretes with crushed rock or pebble aggregates. *J Mater Res* 2011;**14**(1):46–52.
24. Harmuth H, Manhart C. Fractographic investigations of ordinary ceramic refractory materials with reduced brittleness. *Key Eng Mater* 2009;**409**:209–15.
25. Huilin L, Guifang D. Application of wedge splitting test in refractories. *China's Refract* 2006;**15**(2):27–30.
26. Brochen E, Dannert C. Thermo-mechanical characterisation of magnesia-carbon refractories by means of wedge splitting test under controlled atmosphere at high-temperature. In: *Proceedings of 13th biennial worldwide conference on refractories, UNITECR 2013*. 2013.
27. Jin S, Gruber D, Harmuth H. Determination of Young's modulus, fracture energy and tensile strength of refractories by inverse estimation of a wedge splitting procedure. *Eng Frac Mec* 2014;**116**:228–36.
28. Skiera E, Malzbender J, Mönch J, Dudczig S, Aneziris CG, Steinbrech RW. Controlled crack propagation experiments with a novel alumina-based refractory. *Adv Eng Mater* 2012;**14**(4):248–54.
29. Miyaji DY, Otofuji CZ, de Anchieta Rodrigues J. The load–displacement curve of steady crack propagation: an interesting source of information for predicting the thermal shock damage of refractories. In: *Proceedings of 13th biennial worldwide conference on refractories, UNITECR 2013*. 2013.
30. Malzbender J, Skiera E, Mönch J. A simple methodology to visualize crack propagation for ceramic materials. *J Mater Sci* 2014;**49**:403–6.
31. Aksel C. The effect of mullite on the mechanical properties and thermal shock behaviour of alumina–mullite refractory materials. *Ceram Int* 2003;**29**:183–8.
32. Rendtorff NM, Aglietti E. Mechanical and thermal shock behavior of refractory materials for glass feeders. *Mater Sci Eng A* 2010;**527**:3840–7.

33. Aksel C. The role of fine alumina and mullite particles on the thermomechanical behaviour of alumina–mullite refractory materials. *Mater Lett* 2002;**57**:708–14.
34. Romero P, Masad E. Relationship between the representative volume element and mechanical properties of asphalt concrete. *ASCE J Mater Civ Eng* 2001;**13**:77–84.
35. Wagoner MP, Buttlar WG, Paulino GH. Development of a single-edge notched beam test for asphalt concrete mixtures. *J Test Eval* 2005;**33**:1–9.
36. Peret CM, Rodrigues JA. Stability of crack propagation during bending tests on brittle materials. *Cerâmica* 2008;**54**:382–7.
37. García-Prieto A, Baudín C. Crack mouth opening displacement controlled fracture tests of brittle ceramics. *J Eur Ceram Soc* 2010;**30**:3297–302.
38. García-Prieto A, Hernández J, López M, Baudín C. Controlled fracture test for brittle ceramics. *J Strain Anal Eng* 2011;**46**(1):27–32.
39. García-Prieto A, Baudín C. Influence of experimental variables on fracture toughness determined on SEVNB in three points bending. Mullite a case study. *J Eur Ceram Soc* 2012;**32**(16):4241–8.
40. Guinea GV, Pastor JY, Planas J, Elices M. Stress intensity factor, compliance and CMOD for a general three-point-bend beam. *Int J Fract* 1998;**89**:103–16.
41. Irwin GR. Fracture. In: *Encyclopedia of physics*. Berlin: Springer Verlag; 1958. p. 551–69.
42. EN 993-1. *Methods of test for dense shaped refractory products. Part 1: Determination of bulk density, apparent porosity and true density*; 1995.
43. EN 993-2. *Methods of test for dense shaped refractory products. Part 2: Determination of true porosity*; 1995.
44. *International Centre for Diffraction Data (ICDD)*. Newton Square, USA: Powder Diffraction File Database; 1998.
45. EN 993-6. *Methods of test for dense shaped refractory products. Part 6: Determination of modulus of rupture at ambient temperature*; 1995.
46. Lee WE, Rainforth WM. Ceramic microstructures property control by processing. In: *Refractories*. London: Chapman & Hall; 1994. p. 452–507.
47. Pena P, De Aza S. The zircon thermal behaviour: effect of impurities. Part 1. *J Mat Sci* 1984;**19**:135–42.
48. Jones TS, Kimura S, Muan A. Phase relations in the system $FeO–Fe_2O_3–ZrO_2–SiO_2$. *J Am Ceram Soc* 1967;**50**(3):137–42.
49. Agamawi YM, White J. System $Al_2O_3–SiO_2–TiO_2$; high silica region. *Trans Br Ceram Soc* 1952;**51**(5):293–325.
50. Carniglia SC, Barna GL. Principles, types, properties and applications. In: *Handbook of industrial refractories technology*. Noyes Publications; 1992. p. 316–7.
51. Rice RW. *Porosity of ceramics*. Marcel Dekker, Inc; 1998. p. 102.
52. Burgos-Montes O, Moreno R, Baudín C. Effect of mullite additions on the fracture mode of alumina. *J Eur Ceram Soc* 2010;**30**:857–63.
53. Montel JM, Giot R. Fracturing around radioactive minerals: elastic model and applications. *Phys Chem Miner* 2013;**40**:635–45.
54. Pabst W, Gregorová E. Elastic properties of silica polymorphs – a review. *Ceram-Silikáty* 2013;**57**(3):167–84.
55. Bayer G. Thermal expansion of ABO-compounds with zircon – and scheelite structures. *J Less-Common Metals J* 1972;**26**:255–62.
56. Lawn BR. *Fracture of brittle solids*. Cambridge: Cambridge University Press; 1993.

Capítulo 7

TENACIDAD DE FRACTURA DE NANOCOMPUESTOS DE Al_2O_3/SiC

7. TENACIDAD DE FRACTURA DE NANOCOMPUESTOS DE Al_2O_3/SiC

Una vez demostrada la validez del dispositivo experimental, la metodología de ensayo y análisis de resultados para la determinación precisa de la tenacidad de fractura de materiales cerámicos frágiles (capítulos 3-5) y de materiales en los que tienen lugar mecanismos de refuerzo (capítulo 6), se procedió a su aplicación para la caracterización de materiales cerámicos avanzados de alto interés tecnológico como son los nanocompuestos de Al_2O_3/SiC. Como se mencionó en el capítulo 1, apartado 1.8, son uno de los sistemas más estudiados, pero, sin embargo, no se han reportado valores de tenacidad de fractura concluyentes puesto que la mayoría de los valores se han determinado a partir de ensayos inestables o semiestables mediante técnicas de indentación (IT).

Con objeto de comparar los valores obtenidos en este trabajo con los reportados por diferentes autores, se calculó $K_{IC\gamma}$, a partir de la ecuación 7.1:

$$K_{IC\gamma} = \left[\frac{2E\gamma}{1-\nu^2}\right]^{1/2} \tag{7.1}$$

donde E es el módulo de Young, γ es la energía de fractura, ν es el coeficiente de Poisson.

El procesamiento de estos materiales se llevo a cabo durante una estancia de seis meses otorgada por la beca JAE_Pre_2010_00274 en el laboratorio del Departamento de Materiales de la Universidad de Oxford, bajo la dirección del Prof. Dr. Richard I. Todd.

En la actualidad se está elaborando una publicación conjunta con la Universidad de Oxford.

7.1. Condiciones experimentales

Los nanocompuestos de Al_2O_3/SiC fueron obtenidos a partir de polvos comerciales de α-alúmina y α-SiC mediante molienda de bolas en medio acuoso seguido de una liofilización y una calcinación a 400ºC. Los polvos resultantes se prensaron en caliente a 1650ºC durante 30 minutos en atmósfera de argon a 25 MPa. Se obtuvieron materiales con un porcentaje de SiC de 2, 5 y 10 % en volumen. Las características microestructurales de los mismos aparecen reflejadas en la tabla 7.1 donde además se han añadido los valores pertenecientes a la alúmina caracterizada en el capítulo 4. El tamaño de grano de esta alúmina es similar al de la matriz de estos nanocompuestos.

Tabla 7.1. Características microestructurales y propiedades mecánicas de los nanocompuestos de Al_2O_3/SiC caracterizados en este trabajo y de la alúmina de referencia (capítulo 4).

	T.D.(S.D.) (%)	E (S.D.) (GPa)	σ_f (S.D.) (MPa)	σ_0 (MPa)	m
Al_2O_3	98.1 (0.3)	387 (3)	456 (29)	-	-
Al_2O_3/2vol.% SiC	99.7 (0.3)	401(5)	561.2 (35.8)	577.2	18.3
Al_2O_3/5vol.% SiC	99.0 (0.3)	395 (4)	531.6 (63.9)	558.5	9.8
Al_2O_3/10vol.% SiC	98.8 (0.3)	390 (3)	522.6 (52.2)	545.2	11.9

T.D.: Densidad teórica (%); E: Módulo de Young (GPa); σ_f: Tensión de rotura (MPa); σ_0: Tensión característica (MPa); m: Parámetro de Weibull. (S.D.): Desviación estándar.

Para la determinación de la tenacidad de fractura se utilizó la geometría de ensayo de cerámicas técnicas avanzadas (apartado 3.2.1). Las características de las entallas fueron α=0.5 y ρ<10 μm. Una vez mecanizadas las entallas, las probetas fueron sumergidas en aceite de silicona para evitar así el crecimiento subcrítico de grietas por efecto de la humedad del ambiente.

Se realizaron ensayos a velocidades constantes de apertura de los labios de la grieta (CMOD) de 1.8 μm/min.

7.2. Resultados y disusión

En la figura 7.1 se muestran las curvas experimentales características carga-tiempo de los ensayos realizados utilizando el CMOD como variable de control. Se aprecia cómo, una vez alcanzado el punto de carga máxima, ocurre una disminución monótona de la carga con el tiempo conforme la grieta va creciendo. Como ya se ha discutido, este tipo de comportamiento es característico de ensayos de fractura estable.

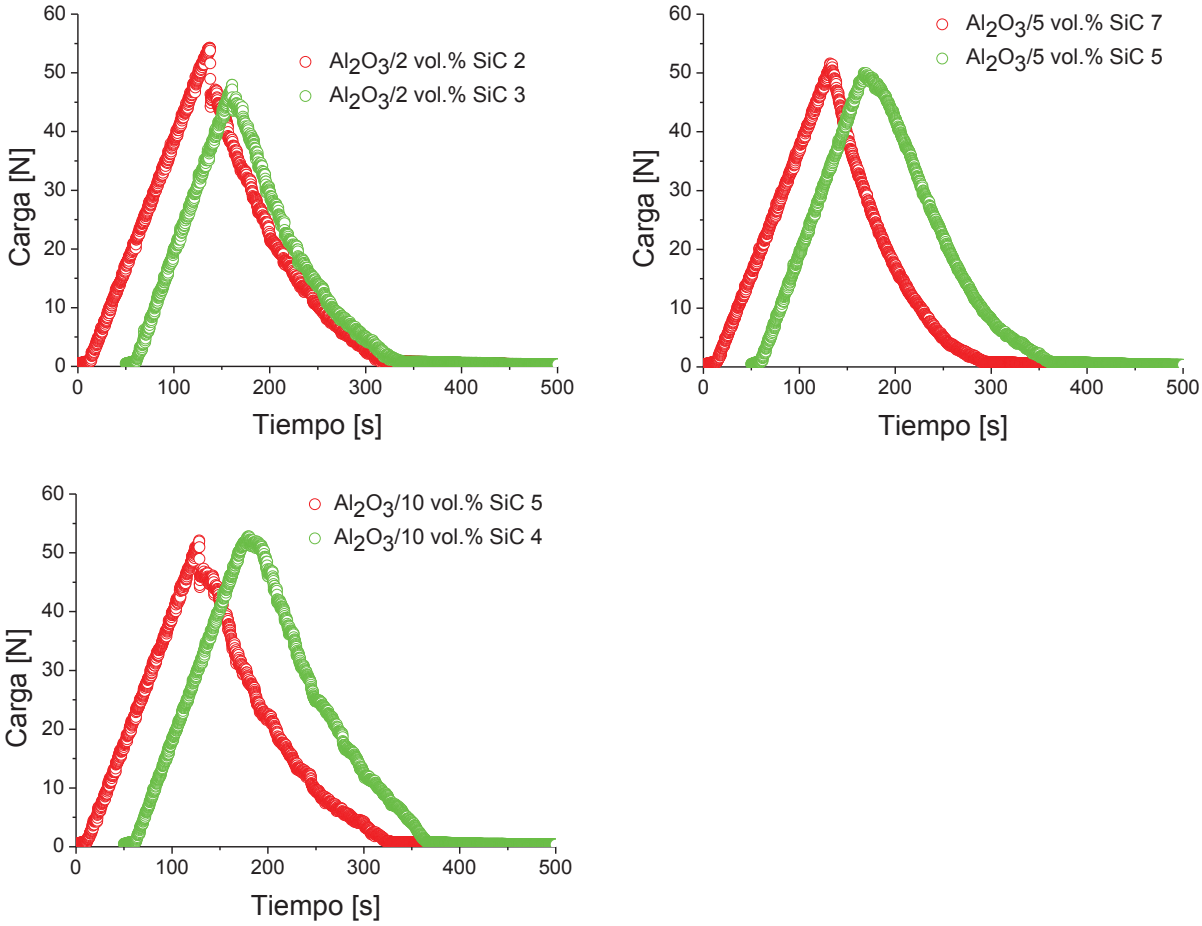

Figura 7.1. Curvas experimentales características carga-tiempo para las probetas de los nanocompuestos de Al_2O_3/SiC:
(a) Al_2O_3/ 2 vol.%SiC
(b) Al_2O_3/ 5 vol.%SiC
(c) Al_2O_3/ 10 vol.%SiC

La figura 7.2 representa las curvas experimentales características carga-desplazamiento de los materiales nanocompuestos. Se observa cómo, a partir del valor

de carga máxima, tiene lugar una disminución del desplazamiento (régimen I) seguida de un aumento del desplazamiento (régimen II). Este tipo de comportamiento es característico de fractura estable de materiales frágiles.

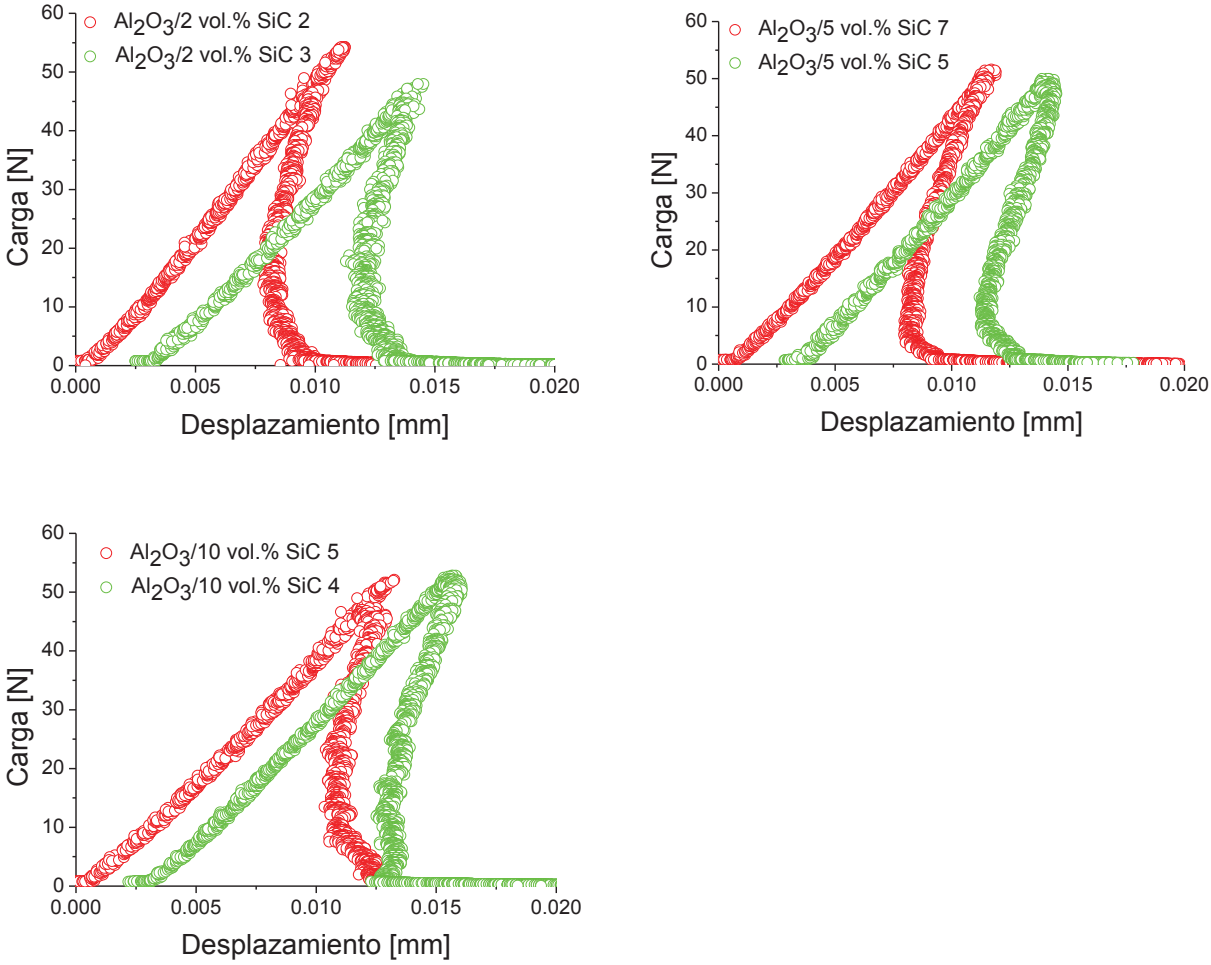

Figura 7.2. Curvas experimentales características carga-desplazamiento para las probetas de los nanocompuestos de Al_2O_3/SiC:
(a) Al_2O_3/ 2 vol.%SiC
(b) Al_2O_3/ 5 vol.%SiC
(c) Al_2O_3/ 10 vol.%SiC

En las figuras 7.1 y 7.2 se observan curvas similares para probetas diferentes.

En la figura 7.3 se comparan los valores de K_{IC} obtenidos en este trabajo mediante ensayos de fractura estable de probetas SEVNB con los valores reportados por diferentes autores utilizando métodos experimentales diferentes a IT (apartado 1.8, tabla 1.5). Se observa cómo los valores de K_{IC} son superiores y presentan mayor variabilidad

para ensayos inestables de probetas SENB con grandes radios de curvatura[181] que para los ensayos estables de probetas SEVNB realizados en este trabajo.

Con objeto de comparar los valores de la tenacidad asociados al proceso de fractura, se ha definido $K_{IC\gamma}$ como el calculado a partir de los valores de G_F (=2γ) utilizando la ecuación 7.1.

Los valores de $K_{IC\gamma}$ determinados a partir de ensayos de probetas SEVNB, en ausencia de aceite de silicona, coinciden con los obtenidos para probetas CT[277]. Demostrando la existencia de SCG durante la fractura de estos materiales en aire. Por lo tanto, es preciso analizar los resultados de ensayos en aceite de silicona. Los valores de $K_{IC\gamma}$ son inferiores a los de K_{IC}, hecho no explicable en ausencia de fatiga estática.

Para explicar este hecho es preciso considerar el efecto de las entallas utilizadas en estos materiales, que presentan fractura transgranular, como se discute a continuación.

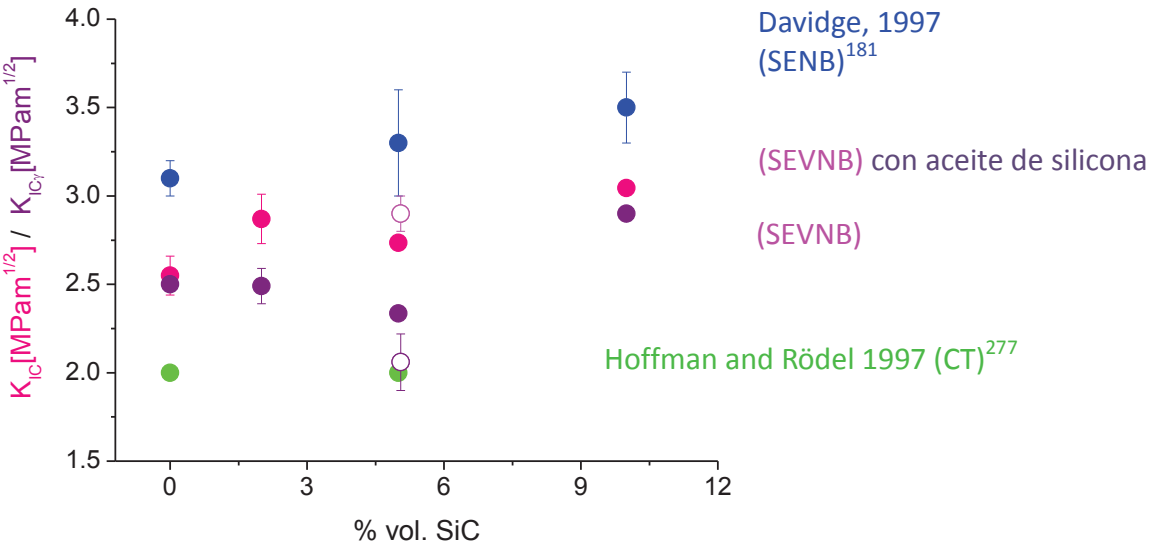

Figura 7.3. Representación de los valores de tenacidad correspondientes al inicio de fractura, K_{IC}, y a todo el proceso de fractura, $K_{IC\gamma}$, para las probetas SEVNB de nanocompuestos de Al_2O_3/SiC caracterizados en este trabajo. Asimismo, se recogen datos correspondientes a ensayos SENB[181] y CT[277] (tabla 1.5).

En el round robin de SEVNB[58] (apartado 1.3.2) se estudiaron cerámicas técnicas como Si_3N_4 y Al_2O_3, con un tamaño de grano superior a 2 μm. Para estos materiales se observó fractura intergranular y que los bordes de grano actuaban como fisuras, este comportamiento se asemeja al modelo de Fett[56] donde el radio del fondo de entalla era tan pequeño que se podía atribuir el inicio de la fractura a una fisura en la punta de la entalla (apartado 1.3.2) y es muy diferente al comportamiento observado para los nanocompuestos de Al_2O_3/SiC caracterizados en este trabajo.

En los nanocompuestos se produjo una fractura transgranular desde la punta de la entalla, donde no hay fisuras (figura 1.4), por lo que el inicio de la fractura a partir de la entalla en estos materiales no es comparable con el modelo de Fett[56] (apartado 1.3.2). En cambio para la alúmina de referencia el modo de fractura fue mixto inter-transgranular donde los bordes de grano sí actuarían como fisuras (figura 7.5).

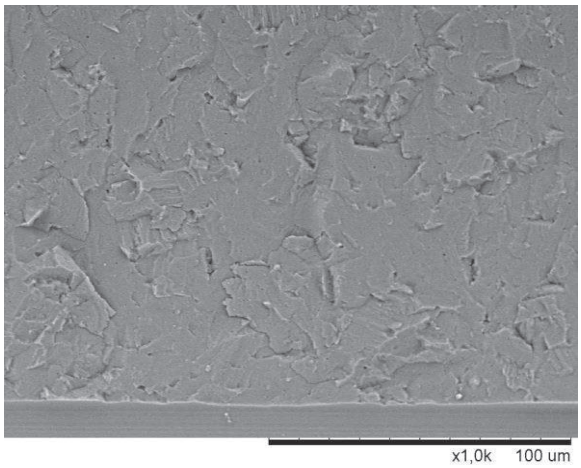

Figura 7.4. Fractura transgranular característica de los nanocompuestos de Al_2O_3/SiC. Esta micrografía corresponde a una microscopía electrónica de barrido de Al_2O_3/10 vol.%SiC.

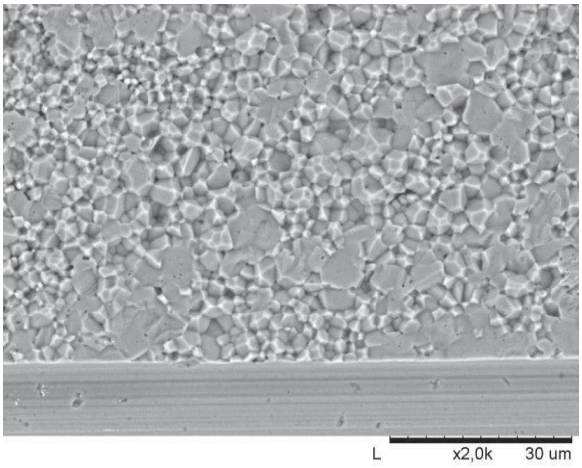

Figura 7.5. Fractura mixta inter-transgranular característica de la alúmina. Microscopía electrónica de barrido.

7.3. Conclusiones

- Se han ensayado materiales homogéneos nanocompuestos de Al_2O_3/SiC en ausencia de fatiga estática.

- Se ha alcanzado fractura estable en ensayos de flexión en tres puntos de probetas SEVNB de nanocompuestos de Al_2O_3/SiC.

- En los nanocompuestos el modo de fractura es transgranular, existiendo un efecto de la influencia del radio de curvatura del fondo de entalla en la iniciación de la fractura, incluso para probetas SEVNB.

- Por lo tanto, para la determinación precisa de la tenacidad es necesario el cálculo de la tenacidad a partir de todo el proceso de fractura ($K_{IC\gamma}$), siendo pues necesaria la realización de ensayos de fractura estable.

- Se ha detectado una dependencia no monótona de la tenacidad con el contenido en nanopartículas, mínima para Al_2O_3/5vol.%SiC.

ANEXO V

Este trabajo ha sido presentado en los siguientes congresos como conferencia invitada:

- A. García-Prieto, T. Rodriguez-Suarez, R. I. Todd and C. Baudín. "Toughness of nanocomposites". XIII Conference of the European Ceramic Society. Limoges, Francia, 23-27 Junio 2013.

- A. García-Prieto, T. Rodriguez-Suarez, R. I. Todd y C. Baudín. "Comportamiento mecánico de nanocomposites cerámicos". VII Congreso Internacional de Materiales. 29 Octubre-1 Noviembre 2013, Medellín, Colombia.

- A. García-Prieto, C. Baudín. "Toughness of Al_2O_3/SiC Nanocomposites". Conference for Young Scientists - The Tenth Students' Meeting. November 6-9, 2013. Novi Sad, Serbia.

Y aparece publicado en los libros colectivos Anales de Mecánica de la Fractura de 2013, que recogen los artículos que corresponden a las comunicaciones al XXX Encuentro del Grupo Español de Fractura:

- A. García-Prieto, T. Rodríguez-Suarez, R.I. Todd, C. Baudín. "Stable fracture testing for toughness characterization of Al_2O_3/SiC nanocomposites". Anales de Mecánica de la Fractura, 30, Vol.3, pp. 590-596. Ed. Secretaría del Grupo Español de Fractura, Madrid, España, 2013.

Capítulo 8

CONCLUSIONES GENERALES

8. CONCLUSIONES GENERALES

Durante el desarrollo de este trabajo se ha llegado a las siguientes conclusiones generales que surgen de las conclusiones parciales presentadas en los capítulos 3-7:

- Se han desarrollado un nuevo dispositivo experimental y una metodología de ensayo y análisis de resultados que permiten caracterizar la tenacidad de una amplia gama de materiales cerámicos, utilizando la apertura de los labios de la grieta (CMOD) como parámetro de control.
- Se ha demostrado la posibilidad de alcanzar ensayos de fractura estable de flexión en tres puntos de probetas prismáticas de materiales cerámicos con entallas rectas en forma de V (SEVNB).
- Se ha demostrado la necesidad de los ensayos de fractura estable para la determinación de los parámetros de tenacidad de los siguientes materiales cerámicos:

  - Espinela de aluminio-magnesio ($MgAl_2O_4$) y alúmina (Al_2O_3) de grano fino, cuyo comportamiento en fractura es frágil (capítulos 3 y 4).

  - Mullita ($3Al_2O_3{\cdot}2SiO_2$), con comportamiento frágil y en la que tiene lugar crecimiento subcrítico de grietas en aire significativo (capítulo 5).

  - Refractarios comerciales, en los cuales ocurren mecanismos de refuerzo (capítulo 6).

  - Nanocompuestos de Al_2O_3/SiC (capítulo 7), que se consideran como modelo de los nuevos nanocompuestos cerámicos.

- La utilización de la apertura de los labios de la grieta (CMOD) como parámetro de control es necesaria para alcanzar ensayos estables en los materiales frágiles de espinela de aluminio-magnesio, alúmina de grano fino, mullita con SCG significativo en aire y nanocompuestos de Al_2O_3/SiC (capítulos 3, 4, 5 y 7). Para

los materiales refractarios comerciales, en los que ocurren mecanismos de refuerzo (capítulo 6), se han alcanzado ensayos estables utilizando el desplazamiento del marco de carga como parámetro de control.

- En la tabla 8.1. se muestran los parámetros intrínsecos de la tenacidad (K_{IC}, G_{IC}, $G_F=2\gamma$) determinados, por primera vez, en este trabajo para los materiales cerámicos avanzados caracterizados.

Tabla 8.1. Parámetros de tenacidad de fractura de los materiales cerámicos avanzados.

Material	K_{IC} (S.D.) (MPa $m^{1/2}$)	G_{IC} (S.D.) (J/m^2)	G_F (S.D.) (J/m^2)
$MgAl_2O_4$	1.04 (0.06)	3.94 (0.01)	-
Al_2O_3	2.5 (0.2)	16.4 (2.3)	14.0 (0.6)
$3\,Al_2O_3{\cdot}2SiO_2$	0.86 (0.06)	3.5 (0.5)	3.8 (0.2)
Al_2O_3/2vol.%SiC	2.87 (0.14)	20 (1)	15 (1)
Al_2O_3/5vol.%SiC	2.89 (0.22)	17.99 (0.05)	13.0 (0.2)
Al_2O_3/10vol.%SiC	3.06 (0.02)	22.59 (0.05)	20.4 (0.4)

K_{IC}: Factor de intensidad de tensiones en modo I (MPa $m^{1/2}$); G_{IC}: Tasa crítica de liberación de energía en modo I (J/m^2); G_F: Energía específica de fractura.

Bibliografía

BIBLIOGRAFÍA

[1] R.J. Brook. Advanced Ceramic Materials: An Overview, p. 1-8 in Concise Encyclopaedia of Advanced Ceramic Materials. Eds. R. J. Brook, R. W. Cahn, M. B. Bever, Pergamon Press, Oxford (UK) (1991).

[2] ASTM C1145:2013. Standard Terminology of Advanced Ceramics. ASTM International, West Conshohocken (PA) (2013).

[3] ISO 20507:2014. Fine ceramics (advanced ceramics, advanced technical ceramics). Vocabulary.

[4] EN ISO 15732:2005. Fine ceramics (advanced ceramics, advanced technical ceramics). Test method for fracture toughness of monolithic ceramics at room temperature by single edge precracked beam (SEPB).

[5] R.W. Davidge. Fundamental of fracture mechanics, p. 31-50 in Mechanical Behaviour of ceramics. Eds. R.W. Cahn, M.W. Thompson, I.M. Ward, Ed. Cambridge University Press, Cambridge (UK) (1979).

[6] G. de Portu, G.N. Balbini. Mechanical properties of ceramics, p. 21-49 in Designing with structural ceramics. Eds. R.W. Davidge, M.H. Van de Voorde, Elsevier Science Publishing, Essex (UK) (1991).

[7] S. Bueno y C. Baudín. Mechanical behaviour of structural ceramics. Boletín de la Sociedad Española de Cerámica y Vidrio, 46 [3] 103-118 (2007).

[8] G.V. Guinea. http://www.mater.upm.es/-> Docencia-> Ingeniero de Materiales-> Propiedades Mecánicas: Comportamiento en Fractura.

[9] A.A. Griffith. The Phenomena of Rupture and Flow in Solids. Philosophical Transactions of the Royal Society of London A: Mathematical, Physical and Engineering Sciences, 221 163-198 (1921).

[10] R.W. Davidge. The Fracture Strength of Ceramics, p. 75-103 in Mechanical Behaviour of Ceramics. Ed. R.W. Cahn, M.W. Thompson, I.M. Ward, Cambridge University Press, Cambridge (UK) (1979).

[11] E. Orowan. Energy criteria of fracture. Welding Research Suplement 34 157-160 (1955).

[12] M. Sakai, R.C. Bradt. Fracture toughness testing of brittle materials. International Materials Reviews 38 53-78 (1993).

[13] R.W. Rice, S.W. Freiman, P.F. Becher. Grain Size Dependence of Fracture Energy in Ceramics: I, Experiment. Journal of the American Ceramic Society 64 [6] 345-350 (1981).

[14] G. Irwin. Analysis of Stresses and Strains Near the End of a Crack Traversing a Plate. Journal of Applied Mechanics 24 361-364 (1957).

[15] H. Westergard. Bearing Pressures and Cracks. Journal of Applied Mechanics 6 49-53 (1939).

[16] A.H. De Aza, J. Chevalier, G. Fantozzi, M. Schehl, R. Torrecillas. Crack growth resistance of alumina, zirconia and zirconia toughened alumina ceramics for joint prostheses. Biomaterials 23 937–945 (2002).

[17] G.R. Irwin. Fracture, p. 551-589 in Encyclopaedia of Physics. Ed. S. Flüge, Springer Verlag, Berlin (Germany) (1958).

[18] D. Casellas, M.M. Nagl, M. Vélez, M. Anglada. Determinación de la presencia de fatiga mecánica en materiales cerámicos. Boletín de la Sociedad Española de Cerámica y Vidrio 38 101-110 (1999).

[19] N. Kondo, T. Ohji, F. Wakai. Strengthening and Toughening of Silicon Nitride by Superplastic Deformation. Journal of the American Ceramic Society 81 [3] 713–16 (1998).

[20] J. Chevalier L. Gremillard, A.V. Virkar, D.R. Clarke. The tetragonal-monoclinic transformation in zirconia: Lessons learned and future trends. Journal of the American Ceramic Society 92 1901-1920 (2009).

[21] K. Niihara. New Design Concept of Structural Ceramics. Ceramic Nanocomposites. Journal of the Ceramic Society of Japan 99 974-982 (1991).

[22] S.M. Choi, H. Awaji. Nanocomposites-a new material design concept. Science and Technology of Advanced Materials 6 2-10 (2005).

[23] G. Evans. Perspective on the Development of High-Toughness Ceramics. Journal of the American Ceramic Society 73 [2] 187-206 (1990).

[24] K.T. Faber. Toughening mechanisms for ceramics in automotive applications. Ceramic Engineering and Science Proceedings 5 [5-6] 408-439 (1984).

[25] P.F. Becher. Microstructural design of toughened ceramics. Journal of the American Ceramic Society 74 [2] 255-269 (1991).

[26] R.W. Steinbrech. Toughening Mechanisms for Ceramic Materials. Journal of the European Ceramic Society 10 131-142 (1992).

[27] M.I. Osendi, J.S. Moya. Fundamentos de la transformación martensítica. Su importancia en el diseño de futuros materiales cerámicos. Boletín de la Sociedad Española de Cerámica y Vidrio 21 [1] 33-40 (1982).

[28] P.M. Kelly, L.R.F. Rose. The martensitic transformation in ceramics – its role in transformation toughening. Progress in Materials Science 47 [5] 463-557 (2002).

[29] J. Rödel. Crack Closure Forces in Ceramics: Characterization and Formation. Journal of the European Ceramic Society 9 323-334 (1992).

[30] P. Miranzo, J.S. Moya. Reforzamiento de materiales cerámicos y vítreos por fibras. Boletín de la Sociedad Española de Cerámica y Vidrio, 27 [3] 145-151 (1988).

[31] R.W. Steinbrech, A. Reichl, W. Schaarwächter. R-Curve Behavior of Long Cracks in Alumina. Journal of the American Ceramic Society 73 [7] 2009-2015 (1990).

[32] H.L. Ewalds, R.J.H. Wanhill. Stable Crack Growth and the R-Curve Concept, p. 86-94 in Fracture Mechanics. Edward Arnold (Publishers) Ltd., London (UK) (1984).

[33] M. Sakai, J. Yoshimura, Y. Goto, M. Inagaki. R-Curve Behaviour of a Polycrystalline Graphite: Microcracking and Grain Bridging in the Wake Region. Journal of the American Ceramic Society 71 [8] 609-16 (1988).

[34] M. Sakai, K. Urashima, M. Inagaki. Energy Principle of Elastic-Plastic Fracture and Its Application to the Fracture Mechanics of a Polycrystalline Graphite. Journal of the American Ceramic Society 66 [12] 868-874 (1983).

[35] G.D. Quinn, R.C. Bradt. On the Vickers indentation fracture toughness test. Journal of the American Ceramic Society 90 673-680 (2007).

[36] 14425-1:2004 (E). Advanced technical ceramics - Test methods for determination of fracture toughness of monolithic ceramics' contains five parts: Part 1: Guide to test method selection.

[37] 14425-2:2004 (E). Advanced technical ceramics - Test methods for determination of fracture toughness of monolithic ceramics' contains five parts: Part 2: Single-edge pre-cracked beam (SEPB) method.

[38] ISO 15732:2003 . Fine ceramics (advanced ceramics, advanced technical ceramics) - Test method for fracture toughness of monolithic ceramics at room temperature by single edge precracked beam (SEPB) method.

[39] EN14425-3:2010. Advanced technical ceramics - Test methods for determination of fracture toughness of monolithic ceramics' contains five parts: Part 3: Chevron notched beam (CNB) method.

[40] 14425-4:2004 (E). Advanced technical ceramics - Test methods for determination of fracture toughness of monolithic ceramics' contains five parts: Part 4: Surface crack in flexure (SCF) method.

[41] ISO 18756:2003 Fine ceramics (advanced ceramics, advanced technical ceramics) - Determination of fracture toughness of monolithic ceramics at room temperature by the surface crack in flexure (SC F) method (ISO 18756:2003).

[42] 14425-5:2004 (E). Advanced technical ceramics - Test methods for determination of fracture toughness of monolithic ceramics' contains five parts: Part 5: Single-edge vee-notch beam (SEVNB) method.

[43] ISO 23146:2012. Fine ceramics (advanced ceramics, advanced technical ceramics) - Test methods for fracture toughness of monolithic ceramics - Single-edge V-notch beam (SEVNB) method.

[44] J.Y. Pastor. Fractura de materiales cerámicos estructurales avanzados, p.37-46. Tesis doctoral. ETSI de Caminos, UPM, Madrid, 1993.

[45] A. H. de Aza, J. Chevalier. Revisión de la técnica de doble torsión y del método experimental en materiales cerámicos. Boletín de la Sociedad Española de Cerámica y Vidrio 40 [2] 93-99 (2001).

[46] D. Wan, Y. Bao, J. Peng, Y. Zhou. Fracture toughness determination of $Ti_3Si(Al)C_2$ and Al_2O_3 using a single gradient notched beam (SGNB) method. Journal of the European Ceramic Society 29 763-771 (2009).

[47] G.D. Quinn, J.J. Kübler, R.J. Gettings. Fracture toughness of advanced ceramics by the surface crack in flexure (SCF) method. A Vamas Round Robin. Technical working area 3 (1994).

[48] K.E. Amin. Toughness, Hardness and Wear, Engineered Materials Handbook: Volume 4, Ceramics and Glasses, ASM International, pp. 599-609 (1991).

[49] T. Nishida, T. Shiono, A. Nagai, T. Nishikawa. Evaluation of fracture toughness for structural ceramics using SEPB specimens. Journal of the Ceramic Society of Japan 96 608-612 (1988).

[50] R.J. Damani, R. Danzer. A method for fracture toughness testing of ceramics-Ready for standardisation. 12th Biennial Conference on Fracture of the European-Structural-Integrity-Society (ECF 12)-Fracture from defects 491-496 (1998).

[51] ESIS TC6 Round Robin on fracture toughness. Fatigue Fracture Engineering Materials Structure 20 513-532 (1997).

[52] R. Damani, R. Gstrein, R. Danzer. Critical notch-root radius effect in SENB-S fracture toughness testing. Journal of the European Ceramic Society 16 695-702 (1996).

[53] S.S. Scherrer, I.L. Denry, H.W.A. Wiskot. Comparison of three fracture toughness testing techniques using a dental glass and a dental ceramic. Dental Materials 14 246–255 (1998).

[54] J. Wang, W.M. Rainforth, I. Wadsworth, R. Stevens. The effects of notch width on the SENB toughness for oxide ceramics. Journal of the European Ceramic Society 10 21-31 (1992).

[55] T. Nishida, Y. Hanaki, G. Pezzotti. Effect of notch-root radius on the fracture toughness of a fine-grained alumina. Journal of the American Ceramic Society 77 606-608 (1994).

[56] T. Fett. Estimated stress intensity factors for semi-elliptical cracks in front of narrow circular notches. Engineering Fracture Mechanics 64 357–62 (1999).

[57] M. Turon-Vinas, M. Anglada. Fracture toughness of zirconia from a shallow notch produced by ultra-short pulsed laser ablation. Journal of the European Ceramic Society 34 3865–3870 (2014).

[58] ESIS Technical Ceramics TC6. VAMAS Technical Working Area 3. Fracture toughness of ceramics using the SEVNB method: round robin (1999).

[59] A. Ghosh, M.G. Jenkins, K.W. White, A.S. Kobayashi, R.C. Bradt. Elevated-temperature fracture resistance of sintered alpha-silicon carbide. Journal of the American Ceramic Society 72 242-247 (1989).

[60] J. Nakayama. Direct Measurement of Fracture Energies of Brittle Heterogeneous Materials. Journal of the American Ceramic Society 48 [11] 583-587 (1965).

[61] J. Nakayama, H. Abe, R.C. Bradt. Crack Stability in the Work-of-Fracture Test: Refractory Applications. Journal of the American Ceramic Society 64 [11] 671-675 (1981).

[62] H.G. Tattersall, G. Tappin. The Work of Fracture and its Measurement in Metals, Ceramics and other Materials. Journal of Materials Science 1 296-301 (1966).

[63] A.M. Calomino, D.N. Brewer. Controlled crack growth specimen for brittle systems. Journal of the American Ceramic Society 75 [1] 206-208 (1992).

[64] B.F. Sorensen, A. Horsewell, O. Jørgensen, A.N. Kumar, P. Engbæk. Fracture resistance measurement method for in situ observation of crack mechanisms. Journal of the American Ceramic Society 81 [3] 661-669 (1998).

[65] J.A. Kuszyk, R.C. Bradt, Influence of Grain Size on Effects of Thermal Expansion Anisotropy in $MgTi_2O_5$. Journal of the American Ceramic Society 56 [8] 420-423 (1973).

[66] B.F. Sorensen, P. Brethe, P. Skov-Hansen. Controlled crack growth in ceramics: The DCB specimen loaded with pure moments. Journal of the European Ceramic Society 16 1021-1025 (1996).

[67] M.E. Ebrahimi, J. Chevalier, G. Fantozzi. R-curve evaluation and bridging stress determination in alumina by compliance analysis. Journal of the European Ceramic Society 23 943-949 (2003).

[68] S. Grendahl, R. Bert, K. Cho, I. Bar-On. Effects of Residual Stress and Loading Geometry on Single-Edge Precracked-Beam (SEPB) Fracture-Toughness Test Results. Journal of the American Ceramic Society 83 [10] 2625–27 (2000).

[69] F.I. Baratta, W.A. Dunlay. Crack Stability in Simply Supported Four-Point and Three-Point Loaded Beams of Brittle Materials. Mechanics of Materials 10 149-159 (1990).

[70] I. Bar-On, F.I. Baratta, K. Cho. Crack Stability and its Effect on Fracture Toughness of Hot Pressed Silicon Nitride Beam Specimens. Journal of the American Ceramic Society 79 [9] 2300-2308 (1996).

[71] R.W. Davidge, G. Tappin. The effective Surface Energy of Brittle Materials. Journal of Materials Science 3 165-173 (1968).

[72] S. Bueno, M.H. Berger, R. Moreno, C. Baudín. Fracture behaviour of microcrack-free alumina-aluminium titanate ceramics with second phase nanoparticles at alumina grain boundaries. Journal of the European Ceramic Society 28 1961-1971 (2008).

[73] LS. Sigl. On the stability of cracks in flexure specimens. International Journal of Fracture 51 241-254 (1991).

[74] L. Biolzi, S. Cangiano, G. Tognon, A. Carpinteri. Snap-back softening instability in high-strength concrete beams. Materials and Structures 22 429-436 (1989).

[75] J.Y. Pastor, J. Planas, M. Elices. Ambient and high-temperature stable fracture tests in ceramics: Applications to Yttria-Partially-Stabilized Zirconia. Journal of the American Ceramic Society 76 [11] 2927-29 (1993).

[76] J.Y. Pastor, J. Planas and M. Elices. A new technique for fracture characterization of ceramics at room and at high temperature. Journal of Testing and Evaluation 23 [3] 209-216 (1995).

[77] J.Y. Pastor, J. Planas, M. Elices. Ensayos de fractura estables en materiales cerámicos. Boletín de la Sociedad Española de Cerámica y Vidrio 31[4] 322-325 (1992).

[78] D. C. Harris. Materials for Infrared Windows and Domes, SPIE Press, Bellingham, WA, (1999).

[79] J.F. Shackelford, W. Alexander, J.S. Park, ed., CRC Materials Science and Engineering Handbook. CRC Press, Boca Raton, Florida, (1994).

[80] S.J. Burnett. Properties of Refractory Materials, UKAEA Research Group Report, Harwell (1969).

[81] C. Aksel, R.W. Davidge, P.D. Warren, F.L. Riley. Investigation of thermal shock resistance in model magnesia-spinel refractory materials. In IV Ceramic Congress, Proceedings Book, Part 1, Eskisehir, Turkey, pp. 193–99, (1998).

[82] O. Khasanov, E. Dvilis, A. Khasanov, E. Polisadova, A. Kachaev. Optical and mechanical properties of transparent polycrystalline $MgAl_2O_4$ spinel depending on SPS conditions. Physica Status Solidi C 10 [6] 918–920 (2013).

[83] R.L. Stewart, R.C. Bradt. Fracture of polycrystalline $MgAl_2O_4$. Journal of the American Ceramic Society 63 619-623 (1980).

[84] C. Baudín, R. Martínez, P. Pena. High-temperature mechanical behavior of stoichiometric magnesium spinel. Journal of the American Ceramic Society 78 1857-1862 (1995).

[85] C. Baudín, P. Pena. Influence of Stoichiometry on Fracture Behaviour of Magnesium Aluminate Spinels at 1200°C. Journal of the European Ceramic Society 17 1501-1511 (1997).

[86] C. Aksel, B. Rand, F.L. Riley, P.D. Warren. Mechanical properties of magnesia-spinel composites. Journal of the European Ceramic Society 22 745–754 (2002).

[87] C.B. Huang, T.C. Lu, L.B. Lin, M.Y. Lei, C.X. Huang. A study on toughening and strengthening of Mg–Al spinel transparent ceramics. Key Engineering Materials 336–338 1207–1210 (2007).

[88] S. Bhaduri, S.B. Bhaduri. Microstructural and mechanical properties of nanocrystalline spinel and related composites. Ceramics International 28 153–158 (2002).

[89] A. Krell , T. Hutzler, J. Klimke. Transmission physics and consequences for materials selection, manufacturing, and applications. Journal of the European Ceramic Society 29 207–221 (2009).

[90] M. Boniecki, Z. Librant, A. Wajler, W. Wesołowski, H. Weglarz. Fracture toughness, strength and creep of transparent ceramics at high temperature. Ceramics International 38 4517–4524 (2012).

[91] A. Ghosh, K.W. White, M.G. Jenkins, R.C. Bradt. Fracture resistance of a transparent $MgAl_2O_4$. Journal of the American Ceramic Society 74 1624-1630 (1991).

[92] K.W. White, G.P. Kelkar. Fracture mechanisms of a coarse-grained, transparent $MgAl_2O_4$ at elevated temperatures. Journal of the American Ceramic Society 75 3440-3444 (1992).

[93] O. Tokariev, R. W. Steinbrech, L. Schnetter, J. Malzbender. Micro- and macro-mechanical testing of transparent $MgAl_2O_4$ spinel. Journal of Materials Science 47 4821–4826 (2012).

[94] O. Tokariev, L. Schnetter, T. Beck, J. Malzbender. Grain size effect on the mechanical properties of transparent spinel ceramics. Journal of the European Ceramic Society 33 749–757 (2013).

[95] O. Borrero-López, A.L. Ortiz, A.D. Gledhill, F. Guiberteau, T. Mroz, L.M. Goldmanc, N.P. Padture. Microstructural effects on the sliding wear of transparent magnesium-aluminate spinel. Journal of the European Ceramic Society 32 3143–3149 (2012).

[96] T. Mroz, L.M. Goldman, A.D. Gledhill, D. Li, N.P. Padture. Nanostructured, infra-red transparent magnesium-aluminate spinel with superior mechanical properties. International Journal of Applied Ceramic Technology 9 83-90 (2012).

[97] K. Morita, B-N. Kim, K. Hiraga, H. Yoshida. Fabrication of high-strength transparent $MgAl_2O_4$ spinel polycrystals by optimizing spark-plasma-sintering conditions. Journal of Materials Research 24 [9] 2863-2872 (2009).

[98] A. Krell, J. Klimke, T. Hutzler. Advanced spinel and sub-μm Al_2O_3 for transparent armour applications. Journal of the European Ceramic Society 29 275–281 (2009).

[99] R.L. Stewart, R.C. Bradt. Fracture of single crystal $MgAl_2O_4$. Journal of Materials Science 15 67-72 (1980).

[100] W. Cao, A. Kundu, Z. Yu, M.P. Harmer, R.P. Vinci. Direct correlations between fracture toughness and grain boundary segregation behavior in ytterbium-doped magnesium aluminate spinel. Scripta Materialia 69 81–84 (2013).

[101] C.C.M. Wu, K.R. McKinney, R.W. Rice. Zig-zag crack propagation in $MgAl_2O_4$ crystals. Journal of Materials Science Letters 14 474-477 (1995).

[102] R.W. Rice, J.J. Mecholsky, Jr.P.F. Becher. Fracture and fracture toughness of stoichiometric $MgAl_2O_4$ crystals at room temperature. Journal of Materials Science 31 1353-1360 (1996).

[103] J. W. McCauley, P. Patel, M. Chen, G. Gilde, E. Strassburger, B. Paliwal, K.T. Ramesh, D.P. Dandekar. AlON: A Brief History of Its Emergence and Evolution. Journal of the European Ceramic Society, 29 [2] 223–236 (2009).

[104] A. Ikesue, T. Kinoshita, K. Kamata, K. Yoshida. Fabrication and Optical Properties of High-Performance Polycrystalline Nd: YAG Ceramics for Solid-State Lasers. Journal of the American Ceramic Society 78 [4] 1033–1040 (1995).

[105] G.C. Wei. Transparent Ceramic Lamp Envelope Materials. Journal of Physics D: Applied Physics 38 3057–3065 (2005).

[106] O. Tokariev, T. Van Gestel, M. Bram, J. Malzbender. Strength enhancement of transparent spinel ceramics. Materials Letters 107 364–366 (2013).

[107] R.W. Rice, J.J. Mecholsky, Jr.P.F. Becher. The effect of grinding direction on flaw caracter and strength of single crystal and polycrystalline ceramics. Journal of Materials Science 16 853-862 (1981).

[108] T.E. Mitchell. Dislocations and Mechanical Properties of $MgO–Al_2O_3$ Spinel Single Crystals. Journal of the American Ceramic Society 82 [12] 3305–16 (1999).

[109] D.H. Chung and W.R. Buessem, in Anisotropy in single crystal refractory compounds, Volume 2, edited by F.W. Valhldrik and S.A. Mersol. Plenum Press, New York, p. 217 (1968).

[110] G. Simmons, H. Wang, in Single crystal elastic constants and calculated aggregate properties: A handbook. MIT Press, Cambridge, Massachusetts, (1971).

[111] J. Briggs. Engineering ceramics in Europe and the USA. Worcester, UK: Menwith Wood (2007).

[112] R.H. Doremus. Alumina. In J. F. Shackelford, & R. H. Doremus (Eds.), Ceramic and glass materials structure, properties and processing. USA: Springer (2008).

[113] E. Dörre, H. Hübner. Alumina. Processing, properties and applications. Berlin, Germany: Springer-Verlag (1984).

[114] W.H. Gitzen. Alumina as a ceramic material. In American ceramic society special publication 4. Ohio, USA: The American Ceramic Society (1970).

[115] L.D. Hart. Alumina chemicals: Science and technology handbook. USA: The American Ceramic Society (1990).

[116] W.D. Kingery. Structure and properties of MgO and Al_2O_3 ceramics. Ohio, USA: The American Ceramic Society (1984).

[117] I. J. McColm. Ceramic hardness. New York, USA: Plenum Press (1990).

[118] F.L. Riley. Structural ceramics. Fundamentals and case studies. Cambridge, UK: Cambridge University Press (2009).

[119] C. Baudín. Processing of alumina and corresponding composites in Comprehensive Hard Materials edited by Vinod K. Sarin, Daniele Mari, Luis Llanes, Christoph E. Nebel. Volume 231-72 (2014).

[120] D. Taylor. Thermal expansion data: III. Sesquioxides, M_2O_3 with the corundum and the A-, B- and C-M_2O_3. British Ceramic Transactions and Journal 83 92–98 (1984).

[121] J.E. Blendell, R.L. Coble. Measurement of stress due to thermal expansion anisotropy in Al_2O_3. Journal of the American Ceramic Society 65 174–178 (1982).

[122] S. Bueno, C. Baudín. Instrumented Vickers microindentation of alumina-based materials. Journal of Material Research, 21, 161–173 (2006).

[123] B. Mussler, M.V. Swain, N. Claussen. Dependence of Fracture Toughness of Alumina on Grain Size and Test Technique. Journal of the American Ceramic Society 65 566-572 (1982).

[124] P.L. Swanson, C.J. Fairbanks, B.R. Lawn, Y-W. Mai, B.J. Hockey. Crack-Interface Grain Bridging as a Fracture Resistance Mechanism in Ceramics: I, Experimental Study on Alumina. Journal of the American Ceramic Society 70 [4] 279-89 (1987).

[125] Y-W. Mai, B.R. Lawn. Crack-interface grain bridging as a fracture resistance mechanism in ceramics: II, Theoretical fracture mechanics model. Journal of the American Ceramic Society 70 [4] 289-94 (1987).

[126] M.N. Rahaman, A. Yao, B.S. Bal, J.P. Garino, M.D. Ries. Ceramics for prosthetic hip and knee joint replacement. Journal of the American Ceramic Society 90 [7] 1965-1988 (2007).

[127] O. Sbaizero, G. Pezzotti and T.Nishida. Fracture energy and R-curve behavior of Al_2O_3/Mo composites. Acta Materialia, 46 [2] 681-687 (1998).

[128] J. Chevalier, L. Gremillard. Ceramics for medical applications: A picture for the next 20 years. Journal of the European Ceramic Society 29 1245–1255 (2009).

[129] P. Palmero, L. Montanaro, H. Reveron, J. Chevalier. Review: Surface Coating of Oxide Powders: A New Synthesis Method to Process Biomedical Grade Nano-Composites. Materials 7 5012-5037 (2014).

[130] N. Claussen, B. Mussler, M.V. Swain. Grain-Size Dependence of Fracture Energy in Ceramics. Journal of the American Ceramic Society C14-C16 (1982).

[131] S.W. Freiman, K.R. McKinney, and H.L. Smith, Slow crack growth in polycrystalline ceramics in Fracture Mechanics of Ceramics, edited by R.C. Bradt, D.P.H. Hasselman, and F.F. Lang (Plenum Press, New York, London), Volume 2, pp. 659–676 (1973).

[132] T.A. Michalske, B.C. Bunker, and S.W. Freiman, Journal of the American Ceramic Society 69 721 (1986).

[133] M.E. Ebrahimi, J. Chevalier, G. Fantozzi. Slow crack-growth behavior of alumina ceramics. Journal of Materials Research 15 142-147 (2000).

[134] S.M. Wiederhorn. Fracture of Sapphire. Journal of the American Ceramic Society 52 [9] 485-91 (1969).

[135] J. Seidel, J. Rödel. Measurement of crack tip toughness in alumina as a function of grain size. Journal of the American Ceramic Society 80 [2] 433-38 (1997).

[136] S. Bueno, C. Baudín. Layered materials with high strength and flaw tolerance based on alumina and aluminium titanate. Journal of the European Ceramic Society 27 1455-1462 (2007).

[137] H. Schneider, J. Schreuer, B. Hildmann. Structure and properties of mullite-A review. Journal of the European Ceramic Society 28 329-344 (2008).

[138] T-I. Mah, K.S. Mazdiyasni. Mechanical properties of mullite. Journal of the American Ceramic Society 66 699-703 (1983).

[139] O. Burgos-Montes, R. Moreno, C. Baudín. Effect of mullite additions on the fracture mode of alumina. Journal of the European Ceramic Society 30 857-63 (2010).

[140] K.S. Mazdiyasni, L.M. Brown. Synthesis and mechanical properties of stoicchiometric aluminum silicate (mullite). Journal of the American Ceramic Society 55 548-552 (1972).

[141] P.C. Dokko, J.A. Pask, K.S. Mazdiyasni. High-Temperature mechanical properties of mullite under compression. Journal of the American Ceramic Society 60 150-155 (1977).

[142] R. Torrecillas, G. Fantozzi, S. de Aza, J.S. Moya. Thermomechanical behaviour of mullite. Acta Materialia 45 897-906 (1997).

[143] E. Fernandez, C. Baudín. Creep damage in different $3Al_2O_3.2SiO_2$ mullites tested in 4-point bending. Journal of the European Ceramic Society 21 2243-2251 (2001).

[144] S. Kanzaki, H. Tabata, T. Kumazawa, S. Ohta. Sintering and mechanical properties of stoichiometric mullite. Journal of the American Ceramic Society 68 C6-C7 (1985).

[145] C. Baudín. Fracture mechanisms in a stoichiometric $3Al_2O_3 \cdot 2SiO_2$ mullite. Journal of Materials Science 32 2077-2086 (1997).

[146] Y. Okamoto, H. Fukudome, K. Hayashi, T. Nishikawa. Creep Deformation of Polycrystalline Mullite. Journal of the European Ceramic Society 6 161-168 (1990).

[147] M.G.M.U. Ismail, Z. Nakai, S. Somiya. Microstructure and mechanical properties of mullite prepared by the sol-gel method. Journal of the American Ceramic Society 70 C7-C8 (1987).

[148] M.I. Osendi, C. Baudín. Mechanical properties of mullite materials. Journal of the European Ceramic Society 16 217-224 (1996).

[149] R. Sivakumar, D. Doni Jayaseelan, T. Nishikawa, S. Honda, H. Awaji. Influence of MgO on microstructure and properties of mullite-Mo composites fabricated by pulse electric current sintering. Ceramics International 27 537-541 (2001).

[150] H. Ohira, M.G.M.U. Ismail, Y. Yamamoto, T. Akiba, S. Somiya. Mechanical Properties of High Purity Mullite at Elevated Temperatures. Journal of the European Ceramic Sociefy 16 225-229 (1996).

[151] M. Itoh, K. Hamano, S. Okada. Preparation of mullite ceramics from kaolin and aluminum hydroxide. In: Abstracts of the 3rd Autumn Symposium on Ceramics, Paper 6-2 A13. Ceramics Society of Japan, Tokyo.

[152] Y. Kumazawa, S. Kanzaki, S. Otha, H. Tabata. Influence of chemical composition on the mechanical properties of SiO_2-Al_2O_3 ceramics. Journal of the Ceramic Society of Japan 96 85-91 (1988).

[153] D. Casellas, C. Baudín, M. Osendi, L. Llanes, M. Anglada. Fracture resistance of mullite under static and cyclic loads. Scripta Materialia 38 39-44 (1998).

[154] B. Subrata. Properties of Refractories in Refractories handbook edited by Charles A. Schacht 1-10 (2004).

[155] R. C. Bradt. Fracture of Refractories in Refractories handbook edited by Charles A. Schacht 10-38 (2004).

[156] H. Harmuth, K. Rieder, M. Krobath, E. Tschegg. Investigation of the nonlinear fracture behaviour of ordinary ceramic refractory materials. Materials Science and Engineering A214 53-61 (1996).

[157] J. Homeny, T. Darroudi, R.C. Bradt. J-Integral measurements of the fracture of 50% alumina refractories. Journal of the American Ceramic Society 63 [5-6] 326-331 (1980).

[158] V.R. Salvini, V.C. Pandolfelli, R.C. Bradt. Extension of Hasselman's thermal shock theory for crack/microstructure interactions in refractories. Ceramics International 38 [7] 5369–5375 (2012).

[159] H. Harmuth, E. K. Tschegg. A fracture mechanics approach for the development of refractory materials with reduced brittleness. Fatigue and Fracture of Engineering Materials and Structures 20 [11] 1585-1603 (1997).

[160] H. Harmuth, R.C. Bradt. Investigation of refractory brittleness by fracture mechanical and fractographic methods. Refractories Manual 6-10 (2010).

[161] G.B. Palmer and G. Baker. A load-cycling technique for R-curve behaviour: application to a low cement refractory. International Journal of Fracture 62 233-244 (1993).

[162] D. R. Larson, J. A. Coppola, D. P. H. Hasselman, R.C. Bradt. Fracture Toughness and Spalling Behavior of High-Al_2O_3. Journal of the American Ceramic Society 57 417-421 (1974).

[163] Z. Chlup, D.N. Boccaccini, C. Leonelli, M. Romagnoli, A.R. Boccaccini. Fracture behaviour of refractory ceramics after cyclic thermal shock. Ceram-Silikaty 50 [4] 245-250 (2006).

[164] Y.C. Ko. Influence of the total fines content on the thermal shock damage resistance of Al_2O_3-spinel castables. Ceramics International 27 [5] 501-507 (2001).

[165] E.K. Tschegg. Austria Patent Specification AT 390 328 (1986).

[166] E. Brühwiler, F.H. Wittmann. The wedge splitting test, a new method of performing stable fracture mechanics tests. Engineering Fracture Mechanics 35 [1/2/3] 117-25 (1990).

[167] H. Harmuth. Stability of crack propagation associated with fracture energy determined by wedge splitting specimen. Theoretical and Applied Fracture Mechanics 23 [1] 103-108 (1995).

[168] H. Harmuth, C. Manhart. Fractographic investigations of ordinary ceramic refractory materials with reduced brittleness. Key Engineering Materials 409 209-215 (2009).

[169] S. Ribeiro, J.A. Rodrigues. The influence of microstructure on the maximum load and fracture energy of refractory castables. Ceramics International 36 263–274 (2010).

[170] S. Ribeiro, D. de Campos Ribeiro, M.B. de Souza Dias, G.C. Ribeiro Garcia, E.M. Bento dos Santos. Study of the Fracture Behavior of Mortar and Concretes with Crushed Rock or Pebble Aggregates. Materials Research 14 [1] 46-52 (2011).

[171] E. Skiera, J. Malzbender, J. Mönch, S. Dudczig, C.G. Aneziris, R.W. Steinbrech. Controlled crack propagation experiments with a novel alumina-based refractory. Advanced Engineering Materials 14 [4] 248-254 (2012).

[172] D.Y. Miyaji, C.Z. Otofuji, J. de Anchieta Rodrigues. The load-displacement curve of steady crack propagation: an interesting source of information for predicting the thermal shock damage of refractories, Proceedings of 13th Biennial Worldwide Conference on Refractories, UNITECR 2013, September 10 to 13, Victoria, BC, Canada (2013).

[173] J. Malzbender, E. Skiera, J. Mönch. A simple methodology to visualize crack propagation for ceramic materials. Journal of Materials Science 49 403–406 (2014).

[174] S. Jin, D. Gruber, H. Harmuth. Determination of Young's modulus, fracture energy and tensile strength of refractories by inverse estimation of a wedge splitting procedure. Engineering Fracture Mechanics 116 228–236 (2014).

[175] Handbook of ceramic composites. Edited by Narottam P. Bansal. Kluwer Academic Publishers (preface) (2005).

[176] M. Sternitzke. Review: structural ceramic nanocomposites. Journal of the European Ceramic Society 1061-1082 (1997).

[177] X. Teng, H. Liu, C. Huang. Effect of Al_2O_3 particle size on the mechanical properties of alumina-based ceramics. Materials Science and Engineering A 452–453 545–551 (2007).

[178] F.C. Zhang, H.H. Luo, T.S. Wang, S.G. Roberts, R.I. Todd. Influence factors on wear resistance of two alumina matrix composites. Wear 265 27–33 (2008).

[179] R.I. Todd, A. Limpichaipanit, Microstructure-property relationships in wear resistant alumina/SiC 'nanocomposites. Advances in Science and Technology 45 555-563 (2006).

[180] A. Mukhopadhyay, R. I. Todd. Microstructure and mechanical properties of Al_2O_3 matrix nanocomposites produced by solid state precipitation. Journal of the European Ceramic Society 1359-1372 (2010).

[181] R.W. Davidge, R.J. Brook, F. Cambier, M. Poorteman, A. Leriche, D. O'Sullivan, S. Hampshire, T. Kennedy. Fabrication, properties, and modelling of engineering ceramics reinforced with nanoparticles of silicon carbide. British Ceramic Transactions 121-127 (1997).

[182] S. Maensiri, S.G. Roberts. Thermal shock resistance of sintered alumina/silicon carbide nanocomposites evaluated by indentation techniques. Journal of the American Ceramic Society 85 [8] 1971-1978 (2001).

[183] S. Maensiri, S.G. Roberts. Thermal shock of ground and polished alumina and Al_2O_3/SiC nanocomposites. Journal of the European Ceramic Society 22 2945-2956 (2002).

[184] C.E. Borsa, N.M.R. Jones, R.J. Brook, R.I. Todd. Influence of processing on the microstructural development and flexure strength of Al_2O_3/SiC nanocomposites. Journal of the European Ceramic Society 17 865-872 (1997).

[185] M. Yoshimura, T. Ohji, K. Niihara. Oxidation-induced toughening and strengthening of Y_2O_3/SiC nanocomposites. Journal of the American Ceramic Society 80 [3] 797-99 (1997).

[186] A. Rendtel, H. Hübner, M. Herrmann, C. Schubert. Silicon nitride/silicon carbide nanocomposite materials: II, Hot strength, creep and oxidation resistance. Journal of the American Ceramic Society 81 [5] 1109-20 (1998).

[187] H. Park, H-E. Kim, K. Niihara. Microstructure and high-temperature strength of Si_3N_4-SiC nanocomposite. Journal of the European Ceramic Society 18 [7] 907-914 (1998).

[188] M. Sternitzke, B. Derby, R.J. Brook. Alumina/silicon carbide nanocomposites by hybrid polymer/powder processing: microstructures and mechanical properties. Journal of the American Ceramic Society 81 [1] 41-48 (1998).

[189] H. Reveron, O. Zaafrani, G. Fantozzi. Microstructure development, hardness, toughness and creep behaviour of pressureless sintered alumina/SiC micro-nanocomposites obtained by slip-casting. Journal of the European Ceramic Society, 30 [6] 1351-1357 (2010).

[190] J. Zhao, L.C. Stearns, M.P. Harmer, H.M. Chan, G.A. Miller. Mechanical behavior of alumina–silicon carbide "nanocomposites". Journal of the American Ceramic Society 76 [2] 503–10 (1993).

[191] J.D. Kuntz, G-D. Zhan, A.K. Mukherjee. Nanocrystalline-Matrix Ceramic Composites for Improved Fracture Toughness. MRS Bulletin 29 [1] 22-27 (2004).

[192] L. Carroll, M. Sternitzke, B. Derby. Silicon carbide particle size effects in alumina-based nanocomposites. Acta Materialia 44 [11] 4543-52 (1996).

[193] R.W. Davidge, P.C. Twigg, F.L. Riley. Effects of silicon carbide nano-phase on the wet erosive wear of polycrystalline alumina. Journal of the European Ceramic Society 16 [7] 799-802 (1996).

[194] D. Zhang, H. Yang, R. Yu, W. Weng. Mechanical properties of alumina composites containing various sizes and fractions of fine SiC particles. Journal of Materials Science Letter 16 877-879 (1997).

[195] A.M. Thompson, H.M. Chan, M.P. Harmer. Tensile creep of alumina-silicon carbide "nanocomposites". Journal of the American Ceramic Society 80 [9] 2221-28, 1997.

[196] M. Sternitzke, E. Dupas, P. Twigg, B. Derby. Surface mechanical properties of alumina matrix nanocomposites. Acta Materialia 45 3963-3973 (1997).

[197] S. Jiao, M.L. Jenkins, R.W. Davidge. Interfacial fracture energy- mechanical behaviour relationship in Al_2O_3/SiC and Al_2O_3/TiN nanocomposites. Acta Materialia 45 [1] 149-156 (1997).

[198] C.C. Anya. Microstructural nature of strengthening and toughening in Al_2O_3-SiC(p) nanocomposites. Journal of Materials Science 34 [22] 5557-5567 (1999).

[199] X. Sun, J-G. Li, Z. Xiu, K. Duan, X. Zhi Hu. Intragranular particle residual stress strengthening of Al_2O_3-SiC nanocomposites. Journal of the American Ceramic Society 88 [6] 1536-1543 (2005).

[200] J.L. Ortiz-Merino, RI. Todd. Relationship between wear rate, surface pullout and microstructure during abrasive wear of alumina and alumina/SiC nanocomposites. Acta Materialia 53 [12] 3345–57 (2005).

[201] A. Limpichaipanit, R.I. Todd. The relationship between microstructure, fracture and abrasive wear in Al_2O_3/SiC nanocomposites and microcomposites. Journal of the European Ceramic Society 29 [13] 2841-2848 (2009).

[202] B. Derby. Ceramic Nanocomposites: mechanical properties. Current Opinion in Solid State and Materials Science 3 490-495 (1998).

[203] H. Awaji, C-H. Chen, N. Kishi, S-M. Choi. Estimation of critical frontal process zone size in ceramics. ECF15. Stockolm 2004.

[204] W.Z. Zhu, J.H. Gao, Z.S. Ding. Microstructure and mechanical properties of a Si_3N_4/Al_2O_3 nanocomposite. Journal of Materials Science 32 537-542 (1997).

[205] Y-K. Jeong, A. Nakahira, K. Niihara. Effects of additives on Microstructure and Properties of alumina-silicon carbide nanocomposites. Journal of the American Ceramic Society 82 [12] 3609-3612 (1999).

[206] U.N.S. Hareesh, M. Sternitzke, R. Janssen, N. Claussen. Processing and properties of sol-gel derived alumina/silicon carbide nanocomposites. Journal of the American Ceramic Society 87 [6] 1024-1030 (2004).

[207] L.P Ferroni, G. Pezzotti. Evidence for bulk residual stress strengthening in Al_2O_3/SiC nanocomposites. Journal of the American Ceramic Society 85 [8] 2033-2038 (2002).

[208] J.L. Ortiz Merino, R.I. Todd. Thermal microstress measurements in Al_2O_3/SiC nanocomposites by Cr^{3+} fluorescence microscopy. Journal of the European Ceramic Society 23 1779-1783 (2003).

[209] I.A. Chou, H.M. Chan, M.P. Harmer. Machining-induced surface residual stress behaviour in Al_2O_3-SiC nanocomposites. Journal of the American Ceramic Society 79 [9] 2403-2409 (1996).

[210] H.Z. Wu, C.W. Lawrence, S.G. Roberts, B.Derby. The strength of Al_2O_3/SiC nanocomposites after grinding and annealing. Acta Materialia 46 [11] 3839-3848 (1998).

[211] C.C. Anya, S.G. Roberts. Indentation fracture toughness and surface flaw analysis of sintered alumina/SiC nanocomposites. Journal of the European Ceramic Society 16 1107-1114 (1996).

[212] G. Pezzotti, T. Nishida, M. Sakai. Physical limitations of the inherent toughness and strength in ceramic-ceramic and ceramic-metal nanocomposites. Journal of the Ceramic Society of Japan 103 [9] 901-909 (1995).

[213] G. Pezzotti, V. Sergo, K. Ota, O. Sbaizero, N. Muraki, T. Nishida, M. Sakai. Residual Stresses and apparent strengthening in ceramic-matrix nanocomposites. Journal of the Ceramic Society of Japan 104 [6] 497-503 (1996).

[214] T. Ohji, A. Nakahira, T. Hirano, K. Niihara, Tensile creep behavior of alumina/silicon carbide nanocomposite. Journal of the American Ceramic Society 77 [12] 3259-3262 (1994).

[215] H. Tomaszewski, M. Boniecki, H. Weglarz. Toughness-curve behaviour of alumina-SiC and ZTA-SiC composites. Journal of the European Ceramic Society 20 1215-1224 (2000).

[216] R.I. Todd, M.A.M. Bourke, C.E. Borsa, R.J. Brook. Neutron diffraction measurements of residual stresses in alumina/SiC nanocomposites. Acta Materialia 45 4 1791-1800 (1997).

[217] S. Jiao, M.L Jenkins, R.W. Davidge. Electron microscopy of crack/particle interactions in Al_2O_3/SiC nanocomposites. Journal of Microscopy 18 2 259-264 (1997).

[218] T. Ohji, T. Hirano, A. Nakahira, K. Niihara. Particle/matrix interface and its role in creep inhibition in alumina/silicon carbide nanocomposites. Journal of the American Ceramic Society 79 1 33-45 (1996).

[219] L.C. Stearns, J. Zhao, M.P. Harmer. Processing and microstructure development in Al_2O_3-SiC 'nanocomposites'. Journal of the European Ceramic Society 10 473-477 (1992).

[220] J. Pérez-Rigueiro, J.Y. Pastor, J. Llorca, M. Elices, P. Miranzo, S. Moya. Revisiting the mechanical behavior of alumina/silicon carbide nanocomposites. Acta Materialia 46 5399-5411 (1998).

[221] L. Gao, H.Z. Wang, J.S. Hong, H. Miyamoto, K. Miyamoto, Y. Nishikawa, D. de la Torre. Mechanical properties and microstructures of nano-SiC-Al_2O_3 composites densified by spark plasma sintering. Journal of the European Ceramic Society 19 609-613 (1999).

[222] C.C. Anya, S.G. Roberts. Pressureless sintering and elastic constants of $A1_20_3$-SiC 'nanocomposites'. Journal of the European Ceramic Society 17 565-573 (1997).

[223] Y.K. Jeong, K. Niihara. Microstructure and mechanical properties of pressureless-sintered Al_2O_3/SiC nanocomposites. Nanostructured Materials 9 193-196 (1997).

[224] H. Kara, S.G. Roberts. Wet erosion behaviour of low SiC alumina-SiC nanocomposites. Journal of Materials Science 37 2421-2426 (2002).

[225] H. Kara, S.G. Roberts. Polishing behavior and surface quality of alumina and alumina/silicon carbide nanocomposites. Journal of the American Ceramic Society 83 5 1219-1225 (2000).

[226] M. Parchoviansky, D. Galusek, J. Sedlácek, P. Svancárek, M. Kasiarová, J. Duszac, P. Sajgalík. Microstructure and mechanical properties of hot pressed Al_2O_3/SiC nanocomposites. Journal of the EuropeanCeramic Society 33 2291–2298 (2013).

[227] M. Jaafar, H. Reveron, C. Esnouf and G. Fantozzia. Highly creep-resistant alumina–SiC nanocomposites processed by spark plasma sintering. Scripta Materialia 68 134–137 (2013).

[228] R. Mohammad-Rahimi, H.R. Rezaie, A. Nemati. Sintering of Al_2O_3–SiC composite from sol–gel method with MgO, TiO_2 and Y_2O_3 addition. Ceramics International 37 1681–1688 (2011).

[229] M. Jaafar, G. Bonnefont, G. Fantozzi, H. Reveron. Intergranular alumina–SiC micro-nanocomposites sintered by spark plasma sintering. Materials Chemistry and Physics 124 377–379 (2010).

[230] I.P. Shapiro, R.I. Todd, J.M. Titchmarsh, S.G. Roberts. Effects of Y_2O_3 additives and powder purity on the densification and grain boundary composition of Al_2O_3/SiC nanocomposites. Journal of the European Ceramic Society 29 1613–1624 (2009).

[231] H. Luo, F. Zhang, T. Wang. Prediction of fracture characteristic of particle reinforced alumina-based composites. Science in China Series E: Technological Sciences 52 864-870 (2009).

[232] A.M. Cock, I.P. Shapiro, RI. Todd, S.G. Roberts. Effects of Yttrium on the Sintering and Microstructure of Alumina–Silicon Carbide ‘‘Nanocomposites”. Journal of the American Ceramic Society 88 [9] 2354–2361 (2005).

[233] D. Sciti, J. Vicens, A. Bellosi. Microstructure and properties of alumina-SiC nanocomposites prepared from ultrafine powders. Journal of Materials Science 37 3747-3758 (2002).

[234] J. Fang, M. P. Harmer, H. M. Chan. Evaluation of subgrain formation in Al_2O_3–SiC nanocomposites. Journal of Materials Science 32 3427-3433 (1997).

[235] X.L. Shi, F.M. Xu, Z.J. Zhang, Y.L. Dong, Y. Tan, L. Wang, J.M. Yang. Mechanical properties of hot-pressed Al_2O_3/SiC composites. Materials Science and Engineering A 527 4646–4649 (2010).

[236] Y.L. Dong, F.M. Xu, X.L. Shi, C. Zhang, Z.J. Zhang, J.M. Yang, Y. Tan. Fabrication and mechanical properties of nano-/micro-sized Al_2O_3/SiC composites. Materials Science and Engineering A 504 49–54 (2009).

[237] A.R. Yazdi, H. Baharvandi, H. Abdizadeh, J. Purasad, A. Fathi, H. Ahmadi. Effect of sintering temperature and siliconcarbide fraction on density, mechanical properties

and fracture mode of alumina–silicon carbide micro/nanocomposites. Materials and Design 37 251–255 (2012).

[238] Y-K. Jeong, A. Nakahira, P.E.D. Morgan, K. Niihara. Effect of Milling Conditions on the Strength of Alumina–Silicon Carbide Nanocomposites. Journal of the American Ceramic Society 80 [5] 1307–309 (1997).

[239] Y. Xu, A. Zangvil, A. Kerber. SiC Nanoparticle-Reinforced Al_2O_3, Matrix Composites: Role of Intra- and Intergranular Particles. Journal of the European Ceramic Society 17 92 l-928 (1997).

[240] Z-Y. Deng, J-L. Shi, Y-F. Zhang, Da-Y Jiang, J-K Guo. Pinning Effect of SiC Particles on Mechanical Properties of Al_2O_3-SiC Ceramic Matrix Composites. Journal of the European Ceramic Society 18 501-508 (1998).

[241] H. Wu, S. G. Roberts and B. Derby. Residual stress and subsurface damage in machined alumina and alumina/silicon carbide nanocomposite ceramics. Acta Materialia 49 507–517 (2001).

[242] G.J. Liu, H.B. Qiu, R.I. Todd , R.J. Brook, and J.K. Guo. Processing and mechanical behaviour of Al_2O_3/ZrO_2 nanocomposites. Materials Research Bulletin 33 [2] 281–288 (1998).

[243] W.H. Tuan, R.Z. Chen, T.C. Wang, C.H. Cheng, P.S. Kuo. Mechanical properties of Al_2O_3/ZrO_2 composites. Journal of the European Ceramic Society 22 2827–2833 (2002).

[244] J. Li, Y-S. Yin, R-X. Shi, L-P. Ma, J. Li. Microstructure and mechanical properties of Al_2O_3–TiC–4vol.%Co composites prepared from cobalt coated powders. Surface & Coatings Technology 200 3705 – 3712 (2006).

[245] J. Li, L. Gao, J. Guo. Mechanical properties and electrical conductivity of TiN–Al_2O_3 nanocomposites. Journal of the European Ceramic Society 23 69–74 (2003).

[246] J. Luo, R. Stevens. The Role of Residual Stress on the Mechanical Properties of Al_2O_3-5vol.% SiC Nano-Composites. Journal of the European Ceramic Society I7 1565-1512 (1991).

[247] R.I. Todd, B. Derby. Thermal stress induced microcracking in alumina–20% SiCp composites. Acta Materialia 52 1621–1629 (2004).

[248] J. Sedlacek, D. Galusek, P. Svancarek, R. Riedel, A. Atkinson, X. Wang. Abrasive wear of Al_2O_3–SiC and Al_2O_3–(SiC)–C composites with micrometer- and submicrometer-sized alumina matrix grains. Journal of the European Ceramic Society 28 2983–2993 (2008).

[249] M. Belmonte, M.I. Nieto, M.I. Osendi, P. Miranzo. Influence of the SiC grain size on the wear behaviour of Al_2O_3/SiC composites. Journal of the European Ceramic Society 26 1273–1279 (2006).

[250] Y.M. Ko, W.T. Kwon, Y-W. Kim. Development of Al_2O_3–SiC composite tool for machining application. Ceramics International 30 2081–2086 (2004).

[251] D. Galusek, J. Sedlacek, R. Riedel. Al_2O_3–SiC composites prepared by warm pressing and sintering of an organosilicon polymer-coated alumina powder. Journal of the European Ceramic Society 27 2385–2392 (2007).

[252] Y-H. Cho, A. Nakahira, K. Niihara. Microstructure and mechanical properties of SiC-platelet reinforced Al_2O_3/SiC-particle hybrid composites. Journal of Materials Science 35 3143-3149 (2000).

[253] J. Wang, S.Y. Lim, S.C. Ng, C.H. Chew, L.M. Gan. Dramatic effect of a small amount of MgO addition on the sintering of Al_2O_3-5vol.% SiC nanocomposite. Materials Letters 33 273-277 (1998).

[254] X. Shi, Y. Tan, F. Xu, J. Li, Y. Dong, L. Wang. Hot-pressed $A1_2O_3$–SiC(–C) composites with polycarbosilane as the precursor. Materials and Design 31 1628–1632 (2010).

[255] Y. Ji, and A. Yeomans. Processing and mechanical properties of Al_2O_3-5 vol.% Cr nanocomposites. Journal of the European Ceramic Society 22 1927-1936 (2002).

[256] T. Sekino, K. Niihara, Microstructural characteristics and mechanical properties for Al_2O_3/metal nanocomposites. Nanostructured Materials 6 663-666 (1995).

[257] T. Sekino, K. Niihara. Fabrication and mechanical properties of fine-tungsten-dispersed alumina-based composites. Journal of Materials Science 32 3943-3949 (1997).

[258] M. Nawa, T. Sekino, K. Niihara. Fabrication and mechanical behaviour of Al_2O_3/Mo nanocomposites. Journal of Materials Science 29 3185-3192 (1994).

[259] T. Sekino, T. Nakajima, S. Ueda, K. Niihara. Reduction and sintering of a nickel-dispersed-alumina composite and its properties. Journal of the American Ceramic Society 80 [5] 1139-1148 (1997).

[260] S-T. Oh, T. Sekino, K. Niihara. Fabrication and mechanical properties of 5 vol.% copper dispersed alumina nanocomposite. Journal of the European Ceramic Society 18 31-37 (1998).

[261] G.D. Zhan, J.D. Kuntz, J. Wan, A.K. Mukherjee. Single-wall carbon nanotubes as attractive toughening agents in alumina-based nanocomposites. Nature materials 2 38-42 (2003).

[262] K.E. Thomson, D. Jiang, W. Yao, R.O. Ritchie, A.K. Mukherjee. Characterization and mechanical testing of alumina-based nanocomposites reinforced with niobium and/or carbon nanotubes fabricated by spark plasma sintering. Acta Materialia 60 622-632 (2012).

[263] R.W. Siegel, B.J. Chang, A.J. Stone, P.M. Ajayan, R.W. Doremus. Mechanical behaviour of polymer and ceramic matrix nanocomposites. Scripta Materialia 44 2061-2064 (2001).

[264] E. Flahaut, A. Peigney, Ch. Laurent, Ch..Marliére, F. Chastel, A. Rousset. Carbon nanotube-metal-oxide nanocomposites: microstructure, electrical conductivity and mechanical properties. Acta Materialia 48 3803-3812 (2000).

[265] I. Levin, W.D. Kaplan, D.G. Brandon, A.A. Layyous. Effect of SiC submicrometer particle size and content on fracture toughness of alumina-SiC 'nanocomposites'. Journal of the American Ceramic Society 78 [1] 254-256 (1995).

[266] H. Awaji, S-M. Choi, E. Yagi. Mechanisms of toughening and strengthening in ceramic-based nanocomposites. Mechanics of Materials 34 411-422 (2002).

[267] H. Yang, F. Shang, L. Gao. Microstructure and mechanical properties of gas pressure sintered Al_2O_3/TiCN composite. Ceramics International 33 1521–1524 (2007).

[268] Z. Shi, J. Wang, G. Qiao, Z. Jin. Effects of weak boundary phases (WBP) on the microstructure and mechanical properties of pressureless sintered Al_2O_3/h-BN machinable composites. Materials Science and Engineering A 492 29–34 (2008).

[269] J. Fang, H.M. Chan, M.P. Harmer. Residual stress relaxation behavior in Al_2O_3-SiC nanocomposites. Materials Science and Engineeriong A 195 163-167 (1995).

[270] I.A. Chou, , H.M. Chan, M.P. Harmer. Effect of annealing environment on the crack healing and mechanical behaviour of silicon carbide-reinforced alumina nanocomposites. Journal of the American Ceramic Society 81 [5] 1203-1208 (1998).

[271] A.M. Thompson, H.M. Chan, M.P. Harmer. Crack healing and stress relaxation in Al_2O_3-SiC 'nanocomposites'. Journal of the American Ceramic Society 78 3 567-571 (1995).

[272] G. Pezzotti, W.H. Müller. Strengthening mechanisms in Al_2O_3/SiC nanocomposites. Computational Materials Science 22 155-168 (2001).

[273] H.Z. Wu, S.G. Roberts, B. Derby. Residual stress distributions around indentations and scratches in polycrystalline Al_2O_3 and Al_2O_3/SiC nanocomposites measured using fluorescence probes. Acta Materialia 56 140–149 (2008).

[274] M.G. Pontin, M.P. Rao, A.J. Sánchez-Herencia, F. Lange. Laminar Ceramics Utilizing the Zirconia Tetragonal-to-Monoclinic Phase Transformation to Obtain a Threshold Strength. Journal of the American Ceramic Society 85 [12] 3041–48 (2002).

[275] HZ. Wang, L. Gao, L.H. Gui, and J.K. Guo. Preparation and properties of intragranular Al_2O_3-SiC nanocomposites. Nanostructured Materials 10 947-953 (1998).

[276] C. Xu, D. Sun. Formation of intragranular nano-structures in micro-sized ceramic composite materials. Materials Science and Engineering A 491 338–342 (2008).

[277] M. Hoffman, J. Rödel. Suggestion for mechanism of strengthening of 'nanotoughened' ceramics. Journal of the Ceramic Society of Japan 105 [12] 1086-1090 (1997).

[278] J. Pérez-Rigueiro, J.Y. Pastor, J. Llorca, M. Elices, J.S. Moya, P.Miranzo, M. Belmonte. Propiedades mecánicas de nanocompuestos de Al_2O_3-SiC. Anales de Mecánica de la Fractura 14 367-371 (1997).

[279] S. Mezquita. Caracterización de Materiales de alúmina-mullita para su uso como herramientas de corte y mecanizado de metales. Proyecto final de carrera ETS Ingeniería de Materiales, UPM.

[280] UNE-EN 993-6:1995. Materiales cerámicos densos conformados. Parte 6: Determinación del modulo de rotura a temperatura ambiente.

[281] G.V. Guinea, J.Y. Pastor, J. Planas and M. Elices. Stress intensity factor, compliance and CMOD for a general three-point-bend beam. International Journal of Fracture 89 103–116 (1998).

[282] J.F. Shackelford, W. Alexander, J.S. Park. CRC Materials Science and Engineering Handbook. CRC Press, Boca Raton, Florida. 537-539 (1994).